

# **Adaptive RF Front-End Circuits**

Proefschrift

ter verkrijgen van de graad van doctor  
aan de Technische Universiteit Delft,  
op gezag van de Rector Magnificus prof. dr. ir. J. T. Fokkema,  
voorzitter van het College voor Promoties,  
in het openbaar te verdedigen op maandag 25 april 2005 om 13:00

door

Aleksandar TASIĆ

Electrical Engineer van Universiteit van Niš, Servie,  
geboren te Niš, Servie.

Dit proefschrift is goedgekeurd door de promotor:  
Prof. dr. J. R. Long

Samenstelling promotiecommissie:

	Rector Magnificus	Voorzitter
Prof. dr.	J.R. Long	Technische Universiteit Delft, promotor
Dr. ir.	W.A. Serdijn	Technische Universiteit Delft, toegevoegd promotor
Prof. dr.	J.N. Burghartz	Technische Universiteit Delft
Prof. dr. ir.	A.H.M. van Roermund	Technische Universiteit Eindhoven
Prof. dr. ir.	B. Nauta	Universiteit Twente
Prof. dr.	L. Larson	University California San Diego
Dr. ir.	M. Sanduleanu	Philips Eindhoven
Prof. dr. ir.	J.H. Huijsing	Technische Universiteit Delft, reservelid

Cover: Adaptive Multi-Standard Image-Reject Downconverter: chip and printed circuit board photographs by A. Tasić.

ISBN 90-9019348-0

Copyright © 2005 by A. Tasić

All rights reserved. No part of the material protected by this copyright notice may be reproduced or utilized in any form or by any means, electronic or mechanical, including photocopying, recording or by any information storage and retrieval system, without prior written permission from the author.

Printed in the Netherlands by Print Partners IPSkamp.

to the missed opportunities,  
to the missed moments of joy,  
to the sleepless nights,  
to you, I owe most.

*Aya*

# CONTENTS

<b>CONTENTS .....</b>	<b>I</b>
-----------------------	----------

<b>LIST OF ABBREVIATIONS .....</b>	<b>VII</b>
------------------------------------	------------

<b>1 INTRODUCTION .....</b>	<b>1</b>
-----------------------------	----------

1.1	<b>Why Silicon?</b>	1
1.2	<b>Why Wireless And RF?</b>	2
1.3	<b>Why Low-Power And Adaptive RF?</b>	4
1.4	<b>Why Multi-Standard And Adaptive RF?</b>	7
1.5	<b>Thesis Objectives</b>	8
1.6	<b>Thesis Outline</b>	8
	<b>References</b>	10

<b>2 PERFORMANCE PARAMETERS OF RF CIRCUITS .....</b>	<b>13</b>
--	-----------

2.1	<b>Gain Parameters</b>	13
2.1.1	Stability	15
2.1.2	Matched Gain Parameters	16
2.2	<b>Nonlinearity Parameters</b>	18
2.2.1	Intermodulation	20
2.2.1.1	Third-order intercept point	21
2.2.1.2	Second-order intercept point	23
2.3	<b>Noise Figure</b>	23
2.4	<b>Phase Noise</b>	26
2.5	<b>Dynamic Range</b>	28
2.6	<b>RF Front-End Performance Parameters</b>	30

2.7	<b>Conclusions</b>	33
	<b>References</b>	33
<b>3</b>	<b>SPECTRUM-SIGNAL TRANSFORMATION . . . . .</b>	<b>39</b>
3.1	<b>Transceiver Architectures</b>	40
3.1.1	Heterodyne Architectures	40
3.1.2	Homodyne Architectures	42
3.1.2.1	Image-reject zero-IF architectures	43
3.1.2.2	Drawbacks of zero-IF architectures	45
3.1.3	Low-IF Architectures	45
3.1.4	Wireless Standards and Employed Architectures	46
3.2	<b>Signal and Spectral Transformations</b>	47
3.3	<b>Mixer-Oscillator Models</b>	52
3.3.1	Double-Real Mixer-Oscillator Model	53
3.3.2	Single-Complex Mixer-Oscillator Model	55
3.3.2.1	Real-to-complex transformation	55
3.3.2.2	Complex-to-real transformation	57
3.3.3	Double-Complex Mixer-Oscillator Model	58
3.4	<b>Image-Rejection Ratio Model</b>	62
3.5	<b>IRR Model of Double-Quadrature Downconverters</b>	64
3.6	<b>Conclusions</b>	67
	<b>References</b>	68
<b>4</b>	<b>SELECTION OF PERFORMANCE PARAMETERS FOR RF FRONT-END CIRCUITS . . . . .</b>	<b>77</b>
4.1	<b>System Considerations</b>	78
4.2	<b>Independent Selection of <i>NF</i> And <i>IIP3</i> Specifications</b>	80
4.3	<b>Mutually Dependent Selection of <i>NF</i> And <i>IIP3</i> Specifications</b>	85
4.3.1	The Optimality Criterion	85

4.3.2	The Equality Criterion	88
4.3.3	Optimality vs. Equality	91
4.4	<b>Equilibrium, Optimality and Equality Criteria</b>	92
4.5	<b>Notes on Power Consumption</b>	94
4.6	<b>Performance Trade-offs in a Single RF Circuit</b>	95
4.7	<b>Conclusions</b>	97
	<b>References</b>	98
<b>5</b>	<b>ADAPTIVITY OF LOW-NOISE AMPLIFIERS . . . . .</b>	<b>101</b>
5.1	<b>Adaptivity Phenomena of Amplifiers</b>	102
5.2	<b>Performance Parameters of Inductively-Degenerated Low-Noise Amplifiers</b>	103
5.2.1	Input-Impedance Model	104
5.2.2	Gain Model	106
5.2.3	Noise Model	107
5.2.3.1	Noise factor	107
5.2.3.2	Minimum noise factor	109
5.2.3.3	Optimum-minimum noise factor	109
5.2.4	Linearity Model	110
5.3	<b>Adaptivity Models for Low-Noise Amplifiers</b>	112
5.4	<b>Conclusions</b>	116
	<b>References</b>	116
<b>6</b>	<b>ADAPTIVE VOLTAGE-CONTROLLED OSCILLATORS . .</b>	<b>119</b>
6.1	<b>Adaptivity Phenomena of Oscillators</b>	120
6.1.1	Phase-Noise Tuning	120
6.1.2	Frequency-Transconductance Tuning	120
6.2	<b>An Adaptive Quasi-Tapped Voltage-Controlled Oscillator</b>	121

<b>6.3</b>	<b>Phase-Noise Model of Quasi-Tapped Voltage-Controlled Oscillators</b>	<b>124</b>
6.3.1	Time-Varying Transfer Function	126
6.3.2	Base-Resistance Noise	127
6.3.3	Transconductor Shot Noise	129
6.3.4	Tail-Current Noise	129
6.3.5	Total Oscillator Noise	131
6.3.6	Resonant-Inductive Degeneration of Tail-Current Source	132
6.3.6.1	Base resistance noise transformation of the resonant-inductive degenerated tail-current source	133
6.3.6.2	Base- and collector-current shot noise transformations of the resonant-inductive degenerated tail-current source	134
6.3.6.3	Total output noise of the resonant-inductive degenerated tail-current source	136
6.3.7	Resistive Degeneration of Tail-Current Source	136
6.3.8	Adaptive Phase-Noise Model	138
6.3.8.1	Linear Phase-Noise Model	138
<b>6.4</b>	<b>Phase-Noise Performance of Quasi-Tapped Voltage-Controlled Oscillators</b>	<b>141</b>
<b>6.5</b>	<b>Adaptivity Figures of Merit of Voltage-Controlled Oscillators</b>	<b>143</b>
6.5.1	Phase-Noise Tuning Range	143
6.5.2	Frequency-Transconductance Sensitivity	144
<b>6.6</b>	<b>K-rail Diagrams – Comprehensive Performance Characterization of Voltage-Controlled Oscillators</b>	<b>147</b>
6.6.1	K-Rail Diagram	148
6.6.2	K-Rails Diagram	149
6.6.3	K-Loop Diagram	151
6.6.4	An All-Round Example	153
<b>6.7</b>	<b>Conclusions</b>	<b>155</b>
	<b>References</b>	<b>156</b>

<b>7</b>	<b>DESIGN OF ADAPTIVE VOLTAGE-CONTROLLED OSCILLATORS AND ADAPTIVE RF FRONT-ENDS . . . . .</b>	<b>159</b>
7.1	<b>An Adaptive Low-Power Voltage-Controlled Oscillator</b>	160
7.1.1	Design for Adaptivity of Voltage-Controlled Oscillators	160
7.1.2	Circuit Parameters of the Adaptive Voltage-Controlled Oscillator	161
7.1.3	Measurement Results for the Adaptive Voltage-Controlled Oscillator	162
7.2	<b>A Multi-Standard Adaptive Voltage-Controlled Oscillator</b>	166
7.2.1	Designing for Adaptivity of Multi-Standard Voltage-Controlled Oscillators	167
7.2.2	Circuit Parameters of the Multi-Standard Adaptive Voltage-Controlled Oscillator	169
7.2.3	Measurement Results for the Multi-Standard Adaptive Voltage-Controlled Oscillator	170
7.3	<b>Multi-Standard Adaptive RF Front-Ends</b>	174
7.3.1	System Considerations for Multi-Standard Adaptive RF Front-Ends	175
7.3.1.1	System requirements for a multi-standard receiver	176
7.3.2	A Multi-Standard Adaptive Quadrature Signal Generator	178
7.3.3	A Multi-Standard Adaptive Quadrature Downconverter	179
7.3.3.1	Mixer circuit parameters	182
7.3.4	Experimental Results for the Multi-Standard Adaptive RF Front-End	183
7.4	<b>Conclusions</b>	188
	<b>References</b>	189
<b>8</b>	<b>CONCLUDING REMARKS . . . . .</b>	<b>193</b>
8.1	<b>Summary</b>	193



<b>A</b>	<b>Real-to-Complex-to-Real Transformation</b>	<b>197</b>
<b>B</b>	<b>Transformed-Feedback Degeneration of Low-Noise Amplifiers</b>	<b>201</b>
	<b>List of Publications</b>	<b>209</b>
	<b>Conclusies</b>	<b>213</b>
	<b>Acknowledgements</b>	<b>217</b>
	<b>Biography</b>	<b>219</b>

# LIST OF ABBREVIATIONS

<b>ADC</b>	Analog to Digital Converter
<b>AFOM</b>	Adaptivity Figure of Merit
<b>BB</b>	Baseband
<b>CAD</b>	Computer-Aided Design
<b>CGM</b>	Frequency-Transconductance Tuning
<b>CMOS</b>	Complementary Metal-Oxide Semiconductor
<b>CPU</b>	Central Processor Unit
<b>D</b> (subscript)	Desired
<b>DC-MO</b>	Double-Complex Mixer-Oscillator
<b>DCS1800</b>	Digital Cellular Communications
<b>DECT</b>	Digital Enhanced Cordless Telecommunications
<b>DR</b>	Dynamic Range
<b>DR-MO</b>	Double-Real Mixer-Oscillator
<b>DSB</b>	Double-Side Band
<b>E</b> (subscript)	Equilibrium
<b>EQ</b> (subscript)	Equivalent
<b>F</b>	Noise Factor
<b>FDD</b>	Frequency-Division Duplex
<b>G (g)</b>	Gain
<b>GMSK</b>	Gaussian Minimum-Shift Keying
<b>GPRS</b>	General Packet Radio Service
<b>GSM</b>	Global System for Mobile Communications
<b>IC</b>	Integrated Circuit
<b>ID</b>	Inductive Degeneration
<b>IDR</b>	Inverse Dynamic Range
<b>IF</b>	Intermediate Frequency
<b>IM2</b>	2 <sup>nd</sup> -Order Intermodulation
<b>IM3</b>	3 <sup>rd</sup> -Order Intermodulation
<b>IIP3TR</b>	Input-Referred 3 <sup>rd</sup> -Order Intercept Point Tuning Range
<b>IITR</b>	Imaginary-Impedance Tuning Range
<b>IP2</b>	2 <sup>nd</sup> -Order Intercept Point
<b>IP3</b>	3 <sup>rd</sup> -Order Intercept Point
<b>IRR</b>	Image-Rejection Ratio
<b>LC</b>	Inductance-Capacitance
<b>LNA</b>	Low-Noise Amplifier

<b>LO</b>	Local Oscillator
<b>MB</b>	Multi-Band
<b>MMS</b>	Multimedia Message Service
<b>MO</b>	Mixer-Oscillator
<b>MP3</b>	Moving Pictures Experts Group Audio Layer 3
<b>MS</b>	Multi-Standard
<b>MSAFE</b>	Multi-Standard Adaptive Front-End
<b>MSK</b>	Minimum Shift Keying
<b>MSM</b>	Multi-Standard Module
<b>NF</b>	Noise Figure
<b>NFTR</b>	Noise-Figure Tuning Range
<b>NI</b>	Noise/Linearity
<b>NT</b>	Non-Tapped
<b>OBT</b> (subscript)	Obtained
<b>OPT</b> (subscript)	Optimum
<b>OPT-MIN</b>	Optimum-Minimum
<b>PCB</b>	Printed-Circuit Board
<b>PN</b>	Phase Noise
<b>PND</b>	Phase-Noise Difference
<b>PN-D</b>	Phase-Noise Demanding
<b>PN-M</b>	Phase-Noise Moderate
<b>PNR</b>	Phase-Noise Ratio
<b>PN-R</b>	Phase-Noise Relaxed
<b>PNTR</b>	Phase-Noise Tuning Range
<b>QPSK</b>	Quadrature-Phase Shift Keying
<b>QT</b>	Quasi-Tapped
<b>RF</b>	Radio Frequency
<b>RD</b>	Resistive Degeneration
<b>RID</b>	Resonant-Inductive Degeneration
<b>RITR</b>	Real-Impedance Tuning Range
<b>RSTR</b>	Source-Impedance Tuning Range
<b>SFDR</b>	Spurious-Free Dynamic Range
<b>SIGE</b>	Silicon-Germanium
<b>SMS</b>	Short Messaging System
<b>SNR</b>	Signal to Noise Ratio
<b>SS</b>	Spectrum Signal
<b>SSB</b>	Single-Side Band
<b>S-UP</b> (subscript)	Start-Up
<b>S_S-UP</b> (subscript)	Safety Start-Up
<b>TCN</b>	Tail-Current Noise
<b>TCS</b>	Tail-Current Source

---

<b>TFD</b>	Transformed-Feedback Degeneration
<b>TDD</b>	Time-Division Duplex
<b>VCO</b>	Voltage-Controlled Oscillator
<b>VG</b>	Voltage Gain
<b>VGTR</b>	Voltage-Gain Tuning Range
<b>WCDMA</b>	Wideband Code Division Multiple Access
<b>WLAN</b>	Wireless Local Area Network
<b>16QAM</b>	16 Symbol Quadrature Amplitude Modulation
<b>2G</b>	2 <sup>nd</sup> -Generation
<b>3G</b>	3 <sup>rd</sup> -Generation

## INTRODUCTION

One emerging worldwide vision of communication is that *wireless communications* and *ambient intelligence* will be highly advantageous in satisfying our yearning for information at any time and anywhere. Electronics that is sensitive to people's needs, personalized to their requirements, anticipatory of their behavior and responsive to their presence is one visionary conception of ambient intelligence [1]. Ambient intelligence technologies are expected to combine concepts of ubiquitous computing and intelligent systems. Technological breakthroughs will allow people to integrate electronics into more friendly environments: roll-up displays [2], intelligent mobiles [3], internet-enabled furniture [4]. People will relate to electronics in a more natural and comfortable way than they do now.

### 1.1 WHY SILICON?

The Greek messenger Phidippides set off for 42km with news of his nation's victory over the invading Persian army at the battle of Marathon in 490 BC, uttering the words "be joyful, we win" on arrival, before promptly dropping dead of exhaustion [5]. Since then, it took humanity some 2400 years to find a harmless way to send a spoken message over a distance.

The technique of using radio waves to send information, exercised by Heinrich Hertz in 1888, and later by Nikola Tesla [6], was demonstrated in 1895 by Guglielmo Marconi [7], who successfully established the first transatlantic radio contact. This event is often referred to as the beginning of wireless communications [8].

At the beginning of the 20<sup>th</sup> century, Lee De Forest developed a triode vacuum tube that allowed for the amplification of an applied signal [9]. Around his amplifier vacuum tube, he developed the first radio- and audio-frequency amplifiers [8]. In the 1930s, scientists at Bell Labs, seeking improved RF demodulation, resorted to the antiquated crystal detector, paving the way to a reliable semiconductor material, *silicon*.

The unreliability, heat dissipation problems and relatively large power consumption of vacuum tubes initiated a search for new means of amplification. In 1947, Walter Brattain and John Bardeen observed that a germanium crystal in touch with wires 0.002 inches apart could amplify an applied signal [10,11]. The point-contact transistor was born. Somewhat later, the junction (sandwich) transistor and field-effect transistor were implemented by William Shockley [12,13]. This trio was awarded the Nobel Prize for the invention of the transistor in 1956. The first commercial use of the transistor was in telephone equipment in the early 1950s [8].

The first transistorized radio appeared in 1954, and was the fastest selling retail object of that time. Using discrete components in those days, transistor circuits occupied a number of printed circuit boards the size of postcards. The idea of integrating a complete circuit on a single slice of silicon was implemented independently in 1958 by Jack Kilby [14] and Robert Noyce [15].

Thanks to techniques such as photolithography and computer-aided design, millions of transistors and other electronic components can be compactly integrated onto a silicon die smaller in size than a cornflake. Integrated circuits (IC) have paved the way to low-cost mass production of electronic equipment. A continuous reduction of the minimum feature sizes, i.e., scaling of microelectronic devices, reduces the cost per function by 25% per year and promotes IC market growth with 17% per year. Doubling of the number of components per chip every 18 months (Moore's Law) [16] has led to improved productivity and improved quality of human life through the proliferation of consumer and industrial electronics.

## 1.2 WHY WIRELESS AND RF?

Progress in silicon IC technology and innovations in IC design have enabled mobility of wireless consumer products and services.

Having started out with limited performance capabilities beyond simple telephony, mobile communications technologies are now entering all aspects of our lives. Mobile equipment today is shaped by user and *application* demands on the one hand and enabling semiconductor process *technologies* as well as radio frequency microelectronics on the other. Main drivers for mobile wireless devices are related to:

- **cost**, which depends on volume of production, size of mobile units, power consumption, and performance.

- **power consumption**, which depends on available frequency spectrum, functionality, and performance.
- **performance**, which depends on applications, standards and protocols.

The factors that make an integrated piece of silicon a desirable item are: mobility, high performance (voice, text and video transfer), low cost (advances in IC processing technology) and long lifetime (low power consumption).

An example of the enormous expansion of the wireless market is shown in Fig. 1.1. At this moment (late 2004), the total number of global mobile users amounts to 1.52 billion, whereas the number of GSM (Global System for Mobile communications) users is estimated at 1.25 billion (82% of the total) [17]. By 2007, the worldwide wireless telephone market is projected to grow to more than 2 billion subscribers [18].

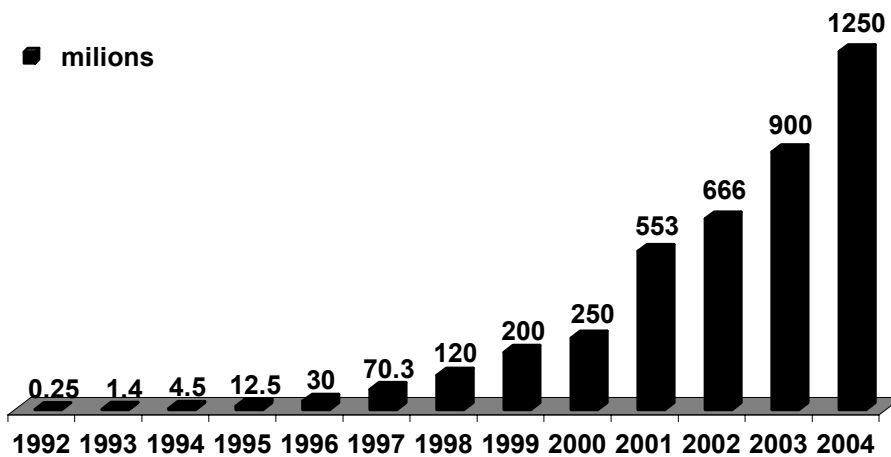


Figure 1.1: GSM growth for the period 1992-2004.

Global handset sales will grow 14% in 2004 to 596 million units, and 11% to 662 million units in 2005, as demand continues in mature markets and surges in developing markets [19]. GSM sales are projected to grow at a Compound Annual Growth Rate of 11% through 2009, as color-, MMS- (Multimedia Messages Service), camera- and Java-enabled devices become widely available, and the cost of wireless services declines [19].

Despite the expansive sales growth of wireless devices, the use of wireless services generates even greater profit for telecom companies. For example, more than 15 billion SMS (Short Messaging System) messages were sent per month across Europe in 2004 [17]. Furthermore, even larger growth requires many new services provided by mobile equipment: MMS, web access, and e-mail. The use of cellular phones for web access is forecast to exceed the use of personal computers as terminals by 2006 [20].

By introducing third-generation (3G) systems [21], more spectrum for voice services has become available, whilst enabling a wider variety of data and multimedia services. 3G handset sales account for 21% of total global sales in 2004. 98% of handsets sold worldwide in 2009 will be 3G devices, with the remainder being primarily GSM handsets sold into emerging markets and very cost sensitive segments of the mature markets [17].

Aside from the mobile phone market [16,21], there are many other wireless applications. Wireless connections to wired computer networks have become feasible. Wireless systems allow for cost-effective installation and deployment of electronics equipment by obviating the need for wires and cables. Wireless RF systems will undoubtedly spawn telemedicine, that is, remote, wireless medical monitoring. An intelligent transportation system that allow for communication and traffic control on the highway is yet another example of a mass market for wireless technology in future. Finally, to support all these applications, more sophisticated RF devices are required.

### **1.3 WHY LOW-POWER AND ADAPTIVE RF?**

The communication devices of today and the future will not only have to support applications ranging from text, telephony, audio, and graphics to video, but they will also have to maintain connections with many other devices in a variety of environments (and not only with a single base station). Moreover, they should be position aware, and perhaps wearable rather than just portable.

Both the lifetime and size of mobile equipment critically depends on the battery. Low-power circuits (e.g., an order of mW for analog front-end circuits [22]) prolong battery lifetime while meeting the performance requirements [22,23]. However, for wearable devices that require the use of the highest-volume and highest-weight density batteries [24], even a low-power design strategy can offer only limited savings.

A combination of multiple functional requirements and a small energy supply is an argument for the design of both adaptive low-power (i.e., power-



aware) hardware and adaptive low-power software. Simply stated, as consumer demands outstrip the cost benefits achieved by Moore's Law and low-power circuit design, a new design direction is found in *adaptivity*. This eventually leads to smaller physical size, longer standby and active times, and enhanced functionality of mobile wearable devices.

The quality of service of mobile devices changes with the position and speed of mobile users. It also depends on the application, the number of users in a cell as well as their activity. A mobile device must handle the variable context efficiently due to scarce resources, especially limited battery power.

A power-aware (i.e., adaptive) RF design approach poses unique challenges: from hardware design to application software, throughout all layers of the underlying communication protocol (i.e., the processing technology, device level, circuit level, system level, as well as protocol level, software and application levels).

A block diagram of the receive part of a typical mobile device is shown in Fig. 1.2. This receiver consists of an analogue RF front-end, an analog baseband (analogue processing of the received signal), and a digital back-end consisting of a dedicated central processing unit (CPU) and a memory.

Whereas the transceiver circuits determine instantaneous power consumption, the average consumption depends on the power management of the complete system [25]. This implies that not only local, but also global (in all layers and at all time) power optimization and awareness are important for extending "lifetime" of mobile devices (time between battery recharges).

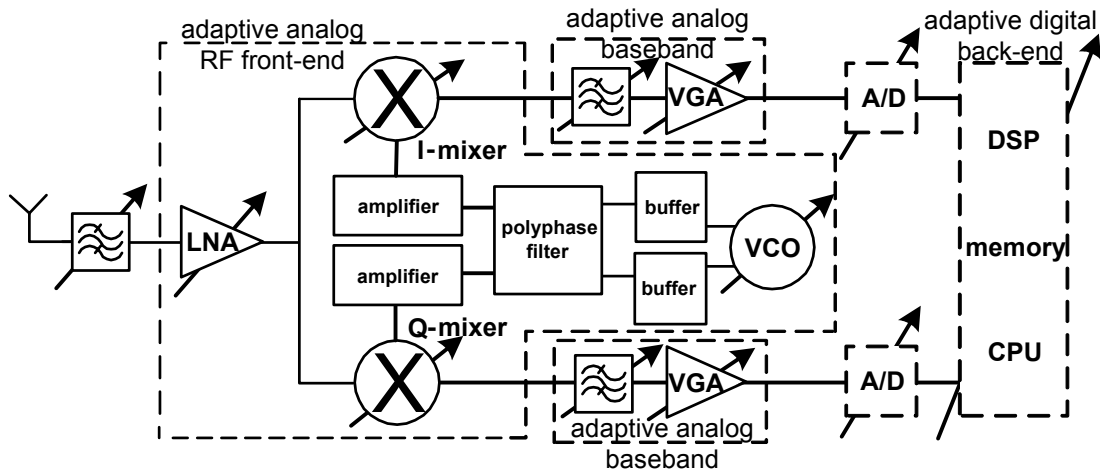


Figure 1.2: Block diagram of an adaptive receiver.

RF and power management have become the fastest growing segments in wireless IC revenue, due to the integration and increasingly complex power requirements, which are driven by advancing functionality (e.g., video, text) and transmission speeds in wireless devices [26]. The RF portion is estimated at \$3.8 billion or 19% of the wireless IC market [26].

Setting the performance parameters of an RF front-end by means of adaptive RF front-end circuitry [27] is a way to manage power consumption in the RF path of a receiver. Adaptive RF front-end circuits (shown in Fig. 1.2), viz., an adaptive low-noise amplifier, an adaptive voltage-controlled oscillator and an adaptive mixer, allow efficient use of scarce battery resources, thereby extending the lifetime of a mobile device. Furthermore, power-conscious adaptive analogue baseband circuits and digital back-end circuits enable complete hardware adaptivity. The theory and design of adaptive RF front-end circuits and adaptive RF front-ends is elaborated in detail in this thesis.

RF front-end robustness can be further improved by control of symbol rates, antenna beam patterns, transmitter power levels, and by control of circuit noise and linearity levels. For example, adaptive modulation and adaptive coding strategies [28], where the system can choose an optimal modulation and coding technique based on the temporal circumstances, can ameliorate the effects of multi-path fading, shadow fading, and path loss.

Graphical interaction with our direct environment combined with mobility is another intriguing concept in which low-power RF circuit design plays an important role [29]. If a lightweight video camera is attached to a mobile display for position tracking and recording of video, the hardware complexity must be reduced in order to keep the power consumption low. Since the RF front-end cannot operate with scarce resources, the power consumption can be reduced by limiting the processing and memory capabilities of the headset unit. In turn, this requires “clever” (power-aware) processing of received and transmitted data.

At an even higher hierarchical level, an example of a power-aware software implementation is the efficiency of a compiled code [30]. An example of application-level adaptivity is scaling the operating power and clock frequency in a general-purpose CPU under the control of power-aware applications, such as video and audio decoding software. Here, dynamic adjustment of the supply voltage can be traded for processor speed, allowing considerable power savings in the digital circuitry [31].

A framework for the exchange of performance and power consumption information between RF receiver, hard disk, CPU, operating system and the application has been developed within the Ubiquitous Communications project [25]. It is an example of a fully adaptive low-power mobile system.

## 1.4 WHY MULTI-STANDARD AND ADAPTIVE RF?

Trends such as the provision of various services (text, audio, video) using different standards and smooth migration towards higher data rates and higher capacities for multimedia applications require designs that work across multiple standards, can easily be reused, and consume the minimum required power.

The increase of the performance per price ratio of radio-frequency integrated circuits (Moore's Law) drives the rapid development of wireless communication systems. The minimum required performance of a certain wireless system is determined by the standard that it implements. By enhancing performance of a system to cover multiple standards, its functionality increases as well. However, more performance for the same price can be achieved if the system hardware can be shared among different standards and adapted to different conditions and requirements [27].

The coexistence of numerous cellular systems requires multi-mode, multi-band, and multi-standard mobile terminals [27]. To prolong talk time, it is desirable to share and/or switch transceiver building blocks in these handsets, without degrading the performance compared to that of single-standard transceivers.

Multi-standard front-ends typically use duplicate circuit blocks, or even entire radio front-ends for each standard. Although this approach is simpler to implement, it is neither optimal in cost nor in power consumption [32]. When different standards do not operate simultaneously, circuit blocks of a multi-standard handset can be shared. By using circuits that are able to trade off power consumption for performance on the fly, i.e., *adaptive multi-standard circuits*, considerable power can be saved. There is currently an apparent migration in RF IC design towards multi-mode multi-band integrated modules for low-noise amplifiers [33], oscillators [34], power amplifiers [12] and transceivers [27]. Design of multi-standard oscillators and multi-standard front-ends is discussed in detail in this thesis.

In addition to multimode capability at radio frequencies, adaptivity should be implemented at baseband frequencies as well. After a signal is downconverted to the baseband, it must be filtered, amplified and digitized. In order to accommodate multiple radio standards with different bandwidths and modulation schemes, such receivers require different channel, and image-reject filter bandwidths and different analogue-to-digital converter (ADC) resolutions. For example, a variable-bandwidth baseband filter and variable-resolution ADC can be used to alternate between different modes of operation [35].

Finally, because adaptive multi-standard low-power RF front-ends are able to share building blocks across different standards, they have advantages over their predecessors: they use a smaller chip area, and most importantly, have a potential for lower overall cost.

## 1.5 THESIS OBJECTIVES

The overall goal of this thesis is to develop design methodologies and a proof-of-concept for analog RF front-end circuits that trade performance for power consumption in an *adaptive* way. This results in a transceiver front-end that either consumes less average power for a given performance or offers better performance for a given average power compared to a conventional transceiver front-end. For low-noise amplifiers and mixers, this comes down to trading off dynamic range for power consumption, whereas for oscillators a trade-off between phase noise or even oscillation frequency and power consumption is possible.

When exploring the fundamental and practical limits of an adaptive radio frequency implementation for multiple communication standards, we have examined basic aspects of the physical mechanisms underlying the operation of *adaptive* RF front-end circuits, and have developed design methodologies for their *structured synthesis*.

The techniques and methodologies developed in this project [36] have been validated by specifying requirements and implementing adaptive wireless receiver circuits and an adaptive wireless receiver front-end for multiple communication standards.

## 1.6 THESIS OUTLINE

After this introductory chapter, basic *definitions* of RF performance parameters are reviewed in Chapter 2, viz., gain, linearity and noise parameters.

Chapter 3 discusses *spectrum* and *signal* (SS) *transformation* in various downconverter topologies. Classification of *mixer-oscillator* (MO) models is then introduced. Using the introduced SS presentation and the MO models, an all-encompassing analysis of a number of RF front-end architectures and RF front-end phenomena is performed.

A procedure to *select* noise and linearity specifications for RF system blocks is described in Chapter 4. Furthermore, an outline is given for the

assigning of the mutually dependent noise and linearity performance parameters to RF front-end circuits. In addition, we derive conditions for the *optimal* dynamic range of a receiver, and for the *equal* noise and linearity improvements with respect to the required performance. Finally, some design trade-offs between performance parameters in a single RF circuit are described by means of a K-rail diagram: this diagram describes graphically the relationships between performance parameters of RF circuits.

Chapter 5 introduces amplifier adaptivity models (i.e., adaptivity figures of merit). They give insight into how low-noise amplifiers can trade performance (noise figure, gain, and linearity) for power consumption in an adaptive way. The performance trade-offs in adaptive low-noise amplifiers are discussed using amplifier K-rail diagrams.

The application of *adaptivity* concepts to voltage-controlled oscillators is discussed in Chapter 6. The concepts of *phase-noise tuning* and *frequency-transconductance tuning* are first introduced. An adaptive oscillator and an adaptive phase-noise model are then presented. The adaptivity figures of merit are derived, viz., the phase-noise tuning range and frequency-transconductance sensitivity. The subject of last section is a comprehensive performance characterization of voltage-controlled oscillators by means of K-rail diagrams. Numerous relationships and trade-offs between oscillator performance parameters, such as voltage swing, tank conductance, power consumption, phase noise, and loop gain, are qualitatively and quantitatively described. Furthermore, the oscillator adaptivity figures of merit are captured using K-rail diagrams.

*Adaptivity* proofs-of-concept are discussed in Chapter 7. An 800MHz voltage-controlled oscillator design is presented with a phase-noise tuning range of 7dB and a factor 3.3 saving in power consumption. In addition, the chapter discusses an *adaptive, multi-standard*, second/third-generation (2G/3G) voltage-controlled oscillator design that satisfies the requirements of DCS1800, WCDMA, WLAN, Bluetooth and DECT standards. Finally, the results of an exploratory circuit design for a multi-standard, adaptive RF receiver front-end (MSAFE) are described. The multi-standard adaptive RF front-end (oscillator and mixers) satisfies the requirements of both 2<sup>nd</sup> and 3<sup>rd</sup> generation standards. This design allows adaptation between different standards by trading RF performance for current consumption. A supply current range from 9.9mA in the relaxed mode (2.4GHz DECT) to 20.2mA in the highest performance mode of operation (1.8GHz DCS1800) is realized.

Chapter 8 concludes and summarizes the thesis.

## REFERENCES

- [1] Philips Research, Ambient Intelligence, [http://www.research.philips.com/technologies/syst\\_softw/ami](http://www.research.philips.com/technologies/syst_softw/ami).
- [2] [http://www.research.philips.com/technologies/syst\\_softw/ami/display.html](http://www.research.philips.com/technologies/syst_softw/ami/display.html)
- [3] Intelligent mobiles: context awareness and Bluetooth, <http://www.research.philips.com/profile/people/researchers/intelligentmobiles.html>
- [4] [http://www.research.philips.com/technologies/syst\\_softw/ami/planet.html](http://www.research.philips.com/technologies/syst_softw/ami/planet.html).
- [5] <http://encyclopedia.thefreedictionary.com/Phidippides>.
- [6] N. Tesla, *Patent No. 645576*, 1897.
- [7] G. Marconi, *Patent No. 763772*, 1904.
- [8] Bell Labs, <http://www.belllabs.com>.
- [9] L. de Forest, “The Audion – Detector and Amplifier”, *Proceedings IRE*, vol. 2, pp. 15-36, March 1914.
- [10] J. Bardeen and W. H. Brattain, “The Transistor, a Semiconductor Triode”, *Physical Review Letters*, 74:230, 1949.
- [11] J. Bardeen and W. H. Brattain, “Conductivity of Germanium”, *Physical Review Letters*, 75:1216, 1949.
- [12] W. Shockley, “The Theory of P-N Junctions in Semiconductors and P-N Junction Transistors”, *Bell System Technology Journal*, 29:435, 1949.
- [13] W. Shockley, “A Unipolar Field-Effect Transistor”, *Proceedings IRE*, vol. 40, pp. 1365-1376, November, 1952.
- [14] U.S. patent number 3138743.
- [15] U.S. patent number 2981887.

[16] ITRS roadmap, 2003 edition, “Radio Frequency and Analog/Mixed-Signal Technologies for Wireless Communications” (a section of the Process Integration Chapter), <http://www.itrs.com>.

[17] *Latest Mobile, GSM, Global, Handset, Base Station, & Regional Cellular Statistics*, <http://www.cellular.co.za/stats/stats-main.htm>.

[18] K. Hyers, Service: Mobile Consumer Markets, Report Number IN0301117GW, Reed Electronics Group, August 2003, <http://www.instat.com>.

[19] N. Mawston, *Global Handset Sales Forecasts 2004 – 2009*, March 2004, <http://www.strategyanalytics.com>.

[20] NEMI Technology Roadmap, 2002 Edition, <http://www.nemi.com>.

[21] 3GPP, <http://www.3gpp.org>.

[22] A. Abidi et al., “Power-Conscious Design of Wireless Circuits and Systems”, *Proceedings IEEE*, vol. 88, no. 10, pp. 1528-1545, October 2000.

[23] M. Pedram and J. Rabaey, *Power Aware Design Methodologies*, Kluwer Academic Publishers, 2002.

[24] L. Holguin et al., “Battery Technology for Mobile Computers”, March 2002, <http://www.dongkang.com.cn/BasicKnowledge/whitepaper/BatteryTechnologyWhitePaper.pdf>

[25] R. L. Lagendijk, Ubiquitous Communications Research Program, Final Program Report, <http://www.ubicom.tudelft.nl>, January 2002.

[26] Electronics Industry Market Research and Knowledge Network, Market Research Report Number DB375, July 2003, [http://www.electronics.ca/reports/ic/rf\\_ics.html#toc](http://www.electronics.ca/reports/ic/rf_ics.html#toc).

[27] A. Tasić, “Design of Adaptive Voltage-Controlled Oscillators and Adaptive RF Front-Ends”, PhD thesis, Chapter 7.

[28] T. Keller and L. Hanzo, “Adaptive Multicarrier Modulation: a Convenient Framework for Time-Frequency Processing in Wireless Communications”, *Proceedings IEEE*, vol. 88, no. 5, pp. 611-640, May 2000.

- [29] W. Pasman et al., "Low-Latency Rendering for Mobile Augmented Reality", *Computers and Graphics*, vol. 23., no. 6, pp. 875-881, 1999.
- [30] A. van der Schaaf et al., "Design of an Adaptive Interface between Video Compression and Transmission Protocols for Mobile Communications", *Proceedings of PV-2001*, pp. 395-404, April 2001.
- [31] J. Pouwelse et al., "Dynamic Voltage Scaling on a Low-Power Microprocessor", *Proceedings Mobicom*, pp. 251-259, July 2001.
- [32] J. Ryyanen, K. Kivekas, J. Jussila, A. Parssinen, K. Halonen, "A dual-band RF front-end for WCDMA and GSM applications", *Proceedings CICC*, pp. 175-178, May 2000.
- [33] H. Hashemi et al., "Concurrent Dual-Band LNAs and Receiver Architectures", *Proceedings VLSI*, pp. 247-250, June 2001.
- [34] A. Tasić, W. A. Serdijn and J. R. Long, "Design of Multi-Standard Adaptive Voltage Controlled Oscillators", *IEEE Transactions on Microwave Theory and Technique*, vol. 53, no. 2, February 2005.
- [35] X. Li and M. Ismail, "Architectures and Specs Help Analysis of Multi-Standard Receivers", <http://www.planetanalog.com/story/OEG20030312S0038>.
- [36] R. L. Lagendijk, Ubiquitous Communications – Updated Technical Annex 2000, P1.4: Low-Power Adaptive Front-End Circuits, STW, January 2000, <http://www.ubicom.tudelft.nl>.



# PERFORMANCE PARAMETERS OF RF CIRCUITS

Interdisciplinarity is essential to RF circuit design. An RF designer is a system designer, an analogue circuit designer, a microwave circuit designer, and a passive and active component designer.

Gain, noise figure, phase noise, distortion, and dynamic range are only a few of the parameters of interest to an RF IC designer, which are reviewed in this chapter. The determination of RF front-end performance parameters closes this chapter.

## 2.1 GAIN PARAMETERS

Current, voltage and power are fundamental circuit design quantities. The choice of the input and output quantities determines the transfer function of a two-port network [1]: power gain, voltage gain, current gain, transconductance gain and transimpedance gain. Usually, signal power is taken as a design variable when maximum power transfer (i.e., conjugate impedance match) is desired [2]. This is required at input of a receiver, because of the impedance match to the receive antenna (in order to avoid signal reflection), between RF front-end circuits in heterodyne receivers, and also when interconnect dimensions are on the order of the signal wavelength (microwave circuit design). On the other hand, voltage and/or current quantities can be the preferable design choice for RF front-end circuits in homodyne receivers where stages reside on-chip and power matching is not required (e.g., the interface between very large and very small impedances).

For a two-port network connected to load impedance  $Z_L$ , source impedance  $Z_S$ , and characterized by a scattering matrix  $[S]$  [3-10] and/or chain matrix  $[ABCD]$  (see Fig. 2.1), a number of gain definitions are in use [11-15].

The *transducer* power gain ( $g_T$ ) stands for the ratio of the power delivered to the load ( $P_L$ ) and the power available from the source ( $P_{AVS}$ ). If  $\Gamma_{IN}$  and  $\Gamma_{OUT}$  are the input and the output reflection coefficients (which characterize quality of input and output two-port impedance matching) and  $\Gamma_S$  and  $\Gamma_L$  the

reflection coefficients of the source and the load respectively, this gain definition becomes [12]:

$$g_T = \frac{P_L}{P_{AVS}} = \frac{|S_{21}|^2 (1 - |\Gamma_L|^2)(1 - |\Gamma_S|^2)}{|1 - \Gamma_{IN}\Gamma_S|^2 |1 - S_{22}\Gamma_L|^2}, \quad (2.1)$$

where  $S_{11}$ - $S_{22}$  are the parameters of the two-port scattering matrix  $[S]$ . The  $S$ -parameters can be directly measured with a vector network analyzer, and are especially useful at high frequencies (e.g., order of GHz) where it is difficult to measure currents and voltages.

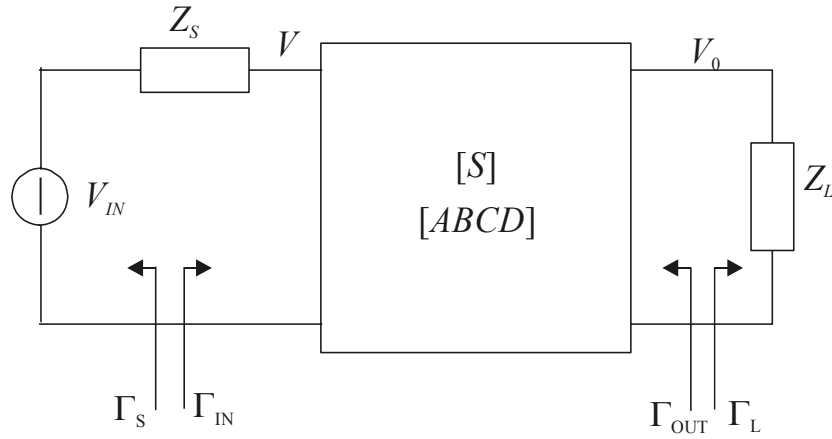


Figure 2.1: A two-port network.

From the relationship between the  $S$ -parameters and chain-matrix parameters ( $A, B, C, D$ ) [13,14], the transducer power gain can also be expressed as:

$$g_T = \frac{4R_L R_S}{|AZ_L + B + CZ_S Z_L + DZ_S|^2}, \quad (2.2)$$

where  $R_S$  and  $R_L$  are the real parts of the source and load impedances, respectively, and  $A$ ,  $B$ ,  $C$  and  $D$  are the parameters of the chain matrix. This matrix is especially useful for characterization of a cascade connection of two-port networks (e.g., a receiver) by multiplying the individual  $ABCD$  matrices of the individual two-ports. In a similar manner, the impedance  $Z$ -parameters and the admittance  $Y$ -parameters can be used to describe the

relationship between total voltages and currents at network ports. Whereas analogue circuit designers are more familiar with voltages and currents (i.e., Z-, Y-, ABCD-parameters), microwave circuit designers prefer S-parameters.

The transducer power gain depends on both the source and the load impedances (i.e., mismatches  $\Gamma_S$  and  $\Gamma_L$ ). This gain parameter can be easily extracted from measurements (required impedance match with signal generator only). Moreover, a maximum operation frequency ( $f_{MAX}$ ) of a device can be directly estimated from the measured unilateral ( $S_{12}=0$ ) transducer power gain.

In the case of matched input and output impedances for a two-port network, the *available* power gain ( $g_A$ ) can be defined. It stands for the ratio of the power available from the two-port network and the power available from the source ( $P_{AVS}$ ). The transducers power gain equals the available power gain when the input and output are power matched simultaneously.

Throughout the thesis we refer to the transducer power gain if only the input power match condition is satisfied. For a simultaneous input and output power match, we refer to the available power gain (that in this case only equals the transducers power gain).

If  $V_S$  is the signal voltage swing at the source and  $V_0$  is the output voltage swing (at the load; see Fig. 2.1), the relationship between the transducer power gain and the voltage gain ( $vg$ , from the source) can be determined:

$$vg^2 = \frac{V_0^2}{V_S^2} = \frac{V_0^2 / R_L}{V_S^2 / 4R_S} \frac{R_L}{4R_S} = g_T \frac{R_L}{4R_S}, \quad (2.3)$$

where the input power match, and real source and load impedances ( $R_S$  and  $R_L$ ) are assumed. When we consider the voltage gain from the input of the two-port network (i.e., not with respect to  $V_S$ ), voltage and power gain definitions are equal when expressed in decibels for  $R_L=R_S$ .

### 2.1.1 STABILITY

Two types of stability are distinguished: unconditional and conditional stability [12,16-18]. If  $\Gamma_{IN}$  and  $\Gamma_{OUT}$  are less than one only for a range of source and load impedances, then the two-port network is conditionally stable, because impedances outside of this range may cause oscillations (i.e., the real part of either the input or output two-port impedance has a negative real part). If  $\Gamma_{IN}$  and  $\Gamma_{OUT}$  are always below one, the two-port is unconditionally stable.

The conditional stability criterion can be expressed as [4]:

$$|\Gamma_{IN}| = \left| S_{11} + \frac{S_{12}S_{21}\Gamma_L}{1 - S_{22}\Gamma_L} \right| < 1 \quad (2.4)$$

$$|\Gamma_{OUT}| = \left| S_{22} + \frac{S_{12}S_{21}\Gamma_S}{1 - S_{11}\Gamma_S} \right| < 1. \quad (2.5)$$

A device is unconditionally stable if *Rollet's* condition [19] (Eq. (2.6)) is satisfied.

$$K = \frac{1 - |S_{11}|^2 - |S_{22}|^2 + |\Delta|^2}{2|S_{21}S_{12}|} > 1 \quad \Delta = S_{11}S_{22} - S_{12}S_{21} < 1. \quad (2.6)$$

As this condition involves constraints on two different parameters, it is difficult to compare the stability of different devices. However, the  $\mu$  test [20,21] for the unconditional stability can be used for both testing and comparison, and is given by Eq. (2.7).

$$\mu = \frac{1 - |S_{11}|^2}{|S_{22} - S_{11}^*\Delta| + |S_{12}S_{21}|} > 1. \quad (2.7)$$

This condition reads as: the larger the  $\mu$ , the better the stability. Generally, figures expressed with  $S$ -parameters can be conveniently mapped and followed using Smith charts [10].

If there is feedback in a circuit, the stability criteria can be related to loop gain and loop phase shift [15].

### 2.1.2 MATCHED GAIN PARAMETERS

Referring to Eq. (2.1), we can distinguish between the gain factors of the source matching network  $g_S$ , Eq. (2.8), of the designed two-port network (Fig. 2.1)  $g_0$ , Eq. (2.9), and of the load matching network  $g_L$ , Eq. (2.10) [11,12].

$$g_S = \frac{1 - |\Gamma_S|^2}{|1 - \Gamma_{IN}\Gamma_S|^2} \quad (2.8)$$

$$g_0 = |S_{21}|^2 \quad (2.9)$$

$$g_L = \frac{1 - |\Gamma_L|^2}{|1 - S_{22}\Gamma_L|^2} \quad (2.10)$$

For the maximum power transfer, the input impedance of the two-port network must be conjugate matched to the impedance of the source-matching network, and the output impedance of the two-port network must be conjugate matched to the impedance of the load-matching network [12]. This condition is satisfied if:

$$\Gamma_{IN} = \Gamma_S^* \quad \Gamma_{OUT} = \Gamma_L^* \quad (2.11)$$

Input and output power match design practice is common to circuits of a heterodyne receiver. If the matching conditions are violated at either the input or the output of an external (usually 50Ω terminated) image-reject or channel-select filter, the passband and stopband characteristics of the filter will exhibit loss and ripples [2].

However, for an ideal voltage or current amplification, different requirements result, as shown in Table 2.1. For example, infinite impedance at the input of the two-port is expected for the maximum voltage gain ( $\Gamma_{IN}=1$ ), whereas zero impedance enables the maximum current gain ( $\Gamma_{IN}=-1$ ). This design practice is common to circuits where power matching is not required (e.g., homodyne receiver circuits).

*Table 2.1: Reflection coefficients for ideal current ( $Z_{IN}=0$ ) and voltage ( $Z_{IN}>\infty$ ) quantities;  $Z_{IN}$  is the input impedance of a two-port network.*

input voltage	input current
$Z_{IN}>\infty, \Gamma_{IN}=1$	$Z_{IN}=0, \Gamma_{IN}=-1$

## 2.2 NONLINEARITY PARAMETERS

As a minimal detectable signal at the input of wireless receivers can be an order of microvolt large, it must be heavily amplified (without distortion) for further processing.

If a system is linear and memoryless, then its output can be presented as:

$$y(t) = ax(t), \quad (2.12)$$

where  $x(t)$  is an input signal and  $y(t)$  is the output signal.

For memoryless nonlinear systems, the input-output relationship has the form

$$y(t) = a_0 + a_1x(t) + a_2x(t)^2 + \dots \quad (2.13)$$

The parameters  $a_i$  are time dependent for time-varying systems.

Whereas a linear model can approximate an RF circuit for small input signals (e.g., -100dBm), for large input signals (e.g., -10dBm) or for heavily amplified signals, an RF circuit is characterized by a nonlinear model.

By inspecting the response to a sinusoidal excitation ( $x(t)=A\cos\omega t$ ) using the nonlinear model (Eq. (2.13)), we can describe numerous nonlinearity phenomena (from Eq. (2.14)).

$$y(t) = \frac{a_2A^2}{2} + (a_1A + \frac{3}{4}a_3A^3)\cos\omega t + \frac{a_2A^2}{2}\cos 2\omega t + \frac{1}{4}a_3A^3\cos 3\omega t + \dots \quad (2.14)$$

In the remainder of this section we will comment on gain compression, desensitization, cross modulation and intermodulation [22-39].

In a symmetric system (odd-order terms eliminated) dominated by the 3<sup>rd</sup>-order term [22,23] (i.e., higher-order terms neglected as they are small compared to lower-order terms), from Eq. (2.14), the gain  $g$  of the nonlinearly modeled system is:

$$g = a_1 + \frac{3}{4}a_3A^2. \quad (2.15)$$

If  $a_3 < 0$ , the gain is a decreasing function of amplitude  $A$ . The 1-dB *compression point* quantifies this gain reduction effect [2]. It is defined as the input signal level at which the gain  $g$  is reduced by 1dB compared to the

linear gain term ( $a_1$ ). From Eq. (2.15), this point is:

$$A_{\text{ldB}} = \sqrt{0.145 \left| \frac{a_1}{a_3} \right|}. \quad (2.16)$$

Note that the signal at the output of an analogue circuit is a result of the combination of the factors: nonlinear model (2.13) as well as bias conditions. Therefore, for very large input signals, the gain can even become zero, because either the output signal is limited by the bias supply quantity (see Fig. 2.2), or  $a_3 < 0$  (see Eq. (2.15)).

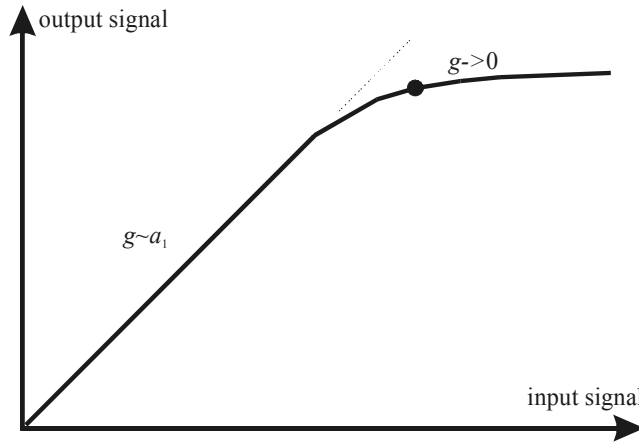


Figure 2.2: A relationship between the input and output signal amplitudes under the constraint of bias (supply) conditions in a nonlinear system.

In the presence of a strong interferer, the desired signal may experience a very small gain. If the signal applied at the input of a nonlinear system has the form (a desired signal at an angular frequency  $\omega_1$  and an interferer at  $\omega_2$ ):

$$x(t) = A_1 \cos \omega_1 t + A_2 \cos \omega_2 t, \quad (2.17)$$

the gain of the desired signal can be calculated after combining Eqs. (2.13) and (2.17). The term representing the content of the output signal around the angular frequency  $\omega_1$  becomes:

$$y(t) \cong \left( a_1 + \frac{3}{2} a_3 A_2^2 \right) A_1 \cos \omega_1 t. \quad (2.18)$$

For sufficiently large  $A_2$ , the gain term may also drop to zero. This effect is referred to as *blocking* [2]. The interferer leading to this effect is called the blocking signal.

If the amplitude of a strong interferer is modulated and applied to the input of a nonlinear system along with a desired signal, then at the output the desired signal experiences the effect of a modulated interferer. This phenomenon is called *cross modulation* [2,24,25].

### 2.2.1 INTERMODULATION

When signals of different frequencies are applied to the input of a nonlinear system, not only does the output exhibit components that are harmonics of the input signals, but also of their combinations. This phenomenon is referred to as *intermodulation* [2,26,27]. If the input signal is given by Eq. (2.17), the following terms are generated at the output of the system (2.13):

$$\text{desired component:} \quad \left(a_1 + \frac{3}{4}a_3A_1^2 + \frac{3}{2}a_3A_2^2\right)A_1 \cos \omega_1 t \quad (2.19)$$

$$2^{\text{nd}}\text{-order distortion component:} \quad a_2A_1A_2 \cos(\omega_1 - \omega_2)t \quad (2.20)$$

$$3^{\text{rd}}\text{-order distortion component:} \quad \frac{3}{4}a_3A_1^2A_2 \cos(2\omega_1 - \omega_2)t \quad (2.21)$$

These are the fundamental component, Eq. (2.19), the second-order intermodulation component, Eq. (2.20), and the third-order intermodulation component, Eq. (2.21).

Due to mismatches in real designs, the distortion that originates from the second-order nonlinearities must be taken into account, even in differential circuits (even components fractional matching below 1% can be critical [28]). Especially, circuits that transform a high-frequency input spectrum to the baseband would suffer from this type of the distortion (e.g., homodyne receivers). This phenomenon is referred to as *second-order intermodulation distortion* [29].

As third-order intermodulation products are located near the desired signal, it is often difficult to filter them out without affecting the information content. It is therefore expected that such in-band products will distort the output signal. The associated phenomenon is referred to as *third-order intermodulation distortion* [2,26,27].



Second- and third-order intercept points characterize the introduced intermodulation distortion phenomena. They are derived in the remainder of this section.

### 2.2.1.1 Third-Order Intercept Point

Referring to Eqs. (2.19) and (2.21), and assuming  $A_1=A_2=A$ , it can be seen that the output power of the third-order products increases with the cube of the input power, whereas the fundamental output power is proportional to the input power [23]. This effect is shown in Fig. 2.3.

A hypothetical intersection point where the first-order power product ( $P_O$ ) and the third-order power product ( $P_{OIM3}$ ) are equal is called *third-order intercept point* (IP3). Table 2.2 describes the notation that is used throughout this thesis.

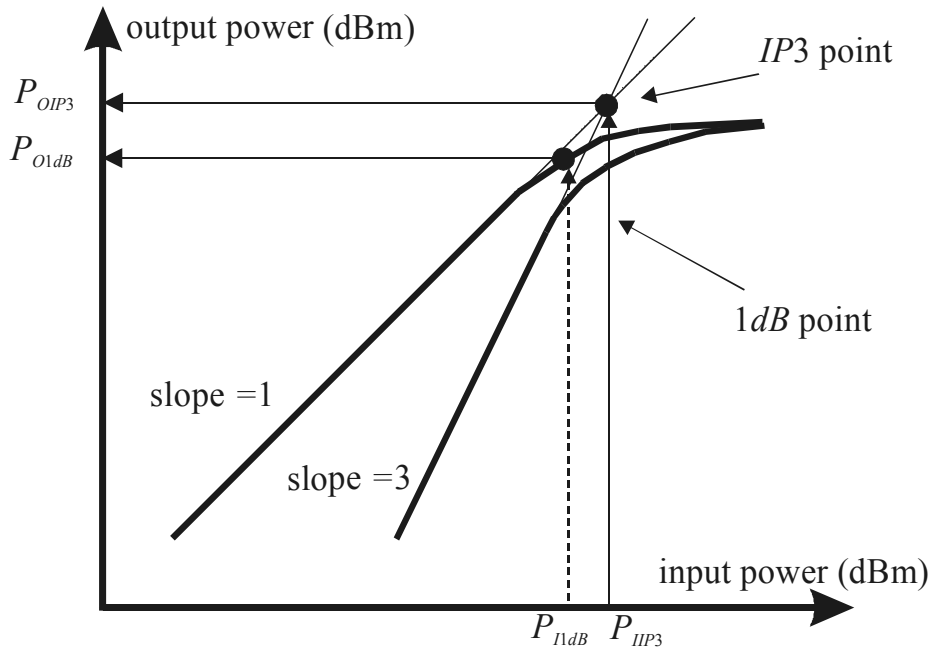


Figure 2.3: Input-output power relationship of a nonlinear device.

If the corresponding power definitions are given by Eq. (2.22),

$$P_O = \frac{1}{2} a_1^2 A^2 \quad P_{OIM3} = \frac{1}{2} \left( \frac{3}{4} a_3 A^2 A \right)^2 = \frac{9}{32} a_3^2 A^6, \quad (2.22)$$

the amplitude of the input-referred 3<sup>rd</sup>-order intercept point ( $A_{IIP3}$ ) becomes

$$A_{IIP3} = \sqrt{\frac{4a_1}{3a_3}}. \quad (2.23)$$

Once the parameters  $a_0, a_1, \dots$  of the corresponding circuit are determined, the intercept point can be calculated. What is more, the effects of distortion can be fully encompassed only by analysis at the circuit level, after all circuit nonlinearity contributors are taken into account [30-37]. For example,  $A_{IIP3}$  for a single bipolar transistor, as derived from Eq. (2.23) using the simplified exponential characteristic [38], is  $A_{IIP3} = \sqrt{8}V_T$  ( $V_T$  is the thermal voltage).

Table 2.2: Amplitude-power-dB scale notation.

parameter\presentation	amplitude	power	dB scale
3 <sup>rd</sup> -order input-intercept point	$A_{IIP3}$	$P_{IIP3}$	$IIP3$
3 <sup>rd</sup> -order output-intercept point	$A_{OIP3}$	$P_{OIP3}$	$OIP3$
3 <sup>rd</sup> -order input-intermodulation point	$A_{IIM3}$	$P_{IIM3}$	$IIM3$
3 <sup>rd</sup> -order output-intermodulation point	$A_{OIM3}$	$P_{OIM3}$	$OIM3$
input desired signal	$A$	$P$	$P$ [dB]
output desired signal	$A_O$	$P_O$	$P_O$ [dB]

The equivalent IIP3 of, most generally, an n-stage cascaded network equals [2,39,40]

$$\frac{1}{A_{IIP3}^2} = \frac{1}{A_{IIP3,1}^2} + \frac{a_1^2}{A_{IIP3,2}^2} + \frac{a_1^2 b_1^2}{A_{IIP3,3}^2} + \dots, \quad (2.24)$$

where  $A_{IIP3,1}, A_{IIP3,2}, \dots$  are the third-order input-intercept amplitudes and  $a_1, b_1, \dots$  are the linear gain coefficients of the corresponding blocks in a receive chain (similar to Eq. (2.13)).

An important conclusion that can be derived from the above result is the inverse proportionality of the first-stage linear gain  $a_1$  and the overall IIP3. Namely, a larger gain of the first stage results in a larger intermodulation product that is responsible for an even larger distortion at the output of the second stage.

Note that IIP3 cannot be obtained directly from measurements, but as an intersection between the extrapolated linear and third-order intermodulation responses (Fig. 2.3), which are, however, obtained for small input signals. The reason for this is that IIP3 is often far beyond the maximal signal range of the system.

### 2.2.1.2 Second-Order Intercept Point

A hypothetical intersection point of the first-order product ( $a_1A$ ) and the second order product ( $a_2A^2$ ) is *second-order intercept point* (IP2) [29]. The amplitude of the input-referred IP2 is defined as:

$$A_{IIP2} = \frac{a_1}{a_2} \quad (2.25)$$

Similar to the derivation of the cascaded IIP3, the cascaded IIP2 can be expressed as:

$$\frac{1}{A_{IIP2}} = \frac{1}{A_{IIP2,1}} + \frac{a_1}{A_{IIP2,2}} + \frac{a_1b_1}{A_{IIP2,3}} + \dots, \quad (2.26)$$

where  $A_{IIP2,i}$  are the input-referred second-order intercept amplitudes of the corresponding cascaded stages.

## 2.3 NOISE FIGURE

The reduction in signal-to-noise ratio (*SNR*) throughout a two-port network is characterized by the *noise factor* [41].

$$F = \frac{SNR_I}{SNR_O} = \frac{S_I / N_I}{S_O / N_O} \quad (2.27)$$

Here,  $SNR_I$  and  $SNR_O$  are the input and output signal-to-noise ratios, respectively.  $S_I$  and  $N_I$  are the input signal power and the input noise power, and  $S_O$  and  $N_O$  are the output signal and noise power (see Fig. 2.4). When expressed in decibels (dB), this ratio is called the *noise figure*.

The general expression for noise factor is given below [42-47],

$$F = F_{MIN} + \frac{R_N}{G_S} \left[ (G_S - G_{OPT})^2 + (B_S - B_{OPT})^2 \right], \quad (2.28)$$

where  $F_{MIN}$  is the minimum noise factor,  $R_N$  the equivalent noise resistance,  $G_S$  and  $B_S$  the source conductance and susceptance, and  $G_{OPT}$  and  $B_{OPT}$  the optimum source admittance parameters corresponding to the minimum noise factor. The source admittances that minimize noise factor and maximize power transfer (impedance match) of a two-port network are usually not the same. Therefore, orthogonal optimization for noise figure and power transfer is required if one wants to enjoy simultaneous noise and power match (if possible). Whereas  $F_{MIN}$  stands for the noise factor achieved under noise-matched conditions, noise resistance  $R_N$  characterizes the sensitivity of the minimum noise figure to changes in the source impedance.

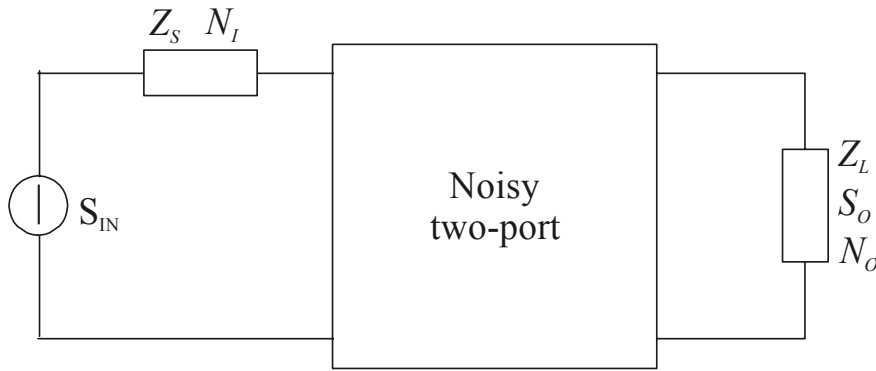


Figure 2.4: A noisy two-port network.

On the other hand, microwave designers are more familiar with the noise-factor definition that is related to reflection coefficients of a two-port network, Eq. (2.29) [4],

$$F = F_{MIN} + 4 \frac{R_N}{Z_0} \frac{|\Gamma_S - \Gamma_{OPT}|^2}{(1 - |\Gamma_S|^2) |1 + \Gamma_{OPT}|^2}, \quad (2.29)$$

where  $\Gamma_{OPT}$  is the optimum reflection coefficient corresponding to the optimum source admittance that provides the minimum noise factor, and  $\Gamma_S$  is the source reflection coefficient.

The noise parameters,  $F_{MIN}$ ,  $R_N$ , and  $\Gamma_{OPT}$ , are characteristics of the device,

and they can be measured with a noise-figure test set, or determined from the device  $S$ -parameters.

Another noise figure of merit is the *noise temperature*,  $T_E$  [48]. By referring to Fig. 2.4, we can establish the relationship between the noise factor and noise temperature as follows.

Parameters of the two-port network are the power gain  $g$ , the bandwidth  $B$ , and the noise temperature  $T_E$ . The noise temperature of the source is  $T_0$ . If the input noise power corresponding to the matched condition and temperature  $T_0=290K$  equals  $N_I=KT_0B$ , the output noise power is:

$$N_O = KB(T_0 + T_E)g. \quad (2.30)$$

Now, the relationship between the noise figure and the equivalent noise temperature can be obtained by combining Eqs. (2.27) and (2.30) as:

$$F = 1 + \frac{T_E}{T_0} \quad T_E = (F - 1)T_0. \quad (2.31)$$

The use of the noise factor is in some situations error prone. Namely, the noise factor for an RF receiver is defined for the input noise level of  $KT_0B$ , i.e., the source temperature  $T_0$ . However, as the noise originating from the source (i.e., an antenna with a noise temperature  $T_A$ ) is generally  $KT_AB$ , the calculation of the output noise power using the noise factor (Eq. (2.32)) is correct only if  $T_A=T_0$ .

$$N_O = N_I F \frac{S_O}{S_I} = N_I F g = KT_A B F g \quad (2.32)$$

Finally, the equivalent noise factor  $F$  for the cascaded connection of the stages is given by Friis formula [49],

$$F = F_1 + \frac{F_2 - 1}{g_1} + \frac{F_3 - 1}{g_1 g_2} + \dots \quad (2.33)$$

where  $g_i$  and  $F_i$  are the power gain and noise factor values of the corresponding stages. Similarly, the equivalent noise temperature  $T_E$  of an  $n$ -stage cascaded system has a form [49]:

$$T_E = T_{E1} + \frac{T_{E2}}{g_1} + \frac{T_{E3}}{g_1 g_2} + \dots \quad (2.34)$$

## 2.4 PHASE NOISE

Power of an oscillation signal (e.g.,  $v(t)$ ) is ideally concentrated at one frequency ( $f_0$ ), so that

$$v(t) = V_0 \cos \omega_0 t \quad (2.35)$$

However, as the oscillation signal is generated by non-ideal (thus noisy) circuit components [46,49-51], the actual power spreads over a number of frequency components (i.e., a frequency range), as shown in Fig. 2.5.

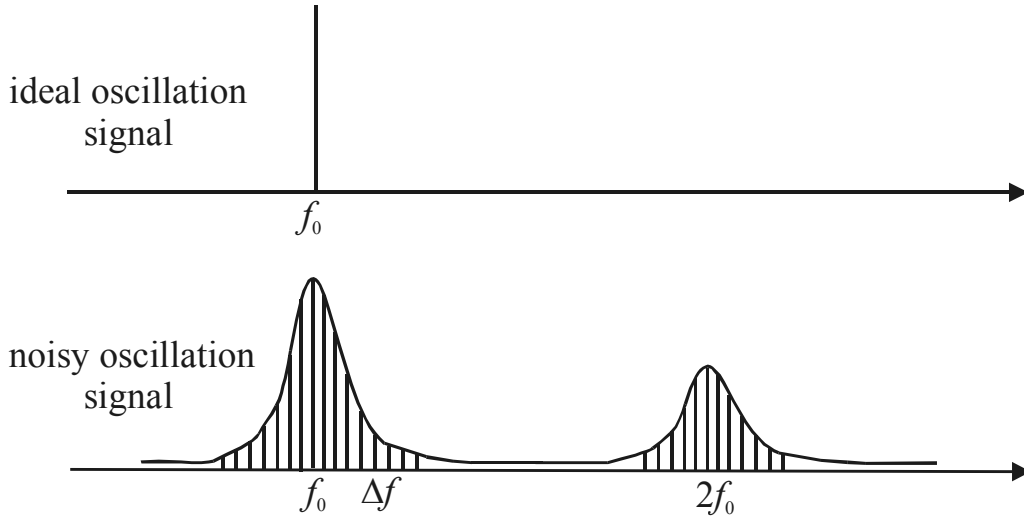


Figure 2.5: Spectra of an ideal and a real (noisy) oscillation signal.

The oscillation-signal skirt is responsible for the mixing of a number of components (desired and undesired) to the same frequency. For example, a desired signal ( $f_{RF}$ ) converts with an oscillation signal ( $f_0$ ) to a low frequency ( $\Delta f = f_{RF} - f_0$ ). On the other hand, an undesired interferer at frequency  $f_{RF} + \Delta f$  converts with the component of the oscillation signal at  $f_0 + \Delta f$  to the same frequency  $\Delta f$ . This phenomenon is referred to as *reciprocal mixing* [2], and it is responsible for the deterioration of the converted desired signal content.

The real (noisy) oscillation signal (Fig. 2.4) has a form,

$$v(t) = V_0(1 + A(t))\cos(\omega_0 t + \Phi(t)) \quad (2.36)$$

where  $A(t)$  is an amplitude-modulated (AM) component and  $\Phi(t)$  is a phase-

modulated (PM) component [52]. The spectral component of the oscillation signal and the corresponding AM and PM noise components at certain offset frequency  $\Delta f$  from the carrier are depicted by Fig. 2.6.

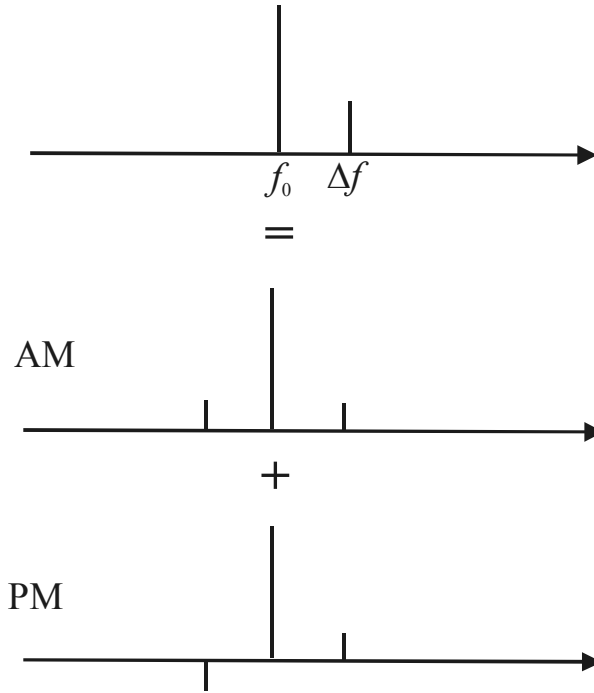


Figure 2.6: AM and PM modulated components of an oscillation signal.

As the AM component can be easily removed by, for example, an amplitude control mechanism of an oscillator [53,54], the PM component determines a deviation from the ideal case (Eq. (2.36)).

Therefore, the noisy nature of oscillators (random variation of oscillation phase) is described by the *phase noise*. This figure of merit is defined as the ratio of the noise power in a 1Hz bandwidth at an offset frequency ( $\Delta f$ ) from the carrier and the signal power (at  $f_0$ ) (see Fig. 2.6) [55,56]. Intuitive Leeson's formulae [56], Eq. (2.37), shows the relationships between the phase noise  $\mathcal{L}$  of a harmonic oscillator and its design parameters, i.e., oscillator noise factor  $F$ , oscillation signal power  $P$ , quality of resonator  $Q$ , and frequency parameters ( $K$  is Boltzman's constant and  $T$  is absolute temperature).

$$\mathcal{L} = F \frac{KT}{2P} \frac{1}{Q^2} \left( \frac{f_0}{\Delta f} \right)^2 \quad (2.37)$$

## 2.5 DYNAMIC RANGE

The capability to process both the weakest and the strongest signals is referred to as *dynamic range*. Among a number of definitions two are most used, viz., the *linear* and *spurious free dynamic range* (SFDR).

The linear dynamic range is defined as a difference between the input signal level that causes 1dB gain compression and the minimum input signal level that can be distinguished from the noise. This is a useful figure for power amplifier designers.

For low-noise amplifiers and mixers, however, operation may be limited by noise at the low end, and the maximum power level for which distortion becomes unacceptable at the high end.

The range where the spurious response is minimal is referred to as spurious free dynamic range. The higher end of the SFDR is determined by the signal power level ( $P_{MAX}$ ) at which the (output) third-order intermodulation product is equal to the noise level ( $N_O$ ). The lower end is related to the *minimum detectable signal*, i.e., a signal power level ( $P_{MIN}$ ) that allows for detection with a desired signal-to-noise ratio and accordingly desired error probability (or bit error rate). The SFDR is defined by Eq. (2.38), whereas a graphical interpretation is given by Fig. 2.7.

$$SFDR[\text{dB}] = P_{MAX}[\text{dB}] - P_{MIN}[\text{dB}] \quad (2.38)$$

In order to calculate the SFDR, we will first determine the relationship between the linear product ( $P_O$ ) and the IM3 product ( $P_{OIM3}$ ) of a nonlinear system (e.g., Eq. (2.13)).

With the aid of Eqs. (2.22) and (2.23), the power of the output 3<sup>rd</sup>-order intermodulation product (see Table 2.1) can be expressed as:

$$P_{OIM3} = \frac{9}{32} a_3^2 A^6 = \frac{a_1^6 A^6 / 8}{4a_1^6 / 9a_3^2} = \frac{P_O^3}{P_{OIP3}^2}. \quad (2.39)$$

Transforming Eq. (2.39) into a dB-scale, the linear input-referred power product becomes:

$$P [\text{dB}] = \frac{2IIP3 + IIM3}{3}. \quad (2.40)$$



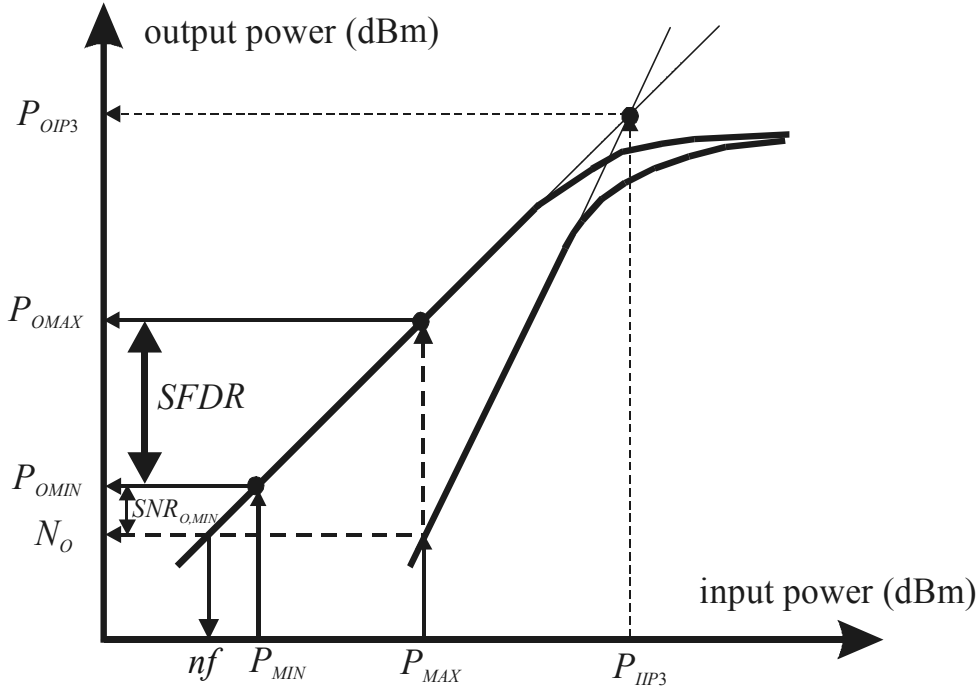


Figure 2.7: Dynamic range analysis.

Now, the maximum input power level ( $P_{MAX}$ ) is obtained by equating the  $IIP3$  with the input-referred system noise floor ( $nf$ ) in accordance with the definition of the  $SFDR$ :

$$P_{MAX} [dB] = \frac{2IIP3 + nf}{3}, \quad (2.41)$$

where

$$nf = 10 \log KTB + NF. \quad (2.42)$$

$K$  is Boltzmann's constant,  $T$  is the absolute temperature, and  $NF$  is the noise figure.

On the other hand, the minimum input power ( $P_{MIN}$ ) refers to the signal power that provides a system with a desired minimal (output) signal-to-noise ratio  $SNR_{O,MIN}$ . This is given by Eq. (2.43).

$$P_{MIN} = nf + SNR_{O,MIN} [dB] \quad (2.43)$$

Finally, the  $SFDR$  is obtained (Eq. (2.44), [2]) as a difference between  $P_{MAX}$  and  $P_{MIN}$ .

$$SFDR[\text{dB}] = \frac{2}{3}(IIP3 - nf) - SNR_{O,MIN}[\text{dB}] \quad (2.44)$$

As the output noise power is  $N_O = g \cdot nf = gkBT_0F$  (assuming a gain  $g$  and an antenna temperature  $T_0$ ), Eq (2.44) transforms into:

$$SFDR[\text{dB}] = \frac{2}{3}(OIP3 - N_O[\text{dB}]) - SNR_{O,MIN}[\text{dB}]. \quad (2.45)$$

This equation allows for the estimation of the distortion-free dynamic range (in 3<sup>rd</sup>-order intermodulation distortion dominated systems) once the output IP3, the output noise power and the minimum signal-to-noise ratio are known.

## 2.6 RF FRONT-END PERFORMANCE PARAMETERS

A block diagram of a part of an RF receiver front-end, consisting of a low-noise amplifier (LNA), a filter, and a mixer, is shown in Fig 2.8. Given the circuit block specifications, a number of receiver performance parameters will be determined, viz., the gain, the noise figure, the linearity, the dynamic range.

In order to put the previously defined parameters into the context of RF front-end circuit design, we will use an example. Let us therefore assume the following operation conditions and circuits' parameters:

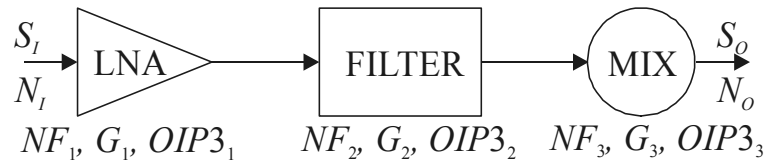


Figure 2.8: A simplified RF front-end receiver model.

- The operation frequency is  $f=1850\text{MHz}$ , the channel bandwidth  $B=200\text{kHz}$ , the bit rate  $R_B=14.4\text{kb/s}$ , the desired error probability  $P_E=10^{-5}$ , and the modulation *GMSK* type [2].

- The transmit power is  $P_T[\text{dBm}]=30$ , the transmit antenna gain  $G_T=1\text{dB}$ , the minimum distance between receiver and transmitter  $R_{MIN}=10\text{m}$ , the receive antenna gain  $G_R=1\text{dB}$ , and the antenna noise temperature  $T_A=900\text{K}$ .
- The power gains  $G_i$ , noise figures  $NF_i$  and output intercept points  $OIP3_i$  of the corresponding blocks (see Fig. 2.8) are given in Table 2.3.

Table 2.3: Performance parameters of the receiver circuits.

Performance\Blocks	LNA	RF Filter	Mixer
$G$	15dB	-2dB	4dB
$NF$	2dB	2dB	14dB
$OIP3$	15dBm	-	10dBm

Referring to the definitions and calculations of the previous sections, we can determine the receiver performance parameters as follows.

- The system power gain is

$$G = G_1 + G_2 + G_3. \quad (2.46)$$

Substituting values given in Table 2.4, results into  $G=17\text{dB}$ .

- The system noise factor is

$$F = F_1 + \frac{F_2 - 1}{g_1} + \frac{F_3 - 1}{g_1 g_2}, \quad (2.47)$$

where  $g_1$  and  $g_2$  are the linear gain terms (total gain  $g=g_1 g_2$ ). For the given noise-figure values,  $NF=10\log F=4.6\text{dB}$ .

- The system  $IIP3$  is

$$IIP3 = -10\log(10^{\frac{OIP3_1 - G_1}{10}} + 10^{\frac{OIP3_2 - G_2 - G_1}{10}} + 10^{\frac{OIP3_3 - G_3 - G_2 - G_1}{10}}). \quad (2.48)$$

For the given  $OIP3$  values,  $IIP3 = -2.1$  dBm.

- The output noise power is

$$N_O = K[T_A + (F - 1)T_0]Bg. \quad (2.49)$$

- The minimum output SNR [52] is

$$SNR_{O,MIN} = \frac{R_B}{B} \frac{E_B}{n_O}, \quad (2.50)$$

where the energy-per-bit-to-noise ratio,  $E_B/n_O$ , can be determined from:

$$P_E = \frac{1}{2} \operatorname{erfc}\left(\sqrt{\frac{E_B}{n_O}}\right) \quad (2.51)$$

- The spurious free dynamic range [2] is

$$SFDR[dB] = \frac{2}{3}(OIP3 - N_0[dB]) - SNR_{O,MIN}[dB]. \quad (2.52)$$

- The minimum detectable input signal (the receiver sensitivity) [2] is

$$S_I = P_{MIN} = SNR_{O,MIN} \frac{N_0}{g} = SNR_{O,MIN} KB[T_A + (F - 1)T_0]. \quad (2.53)$$

- The required receiver dynamic range (DR) [12] is

$$P_{MIN} = S_I \quad P_R \Big|_{R=R_{MIN}} = \frac{g_R g_T P_T \lambda^2}{(4\pi R_{MIN})^2} \quad (2.54)$$

$$DR = P_R \Big|_{R=R_{MIN}} [dB] - P_{MIN}[dB]. \quad (2.55)$$

$P_R$  is the receive signal power (a more accurate model can be found in [57]),  $\lambda$  the signal wavelength, and  $g_T$  and  $g_R$  the corresponding linear gain terms.

As the sensitivity depends on the minimum SNR, which depends on the ratio of the bit energy and the noise-power spectral density, where the latter is

related to the desired probability of error, this implies that the dynamic range is dependent on both the modulation type and the SNR.

- The maximum range of operation,  $R_{MAX}$  [12], is

$$R_{MAX} = \sqrt{\frac{P_T g_T g_R \lambda^2}{(4\pi)^2 P_R}}, \quad (2.56)$$

if the required receive signal power equals

$$P_R = E_B R_B = \frac{E_B}{n_0} n_0 R_B = \frac{E_B}{n_0} K[T_A + (F - 1)T_0]R_B. \quad (2.57)$$

## 2.7 CONCLUSIONS

A number of definitions essential to RF design are outlined in this chapter. The gain, nonlinearity and noise parameters are revisited, followed by a discussion on the dynamic range and the RF system performance.

The reviewed parameter definitions form a base for the characterization of the RF circuits and systems.

## REFERENCES

- [1] E. H. Nordholt, *Design of High-Performance Negative-Feedback Amplifiers*, PhD Thesis, TU Delft, The Netherlands, 1980.
- [2] B. Razavi, *RF Microelectronics*, Prentice Hall, Upper Saddle River, 1998.
- [3] K. Kurokawa, "Power Waves and the Scattering Matrix", *IEEE Transactions on Microwave Theory and Techniques*, vol. MTT-13, no. 2, March 1965.
- [4] F. Weinert, "Scattering Parameters Speed Design of High-Frequency Transistor Circuits", *Electronics*, vol. 39, no. 18, Sept. 5, 1966.

- [5] G. Fredricks, "How to Use S-Parameters for Transistor Circuit Design", *Proceedings IEEE*, vol. 14, no. 12, Dec. 1966.
- [6] H. W. Froehner, "Quick Amplifier Design with Scattering Parameters", *Electronics*, October 16, 1967 [HP Application Note 95, pp. 5-1,511].
- [7] E. G. Bodway, "Two-Port Power Flow Analysis Using Generalized S Parameters," *Microwave Journal*, vol. 10-6, May 1967 [HP Application Note 95, pp. 6-1~6-9].
- [8] R. P. Doland et al., "S-Parameter Techniques for Faster, More Accurate Network Design," *Hewlett-Packard Journal*, V18-6, February 1967 [HP Application Note 95 pp.3-1~3-12].
- [9] R. W. Anderson, "S-Parameter Techniques for Faster, More Accurate Network Design", *Hewlett-Packard Application Note 95-1*, PN 5952-1130. This is a reprint of the article in the Hewlett-Packard Journal, vol.18, no. 6, February 1967.
- [10] P. H. Smith, "Electronic Applications of the Smith Chart in Waveguide, Circuit and Component Analysis", *Noble Publishing Classic Series*, ISBN-1-884932-39-8, Georgia, 1995.
- [11] G. Gonzalez, *Microwave Transistor Amplifiers: Analysis and Design*, ISBN 0-13-581646-7, Prentice Hall, 1984.
- [12] D. Pozar, *Microwave and RF Wireless Systems*, Wiley, New York, 2001.
- [13] F. B. Llewellyn, "Some Fundamental Properties of Transmission Systems", *Proceedings of the IRE*, March 1952.
- [14] I. Bahl and P. Bhartia, *Microwave Solid-State Circuits Design*, John Willey & Sons, INC, 2003.
- [15] C. J. M. Verhoeven et al., *Structured Electronic Design, Negative-Feedback Amplifiers*, Kluwer Academic Publishers, The Netherlands, 2003.
- [16] P. A. Rizzi, *Microwave Engineering Passive Circuitry*, Prentice Hall, INC, NJ07632, 1998.

- [17] A. P. Stern, "Stability and Power Gain of Tuned Transistor Amplifiers", *Proceedings of the IRE*, vol. 45, pp. 335-343, March 1957.
- [18] E. F. Bolinder, "Survey of Some Properties of Linear Networks", *IRE Transactions on Circuit Theory*, September 1957.
- [19] J. M. Rollett, "Stability and Power-Gain Invariants of Linear Two-Ports", *IRE Transactions on Circuit Theory*, vol. 9, no. 3, pp. 29-32, March 1962.
- [20] M. L. Edwards and J. H. Sinsky, "A New Criterion for Linear Two-Port Stability Using a Single Geometrically Derived Parameter," *IEEE Transactions on Microwave Theory and Techniques*, vol. 40, no. 12, pp. 2303-2311, December 1992.
- [21] G. Lombardi, B. Neri, "Criteria for the Evaluation of Unconditional Stability of Microwave Linear Two-Ports: A Critical Review and New Proof", *IEEE Transactions on Microwave Theory and Techniques*, vol. 47, no. 6, pp. 746-751, June 1999
- [22] O. F. Bokk and E. B. Gribov, "Small-Signal Calculation of the Amplitude of the Third-Order Combination Frequency in a Transistor Amplifier", *Telecommunications and Radio Engineering*, vol. 24, no. 3, pp. 125-129, March 1969.
- [23] K. A. Simons, "The Decibel Relationship between Amplifier Distortion Products", *Proceedings IEEE*, no. 7, pp. 1071-1086, July 1970.
- [24] M. Akgun and M. J. O. Strutt, "Cross Modulation and Nonlinear Distortion in RF Transistor Amplifiers," *IRE Transactions on Electron Devices*, pp. 457-467, October 1959.
- [25] B. Ebstein, R. Huenemann and R. Sea, "The Correspondence of Intermodulation and Cross Modulation in Amplifiers and Mixers", *Proceedings of the IEEE*, pp. 1514-1516, August 1967, (see comments in pp. 355-357, March 1968).
- [26] B. H. Goldberg, "Predict Intermodulation Distortion", *Electronic Design*, pp. 76-78, May 1970.
- [27] M. E. Goldfarb, "Intermodulation Products," *Microwave Journal*, pp. 297-301, May 1985.

- [28] L. Sheng, C. Jensen and L. E. Larson, "A Wide-Bandwidth Si/SiGe HBT Direct Conversion Sub-Harmonic Mixer/Downconverter", *IEEE Journal of Solid-State Circuits*, vol. 35, no. 9, pp. 1329-1337, September 2000.
- [29] J. Rudell et al. "An Integrated GSM/DECT Receiver: Design Specifications", UCB Electronics Research Laboratory Memorandum, Memo no. UCB/ERL M97/82, 1998.
- [30] D. Dewitt and A. L. Rossoff, *Transistor Electronics*, McGraw-Hill, 1957.
- [31] C. A. Desoer, "Nonlinear Distortion in Feedback Amplifiers," *IRE Transactions on Circuit Theory*, pp. 2-6, March 1962.
- [32] D. M. Duncan, "Non-Linearity in Transistor Amplifiers", *Proceedings of the IREE* (Australia), pp. 149-157, March 1964.
- [33] Y. L. Kuo, "Distortion Analysis of Bipolar Transistor Circuits", *IEEE Transactions on Circuit Theory*, vol. CT-20, no. 6, pp. 709-716, November 1973.
- [34] G. C. van Slagmaat, "Non-Linear Distortion of Transistorized Amplifiers", *Electronic Applications*, vol. 20, no. 4, pp. 159-168, 1959-1960.
- [35] N. Wiener, *Nonlinear Problems in Random Theory*, New York: Technology Press, 1958.
- [36] S. Narayanan, "Transistor Distortion Analysis Using Volterra Series Representation", *Bell System Technical Journal*, pp. 991-1024, May/June 1967.
- [37] S. A. Maas, *Nonlinear Microwave Circuits*, Norwood, MA: Artech House, 1988.
- [38] P. Wambacq and W. M. C. Sansen, *Distortion Analysis of Analog Integrated Circuits*, Kluwer Academic Publishers, Boston, 1998.
- [39] S. Narayanan, "Intermodulation Distortion of Cascaded Transistors," *IEEE Journal of Solid-State Circuits*, vol. SC-4, no. 3, pp. 97-106, Jun 1969.
- [40] B. P. Gross, "Calculating the Cascade Intercept Point of Communications Receivers", *Ham Radio*, pp. 50-52, August 1980.



- [41] D. O. North, "The Absolute Sensitivity of Radio Receivers", *RCA Review*, vol. 6, pp. 332-343, January 1928.
- [42] H. Rothe and W. Dahlke, "Theory of Noise Fourpoles", *Proceedings IRE*, vol. 44, no. 6, pp. 811-818, June 1956.
- [43] H. A. Haus et al., "Representation of Noise in Linear Two-ports", *Proceedings IRE*, vol. 48, pp. 69-74, January 1960.
- [44] H. Hillbrand and P. H. Russer, "An Efficient Method for Computer-Aided Noise Analysis of Linear Networks," *IEEE Transactions on Circuits Systems*, vol. CAS-23, pp. 235-238, April 1976.
- [45] G. D. Vendelin, A. M. Pavio, and U. L. Rhode, *Microwave Circuit Design Using Linear and Nonlinear Techniques*, New York: Wiley, ch. 2, pp. 93-97, 1990.
- [46] A. van der Ziel, *Noise in Solid-State Devices and Circuits*, New York: Wiley-Interscience, 1986.
- [47] T. Lee, *Design of CMOS Radio-Frequency Integrated Circuits*, Cambridge University Press, 2003.
- [48] F. Friis, "Noise Figure of Radio Receivers", *Proceedings IRE*, vol. 32, pp. 419-422, July 1944.
- [49] E. Hafner, "The Effect of Noise in Oscillators," *Proceedings IEEE*, vol. 54, no. 2, pp. 179-198, February 1966.
- [50] W. A. Edson, "Noise in Oscillators", *Proceedings IRE*, vol. 48, 1454-1472, August 1960.
- [51] J. Rutman, "Characterization of Phase and Frequency Instabilities in Precision Frequency Sources: 15 Years of Progress", *Proceedings IEEE*, vol. 66, no. 9, pp. 1048-1073, September 1978.
- [52] L. W. Couch II, *Digital and Analog Communication Systems*, Prentice-Hall International, Inc, Upper Saddle River, NJ 07458, 1997.
- [53] C. A. M. Boon, *Design of High-Performance Negative-Feedback Oscillators*, PhD Thesis, TU Delft, The Netherlands, 1989.

- [54] J. R. Westra, *High-Performance Oscillators and Oscillation Systems*, PhD Thesis, TU Delft, The Netherlands, 1998.
- [55] W. Robins, *Phase Noise in Signal Sources*, London: Peter Peregrinus Ltd, 1982.
- [56] D. B. Leeson, “A simple Model of Feedback Oscillator Noise Spectrum”, *Proceedings IEEE*, pp. 329–330, February 1966.
- [57] T. S. Rappaport, *Wireless Communications – Principles and Practice*, pp. 120, Prentice Hall, INC, Upper Saddle River, NJ 07458, 2002.

## SPECTRUM-SIGNAL TRANSFORMATION

For the last few decades, there haven't been significant breakthroughs at RF front-end system-level design, as frequently only a few architectures have been exploited: high-IF [1,2] and zero-IF topologies [3,4], and lately low-IF topologies [5]. Even though a small number of different topologies are in use, the high-level RF front-end characterization lacks a unique presentation, which in turn prevents research of new design strategies and architectures at the system level.

Moreover, most of the existing system studies on RF front-ends [6,7,8] fail to present how signals and spectra are transformed from an antenna input to the backend of the receiver in a consistent way. Without an understanding of the signal and spectrum transformations throughout a front-end, it is difficult to grasp all design concepts at the RF system level and the RF circuit level.

Therefore, a unique presentation of spectral and signal transformation in RF front-ends is introduced in this chapter. The approach presented here gives insight into high-level modelling of RF front-ends [9], and accordingly can lead to new design strategies. Various mixer-oscillator models are introduced that allow for an all-encompassing interpretation of both signal and spectral transformations in different receiver architectures.

This chapter is organized as follows. First, the existing RF front-end architectures are briefly outlined followed by a description of the signal and spectral (SS) transformations in a quadrature downconverter topology. Different mixer-oscillator (MO) models are then introduced. Using the presentation of transformation of signals and their spectra, and MO models, a comprehensive analysis of a number of RF front-end topologies is performed. Finally, the mixer-oscillator models and the SS presentation are applied to the calculation of the image-rejection ratio of quadrature receiver topologies, illustrating their utility.

### 3.1 TRANSCEIVER ARCHITECTURES

The increasing use of communication equipment imposes strict regulation on communication standards, and accordingly RF circuit and system designs. To provide users with good quality of service (QoS), a number of issues in various disciplines must be considered. Designers search for more efficient coding techniques and modulation schemes, better transmission and reception schemes, higher-performance circuits and systems, lower-power and higher-speed baseband signal processing, more efficient protocols, and higher energy-density batteries. We will focus on the RF system-level issues in this chapter.

The role of an analogue RF front-end is to downconvert a signal received by a receive antenna to a digital back-end. The receiver architecture is called a high-IF architecture [1,2,10-22] if an intermediate frequency (IF) prior to the back-end processing unit doesn't fall into the range of the baseband signal-processing capabilities of the current era (tens of MHz at the time of writing). The architecture is known as a homodyne or zero-IF [3,4,23-49] for a zero intermediate frequency, and as a low-IF architecture [5,7,50-56] for a low IF (a frequency that falls into the baseband processing capabilities, i.e., on the order of kHz and/or MHz at the current era). The system-level design considerations for these architectures will be outlined in the following sections.

#### 3.1.1 HETERODYNE ARCHITECTURES

A simplified model of a heterodyne receiver architecture [1,2] is shown in Fig. 3.1. It consists of a band-select filter, a low-noise amplifier, an image-reject filter, a mixer, a local-oscillator, and a channel select filter.

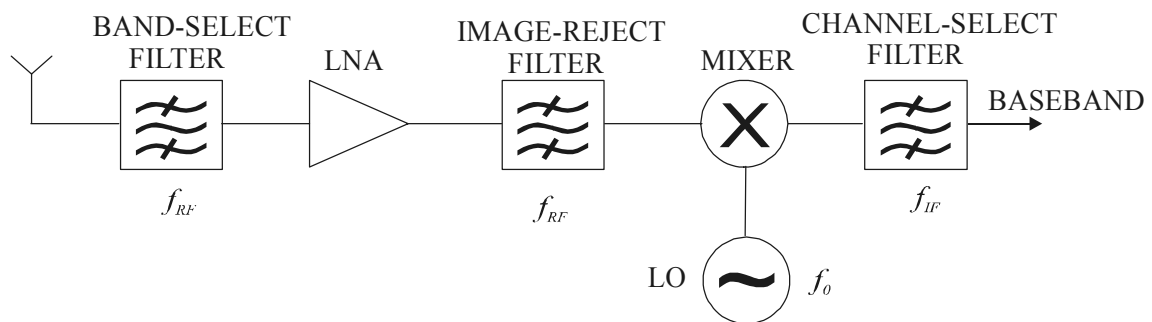


Figure 3.1: A heterodyne receiver.

The RF front-end first selects the spectrum that is allocated to users of a particular standard (band selection), and subsequently it selects the spectrum allocated to a particular user (channel selection) while suppressing interfering signals.

The transformation of the spectra traversing a part of the heterodyne receiver (Fig. 3.1) is shown in Fig. 3.2 (only positive frequencies are shown).

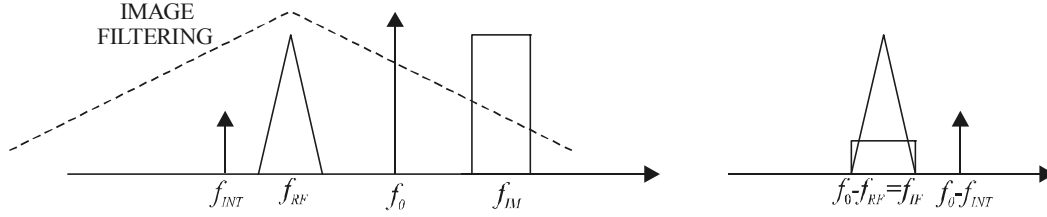


Figure 3.2: High-IF spectral conversion.

Here,  $f_0$  stands for the local-oscillator (LO) frequency,  $f_{RF}$  the frequency of the desired signal,  $f_{IM}$  the image-signal frequency, and  $f_{INT}$  the frequency of the nearby (adjacent-channel) interferer. If  $f_0 < f_{RF}$ , we refer to “low-side injection”. Otherwise ( $f_0 > f_{RF}$ ), it is high-side injection.

A trade-off between suppression of the near and the far interferers (images) dictates the choice of the IF for the illustrated downconversion scheme (see Fig 3.2). Namely, the higher the IF is chosen, the more frequency “space” (bandwidth) there is to filter the image. In contrast, when a lower IF is chosen, only a small portion of an image signal will be suppressed, whereas nearby interferers will be easily removed because higher-order filters can be integrated more easily at low intermediate frequencies.

High-quality image-reject and channel-select filters are required for the efficient suppression of undesired signals. However, as these filters are often implemented with discrete, external components, the increased complexity (e.g., parts count) and large power consumption ( $50\Omega$  matching between filters and front-end circuits) of high-IF receivers are due.

The selection/sensitivity problem, i.e., channel selection and image rejection, is somewhat alleviated in superheterodyne receivers [10] by performing the downconversion in a few steps rather than in one step (see Fig. 3.3).

A higher intermediate frequency after the first downconversion allows for better image suppression, even with moderate- $Q$  filters. On the other hand, a lower final IF allows for better suppression of nearby interferers, having available high- $Q$  filters at this frequency. However, more (discrete) IF filters

are necessary when more IF stages are used, which increases circuit-board and chip-packaging complexity and increases overall cost.

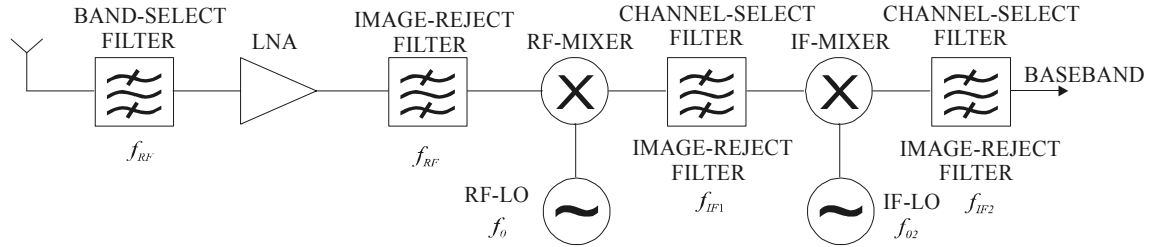


Figure 3.3: A superheterodyne receiver.

### 3.1.2 HOMODYNE ARCHITECTURES

In homodyne or zero-IF receivers [3,4], an intermediate frequency of 0Hz is chosen. At the cost of degraded performance, the external bulky filters can be eliminated, obviating the need for the “power-expensive”  $50\Omega$  inter-stage matching.

An input high-frequency RF signal ( $f_{RF}$ ) is downconverted to the baseband after the mixing with an oscillation signal  $f_0=f_{RF}$  in a zero-IF receiver (Fig. 3.1 with  $f_0=f_{RF}$ ). The signal spectra before and after the downconversion with a single oscillation signal (e.g., *cosine*) are given in Fig. 3.4 (only positive frequencies are shown).

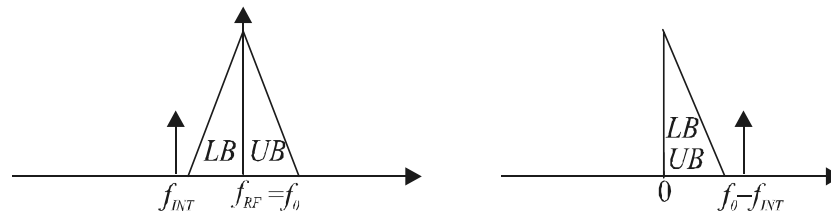


Figure 3.4: Zero-IF spectral conversion.

The lower band (LB) of the spectrum of the desired signal overlaps with the upper band (UB) of the spectrum after the downconversion. In order to avoid loss of information, a zero-IF downconversion with a single LO signal requires identical LB and UB of the signal spectrum (e.g., double side-band amplitude modulated signal) [6,8].

However, frequency- and phase-modulated signals (most often employed modulation techniques in mobile communication systems [57]) don't carry the same information in the lower and the upper parts of the spectra [6,8,58]. Therefore, a certain degree of image rejection is necessary for the correct signal detection in homodyne receivers [6,8], where we can consider that the LB of the information spectrum (Fig. 3.4) is an image of the UB of the spectrum.

### 3.1.2.1 Image-Reject Zero-IF Architectures

In order to avoid the successive and extensive filtering found in heterodyne receivers, without compromising the selectivity and sensitivity of the receiver, other techniques of coping with the image problem have been devised. Two well-known image-reject architectures are those of Hartley [59] and Weaver [60], shown in Figs. 3.5 and 3.6, respectively.

By processing the desired signal and the image signal in a different way, both architectures reject the image signal and transfer the desired signal. Namely, by mixing the incoming signal with two quadrature-phase oscillation signals (*sine* and *cosine*) and subsequently adding the downconverted signals in quadrature ( $90^\circ$  shift in Fig. 3.5a), the desired signal adds constructively whereas the image signal is cancelled.

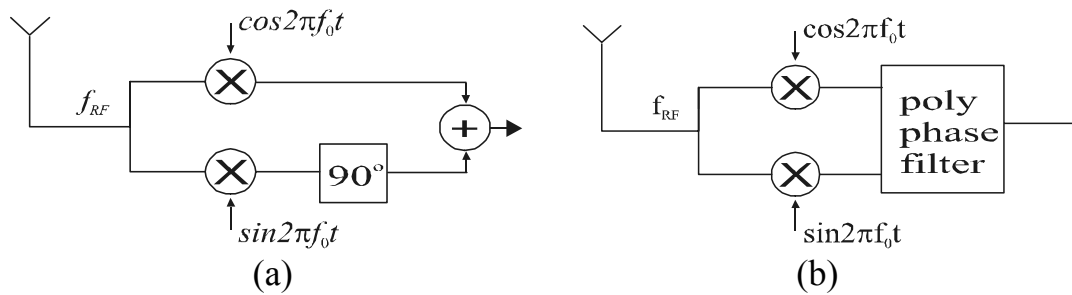


Figure 3.5: The Hartley architecture:  
a) a functional description, b) a practical implementation.

An implementation of Hartley architecture is shown in Fig. 3.5b. Image suppression is achieved by means of complex polyphase filters [61,62] that can distinguish between positive and negative phase sequences, i.e., positive and negative frequencies, and accordingly transfer/suppress parts of spectra.

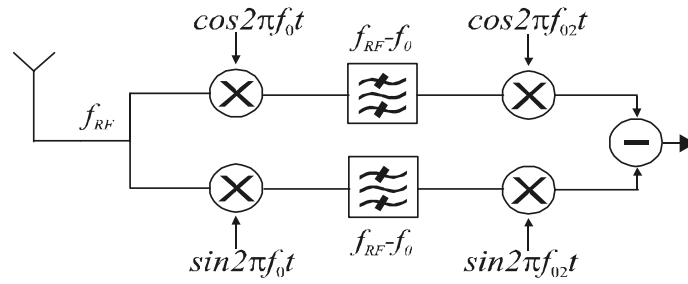


Figure 3.6: The Weaver architecture.

The image signal can also be suppressed by two consecutive downconversions with quadrature LO signals. This is shown in Fig. 3.6.

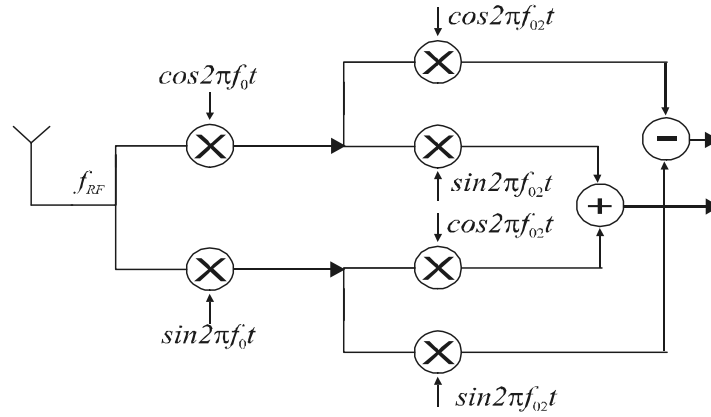


Figure 3.7: A double-quadrature downconverter.

Image suppression using a double-quadrature downconverter [6-8] is shown in Fig. 3.7. After the first quadrature downconversion, signals are again converted in quadrature to lower frequencies, allowing for the image cancellation and transfer of the desired signal.

Section 3.2 describes in detail the transformation of signals and their spectra in image-reject architectures (Figs. 3.5-3.7).

### 3.1.2.2 Drawbacks of Zero-IF Architectures

Although zero-IF receivers offer a higher degree of the integration as well as reduced complexity and reduced power consumption, there are also



drawbacks to this architecture [44,45]. As the RF signals are directly converted to the baseband, any DC and low-frequency signals other than the desired signal cause information distortion.

Firstly, due to finite isolation between the LO and RF ports of a mixer, a portion of the local-oscillator signal is mixed with itself, producing a large undesired DC component. The leakage of the LO signal is the result of the capacitive and substrate coupling, or for externally provided LO signals, bond-wire coupling. Even more problematic is self-mixing of LO signal radiated by the antenna and reflected back to the receiver. In such situations, a time-varying DC component is generated due to time variations between the oscillator signals. Not only does this DC component fall into the band of the desired signal, but it can also saturate the receiver through a subsequent amplification. A way to circumvent the problem of DC offset is to apply DC-free coding schemes [49] or, at circuit level, by filtering [6] and cancellation techniques [46-48].

Secondly, second- and third-order distortion products degrade the performance of zero-IF receivers, both falling into the band of the downconverted desired signal (i.e., baseband). The 2<sup>nd</sup>-order distortion [39,63] can be due to a finite isolation between the IF and RF ports of a mixer, allowing for a feedthrough of the second-order intermodulation products. Second-order intermodulation can be alleviated with differential circuits, albeit at the expense of increased power consumption.

Flicker noise (1/f noise) is another source of hazard. Namely, the 1/f noise of devices (situated at low frequencies) can corrupt the desired signal at baseband. Effects of the 1/f noise are more influential for CMOS technologies than for bipolar technologies, due to the inherently higher 1/f-noise cut-off frequency of CMOS devices.

### 3.1.3 LOW-IF ARCHITECTURE

To circumvent the detrimental effects of DC-offset and to still benefit from a high degree of integration of zero-IF topologies, the final IF can be modified to other than a zero frequency, i.e., a low IF falling into the range of the baseband signal processing capabilities [5]. However, as an image signal, e.g., a nearby interferer, can now be a lot stronger than the desired signal, receivers with a low intermediate frequency (low-IF receivers) employ the quadrature image-reject architectures shown in Figs. 3.5-3.7.

Though low-IF receivers require more rigorous image filtering, they are relieved from problems that arise from the LO self-mixing and the 2<sup>nd</sup>-order intermodulation.

Signals and spectra undergo the same transformations in low-IF topologies as in zero-IF topologies. A detailed treatment of signal and spectral transformations is given in Section 3.2.

### 3.1.4 WIRELESS STANDARDS AND EMPLOYED ARCHITECTURES

The performance of wireless services are determined by the standardization committees [64,65]. The functionality requirements influence the choice of the receiver architecture.

An overview of wireless standards [66-74] is given in Table 3.1.

Table 3.1: Properties of various wireless standards.

standard	range(GHz)	duplex	data rate	modulation	architecture
<b>GSM</b>	0.935-0.96	FDD	14.4Kb/s	GMSK	zero-IF/ /high-IF/low-IF
<b>DCS1800</b>	1.805-1.88	FDD	14.4Kb/s	GMSK	1. zero-IF 2. low-IF/high-IF
<b>IS-95</b>	1.93-1.99	FDD	14.4Kb/s	QPSK, OQPSK	high-IF
<b>WCDMA</b>	2.11-2.17	FDD, TFD	2-10Mb/s	QPSK, 16QAM, 8PSK	zero-IF
<b>DECT</b>	2.4-2.48	TDD	1.152Mb/s	GFSK	1. low-IF 2. zero-IF/high-IF
<b>Bluetooth</b>	2.4-2.48	TDD	0.7232Kb/s	GFSK	low-IF/zero-IF
<b>802.11b(g)</b>	2.4-2.48	TDD	11(54)Mb/s	BPSK, QPSK (OFDM)	1. zero-IF 2. low-IF/high-IF
<b>802.11a</b>	5.15-5.825	TDD	54Mb/s	BPSK, QPSK	1. zero-IF 2. low-IF/high-IF
<b>UWB</b>	3-10	-	600Mb/s	BPSK, QPSK, OFDM	-

For example, mobile devices implementing the GSM standard employ zero-IF [26,34,37,41], low-IF [52,54] and high-IF [21] architectures. On the other hand, mobile devices that implement the WCDMA standard employ mostly a zero-IF topology [30,34,35,38,40,41] as the problem of DC-offset is relaxed due to a large channel bandwidth (5MHz).

### 3.2 SIGNAL AND SPECTRAL TRANSFORMATIONS

Combining complex signal processing techniques with signal and spectral presentations is a powerful tool to both characterize and understand various phenomena related to RF front-ends [6,8]. An all-encompassing spectral analysis method in the form of a spectrum and signal transformation [9] is introduced in this section. It addresses the issue of consistent presentation of signals and their spectra in the receive path of an RF front-end. The spectral and signal transformation broadens the insight into the high-level modelling of the RF front-ends, and can be used as a useful shorthand that facilitates the analysis of RF front-end systems of any complexity.

The transformation of signals and spectra is derived for the quadrature downconverter model shown in Fig. 3.8.

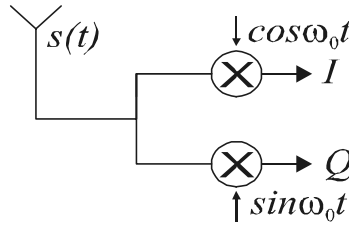


Figure 3.8: A quadrature downconverter (a simplified model).

The input modulated quadrature signal (denoted as  $s(t)$ ) is defined by Eq. (3.1). The components  $A(t)$  and  $B(t)$  are the modulating signal components of the desired signal at an angular (carrier) frequency  $\omega_{RF}$ , and  $C(t)$  and  $D(t)$  are the modulating components of the image signal with a carrier at an angular frequency  $\omega_{IM}$  [58,75].

$$s(t) = A(t)\cos\omega_{RF}t - B(t)\sin\omega_{RF}t + C(t)\cos\omega_{IM}t - D(t)\sin\omega_{IM}t \quad (3.1)$$

Eq. (3.1) can be used for the representation of various modulation schemes. For example, a QPSK (digitally-modulated) signal is generated by using a carrier that is modulated by the digital signal components  $A(t)$  and  $B(t)$  [58]. Most of today's wireless communication systems use digital modulation schemes (e.g., QPSK, MSK, GMSK, GFSK, 16QAM) [57,58].

A visualisation of the spectrum of the signal  $s(t)$  is shown in Fig. 3.9. A continuous spectrum around the corresponding central frequencies ( $\omega_{RF}$  and  $\omega_{IM}$ ) can be assumed [57,58,76-78] for digital modulation schemes. For the

sake of clarity, we have chosen a triangle-like spectrum for the desired signal and a square-like spectrum for the image signal.

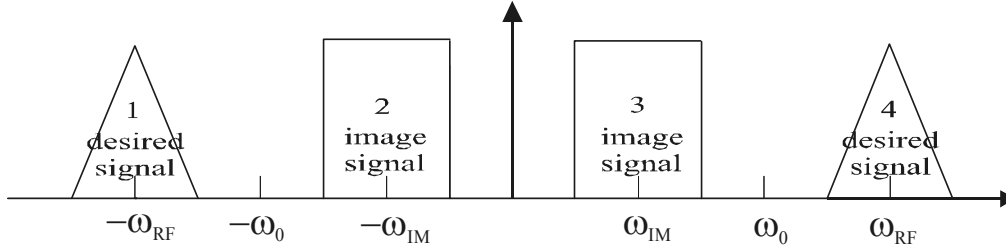


Figure 3.9: The spectra of the desired and the image signals.

The spectra of the quadrature local-oscillator signal components are shown in Fig. 3.10, where  $\omega_0$  is the oscillator angular frequency. The spectrum of the *cosine* function is referred to the real axis, and the spectrum of the orthogonal *sine* function to the imaginary axis [6] (see Eq. (3.2)).

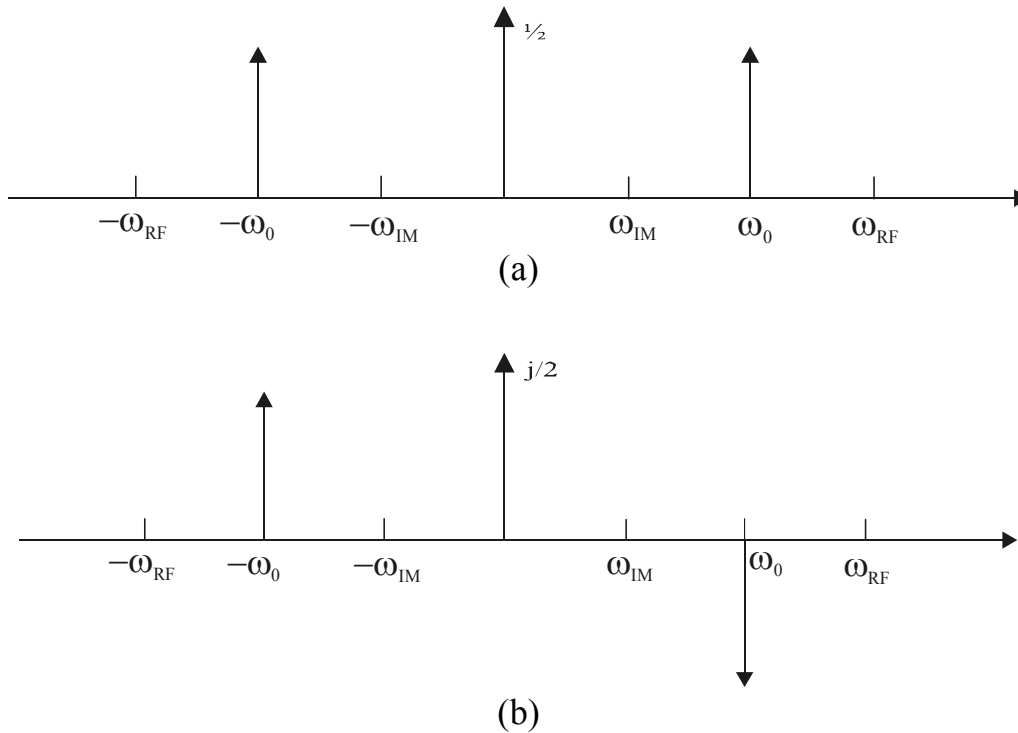


Figure 3.10: Spectra of the local oscillator signals: (a)  $\cos \omega_0 t$ , (b)  $\sin \omega_0 t$ .

For the sake of brevity, we will simplify the notation with  $A=A(t)$ ,  $B=B(t)$ ,  $C=C(t)$  and  $D=D(t)$ . To facilitate the mathematical representation of the signal transformation, the following well-know identities (Eqs. (3.2)-(3.3)) are applied:

$$2\cos\omega_0 t = e^{j\omega_0 t} + e^{-j\omega_0 t} \quad j2\sin\omega_0 t = e^{j\omega_0 t} - e^{-j\omega_0 t}, \quad (3.2)$$

$$R = \sqrt{A^2 + B^2}, \quad \theta = \text{atan}\frac{B}{A} \quad M = \sqrt{C^2 + D^2}, \quad \psi = \text{atan}\frac{D}{C}. \quad (3.3)$$

With the aid of Eq. (3.2), the complex notation [61,62] of the input signal  $s(t)$  becomes:

$$2s(t) = (A + jB)e^{j\omega_{RF}t} + (A - jB)e^{-j\omega_{RF}t} + (C + jD)e^{j\omega_{IM}t} + (C - jD)e^{-j\omega_{IM}t}, \quad (3.4)$$

whereas with the aid of Eq. (3.3) the complex notation transforms into:

$$2s(t) = R \cdot e^{j(\omega_{RF}t + \theta)} + R \cdot e^{-j(\omega_{RF}t + \theta)} + M \cdot e^{j(\omega_{IM}t + \psi)} + M \cdot e^{-j(\omega_{IM}t + \psi)}. \quad (3.5)$$

Components  $A+jB$  and  $C+jD$  are often referred to as *complex envelopes* of the modulated signals [58].

In the following analysis, we will independently investigate the  $I$  and  $Q$  paths (i.e., the downconversion with the  $\cos\omega_0 t$  and  $\sin\omega_0 t$ , respectively).

After the mixing of the input signal  $s(t)$  (Eq. (3.5)) with the quadrature components of the oscillation signal (Eq. (3.2)), the downconverted in-phase ( $I$ ) and quadrature-phase ( $Q$ ) components become:

$$2I = \text{LowPassFilter}[s(t)(e^{j\omega_0 t} + e^{-j\omega_0 t})] = R \cdot \cos(\omega_{IF}t + \theta) + M \cdot \cos(\omega_{IF} - \psi), \quad (3.6)$$

$$2Q = \text{LowPassFilter}[js(t)(e^{-j\omega_0 t} - e^{j\omega_0 t})] = -R \cdot \sin(\omega_{IF}t + \theta) + M \cdot \sin(\omega_{IF} - \psi) \quad (3.7)$$

where  $\omega_{IF} = \omega_{RF} - \omega_0$  is an angular intermediate frequency.

The mixing of the LO signal and the modulated signal  $s(t)$  is equivalent to a convolution of the spectral representation of the  $\cos\omega_0 t$  and  $\sin\omega_0 t$  functions (Fig. 3.10) with the spectral representation of the input signal (Fig. 3.9). The

downconverted spectra of the  $I$  and  $Q$  paths obtained are given by Figs. 3.11 and 3.12.

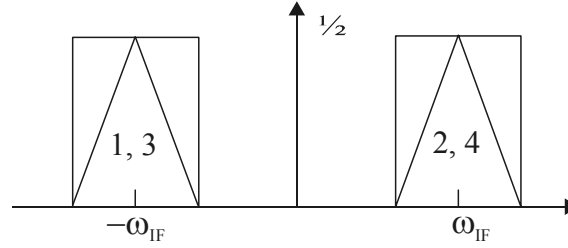


Figure 3.11: The spectrum in the  $I$  channel after low-pass filtering.

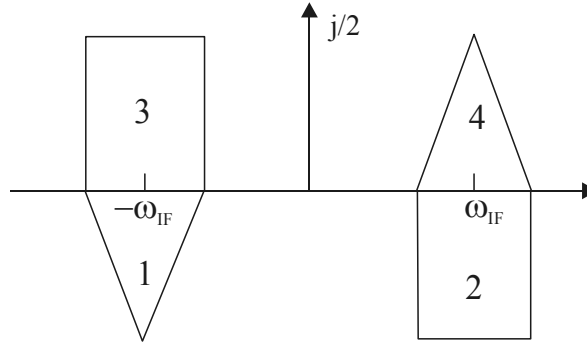


Figure 3.12: The spectrum of the  $Q$  channel after the low-pass filtering.

It is tacitly assumed that each portion of the downconversion is followed by a portion of the filtering (low pass or band-pass). This implies that only the downconverted parts of the spectra are considered.

Finally, the complex downconverted signal that consists of the orthogonal  $I$  and  $Q$  components becomes:

$$2(I + jQ) = (A - jB)e^{-j\omega_{IF}t} + (C - jD)e^{j\omega_{IF}t} . \quad (3.8)$$

We will refer to Eq. (3.8) as the *signal-presentation* model. Here, the term *signal* is referred to the *mathematical representation* of the signal. According to Eq. (3.8), the downconverted signals are situated at the negative frequencies (desired signal) and the positive frequencies (image signal), respectively.

After the transformation of the  $Q$ -spectrum (Fig. 3.12) into the  $jQ$ -spectrum, which is similar to the mathematical transformation of the  $Q$  path, the resulting *spectral presentation* referring to the complex signal presentation  $I+jQ$  is obtained (Fig. 3.13).

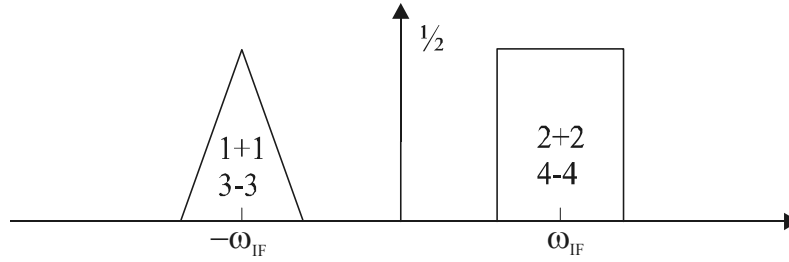


Figure 3.13: The spectrum of the downconverted signal ( $I+jQ$ ).

By combining Eq. (3.8), (signal presentation) and Fig. 3.13 (spectral presentation), an explicit relationship between the spectral and the mathematical presentations of the signal transformed, called the *spectrum-signal (SS) presentation*, is obtained. The SS presentation is shown in Fig. 3.14. Transformation of signals and spectra using SS presentation is referred to as the *SS transformation*.

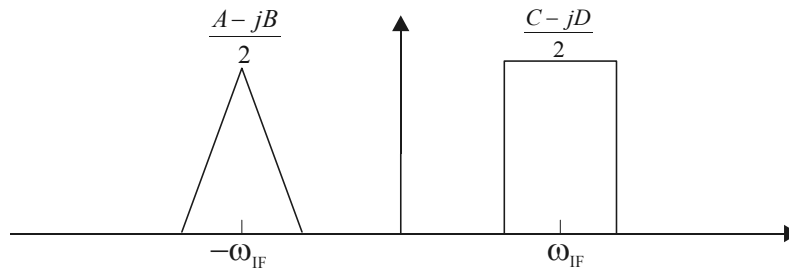


Figure 3.14 : The spectrum-signal presentation.

After frequency conversion, the desired signal is situated around an angular frequency  $-\omega_{IF}$  and its complex presentation has a form  $(A-jB)e^{j\omega_{IF}t}$  (the complex envelope and the carrier), where  $A-jB$  is a mathematical interpretation of the desired quadrature signal entering the receiver. The complex-envelope  $C-jD$  is referred the image signal situated around the positive intermediate angular frequency,  $\omega_{IF}$ .

Not surprisingly, this form is the same as that of the signal entering the receiver. The components of the signal can be still distinguished as signal orthogonality is preserved. *The desired signal is characterized by both a spectrum position (a centre angular intermediate frequency  $\omega_{IF}$ ) and its content (the orthogonal modulation signals  $A(t)$  and  $B(t)$ ).*

To keep track of both the spectrum and the signal content, the spectrum-signal presentation of Fig. 3.14 can be applied to the analysis of receiver topologies of any complexity. SS presentation can be considered as a quadrature-downconverter "shorthand", facilitating a description of the complex RF front-end architectures. Different receiver topologies will be analyzed in the next section using the SS presentation.

### 3.3 MIXER-OSCILLATOR MODELS

Prior to detection (demodulation), an input receive signal is downconverted to an intermediate (low) frequency in accordance with one of the schemes outlined in Section 3.1.

A high-IF receiver (Fig. 3.1) downconverts a receive signal (e.g.,  $s(t)$  in Eq. (3.1)) by an oscillation signal (e.g.,  $\cos\omega_0 t$ ) to an IF.

On the other hand, a quadrature receiver (Figs. 3.4 and 3.6) downconverts an input signal with two oscillation signals ( $\sin\omega_0 t$  and  $\cos\omega_0 t$ ) that are in quadrature. The downconverted IF signal consists of two orthogonal (quadrature) components. What is more, a double-quadrature downconverter (Fig. 3.6) converts an IF quadrature signal (obtained after the first quadrature downconversion) to a baseband quadrature signal.

In order to facilitate the mathematical description of these various downconversion schemes, a complex notation is introduced [8]. Accordingly, the quadrature (orthogonal) signals are represented with two-dimensional vectors [9,58,75], i.e., complex variables (see Eq. (3.8)). For example,  $A+jB$  stands for a quadrature-modulating signal (complex-modulating envelope), whereas  $I+jQ$  is a quadrature downconverted signal.

The mixer-oscillator (MO) models are introduced in this section relying on the (complex) spectrum-signal presentation. They allow for a compact description and a high-level modelling of the receiver topologies. The MO models are classified based on the type of the signal (real or complex) before and after the mixer-oscillator (down)conversion.

- Double-real mixer-oscillator (DR-MO) converts a real input into a real output.



- Single-complex mixer-oscillator (SC-MO) converts a real (complex) input into a complex (real) output.
- Double-complex mixer-oscillator (DC-MO) converts a complex input into a complex output.

The MO models allow for a comprehensive analysis of various RF front-end topologies. Moreover, a number of receiver phenomena can be straightforwardly interpreted by means of the presented MO models, as will be subsequently shown.

### 3.3.1 DOUBLE-REAL MIXER-OSCILLATOR MODEL

A double-real mixer-oscillator (DR-MO) structure is shown in Fig. 3.15. This simple model can be found in (super)heterodyne architectures (Fig. 3.1). Common to this architecture, the desired signal and the image signal cannot be distinguished after the first downconversion without previous image filtering. This will be exemplified by using the SS transformation.

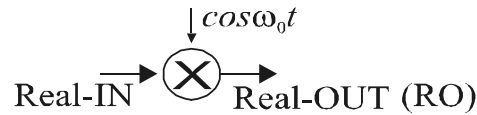


Figure 3.15: A double-real mixer-oscillator model.

If SS forms of the input signal  $s(t)$  and the LO signal ( $\cos \omega_0 t$ ) are shown in Fig. 3.16, the SS form after the downconversion will be as shown in Fig. 3.17.

The DR-MO transforms a real input signal into a real output signal, accordingly performing a *real-to-real* transformation. As can be seen from Fig. 3.17, the spectra of the desired and the image signals overlap after the downconversion, i.e., the image distorts the desired information.

This can be apprehended by referring to the content of the signal. Namely, the signal consists of the components at both the positive and the negative frequencies.

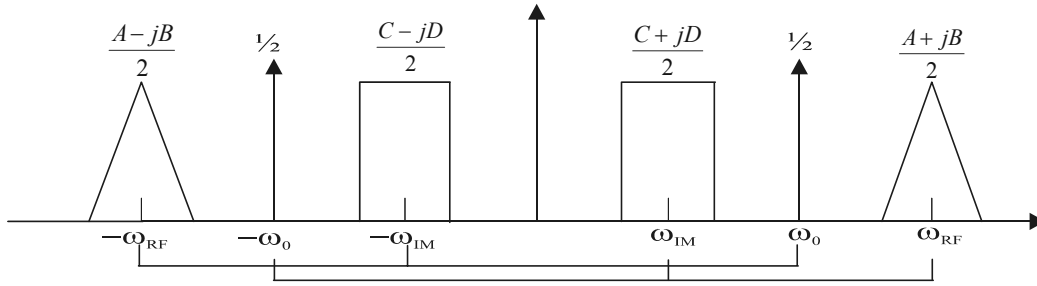


Figure 3.16: DR-MO spectrum-signal form before downconversion.

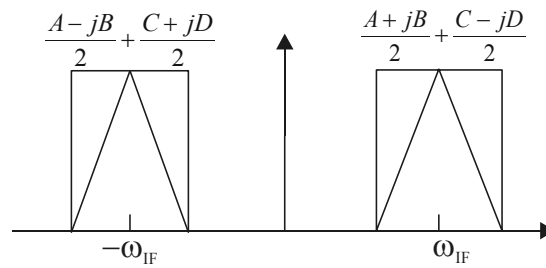


Figure 3.17: DR-MO spectrum-signal form after downconversion.

In the case of the DR-MO, the output signal component (RO in Fig. 3.15) will be:

$$2\text{RO} = (A - jB)e^{-j\omega_{IF}t} + (C - jD)e^{j\omega_{IF}t} + (A + jB)e^{j\omega_{IF}t} + (C + jD)e^{-j\omega_{IF}t}, \quad (3.9)$$

$$\text{RO} = (A + C) \cdot \cos \omega_{IF}t - (B - D) \sin \omega_{IF}t. \quad (3.10)$$

Eq. (3.10) shows that the desired information indeed cannot be recovered with a single downconversion without previous image filtering (see Fig. 3.1).

Note that in the context of the transformation of the spectra, the term signal is referred to the mathematical representation of the signal. Further, the complex representation  $A + jB$  implies that the modulating signals  $A(t)$  and  $B(t)$  are orthogonal, thus distinguishable. On the other hand,  $A + B$  refers to a non-orthogonal signal, where it can not be distinguished between the components  $A(t)$  and  $B(t)$ . In this case, the information about these components is lost and cannot be retrieved.

The first generation Motorola cordless phone [22] is an example of a superheterodyne architecture where the DR-MO models can be employed.

### 3.3.2 SINGLE-COMPLEX MIXER-OSCILLATOR MODEL

For real input and complex output signals, a real to complex transformation model is introduced, whereas for complex input and real output signals, a complex to real transformation is considered.

#### 3.3.2.1 Real-to-Complex Transformation

A real input signal can be transformed into a complex output signal by means of two DR-MOs, as shown in Fig. 3.18a. A symbol of the single-complex mixer-oscillator model (SC-MO), i.e., quadrature downconverter, is shown in Fig. 3.18b.

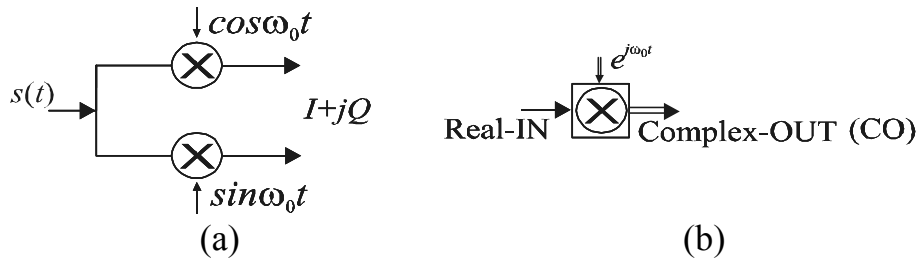


Figure 3.18: (a) Single-complex mixer-oscillator model, (b) symbol.

The “shorthand” for the quadrature downconverter is already discussed in Section 3.1 (the SS form shown in Fig. 3.14). In this section we will just briefly summarize the properties of the SC-MO model.

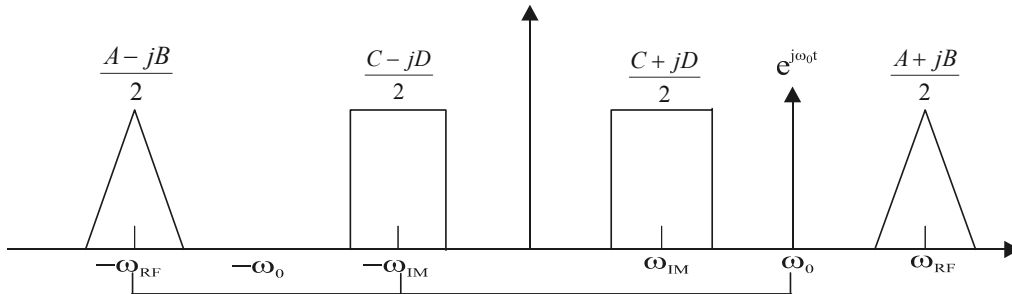


Figure 3.19: SC-MO spectrum-signal form before downconversion.

The SS form of the input signal (Fig. 3.19) is transformed by the complex LO signal  $e^{-j\omega_0 t}$  [8] into the output SS form, as shown in Fig 3.20.

The *content* of the output *complex signal* (Fig. 3.20) can be found as:

$$\text{CO} = \frac{A - jB}{2} e^{-j\omega_{IF} t} + \frac{C - jD}{2} e^{j\omega_{IF} t} . \quad (3.11)$$

Referring to either negative or positive frequencies, the frequency independent *complex presentation of the signal content* becomes:

$$\text{CO}@(-\omega_{IF}) = (A - jB + C + jD)/2 . \quad (3.12)$$

This suggests that the phase sequences [62] of the desired signal ( $A - jB$ ) and the signal of image ( $C + jD$ ) are of different polarities. The phase sequence of the desired signal is positive, whereas that of the image signal is negative. Polyphase filters (see Fig 3.6) can distinguish between the desired and image signals after the quadrature downconversion as they discriminate between the opposite phase sequences of these signals.

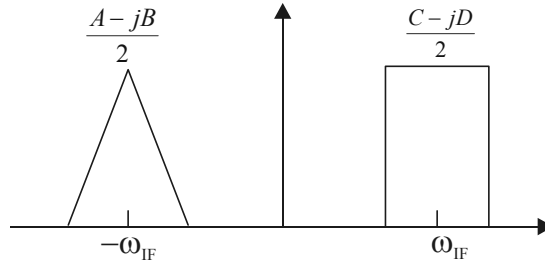


Figure 3.20: SC-MO spectrum-signal form after downconversion.

The polyphase filters are both the phase and the frequency discriminative. Fig. 3.20 and Eqs. (3.11) and (3.12) just prove that, whichever domain we refer to, the image can still be filtered out after the quadrature downconversion, i.e., it is still distinguishable. For example, the Hartley image-reject architecture (Fig. 3.5b) consists of a SC-MO topology and a polyphase filter (90° shifter) that is responsible for the final image rejection.

A zero-IF Philips receiver for paging applications [43] is an example where the SC-MO model can be used for the description of the spectral transformations.

### 3.3.2.2 Complex-to-Real Transformation

A complex input signal can be transformed into a real signal as shown in Fig. 3.21a. The accompanying symbol of this single-complex mixer-oscillator is shown in Fig. 3.21b. This intuitive symbol infers a transformation of a complex input signal (square in the symbol) into a real output signal (circle in the symbol). Other symbols are constructed applying the same rules.

If the complex input signal and the complex LO signal are shown in Fig. 3.22, the final downconverted signal will be as shown in Fig. 3.23. In this example, the input complex signal is situated around an angular frequency  $\omega_{IF}$ , the oscillation signal at an angular frequency  $\omega_{02}$  and the downconverted signal around an angular frequency  $\omega_{IF2}$ .

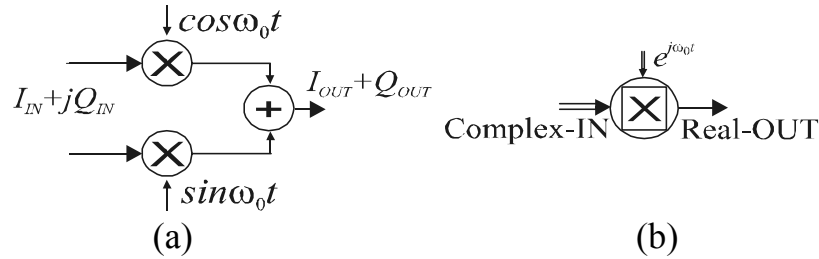


Figure 3.21: (a) Single-complex mixer-oscillator model, (b) symbol.

Note that the signal content referred to Fig. 3.19 is real, whereas the signal content shown in Fig. 3.22 is complex. Therefore, the input of a complex-to-real SC-MO model can be provided as the output of a real-to-complex SC-MO model.

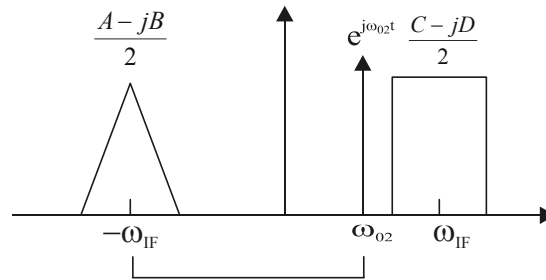


Figure 3.22: SC-MO spectrum-signal form before downconversion.

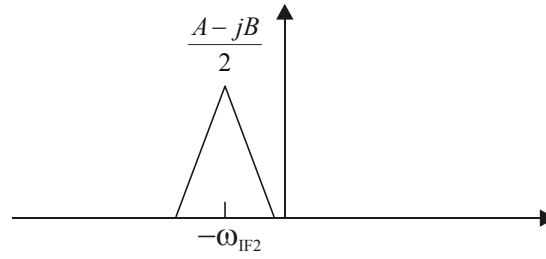


Figure 3.23: SC-MO spectrum-signal form after downconversion.

The complex-to-real SC-MO model have application in both upconversion and downconversion architectures. It can be used for a single-sideband (SSB) modulation of the input signals if the input signal  $I_{IN}$  is a Hilbert transform counterpart ( $90^\circ$  phase-shifted equivalent) of the input signal  $Q_{IN}$  [58]. On the other hand, various digital modulation schemes can be obtained if  $I_{IN}$  and  $Q_{IN}$  (Fig. 3.21) are the binary signals [58]. Finally, SC-MO model of Fig. 3.21 can be employed for the final downconversion in the Weaver receiver architecture (see Fig. 3.5).

### 3.3.3 DOUBLE-COMPLEX MIXER-OSCILLATOR MODEL

Fig. 3.24 shows a part of a double-quadrature downconverter that is shown in Fig. 3.7. This double-complex mixer-oscillator (DC-MO) topology transforms an input complex signal, e.g., obtained after a quadrature downconversion with a SC-MO, into a complex signal at the output. The symbol of the DC-MO is shown in Fig. 3.24b.

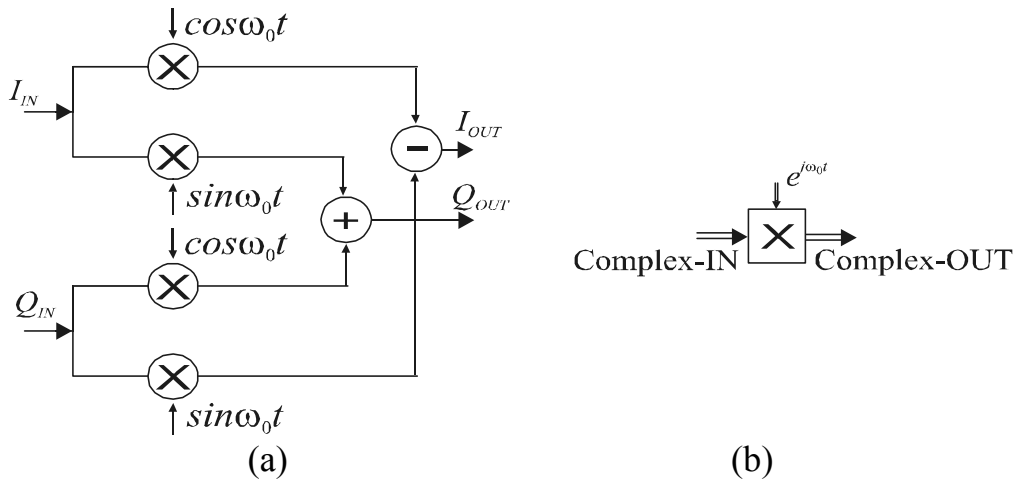


Figure 3.24: (a) Double-complex mixer-oscillator model, (b) symbol.

In this section we will introduce a “shorthand” for the DC-MO model and then examine it with the already validated DR-MO and SC-MO models.

First, let us derive the relationship between the input and output complex signals. By mixing and combining  $I_{IN}$  and  $Q_{IN}$  with  $\cos \omega_0 t$  and  $\sin \omega_0 t$ , as shown in Fig. 3.24, the output signals  $I_{OUT}$  and  $Q_{OUT}$  can be calculated as:

$$2I_{OUT} = 2I_{IN} \cos \omega_0 t - 2Q_{IN} \sin \omega_0 t = I_{IN}(e^{j\omega_0 t} + e^{-j\omega_0 t}) + jQ_{IN}(e^{j\omega_0 t} - e^{-j\omega_0 t}), \quad (3.13)$$

$$2Q_{OUT} = 2I_{IN} \sin \omega_0 t + 2Q_{IN} \cos \omega_0 t = -jI_{IN}(e^{j\omega_0 t} - e^{-j\omega_0 t}) + Q_{IN}(e^{j\omega_0 t} + e^{-j\omega_0 t}), \quad (3.14)$$

$$I_{OUT} + jQ_{OUT} = (I_{IN} + jQ_{IN})e^{j\omega_0 t}. \quad (3.15)$$

As suggested by Eq. (3.15) the two quadrature LO signals (Fig. 3.24) can be presented with the complex LO signal  $e^{j\omega_0 t}$  [8]. This further implies that the same transformation rules can be applied for both the SC-MO (real-to-complex; Fig. 3.22) and the DC-MO models. Fig. 3.25a shows the spectrum-signal form of the complex input signal and the complex LO signal, where it is assumed that the first downconversion has already been done with a quadrature downconverter (Section 3.3.2.1 and Fig. 3.20). The SS form referring to the complex downconverted signal is now simply obtained as shown in Fig. 3.25b.

The SS presentation “shorthand” for the DC-MO model will be verified through an all-encompassing spectral analysis of a double-quadrature downconverter, shown in Fig. 3.23a, by applying the SS transformation rules of the DR-MO and SC-MO models.

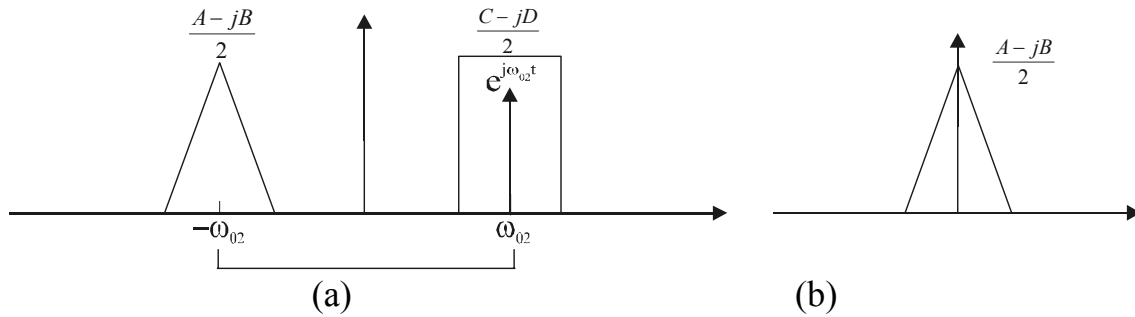


Figure 3.25: DC-MO SS form:

a) after the quadrature conversion, b) after the double-quadrature conversion.

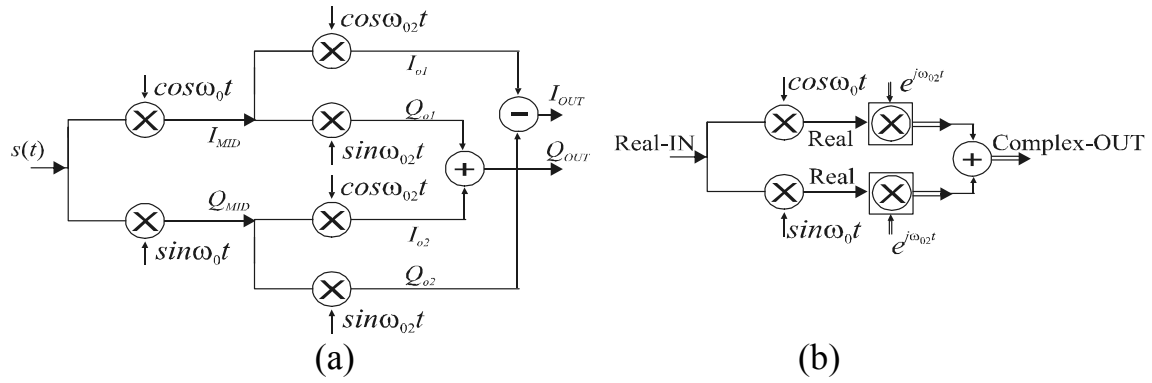


Figure 3.26: (a) Double-quadrature downconverter, (b) MO model.

A double-quadrature downconverter can be equivalently represented with two DR-MOs and two SC-MOs, as shown in Fig. 3.26b. The spectrum-signal form of the input signal  $s(t)$  and the LO signal is shown in Figs. 3.9 and 3.10. Applying the transformation rules of the DR-MO model, the SS form of the real signals  $I_{MID}$  and  $Q_{MID}$  is obtained (Figs. 3.27a and 3.27b).

Applying the SS transformation rules of the SC-MO (see Figs. 3.19 and 3.20) to the SS form of Fig. 3.27 results into the complex signals  $C_{OUT1}=I_{O1}+jQ_{O1}$  and  $C_{OUT2}=I_{O2}+jQ_{O2}$ , shown in Figs. 3.28a and 3.28b, and the output complex signal  $I_{OUT}+jQ_{OUT}=C_{OUT1}+jC_{OUT2}$ , shown in Fig. 3.29.

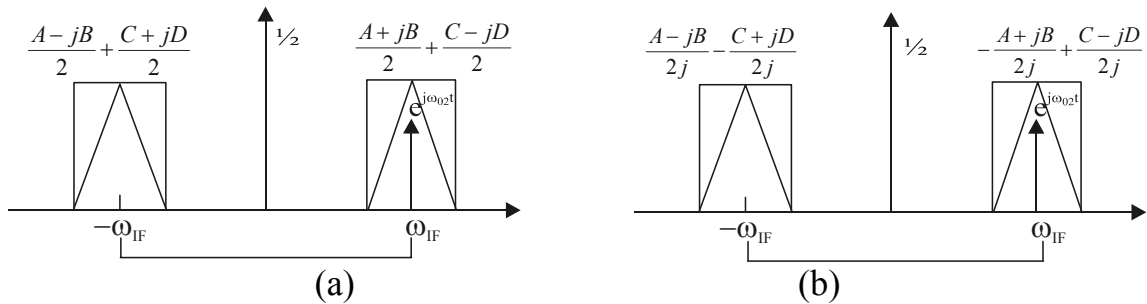


Figure 3.27: Spectrum-signal form after the first downconversion  
a)  $I_{MID}$  path, b)  $Q_{MID}$  path.

Expectedly, the image is suppressed after the final downconversion. Furthermore, the equality of the resulting spectra of Figs. 3.29 and 3.25b proves the validity of the proposed spectrum-signal form of the DC-MO model.



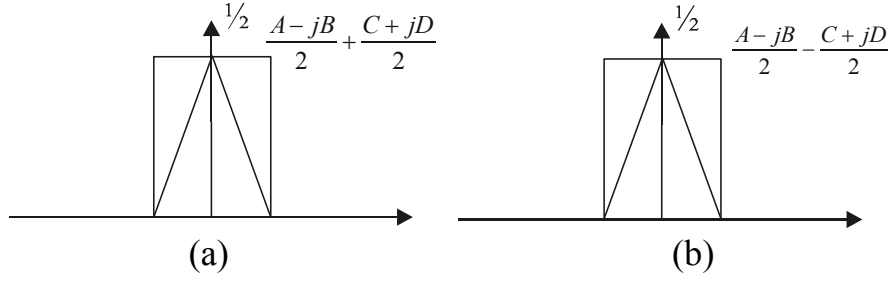


Figure 3.28: Spectrum-signal form after second downconversion

(a)  $C_{OUT1}=I_{O1}+jQ_{O1}$  (b)  $C_{OUT2}=I_{O2}+jQ_{O2}$ .

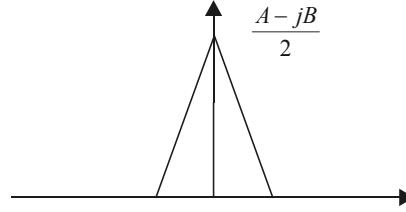


Figure 3.29:  $I_{OUT}+jQ_{OUT}$ .

With the advantage of the DC-MO model (Fig. 3.25) we can manipulate content and spectra of signals in a simpler manner compared to the transformations shown in Figs. 3.27, 3.28 and 3.29, or even more complicated analysis found in [6,7].

### 3.4 IMAGE-REJECTION RATIO MODEL

The spectrum-signal presentation models allow for a straightforward derivation of various RF receiver performance parameters. Accordingly, this section elaborates on the image-rejection-ratio (IRR) of a quadrature downconverter [79] by means of MO models.

First, let us denote  $\varepsilon$  and  $\varphi$  as the amplitude and the phase mismatch of the oscillation signal, as shown in Fig. 3.30a.

Taking mismatch into account, the complex LO signal presentation becomes:

$$(1 + \varepsilon) \cos(\omega_0 t + \varphi) + j \sin \omega_0 t = [X_1(\varepsilon, \varphi) e^{j\omega_0 t} + X_2(\varepsilon, \varphi) e^{-j\omega_0 t}], \quad (3.16)$$

where  $X_1$  and  $X_2$  represent the desired and undesired (parasitic) complex LO signals, respectively.

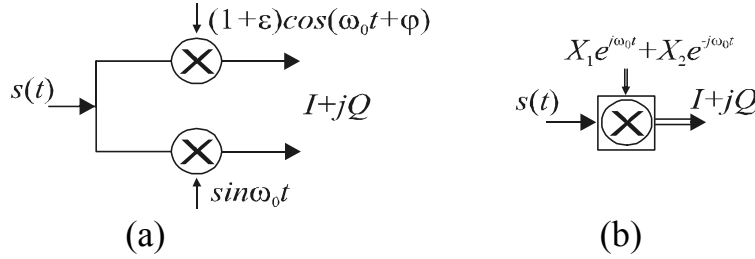


Figure 3.30: (a) Quadrature downconverter, (b) IRR model.

$$X_1(\varepsilon, \varphi) = (1 + \varepsilon)e^{j\varphi} + 1 \quad (3.17)$$

$$X_2(\varepsilon, \varphi) = (1 + \varepsilon)e^{-j\varphi} - 1 \quad (3.18)$$

Without loss of generality, the constants  $\frac{1}{2}$  and 2 that originate from the mixing with the LO signal are omitted, as we are only interested in the form of the signals as well as the position of their spectra, which is not affected using this simplification. Also, this does not affect the ratio of the signal contents.

The IRR model is presented in Fig. 3.30b with the aid of Eq. (3.16) and a SC-MO model. We will determine the IRR by using a strictly mathematical interpretation of signals. Then, a method that relies on the spectrum-signal presentation and transformation will be described proving to be simpler and more intuitive.

By mixing the input signal  $s(t)$  (Eq. (3.1)) and the LO signal (Eq. (3.16)) the low-filtered version of the output signal becomes:

$$I + jQ \propto RX_1(\varepsilon, \varphi)e^{-j(\omega_{IF}t + \theta)} + MX_2(\varepsilon, \varphi)e^{-j(\omega_{IF}t - \psi)} + \\ + RX_2(\varepsilon, \varphi)e^{j(\omega_{IF}t + \theta)} + MX_1(\varepsilon, \varphi)e^{j(\omega_{IF}t - \psi)} \quad (3.19)$$

where  $R$  and  $M$  are the magnitudes of the desired and the mirror signals, respectively (see Eq. (3.3)). The ratio of the power of the image and desired signals at either positive or negative frequencies can be now calculated as:

$$IRR = \left| \frac{X_2(\varepsilon, \varphi) e^{-j(\omega_{IF}t - \psi)}}{X_1(\varepsilon, \varphi) e^{-j(\omega_{IF}t + \theta)}} \right|^2 = \left| \frac{-1 + (1 + \varepsilon) e^{-j\varphi}}{1 + (1 + \varepsilon) e^{j\varphi}} \right|^2, \quad (3.20)$$

$$IRR = \frac{1 - 2(1 + \varepsilon) \cos \varphi + (1 + \varepsilon)^2}{1 + 2(1 + \varepsilon) \cos \varphi + (1 + \varepsilon)^2}. \quad (3.21)$$

Not surprisingly, the well-known expression for the  $IRR$  [6] is obtained.

Let us now examine the same phenomenon by using the spectrum-signal analysis method described in the previous sections.

The SS forms of the input signal before the conversion and the SS form of the complex LO signal are presented in Fig. 3.31. The SS form of the downconverted signal is shown in Fig. 3.32. From Fig. 3.32 it can be straightforwardly determined to what extent the image signal affects the desired signal. Referring to an angular frequency  $\omega_{IF}$ , the  $IRR$  can readily be calculated by Eq. (3.22).

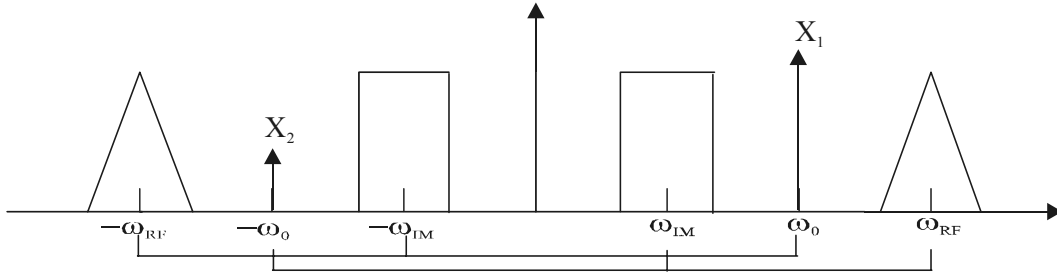


Figure 3.31: Spectrum-signal form before downconversion.

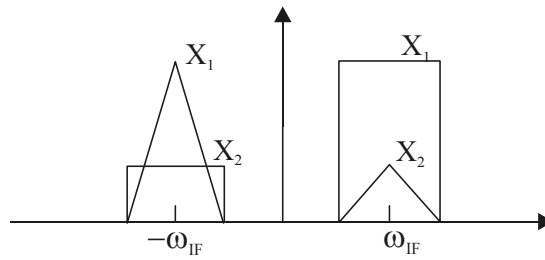


Figure 3.32: Spectrum-signal form after downconversion.

$$IRR = \left| \frac{X_2(\varepsilon, \varphi)}{X_1(\varepsilon, \varphi)} \right|^2 \quad (3.22)$$

Calculation of the IRR without the model proposed would be complicated if we consider the deviation in both quadrature LO signals, viz., the amplitude and the phase deviation ( $\varepsilon_1$  and  $\varphi_1$ ) of the  $I$ -phase and the amplitude and the phase deviation ( $\varepsilon_2$  and  $\varphi_2$ ) of the  $Q$ -phase components. However, by means of the functions  $X_1$  and  $X_2$  of the form:

$$X_1(\varepsilon_1, \varphi_1, \varepsilon_2, \varphi_2) = (1 + \varepsilon_1)e^{j\varphi_1} + (1 + \varepsilon_2)e^{j\varphi_2}, \quad (3.23)$$

$$X_2(\varepsilon_1, \varphi_1, \varepsilon_2, \varphi_2) = (1 + \varepsilon_1)e^{-j\varphi_1} - (1 + \varepsilon_2)e^{-j\varphi_2}, \quad (3.24)$$

the *IRR* can be easily determined from Fig. 3.32 and Eq. (3.22).

The *IRR* model of Fig. 3.32 allows for efficient calculation of *IRR* in various quadrature topologies.

### 3.5 IRR MODEL OF DOUBLE-QUADRATURE DOWNCONVERTERS

All the properties of the spectrum-signal presentation model can be examined with the image-reject, double-quadrature downconversion architecture, shown in Fig. 3.26a (standard form) and Fig. 3.26b (mixer-oscillator model).

We will focus only on the derivation of the *IRR* by using the SS presentation.

Using the introduced mixer-oscillator models, a rather complex double-quadrature downconverter structure, especially for the calculation of *IRR*, reduces to the topology shown in Fig. 3.33b (Weaver topology). The obtained *IRR* model consists of a real-to-complex SC-MO and a complex-to-real SC-MO.

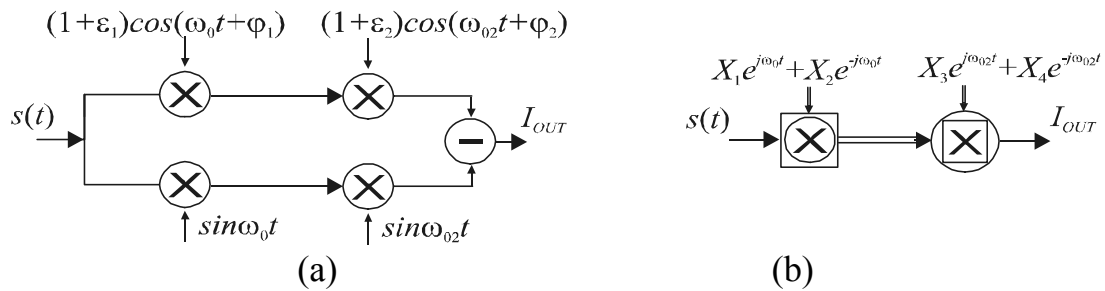


Figure 3.33: (a) A double-quadrature downconverter, (b) an *IRR* model.

The result of the first downconversion with a SC-MO is already shown in Figs. 3.31 and 3.32. Final downconversion to the baseband is done with the second complex LO signal ( $X_3$  and  $X_4$ ), as shown in Figs. 3.34 and 3.35.

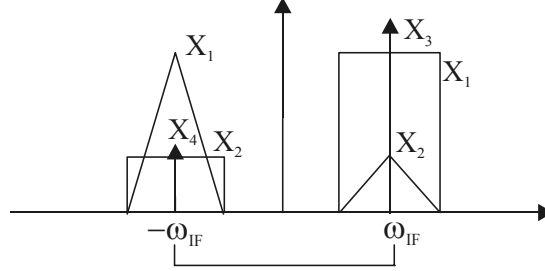


Figure 3.34: Spectrum-signal form before the second downconversion.

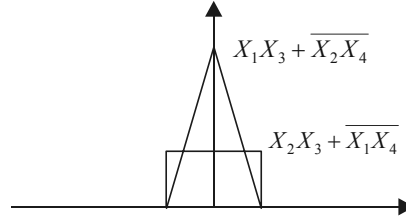


Figure 3.35: Spectrum-signal form after the second downconversion.

If the first LO signal is given by Eqs. (3.25)-(3.27), and the second LO signal by Eq. (3.28)-(3.30),

$$(1 + \varepsilon_1) \cos(\omega_0 t + \varphi_1) + j \sin \omega_0 t = [X_1(\varepsilon_1, \varphi_1) e^{j\omega_0 t} + X_2(\varepsilon_1, \varphi_1) e^{-j\omega_0 t}], \quad (3.25)$$

$$X_1(\varepsilon_1, \varphi_1) = (1 + \varepsilon_1) e^{j\varphi_1} + 1, \quad (3.26)$$

$$X_2(\varepsilon_1, \varphi_1) = (1 + \varepsilon_1) e^{-j\varphi_1} - 1, \quad (3.27)$$

$$(1 + \varepsilon_2) \cos(\omega_{02} t + \varphi_2) + j \sin \omega_{02} t = [X_3(\varepsilon_2, \varphi_2) e^{j\omega_{02} t} + X_4(\varepsilon_2, \varphi_2) e^{-j\omega_{02} t}], \quad (3.28)$$

$$X_3(\varepsilon_2, \varphi_2) = (1 + \varepsilon_2) e^{j\varphi_2} + 1, \quad (3.29)$$

$$X_4(\varepsilon_2, \varphi_2) = (1 + \varepsilon_2)e^{-j\varphi_2} - 1, \quad (3.30)$$

the resulting *IRR* can be calculated from the SS from of the finally downconverted signal, shown in Fig. 3.35. This is given by Eqs. (3.31) and (3.32).

$$IRR = \left| \frac{X_2X_3 + \overline{X_1X_4}}{X_1X_3 + \overline{X_2X_4}} \right|^2 \quad (3.31)$$

$$IRR = \frac{1 - 2(1 + \varepsilon_1)(1 + \varepsilon_2)\cos(\varphi_1 - \varphi_2) + (1 + \varepsilon_1)^2(1 + \varepsilon_2)^2}{1 + 2(1 + \varepsilon_1)(1 + \varepsilon_2)\cos(\varphi_1 + \varphi_2) + (1 + \varepsilon_1)^2(1 + \varepsilon_2)^2} \quad (3.32)$$

As stated in Section 3.3.1, the components that originate from the opposite frequencies are added in complement (Fig. 3.35) in Eq. (3.31). This result is in accordance with [6], which proves the validity of the application of the mixer-oscillator models for estimation of IRR.

The SS presentation, MO models, and IRR model are useful tools (“shorthands”) for the signal and spectral analysis in receiver topologies of any complexity.

### 3.6 CONCLUSIONS

Combining complex signal processing techniques with signal and spectral presentations is a powerful tool to both characterize and understand various phenomena related to RF front-ends.

An all-encompassing spectral analysis method called the spectrum-signal transformation has been introduced in this chapter. It addresses the issue of consistent presentation of transformation of signals and their spectra in the receive path of an RF front-end.

The mixer-oscillator models proposed in this chapter are based on the spectrum-signal formulation and offer a full interpretation of how signals and spectra are transformed from an RF range at the input up to a lower-frequency range at the output of different receiver topologies. Table 3.2 summarizes the classification of the mixer-oscillator models introduced in this chapter.

The mixer-oscillator models allow for examination of various RF system phenomena. The application of these models to the calculation of the image-rejection ratio in quadrature downconverters is an example of their utility.

Table 3.2: Mixer-oscillator models.

<b>DOUBLE-REAL MO-MODEL</b>	
<b>SINGLE-COMPLEX MO-MODEL</b>	
<b>DOUBLE-COMPLEX MO-MODEL</b>	

## REFERENCES

- [1] J. L. Hogan, "The Heterodyne Receiving System and Notes on the Recent Arlington-Salem Tests", *Proceedings IRE*, vol. 1, pp. 75-79, July 1913.
- [2] B. Liebowitz, "The Theory of Heterodyne Receivers", *Proceedings IRE*, vol. 3, pp. 185-204, September 1915.
- [3] F. M. Colebrook, "Homodyne", *Wireless World and Radio Review*, vol. 13, pp. 645-648, 1924.
- [4] D. G. Tucker, "The History of Homodyne and Synchrodyne", *Journal of the British Institution of Radio Engineers*, vol. 14, no. 4, pp. 143-154, April 1954.
- [5] J. Crols and M. S. J. Steyaert, "A Single-Chip 900 MHz CMOS Receiver Front-End with a High-Performance Low-IF Topology", *IEEE Journal of Solid-State Circuits*, vol. 31, pp. 1483-1492, December 1995.
- [6] B. Razavi, *RF Microelectronics*, Englewood Cliffs, NJ: Prentice-Hall, 1997.
- [7] J. C. Rudell et al., "A 1.9GHz Wide-Band IF Double Conversion CMOS Receiver for Cordless Telephone Applications", *IEEE Journal of Solid-State Circuits*, vol. 32, no. 12, pp. 2071-2088, December 1997.
- [8] J. Crols and M. Steyaert, *CMOS Wireless Transceiver Design*, Kluwer Academic Publishers, Boston, 1997.
- [9] A. Tasić and W. A. Serdijn, "Comprehensive Spectral Analysis Method of RF Front-Ends", *Proceedings ISCAS*, pp. 449-452, May 2001.
- [10] E. H. Armstrong, "The Super-Heterodyne – Its Origin, Developments, and some Recent Improvements", *Proceedings IRE*, vol. 12, pp. 539-552, October 1924.
- [11] A. N. Karanicolas, "A 2.7 V 900 MHz CMOS LNA and Mixer", *Proceedings ISSCC*, pp. 50-51, 416, February 1996.



- [12] R. G. Meyer *et al.*, “A 2.5-GHz BiCMOS Transceiver for Wireless LAN's”, *IEEE Journal of Solid-State Circuits*, vol. 32, no. 12, pp. 2097–2104, December 1997.
- [13] J. A. Macedo and M. A. Copeland, “A 1.9-GHz Silicon Receiver with Monolithic Image Filtering”, *IEEE Journal of Solid-State Circuits*, vol. 33, no. 3, pp. 378-386, March 1998.
- [14] F. Pizza and Q. Huang, “A 1.57-GHz RF Front-End for Triple Conversion GPS Receiver”, *IEEE Journal of Solid-State Circuits*, vol. 33, no. 2, pp. 202-209, February 1998.
- [15] H. Samavati *et al.*, “A 5-GHz CMOS Wireless LAN Receiver Front-End”, *IEEE Journal of Solid-State Circuits*, vol. 35, no. 5, pp. 7650772, May 2000.
- [16] E. Abou-Allam *et al.*, “Low-Voltage 1.9-GHz Front-End Receiver in 0.5- $\mu\text{m}$  CMOS Technology”, *IEEE Journal of Solid-State Circuits*, vol. 36, no. 10, pp. 1434-1443, October 2001.
- [17] S. Cosentino *et al.*, “An Integrated RF Transceiver for DECT Application”, *IEEE Journal of Solid-State Circuits*, vol. 37, no. 3, pp. 443-449, March 2002.
- [18] G. Chunbing *et al.*, “A Fully Integrated 900-MHz CMOS Wireless Receiver with on-Chip RF and IF Filters and 79-dB Image Rejection”, *IEEE Journal of Solid-State Circuits*, vol. 37, no. 8, pp. 1084-1089, August 2002.
- [19] M. Zargari *et al.*, “A 5-GHz CMOS Transceiver for IEEE 802.11a Wireless LAN Systems”, *IEEE Journal of Solid-State Circuits*, vol. 37, no. 12, pp. 1688-1694, December 2002.
- [20] V. Aparin *et al.*, “A Highly-Integrated Tri-Band/Quad-Mode SiGe BiCMOS RF-to-Baseband Receiver for Wireless CDMA/WCDMA/AMPS Applications With GPS Capability”, *Proceedings ISSCC*, vol. 1, pp. 234-235, February 2002.
- [21] C. Marshall *et al.* “2.7V GSM Transceiver ICs with On-Chip Filtering”, *Proceedings ISSCC*, pp. 148-149, February 1995.
- [22] Motorola Semiconductor, *Motorola Communication Device Data*, 1996.

- [23] Y. Oishi, T. Takano, and H. Nakamura, "Sensitivity Simulation Results for a Direct-Conversion FSK Receiver," *Proceedings of Vehicular Technology Conference*, pp. 588–595, June 1988.
- [24] A. Bateman and D. M. Haines, "Direct-Conversion Transceiver Design for Compact Low-Cost Portable Mobile Radio Terminals," *Proceedings of Vehicular Technology Conference*, pp. 57–62, May 1989.
- [25] K. Anvari, M. Kaube, and B. Hriskevich, "Performance of a Direct Conversion Receiver with  $\pi/4$ -DQPSK Modulated Signal," *Proceedings of Vehicular Technology Conference*, pp. 822–827, May 1991.
- [26] J. Sevenhans *et al.*, "An Integrated Si Bipolar RF Transceiver for a Zero-IF 900 MHz GSM Digital Mobile Radio Front-end of a Hand Portable Radio", *Proceedings CICC*, pp. 7.7.1–7.7.4, May 1991.
- [27] A. A. Abidi, "Direct-Conversion Radio Transceivers for Digital Communications," *IEEE Journal of Solid-State Circuits*, vol. 30, pp. 1399–1410, December 1995.
- [28] B. Razavi, "Design Considerations for Direct-Conversion Receivers", *IEEE Transactions on Circuits and Systems II: Analog and Digital Signal Processing*, vol. 44, no. 6, pp. 428 – 435, June 1997.
- [29] S. Wu and B. Razavi, "A 900-MHz/1.8-GHz CMOS Receiver for Dual-Band Applications", *IEEE Journal of Solid-State Circuits*, vol. 33, no. 12, pp. 2178-2185, December 1998.
- [30] A. Parssinen *et al.*, "A 2-GHz Wide-Band Direct Conversion Receiver for WCDMA Applications", *IEEE Journal of Solid-State Circuits*, vol. 34, no. 12, pp. 1893-1903, December 1999.
- [31] L. Ting-Ping and E. Westerwick, "5-GHz CMOS Radio Transceiver Front-End Chipset", *IEEE Journal of Solid-State Circuits*, vol. 35, no. 12, pp. 1927-1933, December 2000.
- [32] O. K. Jensen *et al.*, "RF Requirements for 3G WCDMA Mobile Equipment", *Microwave Journal*, pp. 22-46, February 2000.

- [33] P. M. Stroet et al., "A zero-IF Single-chip Transceiver for up to 22 Mb/s QPSK 802.11b Wireless LAN", *Proceedings ISSCC*, pp. 204-205, 447, February 2001.
- [34] J. Ryynanen et al., "A Dual-Band RF Front-End for WCDMA and GSM Applications", *IEEE Journal of Solid-State Circuits*, vol. 36, no. 8, pp. 1198-1204, August 2001.
- [35] D. Manstretta et al., "A 0.18  $\mu\text{m}$  CMOS Direct-Conversion Receiver Front-End for UMTS", *Proceedings ISSCC*, vol. 1, pp. 240,463, February 2002.
- [36] S. Mahadavi and A. A. Abidi, "Fully Integrated 2.2-mW CMOS Front End for a 900-MHz Wireless Receiver", *IEEE Journal of Solid-State Circuits*, vol. 37, no. 5, pp. 662-669, May 2002.
- [37] R. Magoon et al., "A Single-Chip Quad-Band (850/900/1800/1900 MHz) Direct-Conversion GSM/GPRS RF Transceiver with Integrated VCOs and Fractional-N Synthesizer", *IEEE Journal of Solid-State Circuits*, vol. 37, no. 12, pp. 1710-1720, December 2002.
- [38] D. Brunel et al., "A Highly Integrated 0.25  $\mu\text{m}$  BiCMOS Chipset for 3G UMTS/WCDMA Handset RF Sub-System", *Proceedings RFIC*, pp. 191-194, June 2002.
- [39] D. Manstretta and F. Svelto, "Analysis and Optimization of  $IIP2$  in CMOS Direct Downconverters", *Proceedings CICC*, pp. 243-246, May 2002.
- [40] R. Gharpurey et al., "A Direct-Conversion Receiver for the 3G WCDMA Standard", *IEEE Journal of Solid-State Circuits*, vol. 38, no. 3, pp. 556-560, March 2003.
- [41] J. Ryynanen et al., "A Single-Chip Multimode Receiver for GSM900, DCS1800, PCS1900, and WCDMA", *IEEE Journal of Solid-State Circuits*, vol. 38, no. 4, pp. 594-602, April 2003.
- [42] R. Svitek and S. Raman, "A SiGe Active Sub-Harmonic Receiver Front-End for 5-6 GHz Wireless Applications", *Topical Meeting on Silicon Monolithic IC in RF Systems*, pp. 64-67, April 2003.

[43] Philips Semiconductors, *Philips RF/Wireless Communications Data Handbook*, 1996.

[44] P. Baltus and A. Tombeur, "DECT Zero-IF Receiver Front-End", *Proceedings AACD Workshop*, vol. 2, pp. 295-318, March 1993.

[45] D. Rabey and J. Sevenhans, "The Challenges for Analog Circuit Design in Mobile Radio VLSI Chips", *Proceedings AACD Workshop*, vol. 2, pp. 225-236, March 1994.

[46] S. Sampei and K. Feher, "Adaptive DC-offset Compensation Algorithm for Burst Mode Operated Direct Conversion Receivers", *Proceedings of Vehicular Technology Conference*, pp. 93-96, May 1992.

[47] J. K. Cavers and M. W. Liao, "Adaptive Compensation for Imbalance and Offset Losses in Direct Conversion Transceivers", *IEEE Transactions on Vehicular Technology*, vol. 42, pp. 581-588, November 1993.

[48] J. Ryynanen et al., "RF Gain Control in Direct-Conversion Receivers", *Proceedings ISCAS*, vol. 4, pp. 117-120, May 2002.

[49] N. Won and T. H. Meng, "Direct-Conversion RF Receiver Design", *IEEE Transactions on Communications*, vol. 49, no. 3, pp. 518-529, March 2001.

[50] M. Steyaert et al., "A 2-V CMOS Cellular Transceiver Front-End", *IEEE Journal of Solid-State Circuits*, vol. 35, no. 12, pp. 1895-1907, December 2000.

[51] F. Behbahani et al., "A 2.4-GHz Low-IF Receiver for Wideband WLAN in 6- $\mu$ m CMOS - Architecture and Front-End", *IEEE Journal of Solid-State Circuits*, vol. 35, no. 12, pp. 1908-1916, December 2000.

[52] S. Tadjpour et al., "A 900-MHz Dual-Conversion Low-IF GSM Receiver in 0.35- $\mu$ m CMOS", *IEEE Journal of Solid-State Circuits*, vol. 36, no. 12, pp. 1992-2002, December 2001.

[53] H. Darabi et al., "A 2.4-GHz CMOS Transceiver for Bluetooth", *IEEE Journal of Solid-State Circuits*, vol. 36, no. 12, pp. 2016-2024, December 2001.

[54] Adiseno et al., “A Wide-band RF Front-End for Multi-band, Multi-standard High-Linearity Low-IF Wireless Receivers”, *IEEE Journal of Solid-State Circuits*, vol. 37, no. 9, pp. 1162-1168, September 2002.

[55] M. Y. Wang et al., “A Dual-band RF Front-End for WCDMA and GPS Applications”, *Proceedings ISCAS*, vol. 4, pp. 26-29, May 2002.

[56] R. Mohindra, “Isolator for DECT Open-Loop Modulator”, *RF Design*, pp. 30-42, January 1996.

[57] T. S. Rappaport, *Wireless Communications – Principles and Practice*, Prentice Hall, INC, Upper Saddle River, NJ 07458, 2002.

[58] L. W. Couch II, *Digital and Analog Communication Systems*, Prentice Hall International, INC, Upper Saddle River, NJ 07458, 1997.

[59] R. Hartley, “Single-Sideband Modulator”, U.S. Patent 1 666 206, April 1928.

[60] D. Weaver, “A Third Method of Generation and Detection of Single-Sideband Signals”, *Proceedings of the IRE*, pp. 1703-1705, June 1956.

[61] D. Weaver, “Design of RC Wide-Band 90-degree Phase-Difference Network”, *Proceedings of the IRE*, vol. 42, no.4, pp. 671-676, April 1954.

[62] S. H. Galal et al., “RC Sequence Asymmetric Polyphase Networks for RF Integrated Transceivers”, *IEEE Transactions of Circuits and Systems, Part II*, vol. 47, no. 1, pp. 18-27, January 2000.

[63] J. Rudell et al. “An Integrated GSM/DECT Receiver: Design Specifications”, UCB Electronics Research Laboratory Memorandum, Memo no. UCB/ERL M97/82, 1998.

[64] Federal Communications Commission – FCC, <http://www.fcc.gov>.

[65] European Telecommunications Standard Institute – ETSI, <http://www.etsi.org>.

[66] “European Digital Cellular Telecommunications System (Phase 1); Radio Transmission and Reception”, *European Telecommunications Standard*

Institute, ETSI 0505-DCS, 1994, <http://www.3gpp.org/specs/releases-contents-earlyGSM.htm>.

[67] ETSI 300 190 (GSM 05.05 version 5.4.1): *Digital Cellular Communication System (Phase 2), Radio Transmission and Reception*, European Telecommunications Standards Institute, August 1997.

[68] Telecommunications Industry Associations / Electronic Industries Associations Interim Standard - 95, (TIA/EIA IS-95B), "Mobile Station-Base Station Compatibility Standard for Dual-Mode Wideband Spread Spectrum Cellular Systems," 1998.

[69] Third Generation Partnership Project (3GPP), "UE Radio Transmission and Reception (FDD)", Technical Specification, 25.101, vol. 3.0.0, October 1999, <http://www.3gpp.org>.

[70] ETSI EN 300 175-2: "Digital Enhanced Cordless Telecommunications (DECT); Common Interface (CI); Part 2: Physical Layer (PHL)", <http://docbox.etsi.org/Reference>.

[71] *Specification of the Bluetooth System*, Version 1.1, February 2001, <http://www.bluetooth.com>.

[72] IEEE standard 802.11b, "Wireless Local Area Network, Medium Access Control (MAC) and Physical Layer (PHY) Specifications: Higher-Speed Physical Layer Extension in the 2.4 GHz Band", part 11, September 1999, [http://standards.ieee.org/getieee802/download/802.11b-1999\\_Cor1-2001.pdf](http://standards.ieee.org/getieee802/download/802.11b-1999_Cor1-2001.pdf).

[73] IEEE standard 802.11a, "Wireless LAN MAC: High-speed Physical Layer in the 5 GHz Band", <http://standards.ieee.org/getieee802/download/802.11a-1999.pdf>.

[74] Ultra Wide Band Alliance, Multi-Band OFDM Physical Layer Proposal for IEEE 802.15 Task Group 3a, September 2004, [http://www.multibandofdm.org/papers/MultiBand\\_OFDM\\_Physical\\_Layer\\_Proposal\\_for\\_IEEE\\_802.15.3a\\_Sept\\_04.pdf](http://www.multibandofdm.org/papers/MultiBand_OFDM_Physical_Layer_Proposal_for_IEEE_802.15.3a_Sept_04.pdf).

[75] N. Boutin, "Complex Signals", *RF Design*, pp. 27-33, December 1989.

[76] R. R. Anderson and J. Salz, "Spectra of Digital FM", *Bell System Technical Journal*, vol. 44, pp. 1165-1189, July 1965.

- [77] R. R. Goldberg, *Fourier Transforms*, Cambridge University Press, New York, 1961.
- [78] J. B. Thomas, *An Introduction to Statistical Communication Theory*, John Wiley & Sons, New York, 1965.
- [79] M. D. McDonald, “A 2.5 GHz BiCMOS Image-Reject Front-End”, *Proceedings ISSCC*, pp. 144–145, February 1993.

## SELECTION OF PERFORMANCE PARAMETERS FOR RF FRONT-END CIRCUITS

In the last decades, a rigorous procedure to select specifications for individual blocks in a radio receiver system has not been established: it rather relies on the judgement of an experienced designer [1,2]. Therefore, performance selection criteria are introduced in this chapter [3], resulting in a procedure for assigning the specifications to the receiver circuits.

One way to optimize performance is to design each RF circuit independently for minimum noise figure and good linearity. However, this approach requires more power than necessary. An alternative method to allocate each performance parameter to RF front-end *blocks* is introduced in this chapter, resulting in equal performance (noise, linearity) contributions of all circuits – equilibrium criterion.

On the other hand, noise figure ( $NF$ ) and 3<sup>rd</sup>-order input-intercept point ( $IIP3$ ) optimization procedures are not independent, as both the noise and linearity performance of a circuit depend on its gain. By optimizing the *system* performance with respect to the ratio  $F/P_{IIP3}$  (the noise factor over the 3<sup>rd</sup>-order power intercept point), a mutually dependent noise-linearity allocation procedure is developed in this chapter, resulting in the noise and linearity requirements satisfied – optimality criterion. Furthermore, the assignment of the specifications to the receiver circuits for the equal *system* noise and linearity margins with respect to the requirements is proposed – equality criterion.

This chapter is organized as follows. Some system considerations are discussed in the next section. Section 4.2 describes a procedure for selecting individual noise and linearity specifications for RF system blocks. The allocation of the mutually dependent noise and linearity performance parameters to RF front-end receiver circuits is outlined in Section 4.3. Subsequently, the condition for the optimal dynamic range of a receiver is derived. The criterion for equal contribution of the noise and the linearity to the receiver dynamic range (i.e.,  $IIP3-NF$ ) is also derived. The chapter continues with a discussion on the “cost” (i.e., power consumption) of these



design criteria. Finally, some design trade-offs between performance parameters of a single RF circuit are described by means of a K-rail diagram.

## 4.1 SYSTEM CONSIDERATIONS

For the sake of simplicity, we will refer to an RF receiver as a system consisting of an LNA, a mixer, and baseband (BB) circuitry (with channel selection included), as shown in Fig. 4.1.  $F$ ,  $P_{IIP3}$  and  $g$  are the noise factor, input-referred 3<sup>rd</sup>-order power intercept point and power gain of the corresponding RF blocks. Their logarithmic equivalents are indicated in Fig. 4.1:  $G$  is power gain in dB,  $NF$  noise figure and  $IIP3$  3<sup>rd</sup>-order input intercept point. Eqs. (4.1) and (4.2) express the equivalent system noise and linearity performance (see Chapter 2).

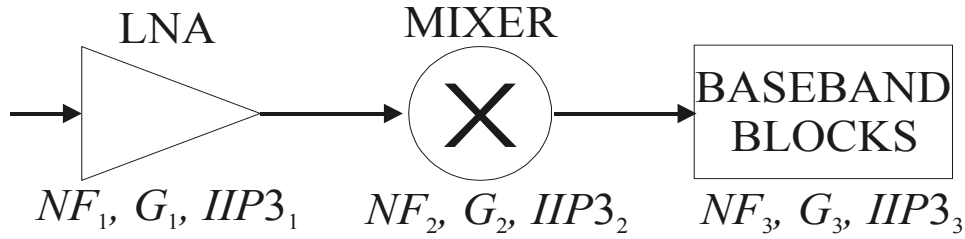


Figure 4.1: A simplified RF front-end receiver model.

$$F = F_1 + \frac{F_2 - 1}{g_1} + \frac{F_3 - 1}{g_1 g_2} + \dots \quad (4.1)$$

$$\frac{1}{P_{IIP3}} = \frac{1}{P_{IIP3,1}} + \frac{g_1}{P_{IIP3,2}} + \frac{g_1 g_2}{P_{IIP3,3}} + \dots \quad (4.2)$$

Typical  $G$ ,  $NF$ , and  $IIP3$  values for the receiver blocks are shown in Table 4.1 [4,5,6].

The blocks preceding the LNA (between LNA and antenna), viz., a T/R switch (TDD), an RF preselect filter (TDD/FDD) and a duplexer (FDD), are not considered in the analysis (and Fig. 4.1) as the noise/linearity parameters of these passive circuits are known prior to the integration (e.g., Tab. 4.1) of the RF circuits and the allocation of the specifications: the specifications

#### 4. Selection of Performance Parameters for RF Front-End Circuits 79

referred to the input of the LNA implicitly take into account the specifications of these blocks by adding/subtracting them from those referred to the antenna.

Table 4.1: Typical performance parameters of the receiver blocks.

	<b>T/R switch</b>	<b>RF filter</b>	<b>duplexer</b>	<b>LNA</b>	<b>mixer</b>	<b>BB</b>
$G$ [dB]	-1	-2	-3	10–20	5–15	40–60
$NF$ [dB]	1	2	3	1–3	10–20	20–10
$IIP3$ [dBm]	100	100	100	-5–2	-5–5	20–10

Design of receiver circuits imposes trade-offs between gain, noise, linearity, and power consumption. Goals of this multi-objective design problem are:

- provision of a sufficiently large gain in order to minimize noise contribution of the receiver circuits, while ensuring a signal large enough to drive an analogue-to-digital converter.
- provision of a sufficiently small gain in order not to degrade linearity of a system, i.e., to avoid saturation and clipping.
- operation at a low power-consumption level in order to ensure long battery life in a mobile device.

The selection of  $g$ ,  $F$  and  $P_{IIP3}$  for each receiver stage is usually solved by extensively exercising Eqs. (4.1) and (4.2) for a large number of  $(g, F, P_{IIP3})$  combinations until all the requirements are satisfied. The final choice is consciously directed towards the apriori known capabilities of the employed technology (e.g., an LNA  $NF < 2$  dB as a starting point).

Another possibility is (over)designing of the RF front-end circuits, i.e., optimizing each circuit independently for the best noise figure, linearity and gain [7], with penalties in power consumption.

In the following sections alternative criteria for the selection of performance parameters are proposed:

- the equilibrium criterion (point): separate (input-referred) contributions of the noise (linearity) performance parameters of each receiver block are equal.

- the optimality criterion (point): mutual optimization of the system noise and linearity performance via the ratio  $F/P_{IIP3}$ .
- the equality criterion (point): equal system noise and linearity performance improvements with respect to the requirements.

## 4.2 INDEPENDENT SELECTION OF $NF$ AND $IIP3$ SPECIFICATIONS

A procedure for the allocation of each performance parameter to the RF front-end blocks is introduced in this section.

As we can apply the same analysis procedure to calculate both the noise and linearity properties of a system, we introduce the following notation:  $ni$  refers to the noise factor and/or the input-referred 3<sup>rd</sup>-order power intercept point. Using this notation, Eqs. (4.1) and (4.2) become:

$$ni = ni_1 + ni_2 + ni_3 = \alpha \cdot ni_E + \beta \cdot ni_E + \gamma \cdot ni_E. \quad (4.3)$$

Here,  $ni_1$ ,  $ni_2$  and  $ni_3$  stand for the noise (linearity) contribution of each block in the receive chain (see Fig. 4.1) after being transformed to the input of the receiver. The coefficients  $\alpha$ ,  $\beta$  and  $\gamma$  represent the noise (linearity) deviation of the LNA, mixer and baseband circuitry from the *equilibrium point*  $ni_E$ , respectively. The  $ni_E$  point is calculated as:

$$ni_E = ni_D / n, \quad (4.4a)$$

or in dB as ( $NI$  is a dB counterpart of  $ni$ ;  $NI$  refers to the noise figure and/or the 3<sup>rd</sup>-order input-intercept point):

$$NI_E = NI_D - 10 \log n, \quad (4.4b)$$

where  $ni_D$  and  $NI_D$  are the *desired* (required) performance parameters of the complete RF front-end, and  $n$  is the number of the considered front-end circuits (in this case  $n=3$ ). The noise (linearity) equilibrium point ( $ni_E$  and  $NI_E$ ) refers to the condition when the noise (linearity) contributions of all receiver blocks are equal [5]. It is calculated from Eq. (4.3) when  $\alpha=\beta=\gamma=1$ .

#### 4. Selection of Performance Parameters for RF Front-End Circuits 81

Generally, when circuit noise (linearity) parameters deviate from the equilibrium point, then in order to satisfy the required system specifications ( $NI_D$ ), condition (4.5a) must be satisfied ( $NI=NI_D$ ),

$$10^{\frac{NI_D}{10}} = 10^{\frac{10\log n + NI_E}{10}} = 10^{\frac{A + NI_E}{10}} + 10^{\frac{B + NI_E}{10}} + 10^{\frac{C + NI_E}{10}}, \quad (4.5a)$$

where  $A=10\log\alpha$ ,  $B=10\log\beta$  and  $C=10\log\gamma$  (dB scale). For a three-block system, condition (4.5a) can be transformed into Eq. (4.5b).

$$B = 10\log\left(3 - 10^{A/10} - 10^{C/10}\right) \quad (4.5b)$$

The relationship between the deviations  $A$  and  $B$  is graphically shown in Fig. 4.2,  $C$  being the parameter. Even though rather simple, Eq. (4.5) and Fig. 4.2 determine a design space and a design central point for RF front-end circuits. As the circuits' noise (linearity) parameters depend equally on  $\alpha$  ( $A$ ) and  $\beta$  ( $B$ ) (Eq. (4.3)), also the dependency of the deviation  $A$  with respect to the deviation  $B$  is the same as the dependency of the parameter  $B$  with respect to the parameter  $A$ . Accordingly, the central design point satisfies equality (4.15):

$$\left.\frac{\partial A}{\partial B}\right|_{C=const} = \left.\frac{\partial B}{\partial A}\right|_{C=const}. \quad (4.6)$$

Solving Eq. (4.6) with the aid of Eq. (4.5) results in the central design point:

$$A = B. \quad (4.7)$$

The *slopes* of both dependences are the same at this point:  $A$  and  $B$  are in balance at this point (see Fig. 4.2). However, as the explicit solution of Eq. (4.5) depends also on the performance of the baseband circuitry, i.e., parameter  $C$ , two cases are distinguished.

First, if  $C=0$ , i.e., the noise (linearity) parameters of the baseband block are in the equilibrium, the central design point satisfies  $A=B=0$  (point  $O$  in Fig. 4.2), being the already defined equilibrium point.

In case of a negligible contribution of baseband circuitry to the equivalent (input) noise (linearity) parameter of the receiver ( $C \rightarrow -\infty$ ), Eqs. (4.5) and (4.6) result in  $A=B=1.76$  (equilibrium for a two-block system) as the central design point (point  $N$  in Fig. 4.2).

The result of Eq. (4.7) can also be justified as follows. Negative deviation from the equilibrium point ( $A < 0$ ,  $B < 0$ , and/or  $C < 0$ ) results in an improvement of a block performance that is always smaller than an improvement in the overall receiver performance. For example, improving the  $NF$  ( $IIP3$ ) of an LNA by 3dB ( $A = -3$ dB; point  $L$ ) with respect to the equilibrium design point relaxes the  $NF$  ( $IIP3$ ) requirement of a mixer for  $B = 1.76$ dB (if  $C = 0$ ). This results in  $3$ dB  $- 1.76$ dB  $= 1.24$ dB “waste” of the noise (linearity) performance for the same desired receiver noise figure (linearity)  $NF_D$  ( $IIP3_D$ ). On the other hand, relaxing the  $NF$  ( $IIP3$ ) of an LNA for  $A = 3$ dB would require an infinite noise-figure (linearity) improvement of a mixer (if  $C = 0$ ). Furthermore, for an over-designed noise (linearity) parameter of the LNA ( $A < -3$ ), the corresponding parameter of the mixer is just slightly relaxed ( $B < 3$ ).

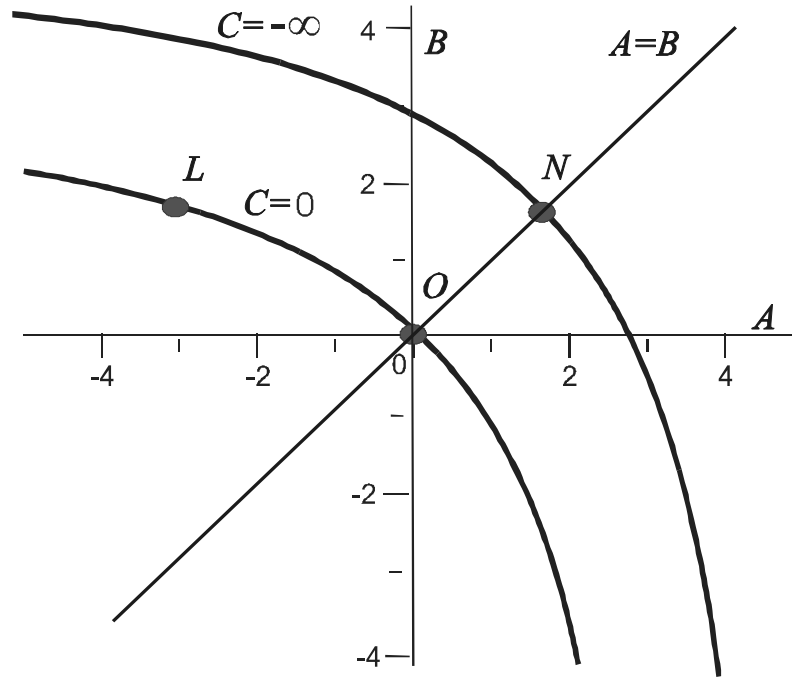


Figure 4.2: Deviation of the  $NF$  ( $IIP3$ ) of a mixer from the equilibrium point with respect to the  $NF$  ( $IIP3$ ) deviation of an LNA from the equilibrium point.

As discussed above, the rather common practice of taking into account only the noise (linearity) parameters of the LNA and mixer (i.e.,  $C \rightarrow -\infty$ ) would result in the 1.76dB relaxed required  $NF$  ( $IIP3$ ) performance of the very same blocks (point  $N$ ), when assigning the specifications. This under-estimation could in the end lead to a design not satisfying the specifications of a complete receiver chain, i.e., an LNA-mixer-baseband configuration.

#### 4. Selection of Performance Parameters for RF Front-End Circuits 83

Given Eq. (4.5b), the blocks' input-referred (i.e., at the input of the receiver in Fig. 4.1) noise (linearity) parameters ( $NI$ ) can be calculated as:

$$NI_1 = NI_E + A, \quad (4.8)$$

$$NI_2 = NI_E + B, \quad (4.9)$$

$$NI_3 = NI_E + C. \quad (4.10)$$

For the noise figure, Eqs. (4.8)-(4.10) read:

$$NF_1 = NF_E + A_{NF}, \quad (4.11)$$

$$NF_2 = NF_E + G_1 + B_{NF}, \quad (4.12)$$

$$NF_3 = NF_E + G_1 + G_2 + C_{NF}, \quad (4.13)$$

whereas for the third-order input-intercept point, Eqs. (4.8)-(4.10) become:

$$IIP3_1 = IIP3_E - A_{IIP3}, \quad (4.14)$$

$$IIP3_2 = IIP3_E + G_1 - B_{IIP3}, \quad (4.15)$$

$$IIP3_3 = IIP3_E + G_1 + G_2 - C_{IIP3}. \quad (4.16)$$

Indices  $NF$  and  $IIP3$  refer to the deviations from the equilibrium of noise figure and 3<sup>rd</sup>-order input intercept point, respectively. Eqs. (4.5b) and (4.11)-(4.16) establish the relationship between the noise (linearity) parameters of the receiver circuit blocks, satisfying the required system performance.

Whether the equilibrium design point is also power efficient depends on the power budget and the chosen circuit topology. Only at the circuit level the relationship between the gain, linearity, noise, and power consumption can be explicitly determined.

For example, it can be that an LNA topology with fewer components (transistors) than a mixer topology is still power efficient even if  $A \ll 0$ . In this case it would be advantageous to relax the mixer performance (though  $B$  would not increase much; e.g.,  $A \rightarrow -\infty$  and  $C=0$  result in  $B=3$  only), decreasing the absolute power consumption of a system.

**Example 4.1:**

Let us consider an example with the NF and IIP3 over-designed LNA.

Given the NF and IIP3 of both the RF front-end (as given in Fig. 4.1) and the LNA as  $NF_D=10\text{dB}$ ,  $IIP3_D=-10\text{dBm}$ ,  $NF_1=2\text{dB}$ ,  $IIP3_1=-1\text{dBm}$ , we will allocate the noise figure and the 3<sup>rd</sup>-order intercept point to the mixer, following the analysis outlined above.

With the aid of Eq. (4.4), the equilibrium NF and IIP3 equal  $NF_E=5\text{dB}$  and  $IIP3_E=-5\text{dBm}$ . If we assume  $G_1=12\text{dB}$ , and  $C_{NF}=-10\text{dB}$  and  $C_{IIP3}=-10\text{dB}$ , noise and linearity parameters of the mixer will be, as calculated from Eqs. (4.5), (4.10) and (4.13),  $IIP3_2=2.85\text{dB}$  and  $NF_2=21\text{dB}$ . These specifications satisfy the system requirements.

This noise and the linearity over-designed LNA allows for the relaxed noise and linearity performance of the mixer, while still satisfying the required specifications. The contribution of the mixer noise figure and 3<sup>rd</sup>-order input-intercept point at the input of the receiver (input of the LNA) are  $9\text{dB} \gg NF_1$  and  $-9.15\text{dBm} \ll IIP3_1$ , respectively.

In order to determine the gain of the mixer, let us assume that the baseband circuitry hardly affects the equivalent input noise figure or linearity (i.e.,  $\gamma \ll 1$ , e.g.,  $\gamma=0.1$  and  $C=-10\text{dB}$ ). Now, from Eq. (4.11),  $G_2=8\text{dB}$  for  $NF_3$  to be negligible, and from Eq. (4.14),  $G_2=-2\text{dB}$  for  $IIP3_3$  to be dominant. Here, we assumed typical values for the baseband performance parameters, being  $NF_3=15\text{dB}$ ,  $IIP3_3=15\text{dBm}$  and  $G_3=70\text{dB}$  [8,9].

Choosing  $G_2=8\text{dB}$  results in  $C_{IIP3}=0\text{dB}$  and  $C_{NF}=-10\text{dB}$ , with the required value for  $IIP3_2=5\text{dBm}$  and  $NF_2=21\text{dB}$ . For  $G_2=-2\text{dB}$ ,  $C_{NF}=0\text{dB}$  and  $C_{IIP3}=-10\text{dB}$ , the requirements are  $NF_2=18.75\text{dB}$  and  $IIP3_2=2.85\text{dBm}$ . The  $(G_2, NF_2, IIP3_2)$  combination (8dB, 21dB, 5dBm) requires a larger gain, a better linearity, and allows for a higher noise figure than the combination (-2dB, 18.75dB, 2.85dBm). The designer will make the final choice for the mixer performance parameters, having available circuit topology and power consumption information. This issue is discussed in more detail in Section 4.4.

Finally, we can conclude that by improving receiver block specifications by more than a few dB from the equilibrium point ( $O$  and  $N$  in Fig. 4.2), the requirements for the other blocks in the receive chain don't relax much (e.g.,  $A \rightarrow -\infty$  results only in  $B < 3$ ). This implies that (over)design, i.e., design for the best NF and IIP3, for each circuit can outperform a rather moderate design with an equal specification selection scheme, but with penalties in power consumption ( $A \rightarrow -\infty$  may have penalty in power consumption; more detail in Section 4.4).

This completes the discussion on the independent selection of performance parameters for the RF circuits, where in the end the performance selection procedure has been illustrated referring to the example of the NF and IIP3 over-designed LNA.

### 4.3 MUTUALLY DEPENDENT SELECTION OF *NF* AND *IIP3* SPECIFICATIONS

When assigning the system specifications to each block in the receive chain, it is common practice to consider each performance parameter separately [10,11]. However, as both the noise and the linearity performance depend on the gain of the corresponding blocks, optimizations of noise figure and 3<sup>rd</sup>-order intercept point are not mutually exclusive. Because there has not yet been developed an exact optimization procedure, Eqs. (4.1) and (4.2) are employed for a large number of  $(g, F, P_{IIP3})$  combinations, until all the requirements are satisfied. As there are many combinations that satisfy the desired specifications, the experience of the designer is what usually guides to the final decision.

We will develop a procedure for assigning *NF* and *IIP3* specifications not by optimizing the system performance to *NF* and *IIP3*, but to the ratio  $F/P_{IIP3}$  (*NF-IIP3* in dB). This appears to be a logical optimization parameter, establishing a direct relationship with the spurious free dynamic range (SFDR; Chapter 2) of the system that is proportional to  $P_{IIP3}/F$  (*IIP3-NF* in dB). Being inversely proportional to the *SFDR*, we will refer to the  $F/P_{IIP3}$  as to the *inverse dynamic range* (linear term *idr*; logarithmic term *IDR*=*NF-IIP3*).

#### 4.3.1 THE OPTIMALITY CRITERION

For the sake of easier interpretation of the optimization procedure, we will resort to a two-block RF front-end, consisting of an LNA and a mixer (e.g., assuming an ideal baseband block). Combining Eqs. (4.1) and (4.2), the inverse dynamic range (for 3<sup>rd</sup>-order intermodulation-distortion dominated systems) can be expressed as:

$$idr = \frac{F}{P_{IIP3}} = \left( F_1 + \frac{F_2 - 1}{g_1} \right) \left( \frac{1}{P_{IIP3,1}} + \frac{g_1}{P_{IIP3,2}} \right). \quad (4.17)$$



Assuming that for any  $(NF_1, IIP3_1)$  and  $(NF_2, IIP3_2)$  performance parameters combination there exists an optimal gain value  $g_{1,OPT}$ , it can be found by solving Eq. (4.18).

$$\left. \frac{\partial idr}{\partial g_1} \right|_{g_1=g_{1,OPT}} = 0 \quad (4.18)$$

This optimum gain  $G_{1,OPT}$  (in dB) equals:

$$G_{1,OPT}[dB] = \frac{NF_2 + IIP3_2 - NF_1 - IIP3_1}{2}. \quad (4.19)$$

Substituting the optimum gain into Eq. (4.17), the optimum inverse dynamic range  $IDR_{OPT}$  ( $NF$ - $IIP3$ ) becomes:

$$IDR_{OPT} = 20 \log \left( 10^{\frac{NF_1 - IIP3_1}{20}} + 10^{\frac{NF_2 - IIP3_2}{20}} \right). \quad (4.20)$$

The optimum gain  $G_{1,OPT}$  of an LNA, Eq. (4.19), provides the RF front-end with the optimum inverse dynamic range, Eq. (4.20) (i.e., the maximum spurious free dynamic range). The lower the  $IDR$ , the larger the spurious-free dynamic range.

Fig. 4.3 shows an *inverse dynamic range (IDR) diagram* for an optimal dynamic range design point. The IDR diagram describes graphically the selection of noise and linearity parameters throughout the receive chain. Each step in the IDR diagram corresponds to one stage of the receive chain, where the sloped transition indicates a transformation (gain) between the stages. For example, the  $NF$  and  $IIP3$  of the mixer ( $NF_2$  and  $IIP3_2$ ) transform with the gain  $G_{1,OPT}$  to the input of the LNA as  $NF_{2-to-1}$  and  $IIP3_{2-to-1}$ .

As can be seen from Fig. 4.3, all input referred noise-figure and third-order intercept point combinations (or  $IDR_1$ ,  $IDR_2$ ) *balance* the equivalent  $IDR$ , and accordingly the dynamic range of the system [12,13].

Let us now elaborate in more detail on the simultaneous noise and linearity performance optimization procedure, i.e., IDR optimization. The optimum IDR design point doesn't always satisfy the individual noise and linearity specifications, even though it provides the RF front-end (prior to the LNA) with the maximum dynamic range. The condition that provides optimum  $IDR$  and satisfies system specifications can be derived from Eqs. (4.1) and (4.2). Namely, with the aid of Eq. (4.19), the system's  $F$  and  $P_{IIP3}$  can be written as:

$$F = \sqrt{F_1 P_{IIP3,1}} \left[ \sqrt{\frac{F_1}{P_{IIP3,1}}} + \sqrt{\frac{F_2}{P_{IIP3,2}}} \right], \quad (4.21)$$

$$\frac{1}{P_{IIP3}} = \frac{1}{\sqrt{F_1 P_{IIP3,1}}} \left[ \sqrt{\frac{F_1}{P_{IIP3,1}}} + \sqrt{\frac{F_2}{P_{IIP3,2}}} \right]. \quad (4.22)$$

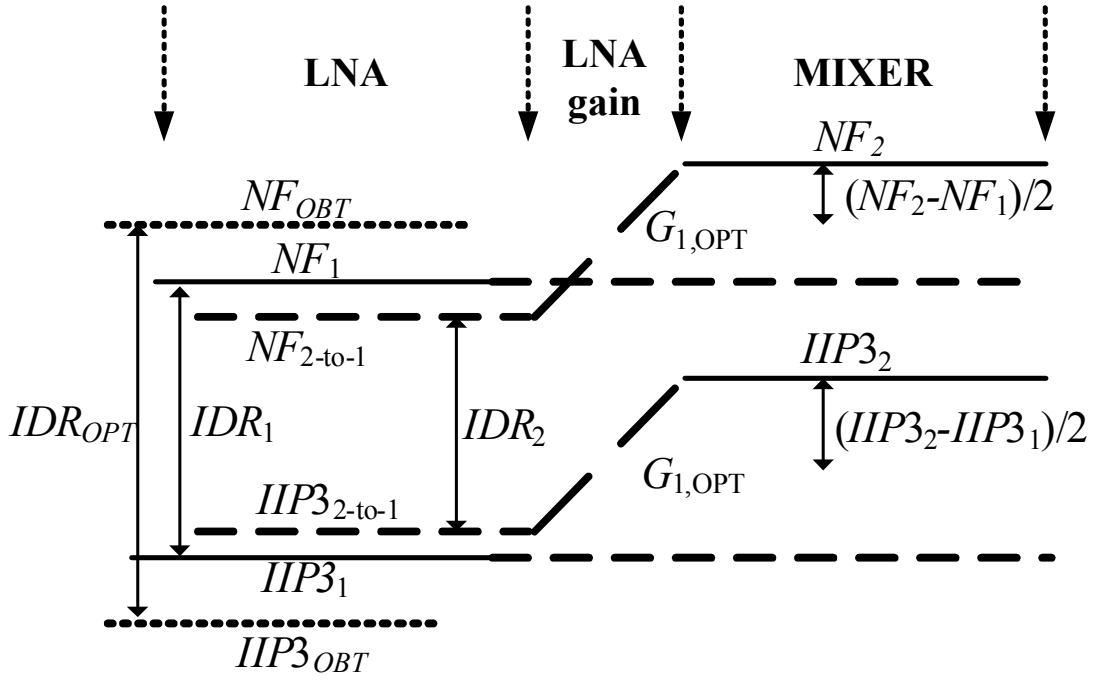


Figure 4.3: The inverse dynamic range diagram for an optimal dynamic range design point.

The condition for the  $IDR_{OPT}$  that also satisfies the system requirements is obtained by substituting Eq. (4.20) into Eqs. (4.21) and (4.22), which gives:

$$2NF_{OBT} = NF_1 + IIP3_1 + IDR_{OPT} < 2NF_D, \quad (4.23)$$

$$2IIP3_{OBT} = NF_1 + IIP3_1 - IDR_{OPT} > 2IIP3_D, \quad (4.24)$$

$NF_{OBT}$  and  $IIP3_{OBT}$  are the obtained noise and linearity parameters.

Suppose that the noise and the linearity performance of the LNA are known, then the above conditions (and Eq. (4.20)) can be transformed into Eqs. (4.25)

and (4.26) that give an explicit relationship between the  $(NF_1, IIP3_1)$  and  $(NF_2, IIP3_2)$  pairs.

$$NF_2 - IIP3_2 < 20 \log \left( 10^{\frac{2NF_D - NF_1 - IIP3_1}{20}} - 10^{\frac{NF_1 - IIP3_1}{20}} \right) \quad (4.25)$$

$$NF_2 - IIP3_2 < 20 \log \left( 10^{\frac{-2IIP3_D + NF_1 + IIP3_1}{20}} - 10^{\frac{NF_1 - IIP3_1}{20}} \right) \quad (4.26)$$

Conditions (4.23)-(4.26) obey condition (4.27) as well.

$$NF_1 + IIP3_1 = NF_{OBT} + IIP3_{OBT} \quad (4.27)$$

In the remainder of this chapter we will often refer to the above conditions as the optimality criterion.

Given partly the specifications of receiver blocks, the optimality criterion allows the selection of undetermined performance parameters for maximal dynamic range.

#### **Example 4.2:**

Let us clarify the outlined selection procedure with an example (in this case a noise-figure limited system).

Given  $NF_D=10\text{dB}$ ,  $IIP3_D=-10\text{dBm}$ ,  $NF_1=9\text{dB}$ ,  $IIP3_1=5\text{dBm}$ , the noise figure and 3<sup>rd</sup>-order input-intercept points of the mixer must satisfy the inequality  $NF_2 - IIP3_2 < -7.7\text{dB}$  (Eqs. (4.25) and (4.26)), in order to provide the system with the desired specifications. Pair  $NF_2=10\text{dB}$  and  $IIP3_2=17.7\text{dBm}$  can be, for example, an IDR optimal design point, resulting in an optimum gain  $G_{1,OPT}=6.85\text{dB}$  and  $IDR_{OPT}=6\text{dB}$ . As will be explained in the next section, for a system with poor noise or linearity performance, as it is the case in this example (poor noise figure), the optimum design point can be rather unrealistic with respect to the requirements that it imposes on the system blocks.

### **4.3.2 THE EQUALITY CRITERION**

In this section we will consider the criterion for the equivalent improvements in the noise and linearity from the desired (required) RF front-end specifications  $NF_D$  and  $IIP3_D$  (referred to the input of the LNA).

#### 4. Selection of Performance Parameters for RF Front-End Circuits 89

The  $IDR$  equivalent-contribution gain  $G_{1,EQ}$  can be found from Eqs. (4.28) and (4.29), which can also be expressed as Eq. (4.30).

$$NF_D - NF_{OBT} = -\Delta \quad (4.28)$$

$$IIP3_{OBT} - IIP3_D = -\Delta \quad (4.29)$$

$$NF_{OBT} + IIP3_{OBT} = NF_D + IIP3_D \quad (4.30)$$

Here,  $\Delta < 0$  (in dB) stands for the improvement (margin) in both the  $NF$  and the  $IIP3$  of the RF front-end, with the obtained specifications being always better than the desired ones, i.e.,  $NF_{OBT} < NF_D$  and  $IIP3_{OBT} > IIP3_D$ . The range of the margin  $\Delta$  is:

$$\Delta \in (\max\{IIP3_D - IIP3_1, NF_1 - NF_D\}, 0]. \quad (4.31)$$

Given, for example,  $NF_1$  and  $IIP3_1$ , the range of  $NF_2 - IIP3_2$  values can be determined by modifying Eqs. (4.1) and (4.2), as given by Eqs. (4.32) and (4.33):

$$\frac{F_2}{g_{1,EQ}} \cong \delta F_D - F_1, \quad (4.32)$$

$$\frac{g_{1,EQ}}{P_{IIP3,2}} = \frac{\delta}{P_{IIP3,D}} - \frac{1}{P_{IIP3,1}}, \quad (4.33)$$

where  $\Delta = 10 \log \delta$ . Now, a combination of the noise figure and the linearity of the mixer that satisfies the system specifications can be determined from Eq. (4.34), which is obtained by combining Eqs. (4.32) and (4.33).

$$NF_2 - IIP3_2 = 10 \log \left( 10^{\frac{\Delta + NF_D}{10}} - 10^{\frac{NF_1}{10}} \right) + 10 \log \left( 10^{\frac{\Delta - IIP3_D}{10}} - 10^{\frac{-IIP3_1}{10}} \right) \quad (4.34)$$

Similarly, the equivalent gain  $G_{1,EQ}$  of the first receiver block (LNA) is calculated from Eqs. (4.32) and (4.33), and given by Eqs. (4.35) and (4.36).

$$G_{1,EQ} = NF_2 - 10 \log \left( 10^{\frac{\Delta + NF_D}{10}} - 10^{\frac{NF_1}{10}} \right) \quad (4.35)$$

$$G_{1,EQ} = IIP3_2 + 10 \log \left( 10^{\frac{\Delta - IIP3_D}{10}} - 10^{\frac{-IIP3_1}{10}} \right) \quad (4.36)$$

If the performance parameters of the LNA and mixer are selected as suggested by Eqs. (4.34)-(4.36), both the noise and linearity contribute equally to the desired dynamic range (i.e., the obtained  $NF$  and  $IIP3$  are equally improved by  $\Delta$  as given by Eqs. (4.28) and (4.29)). This is illustrated by the following example and the IDR diagram shown in Fig. 4.4.

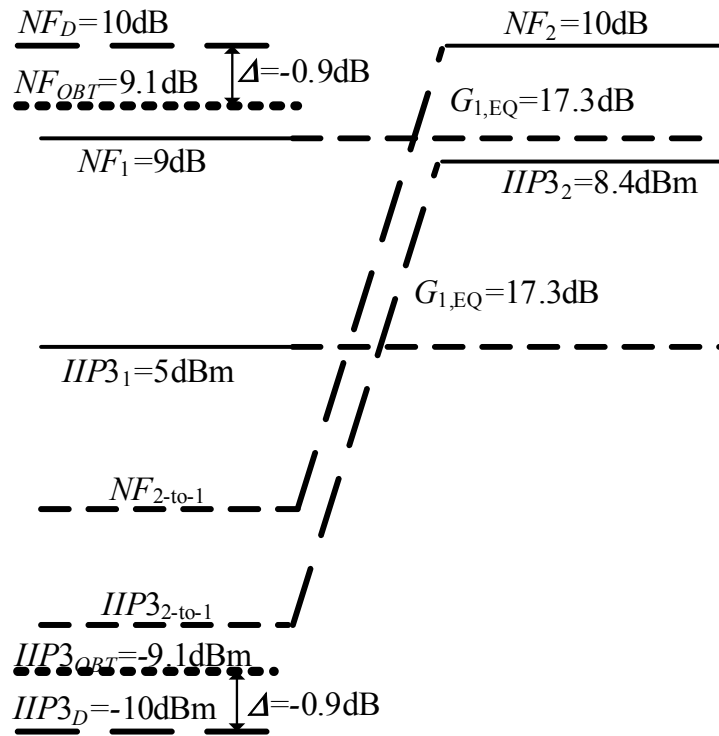


Figure 4.4: The inverse dynamic range diagram for the equivalent noise and linearity improvements with respect to the desired inverse dynamic range.

#### Example 4.3:

Referring to the example for the optimum design point (Example 4.2), the following is obtained:  $NF_2 - IIP3_2 = 1.6$  dB for the chosen  $\Delta = -0.9$  dB ( $\Delta \in (-1, 0]$ ).

One solution,  $NF_2=10\text{dB}$  and  $IIP3_2=8.4\text{dBm}$  with the gain  $G_{1,EQ}=17.3\text{dB}$ , provides the system with the  $IDR_{EQ}=18.2\text{dB}$  ( $NF_{OBT}=9.1\text{dB}$  and  $IIP3_{OBT}=-9.1\text{dBm}$ ), i.e., an equal improvement of  $0.9\text{dB}$  for both the noise figure and the 3<sup>rd</sup>-order input-intercept point. The corresponding performance parameters are shown in Fig. 4.4.

### 4.3.3 OPTIMALITY VS. EQUALITY

As suggested in Example 4.2, for systems with poor noise and/or linearity from one circuit, the optimum design point can be rather unrealistic, i.e., “expensive” with respect to the requirements that it imposes on other circuits. This becomes obvious if we look at the IDR diagram of Example 4.2 that is shown in Fig. 4.5.

In this noise-limited system (i.e., a poor  $NF$  of the LNA) the optimum IDR point, which also satisfies the system performance, requires a mixer with very high linearity,  $IIP3_2=17.7\text{dBm}$ , and a moderate noise figure  $NF_2=10\text{dB}$  (see Table 4.2). As given by Example 4.2, this results in  $G_{1,OPT}=6.85\text{dB}$ ,  $IDR_{OPT}=6\text{dB}$ , and the system noise figure and linearity  $NF_{OBT}=10\text{dB}$  and  $IIP3_{OBT}=4\text{dBm}$ . As the system just satisfies the noise requirement, it is over-designed for linearity.

However, by choosing for a moderate linearity of the mixer,  $IIP3_2=8.4\text{dBm}$ , as suggested by Example 4.3, and  $NF_2=10\text{dB}$  results in  $G_{1,OPT}=2.2\text{dB}$ ,  $IDR_{OPT}=8.9\text{dB}$ , and  $NF_{OBT}=11.5\text{dB}$  and  $IIP3_{OBT}=2.6\text{dBm}$  (see Table 4.2). This suggests that violating condition (4.25) results in the unsatisfactory noise performance of the system.

Table 4.2: Block performance for  $NF_D=10\text{dB}$ ,  $IIP3_D=-10\text{dBm}$ ,  $NF_1=9\text{dB}$ ,  $IIP3_1=5\text{dBm}$ . OP-1: optimum design point for satisfied system requirements; OP-2: optimum design point for unsatisfied system requirements; EQ: equality design point for satisfied system requirements.

	$NF_2$ [dB]	$IIP3_2$ [dBm]	$G_1$ [dB]	$NF_{OBT}$ [dB]	$IIP3_{OBT}$	$IDR_{OBT}$
OP-1	10	17.7	6.85	10	4 dBm	6 dB
OP-2	10	8.4	2.2	11.5	2.6 dBm	8.9 dB
EQ	10	8.4	17.4	9.1	-9.1 dBm	18.2 dB

These findings imply that the optimum design point imposes moderate requirements on circuit blocks only in the vicinity of conditions (4.27) and

(4.30). The further from these conditions, the more demanding the design requirements result from Eqs. (4.25) and (4.26). Therefore the design requirements from the equality criterion should be considered in such situations (Example 4.3).

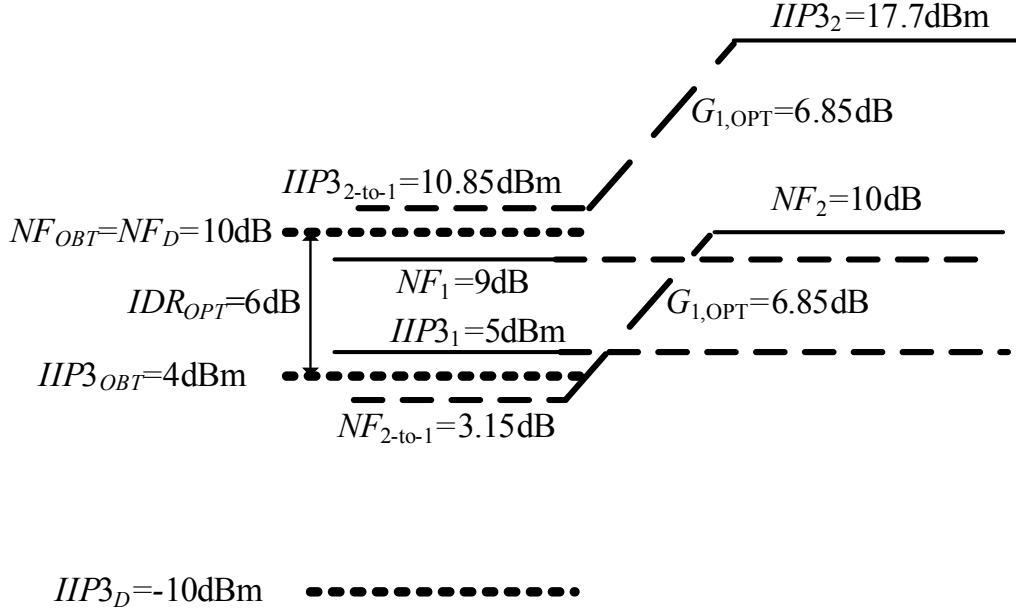


Figure 4.5: IDR diagram for an “expensive” optimum design point.

#### 4.4 EQUILIBRIUM, OPTIMALITY AND EQUALITY CRITERIA

With the aid of Eq. (4.27), being the optimality criterion, and Eq. (4.30), being the equality criterion, the condition where these criteria meet has a form:

$$NF_1 + IIP3_1 = NF_D + IIP3_D. \quad (4.37)$$

with conditions (3.23), (3.24), (3.28) and (3.29) satisfied.

This condition can be simply obtained by substituting the optimal design point, Eqs. (4.23) and (4.24), into the conditions for the equivalent performance improvements, Eqs. (4.28) and (4.29). Accordingly, the simultaneous optimality and equality criteria impose the condition:

$$NF_D - \frac{NF_1 + IIP3_1 + IDR_{OPT}}{2} = \frac{NF_1 + IIP3_1 - IDR_{OPT}}{2} - IIP3_D, \quad (4.38)$$

which is equal to Eq. (4.37), as expected.

A property of this *optimality-equality condition* (Sections 4.3.1 and 4.3.2) is that it coincides with the condition for the independent selection of performance parameters (Section 4.2). Namely, if condition (4.37) is satisfied, the equilibrium design point (the equal contribution of each block performance parameter to the system performance) encompasses the optimum design point (maximum inverse dynamic range) and the equality point (equal contribution of the noise figure and the 3<sup>rd</sup>-order input-intercept point to the IDR). The IDR diagram, corresponding to the simultaneously satisfied equilibrium-optimum-equality condition is shown in Fig. 4.6.

Complying with Eq. (4.37), the allocation of all the specifications to each of the blocks in the RF front-end receive chain is rather simple and fully controlled by means of Eqs. (4.5), (4.8)-(4.10), (4.19), (4.25), (4.26) and (4.34)-(4.36).

**Example 4.4:**

We will illustrate the aforementioned findings by an example. The required specifications are:  $NF_D=10\text{dB}$ ,  $IIP3_D=-10\text{dBm}$ .

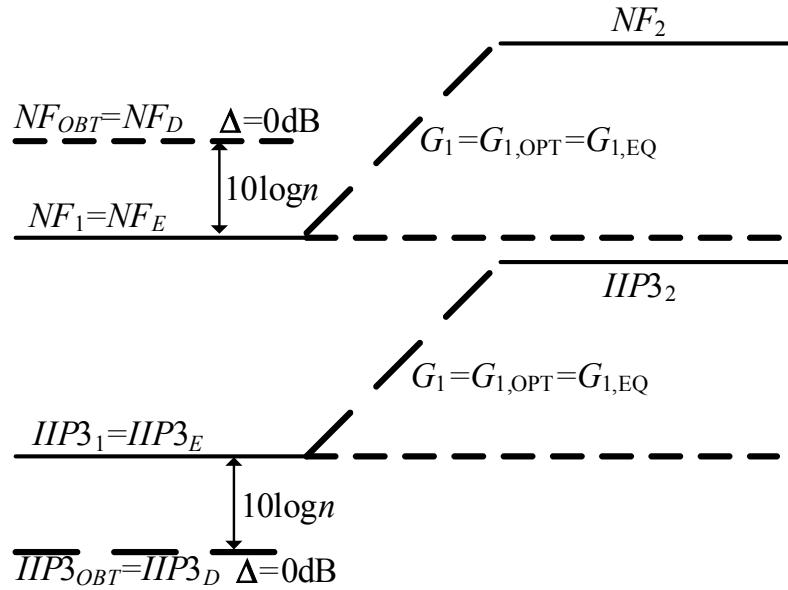


Figure 4.6: The inverse dynamic range diagram for the simultaneously satisfied equilibrium-optimum-equality conditions.

The performance parameters allocated to the LNA according to Eqs. (4.4) and (4.8) result in a design point satisfying all the design criteria, i.e., the



optimal distribution of both the individual and the mutually dependent specifications. From Eq. (4.4),  $NF_E=7\text{dB}$  and  $IIP3_E=-7\text{dBm}$ , if  $n=2$  (LNA and mixer). Referring to Eq. (4.8), the performance parameters of the LNA become  $NF_1=7\text{dB}$  and  $IIP3_1=-7\text{dBm}$ .

From Eq. (4.34), the equality condition is  $NF_2-IIP3_2=14\text{dB}$ . Choosing, for example, for  $NF_2=16\text{dB}$  and  $IIP3_2=2\text{dBm}$  results in  $G_{1,EQ}=9\text{dB}$ .

On the other hand, the optimum IDR condition is determined from Eq. (4.25) to be  $NF_2-IIP3_2<19\text{dB}$ . The already chosen mixer parameters automatically satisfy this condition. From Eq. (4.19), the optimum gain equals  $G_{1,OPT}=9\text{dB}$ , being the same as  $G_{1,EQ}$ .

Finally, referring the noise and linearity properties of the mixer to the input of the receiver we obtain:  $NF_{2-to-1}=16-9=7\text{dB}$  and  $IIP3_{2-to-1}=2-9=-7\text{dBm}$ , being the equilibrium quantities already calculated by Eq. (4.4).

## 4.5 NOTES ON POWER CONSUMPTION

In the foregoing discussion, the selection of specifications for receiver circuits is considered without explicitly addressing the power consumption issue. Namely, whether the equilibrium point, the optimum point and the equality point are also power-consumption efficient depends upon a number of factors. *The available power budget and the chosen circuit implementation are just some of them.*

In Sections 4.2 and 4.3 it has been advocated for the *desired* ( $NF, IIP3, G$ ) combination of each circuit block. However, only at the circuit level, the relationship between the four parameters, viz.,  $NF$ ,  $IIP3$ ,  $G$ , and power consumption, can be exactly determined. Whether the *obtained* specifications coincide the *desired* specifications depends on the available power budget (i.e., power consumption).

Just like a picture says more than a thousand words, an example says more than a hundred pages of theory.

### **Example 4.5:**

Let us consider a two-block system, consisting of an inductively degenerated single-ended low-noise amplifier [14,15] and a Gilbert mixer [16]. Referring to Example 4.4, the equilibrium point of the LNA is  $NF_1=7\text{dB}$ ,  $IIP3_1=-7\text{dBm}$ ,  $G_1=9\text{dB}$  and power consumption  $PC_1$ . The mixer equilibrium point is determined to be  $NF_2=16\text{dB}$ ,  $IIP3_2=2\text{dBm}$  (Example 4.4,) with power consumption  $PC_2$ . We will assume that  $PC_2 \gg PC_1$ , as the mixer has more transistor branches compared to the LNA, which has only one branch.

#### 4. Selection of Performance Parameters for RF Front-End Circuits 95

As the LNA power consumption is rather low (poor performance LNA), even by increasing it a few times it is still relatively small in comparison with the power consumption of the mixer. For a factor 3 increase in power consumption ( $PC_1' = 3PC_1$ ) for the LNA, the new specifications would be, for example,  $NF_1' = 2\text{dB}$ ,  $IIP3_1' = 3\text{dBm}$ ,  $G_1' = 16\text{dB}$  [15,17,18]. As now the deviation  $A_{NF} = -5\text{dB}$ , the noise figure of the mixer referred to the input of the system will be relaxed for  $B_{NF} = -2.26\text{dB}$  (Eq. (4.5)). On the other hand,  $A_{IIP3} = -10\text{dB}$  results in  $B_{IIP3} = -2.78\text{dB}$ .

The mixer performance parameters that satisfy the system requirements, i.e.,  $NF_D = 10\text{dB}$ ,  $IIP3_D = -10\text{dBm}$ , are finally obtained from Eqs. (4.11)-(4.16) as:  $NF_2' = 25.26\text{dB}$  and  $IIP3_2' = 6.22\text{dBm}$ . Concerning the  $NF$  requirement of the mixer, this implies a considerable reduction of its power consumption. However, the linearity requirement implies an increase in power consumption if a realistic assumption is acquired, viz., noise figure and linearity improve with power consumption, being contradictory to the mixer  $NF$  requirement.

What is more, a choice of  $NF_2' = 25.26\text{dB}$  and  $G_1 = G_{1,OPT} = 16\text{dB}$  results in the mixer optimum linearity point  $IIP3_{2,OPT} = 11\text{dBm}$ . However, by reducing the mixer power consumption, the obtained mixer linearity will be even more degraded ( $\ll IIP3_2 = 2\text{dBm} \ll IIP3_{2,OPT}$ ). This will finally lead not only away from the equilibrium, the optimum and/or the equality design point, but also to unsatisfactory linearity behaviour of the complete system.

### **4.6 PERFORMANCE TRADE-OFFS IN A SINGLE RF CIRCUIT**

There is just a rough impression of how RF circuits trade power consumption for performance. Moreover, if the key circuit parameters are set by a communication system in an adaptive way and not fixed by a hardware design, many concepts fail due to incomplete knowledge of how the change of one parameter is reflected in the others.

Various phenomena and concepts related to RF circuits can be both qualitatively and quantitatively interpreted by means of the K-rail diagrams that are introduced in this section. K-rail diagrams allow for the performance characterization of RF circuits, and describe (visualize) relationships and trade-offs between their performance parameters: these are voltage swing, tank conductance, power consumption, phase noise and loop gain for oscillators as well as noise figure, linearity, gain and power consumption for amplifiers.

In the remainder of this section, trade-offs between the performance parameters of an inductively-degenerated (ID) [15] low-noise amplifier are discussed with the aid of the K-rail diagram, shown in Fig. 4.7. The design of LNAs imposes many trade-offs between gain, noise figure, linearity, and power consumption. Some of the challenging goals of the multi-objective LNA design procedure are:

- provision of a sufficient gain in order to minimize noise contribution of the receiver circuits proceeding an LNA, while not degrading system linearity.
- optimization of amplifier's noise figure with simultaneous noise and power match at input of an LNA.
- operation at low power-consumption levels in order to ensure long battery life of a mobile device.

The relationships between the noise figure, linearity, gain, optimum source resistance, input impedance and power consumption of an ID-LNA are described in Fig. 4.7 [18].

The arrows in the diagram perpendicular to the corresponding axes represent lines of constant gain, NF, IIP3, input impedance, optimum source impedance, and power consumption. Namely, each point in the design space (in this case a line; the k-rail) corresponds to a set of design parameters that are obtained as a normal projection of the design point on the rail to the indicated axes.

For example, a point that corresponds to the optimum of the minimum noise figure (minimum noise figure under noise-matched conditions) is shown as OPT-MIN. Parameters of this point are noise figure  $NF_{OPT-MIN}$ , voltage gain  $VG_{OPT-MIN}$ , linearity  $IIP3_{OPT-MIN}$ , and optimum (noise) source resistance and input impedance  $R_S$  (both equal to source resistance). A parameter  $k_{OPT-MIN}$  is related to power consumption.

With the aid of the K-rail diagram, we can describe the effects of a particular design choice on the performance of amplifiers.

Consider a situation where radio-channel conditions improve, i.e., a receive signal is much larger than noise and interferers (large input signal-to-noise-and-interference ratio). Here, the LNA doesn't have to operate with the best noise figure and gain and accordingly waste power. It is possible to operate at a moderate gain to the extent that the noise figure and sensitivity of an RF front-end system are not degraded, with considerable power savings in turn. This situation corresponds to point LOW in the K-rail diagram.

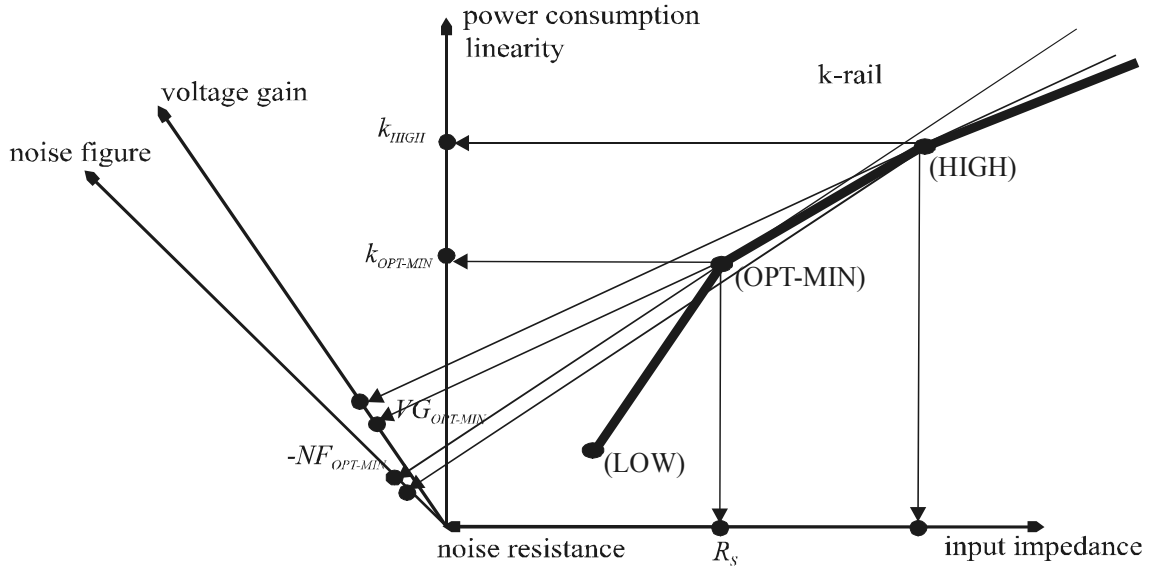


Figure 4.7: LNA K-rail diagram.

On the other hand, a weak receive signal requires large amplification and low noise figure from an LNA in order to achieve the desired signal-to-noise ratio at the end of a receive chain. In this situation, a HIGH design point can be chosen.

Finally, point OPT-MIN has the advantage of lower NF and power consumption, but at the cost of lower gain and IIP3 compared to point HIGH. Compared to point LOW, better gain, NF and linearity and higher power consumption result.

Similarly, design trade-offs for other RF circuits can be mapped onto corresponding K-rail diagrams [19]. K-rail diagrams for low-noise amplifiers and voltage-controlled oscillators are detailed in Chapters 5 and 6, respectively.

## 4.7 CONCLUSIONS

The procedure for allocation of the performance parameters to the RF front-end circuits has been introduced in this chapter. By optimizing the system performance with respect to the ratio  $F/P_{IIP3}$ , the optimal dynamic range design point can be found which satisfies both the noise and the linearity requirements.

It has been shown that there exists an equilibrium design point for which the contributions of each block performance parameter to the equivalent system

performance parameter are equal. Furthermore, the equilibrium design choice coincides with both design for the optimal dynamic range and design for the equal margins of each performance parameter with respect to the required specifications. Finally, some design trade-offs in a single RF circuit are discussed using the K-rail diagram.

## REFERENCES

- [1] M. Steyaert et al., "A 2V CMOS Cellular Transceiver Front-End", *IEEE Journal of Solid-State Circuits*, vol. 35, no. 12, pp. 1895-1907, December 2000.
- [2] F. Behbahani et al., "An Adaptive 2.4GHz Low-IF Receiver in 0.6um CMOS for Wideband WLAN", *Proceedings ISSCC*, pp. 146-147, February 2000.
- [3] A. Tasić, W. A. Serdijn and J. R. Long, "Optimal Distribution of the RF Front-End System Specification to the RF Front-End Circuit Blocks", *Proceedings ISCAS*, pp. 23-26, May 2004.
- [4] B. Razavi, *RF Microelectronics*, Englewood Cliffs, Prentice-Hall, 1997.
- [5] J. Rudell et al. "An Integrated GSM/DECT Receiver: Design Specifications", UCB Electronics Research Laboratory Memorandum, Memo no. UCB/ERL M97/82, 1998.
- [6] O. K. Jensen et al. "RF Receiver Requirements for 3G W-CDMA Mobile Equipment", *Microwave Journal*, pp. 22-46, February 2000.
- [7] G. Gramegna et al., "A Sub 1-dB NF 2.3kV ESD-Protected 900MHz CMOS LNA", *IEEE Journal of Solid-State Circuits*, vol. 36, no. 7, pp. 1010-1017, July 2001.
- [8] J. Ryynanen et al., "A Single-Chip Multimode Receiver for GSM900, DCS1800, PCS1900, and WCDMA", *IEEE Journal of Solid-State Circuits*, vol. 38, no. 4, pp. 594-602, April 2003.
- [9] A. K-Sanjani, H. Sjoland and A. A. Abidi, "A 2GHz Merged CMOS LNA and Mixer for WCDMA", *Proceedings VLSI*, pp. 19-23, June 2001.

#### 4. Selection of Performance Parameters for RF Front-End Circuits 99

[10] D. K. Shaeffer and T. H. Lee, "A 1.5-V, 1.5-GHz CMOS Low-Noise Amplifier", *IEEE Journal of Solid-State Circuits*, vol. 32, no. 5, pp. 745-759, May 1997.

[11] K. L. Fong and R. G. Meyer, "Monolithic RF Active Mixer Design", *IEEE Transactions on Circuits and Systems II: Analog and Digital Signal Processing*, vol. 46, no. 3, pp. 231-239, March 1999.

[12] D. Shaeffer and T. H. Lee, *Low-Power CMOS Radio Receiver*, Kluwer Academic Publishers, Norwell, Massachusetts, 2000.

[13] G. Groenewold, *Optimal Dynamic Range Integrated Continuous-Time Filters*, PhD Thesis, Delft University of Technology, 1992.

[14] M. J. O. Strutt and A. van der Ziel, "The Causes for the Increase of Admittance of Modern High-Frequency Amplifier Tubes on Short Waves", *Proceedings IRE*, vol. 26, no. 8, pp. 1011-1032, August 1938.

[15] S. P. Voinigescu et al. "A Scalable HF Noise Model for Bipolar Transistors with Application to Optimal Transistor Sizing for LNA Design", *IEEE Journal Solid State Circuits*, vol. 32, no. 9, pp. 1430-1439, September 1997.

[16] B. Gilbert, "Design Considerations for Active BJT Mixers", *Low-Power HF Microelectronics, A Unified Approach*, G. Machado, Ed. London: IEE, Chapter 23, pp. 837-927, 1996.

[17] O. Shana et al., "Frequency-Scalable SiGe Bipolar RF Front-End Design" *IEEE Journal of Solid-State Circuits*, vol. 36, no.6, pp. 888-895, 2001.

[18] A. Tasić, W. A. Serdijn and J. R. Long, "Concept of Noise-Figure Tuning of Low-Noise Amplifiers", *Proceedings ECCTD*, vol. 1, pp. 74-77, September 2003.

[19] A. Tasić, W. A. Serdijn and J. R. Long, "Adaptivity Figures of Merit and K-rail Diagrams - Comprehensive Performance Characterization of Low-Noise Amplifiers and Voltage-Controlled Oscillators", *Proceedings ISCAS*, pp. 401-404, May 2003.

## ADAPTIVITY OF LOW-NOISE AMPLIFIERS

The wireless telecommunication transceivers of both today and the future have to be broadband [1], low power [2], and adaptive [3]. Broad bandwidth supports the high data rates demanded by emerging applications. Adaptivity accommodates varying channel conditions and application requirements, while consuming as little energy as possible ensures long talk time on one battery charge.

However, analog RF front-end circuits are typically designed to perform one specific task, while key parameters such as dynamic range, bandwidth and selectivity are fixed by hardware design and not by the communication system in an adaptive way. As a result, today's receiver topologies are designed to function under the most stringent conditions, which increases circuit complexity and power consumption.

The variant nature of radio-channel conditions and accordingly variable requirements imposed on RF circuits in the direct signal path urge for designs that can respond to such changes “on-the-fly” (adaptive designs).

Adaptivity figures of merit (AFOM) (i.e., adaptivity models) of low-noise amplifiers are derived in this chapter. They reveal the relationships and trade-offs between the performance parameters, being noise figure, gain, linearity and power consumption, of an adaptive low-noise amplifier. Moreover, adaptivity models form the basis for the design of low-noise amplifiers (LNAs) that operate across multiple standards.

This chapter is organized in the following way. Adaptivity of amplifiers is discussed next. The subject of Section 5.2 is performance characterization of low-noise amplifiers: input-impedance (power-matching) model, gain-model and noise-model parameters are determined. Adaptivity models are derived in Section 5.3, giving insight into the extent to which LNA performance parameters can vary while still not degrading overall performance. The relationships between the performance and power consumption of adaptive low-noise amplifiers are graphically described by means of the amplifier K-rail diagram.

## 5.1 ADAPTIVITY PHENOMENA OF AMPLIFIERS

In order to understand how the change in one parameter is reflected to the others, adaptivity phenomena and their models are introduced [4].

Some of the low-noise amplifier adaptivity phenomena are: noise-figure, linearity, gain, and input-impedance tuning. Corresponding adaptivity figures of merit are shown in Fig. 5.1 on the amplifier K-rail diagram: input- and optimum source-resistance tuning ranges ( $RITR$  and  $RSTR$ ), voltage-gain tuning range ( $VGTR$ ), noise-figure tuning range ( $NFTR$ ), and tuning range of input-referred 3<sup>rd</sup>-order intercept point ( $IIP3TR$ ). Adaptivity phenomena and their figures of merit describe the change of circuit performance with respect to power consumption (which is related to parameter  $k$ ). For example,  $NFTR$  relates to noise-figure difference for different biasing conditions.

The amplifier K-rail diagram is constructed for an inductively-degenerated low-noise amplifier (ID-LNA) [5,6], shown in Fig. 5.2, following the rules outlined in the previous chapter. This amplifier topology allows for simultaneous input power and noise matching: optimum source (noise) resistance and amplifier input resistance can be adjusted independently, whereas their imaginary parts cancel simultaneously [6].

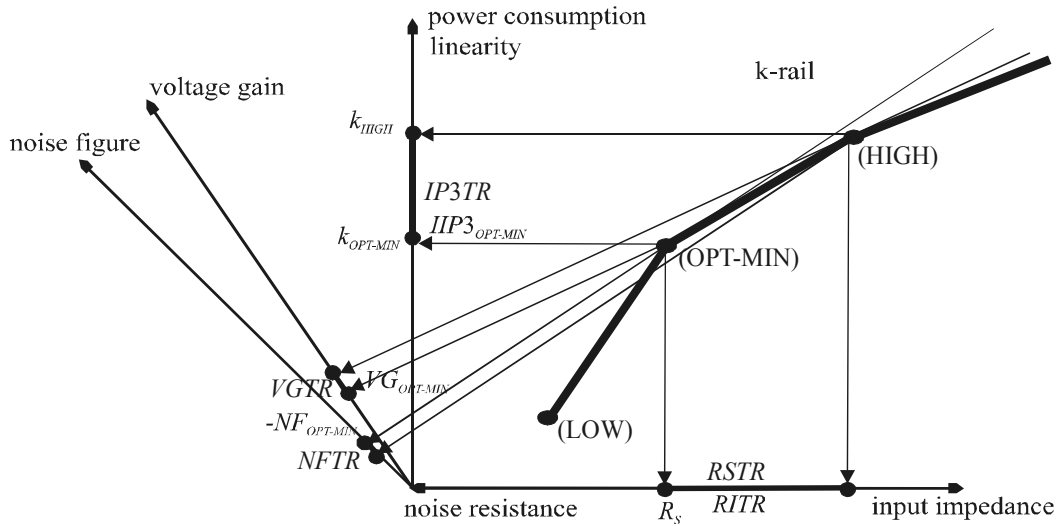


Figure 5.1: K-rail diagram for an adaptive LNA.

Points LOW and HIGH of the K-rail diagram have already been defined in Section 4.6. We refer to the noise-figure difference between points HIGH and OPT-MIN (or OPT-MIN and LOW) as the noise-figure tuning range: it corresponds to change of amplifier's noise figure with respect to power



consumption. Designing for noise figure of an amplifier that covers a noise-figure tuning range  $NF_{HIGH}-NF_{OPT-MIN}$  (shown as  $NFTR$  in Fig. 5.1) accounts for different operating conditions and satisfies LNA's performance over a certain range rather than in a fixed design point. This is an example of the application of the design for adaptivity to amplifiers.

Furthermore, this K-rail diagram shows that an increase in power results in an improvement of noise figure and voltage gain, but only to the levels determined by  $k_{OPT-MIN}$  (point OPT-MIN), and  $k_{HIGH}$  (point HIGH corresponds to maximum transit frequency of input transistor  $Q_1$  in Fig. 6.2), respectively. Due to shallow nature of the noise figure (small  $NFTR$ ) near the optimum-minimum noise-figure point for ID-LNAs, considerable power savings (point LOW) as well as linearity improvements (point HIGH) can be achieved.

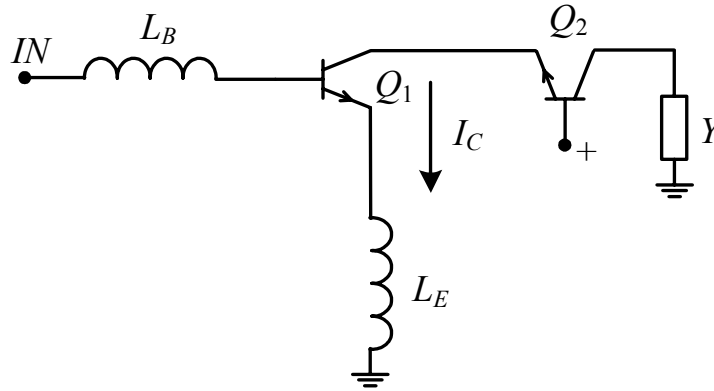


Figure 5.2: Inductively-degenerated LNA:  $L_E$  and  $L_B$  stand for the emitter and base matching inductors; biasing not shown.

The adaptivity models (and adaptivity tuning ranges) are described analytically later in this chapter. Relationships between power consumption and input impedance, gain, noise figure and linearity are determined. The procedure proposed forms a base for design of adaptive LNAs.

## 5.2 PERFORMANCE PARAMETERS OF INDUCTIVELY-DEGENERATED LOW-NOISE AMPLIFIERS

In this section, we will derive adaptivity models for an ID-LNA. This amplifier topology, shown in Fig. 5.2, is a traditional cascode configuration, where  $Y$  stands for the load admittance of the amplifier, and  $L_E$  and  $L_B$  for the

degenerative emitter and base inductors, respectively. Performance of this amplifier topology (i.e., gain, noise, and linearity) is characterized. The following analytical models are derived: an input-impedance model, a gain model, and a noise model. Finally, an intuitive linearity model is elaborated.

### 5.2.1 INPUT-IMPEDANCE MODEL

The input circuit of the ID-LNA is shown in Fig. 5.3 (base resistance and inductance are not shown). Here,  $Y_{\Pi}$  is the base-emitter admittance (dominated by capacitance  $C_{\Pi}$  for high frequencies),  $C_{\mu}$  the Miller capacitance,  $g_m$  the transconductance of input bipolar transistor  $Q_1$ ,  $Y_L$  the input admittance of the cascoding stage (in this case the input admittance of the common-base transistor  $Q_2$ ), and  $Y_E$  is the equivalent admittance in series with emitter of transistor  $Q_1$ . The transconductances of both transistors are assumed equal.

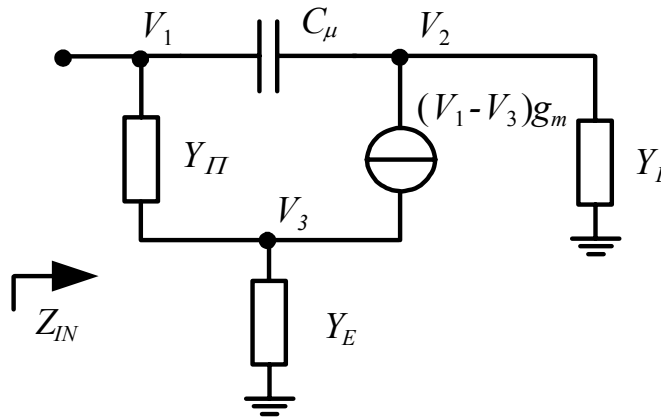


Figure 5.3: Input circuit of an ID-LNA ( $L_B$  not shown).

Applying Kirchoff's current law to the circuit shown in Fig. 5.3, the admittance at the input of transistor  $Q_1$ ,  $Y_{IN-Q1}$ , is calculated as:

$$Y_{IN-Q1} = Y_{\Pi}(1 - V_3/V_1) + sC_{\mu}(1 - V_2/V_1). \quad (5.1)$$

With the assumption that at the frequency of interest,

$$\omega C_{\mu} \ll g_m, \quad \omega C_{\mu} \ll Y_L = g_m, \quad (5.2)$$

the admittance  $Y_{IN-Q1}$  becomes:

$$Y_{IN-Q1} = Y_{II} \cdot f(Y_E) + sC_\mu[1 + g_m f(Y_E)/Y_L], \quad (5.3)$$

where  $f(Y_E)$  is the *feedback function* equal to:

$$f(Y_E) = 1 - V_3/V_1. \quad (5.4)$$

The input impedance can be estimated from Eq. (5.2) (it accounts for the feedback over capacitance  $C_\mu$ ) by determining the function  $f(Y_E)$  (which neglects the Miller effect). From Fig. 5.3, the feedback function reads:

$$f(Y_E) = \frac{Y_E}{Y_{II} + Y_E + g_m}, \quad (5.5)$$

and hence the input impedance  $Z_{IN}$ , neglecting the Miller effect ( $C_\mu=0$ ), and taking into account the base inductance  $L_B$  (see Fig. 5.2), becomes:

$$Z_{IN} = \omega_T L_E + j \left[ \omega(L_E + L_B) - \frac{\omega_T}{\omega} \frac{1}{g_m} \right]. \quad (5.6)$$

The condition for the power matching at the input of the amplifier can be derived from Eq. (5.6). The power matching condition can be transformed into two corresponding conditions: the real part of input impedance equals the source resistance ( $R_S$ ), and the imaginary part of input impedance is canceled (the source impedance is assumed real). This is given by Eqs. (5.7) and (5.8) (transistor's parasitic resistances are neglected).

$$\text{Re}\{Z_{IN}\} = 2\pi f_T L_E = R_S \quad (5.7)$$

$$\text{Im}\{Z_{IN}\} = \omega_0(L_E + L_B) - \frac{\omega_T}{\omega} \frac{1}{g_m} = 0 \quad (5.8)$$

Another option for power matching is discussed in Appendix B.

### 5.2.2 GAIN MODEL

From Figs. 5.2 and 5.3, and the feedback function given by Eq. (5.5), the effective transconductance  $g_{EFF}$  and voltage gain  $vg$  (from the source) can be expressed as:

$$g_{EFF} = -g_m \frac{(1 - V_3/V_1)}{1 + Y_{II}/Y_S(1 - V_3/V_1)} = -g_m \frac{f(Y_E)}{1 + Y_{II}/Y_S f(Y_E)}, \quad (5.9)$$

$$vg = -g_m Z \frac{(1 - V_3/V_1)}{1 + Y_{II}/Y_S(1 - V_3/V_1)} = -g_m Z \frac{f(Y_E)}{1 + Y_{II}/Y_S f(Y_E)}, \quad (5.10)$$

where  $Y_S$  represents the source resistance and base inductance, and  $Z$  is the load impedance (see Fig. 5.2).

For the input power match, given by conditions (5.7) and (5.8), the effective transconductance and the voltage gain of the ID-LNA become (for the sake of simplicity, the source and load impedances are assumed identical  $Z=R_S$ ):

$$g_{EFF} = -\frac{g_m}{Y_{II}} \frac{1}{Z_{IN} + Z_S} = -\frac{1}{2R_S} \frac{\omega_T}{\omega}, \quad (5.11)$$

$$|vg| = \left| \frac{g_m}{Y_{II}} \right| \frac{Z}{Z_{IN} + Z_S} = \frac{1}{2} \frac{\omega_T}{\omega}. \quad (5.12)$$

It is very convenient to relate the performance parameters of ID-LNAs to the ratio  $\omega_T/\omega$ , as it establishes a direct relationship between the gain and other performance parameters (e.g., noise figure). Eq. (5.13) refers to this ratio as  $x$ :

$$x = \frac{\omega_T}{\omega}. \quad (5.13)$$

The voltage gain transforms simply into:

$$|vg| = \frac{1}{2} x. \quad (5.14)$$

### 5.2.3 NOISE MODEL

In the following sections, we will calculate the noise-related parameters that are used for derivation of adaptivity models of ID-LNAs. These are the noise factor ( $F$ ), the optimum source resistance providing minimum noise factor ( $R_{S,OPT}$ ), the minimum noise factor ( $F_{MIN}$ ) (see Chapter 2), and the optimum of the minimum noise-factor ( $F_{OPT-MIN}$ ; the minimum noise factor under the noise-matched condition  $R_S = R_{S,OPT}$ ).

#### 5.2.3.1 Noise Factor

The corresponding noise circuit model of the amplifier is shown in Fig. 5.4, where  $\bar{V}_N$  and  $\bar{I}_N$  are the equivalent input noise sources of a transistor in common-emitter configuration [6-8].

Applying the Blakesley transformation to the voltage noise source and splitting the current noise source, at the same time keeping track of their orientation, the voltage noise source at the input of the LNA is calculated.

$$\bar{V}_{N,EQ} = \bar{V}_N + (Z_S + Z_E + Z_B)\bar{I}_N \quad (5.15)$$

$Z_S = R_S$ ,  $Z_E = j\omega L_E$  and  $Z_B = j\omega L_B$ .

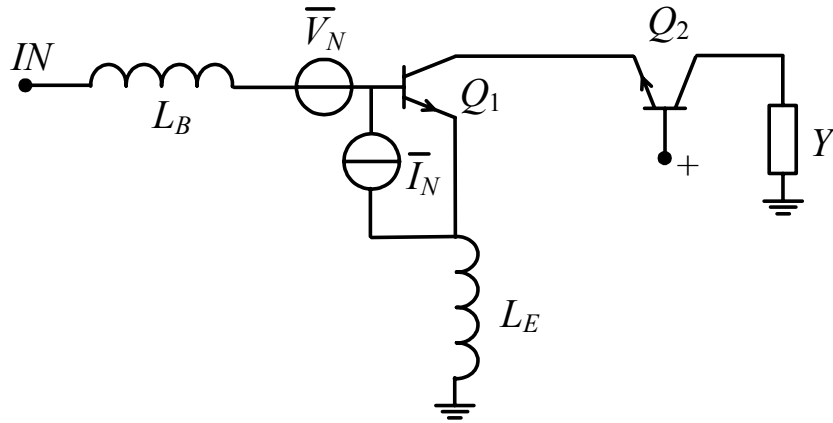


Figure 5.4: Noise model of the ID-LNA.

The equivalent common-emitter transistor noise sources are given by Eqs. (5.16)-(5.18) [7]:

$$\bar{V}_N = \bar{V}_B - B_N \bar{I}_C + (r_B + r_E)(\bar{I}_B - D_N \bar{I}_C), \quad (5.16)$$

$$\bar{I}_N = \bar{I}_B - D_N \bar{I}_C, \quad (5.17)$$

$$\bar{I}_B^2 = 2qI_B \quad \bar{I}_C^2 = 2qI_C \quad \bar{V}_B^2 = 4KT(r_B + r_E), \quad (5.18)$$

where  $\bar{I}_B$  is the base-current shot noise,  $\bar{I}_C$  the collector-current shot noise,  $\bar{V}_B$  the base and emitter resistance ( $r_B + r_E$ ) thermal noise.  $I_B$  and  $I_C$  are the input transistor base and collector currents,  $B_N = -1/g_m$  and  $D_N = -(1/\beta_F + j\omega/\omega_T)$  the input transistor transmission parameters [7],  $K$  is Boltzmann's constant and  $T$  the absolute temperature. Yet,  $B_F (\cong \beta_F)$  and  $\beta_F$  are the DC and AC transistor's current gain factors, respectively.

With the aid of Eqs. (5.15)-(5.18), the *adaptive* noise-factor model is determined [8].

$$F = \frac{\bar{V}_{N,EQ}^2}{4KTR_S} = 1 + k\delta + \frac{g_m}{2} \delta R_S + \frac{1 + 2k + k^2\delta + \delta L_G^2 - \frac{L_G\omega}{2\omega_T}}{2g_m R_S} \quad (5.19)$$

$$k = r_{EF} g_m (1 + 1/\beta_F) \quad (5.20)$$

$$L_G = g_m \omega L_{EB} (1 + 1/\beta_F) \quad \delta = \frac{1}{\beta_F} + \left(\frac{\omega}{\omega_T}\right)^2 \quad (5.21)$$

$$r_{EF} = r_B + r_E \quad L_{EB} = L_E + L_B \quad (5.22)$$

This model is parameterized with respect to power consumption via the *biasing parameter*  $k$ , Eq. (5.20). The introduced biasing parameter  $k$  is the corner-stone adaptivity parameter. Assuming  $r_{EF}$  is independent of current and  $\beta_F \gg 1$ , parameter  $k$  is proportional to the biasing condition, i.e., power consumption, via  $k \sim g_m \sim I_C$ . Amplifier performance parameters, viz., gain, noise, and linearity, are controlled by the bias current  $I_C$ , shown in Fig. 5.2. This allows for adaptation of the amplifier performance to different conditions.

### 5.2.3.2 Minimum Noise Factor

A source resistance  $R_S$  that satisfies condition (5.23),

$$\left. \frac{dF}{dR_S} \right|_{R_S=R_{S,OPT}} = 0, \quad (5.23)$$

is the *optimum source resistance*  $R_{S,OPT}$ , providing an amplifier with the minimum noise factor at the desired frequency (optimum source reactance ( $X_{S,OPT}$ ) and reactive part of input impedance of an ID-LNA are equal: this implies that  $X_{S,OPT}$  is canceled [6,9], if the matching condition, Eq. (5.8), is satisfied). From Eq. (5.23), the most comprehensive form for  $R_{S,OPT}$  becomes:

$$R_{S,OPT} = \frac{1}{g_m \sqrt{\delta}} \sqrt{1 + 2k + \frac{(1+k)^2}{\beta_F} + \frac{k^2}{x^2} + \delta L_G^2 - \frac{L_G}{2x}}. \quad (5.24)$$

Assuming  $\beta_F \gg 1$ , Eq. (5.24) simplifies to:

$$R_{S,OPT} = \frac{1}{g_m} \sqrt{(r_{EF} g_m)^2 + \frac{1 + 2r_{EF} g_m}{1/\beta_F + (\omega/\omega_T)^2}}. \quad (5.25)$$

With the aid of Eqs. (5.19) and (5.24), the *minimum noise factor* can be calculated:

$$F_{MIN} \cong 1 + k\delta + \sqrt{\delta \left[ 1 + 2k + \frac{(1+k)^2}{\beta_F} + \frac{k^2}{x^2} \right]}, \quad (5.26)$$

which after some simplifications (i.e.,  $\beta_F \gg 1$  and  $k\delta \ll 1$ ) reduces to:

$$F_{MIN} \cong 1 + \sqrt{(1 + 2r_{EF} g_m) \left[ \frac{1}{\beta_F} + \left( \frac{\omega}{\omega_T} \right)^2 \right]}. \quad (5.27)$$

### 5.2.2.3 Optimum-Minimum Noise Factor

Once the noise-matching parameters are found, viz., the optimum noise resistance and the minimum noise factor, the optimum of the minimum noise

factor can finally be obtained for a certain biasing condition. Namely, solving Eq. (5.28) results in a bias current (i.e., transconductance) providing the optimum of the noise factor under the noise-matched condition (i.e., optimum of  $F_{MIN}$ ).

$$\left. \frac{dF_{MIN}}{dg_m} \right|_{g_m = g_{m,OPT-MIN}} = 0 \quad (5.28)$$

With the aid of Eqs. (5.27) and (5.28), the simplified condition for the optimum of the minimum noise factor becomes:

$$g_{m,OPT-MIN} \cong \omega C_{\Pi} \sqrt{\beta_F \left[ 1 + \frac{1}{r_{EF} g_{m,OPT-MIN}} \right]}. \quad (5.29)$$

The solution for the transconductance  $g_{m,OPT-MIN}$  can be found iteratively from this equation.

The *optimum-minimum source resistance* can be written as:

$$R_{S,OPT-MIN} = \frac{1}{g_{m,OPT-MIN}} \sqrt{\frac{1}{\beta_F} (1 + k_{OPT-MIN})}, \quad (5.30)$$

where  $k_{OPT-MIN} = r_{EF} g_{m,OPT-MIN}$ .

From Eqs. (5.26)-(5.29), the optimum of the minimum noise factor equals:

$$F_{OPT-MIN} = 1 + \frac{k_{OPT-MIN} (1 + 2k_{OPT-MIN})}{\beta_F (1 + k_{OPT-MIN})} + \sqrt{\left[ \frac{k_{OPT-MIN} (1 + 2k_{OPT-MIN})}{\beta_F (1 + k_{OPT-MIN})} \right]^2 + \frac{(1 + 2k_{OPT-MIN})^2}{\beta_F (1 + k_{OPT-MIN})}}, \quad (5.31)$$

or when simplified:

$$F_{OPT-MIN} = 1 + \frac{1 + 2r_{EF} g_{m,OPT-MIN}}{\sqrt{\beta_F (1 + r_{EF} g_{m,OPT-MIN})}}. \quad (5.32)$$

After solving Eq. (5.29) for the optimum transconductance, i.e., optimum current density of a minimum dimension transistor, the final transistor



dimensions as well as its current consumption are determined from Eq. (5.24) (e.g., by setting the resistance  $R_{S,OPT}$  to a certain value, typically  $50\Omega$ ). This is because parameters  $k$  and  $\omega_T$  are assumed independent of transistor dimensions for the same current density.

However, the current for the optimum of the minimum noise factor does not coincide with the peak gain for the ID-LNA [9], and therefore if more gain is desired, the minimum noise factor will not be at its optimum. Moreover, a  $50\Omega$  noise match (i.e.,  $R_{S,OPT}=50\Omega$ ) often requires a large input transistor, and accordingly large current consumption for the determined optimum bias point (see Example 5.1). The choice of a smaller transistor would result in a larger  $R_{S,OPT}$  and lower current consumption for the optimum of the minimum noise factor at the cost of the minimum noise factor increased [9]. If a degradation of noise factor is tolerable, a slight increase of the bias current provides a larger gain, and accordingly reduces the cascaded noise factor of a system.

#### 5.2.4 LINEARITY MODEL

Algebraic expressions describing the 3<sup>rd</sup>-order intercept point (IP3, linearity performance parameter) of an ID-LNA consist of many multidimensional terms: base-emitter diffusion capacitance, base-emitter junction capacitance, base resistance, emitter degenerative inductance, load impedance, and DC bias current [10]. Even though the dominant nonlinearities can be identified using the Volterra-series method [10-12], the relationships between these parameters and linearity are often not clear to the designer. However, the level of detail required to accurately describe transistor nonlinearity is adequately captured in modern CAD tools.

Some conclusions found in literature are reviewed here [12]. Emitter degeneration improves linearity of common-emitter transistors (i.e., the larger the inductance  $L_E$  (see Fig. 5.2), the better the linearity, but the lower the gain). The 3<sup>rd</sup>-order intermodulation product for an inductively-degenerated common-emitter bipolar stage is inversely proportional to the cube of the DC bias current. When high linearity is desired, the bias current of an ID-LNA should be increased.

##### **Example 5.1:**

The introduced amplifier performance models are examined by comparing simulated and calculated performance of an inductively-degenerated LNA.

Referring to a 50GHz SiGe technology and frequency of operation  $f=2.4\text{GHz}$ , the dimensions of the amplifier transistors are  $0.4\times 5\mu\text{m}^2$  (20 transistors), the collector current is 7mA, and the inductors in the emitter and

base of the input transistor are  $L_B=3.2\text{nH}$  and  $L_E=0.36\text{nH}$  (this is an example of a power consuming  $50\Omega$  noise match). The simulation results of the ID-LNA performance are shown in Table 5.1. The results predicted by the calculations are shown in Table 5.2 (given the transistor dimensions, its parameters are determined).

Referring to these results, the validity of the introduced performance models is due. They can be readily used for the estimation of amplifier performance prior to extensive simulations.

Table 5.1: Simulated parameters of the matched ID-LNA.

$f_T[\text{GHz}]$	$V_G[\text{dB}]$	$R_{S,OPT}[\Omega]$	$NF_{MIN}[\text{dB}]$	$IIP3[\text{dBm}]$
26	16	60	1.2	1.5

Table 5.2: Calculated parameters of the matched ID-LNA.

$f_T[\text{GHz}]$	$V_G[\text{dB}]$	$R_{S,OPT}[\Omega]$	$NF_{MIN}[\text{dB}]$
29.6	15.8	59.3	1

### 5.3 ADAPTIVITY MODELS FOR LOW-NOISE AMPLIFIERS

Amplifier performance models, Eqs. (5.11), (5.12), (5.25), (5.27), (5.30) and (5.32), are used to derive the following adaptivity figures of merit (adaptivity models; tuning models): noise-factor, gain, linearity, and input-impedance tuning ranges. These figures describe the relationship between performance parameters and power consumption: by changing power consumption, the noise factor, input impedance, gain, and linearity of amplifiers can be adapted to different operating conditions (e.g., different standards).

We will first introduce the gain related tuning parameters. From Eqs. (5.7) and (5.8), the tuning ranges of the real ( $RITR$ ) and the imaginary part ( $IITR$ ) of the ID-LNA input impedance, for a  $k/k_{OPT-MIN}$  times change in a biasing condition (i.e., power consumption), are found to be:

$$RITR(k, k_{OPT-MIN}) = \left( \frac{x}{x_{OPT-MIN}} - 1 \right) R_S, \quad (5.33)$$

$$IITR(k, k_{OPT-MIN}) = \frac{x}{g_m} - \frac{x_{OPT-MIN}}{g_{m,OPT-MIN}}, \quad (5.34)$$

where index OPT-MIN refers to optimum-minimum condition (5.29).

The *voltage-gain tuning range* (*vgTR*), for the same power-consumption range ( $PCR = k/k_{OPT-MIN}$ ), can be found from Eq. (5.12) as:

$$vgTR(k, k_{OPT-MIN}) = \frac{x}{x_{OPT-MIN}}. \quad (5.35)$$

On the other hand, the noise related tuning parameters, being optimum noise-resistance tuning range (*RSTR*) and *optimum noise-factor tuning range* (*FTR*), can be found from Eqs. (5.25) and (5.30) as well as Eqs. (5.27) and (5.32), respectively.

$$RSTR(k, k_{OPT-MIN}) = \frac{k_{OPT-MIN}}{k} \sqrt{\frac{1+2k}{\beta_{F,OPT-MIN}(1+k_{OPT-MIN})(\beta_F^{-1} + x^{-2})}} \quad (5.36)$$

$$FTR(k, k_{OPT-MIN}) = \frac{1 + \sqrt{(1+2k)(\beta_F^{-1} + x^{-2})}}{1 + (1+2k_{OPT-MIN}) / \sqrt{\beta_{F,OPT-MIN}(1+k_{OPT-MIN})}} \quad (5.37)$$

From the discussion of the previous section, the linearity parameter (*IIP3*) increases roughly by 5dB [12,13] when bias current is doubled in an ID-LNA.

In order to determine the range of tuning (adaptivity), the maximum and the minimum values of the biasing parameter  $k$  must be determined.

Accordingly, the minimum biasing point  $I_{C,LOW}(k_{LOW})$  depends on both LNA and RF front-end *system specifications*: it is the power level that provides acceptable dynamic range and sensitivity of a complete system, with satisfactory noise figure, voltage gain and linearity of the amplifier. This mode of operation can be chosen when environmental (channel) conditions improve, i.e., a receive desired signal is stronger and interference signals are weaker.

On the other hand, the maximum biasing point  $I_{C,HIGH}(k_{HIGH})$  depends on RF front-end worst-case condition specifications as well as the system *power budget*: how much power can be “burned” in the amplifier and RF system. This mode of operation can be chosen when, for example, a receive signal is rather weak.

The introduced adaptivity figures of merit (tuning ranges) provide a full control over the LNA performance parameters in any mode of operation. These tuning models show how low-noise amplifiers can trade performance for power consumption in an adaptive way. Moreover, tuning models form the basis for the design of LNAs that can operate across multiple standards: multi-standard low-noise amplifiers.

### Example 5.2:

The introduced adaptivity figures of merit are determined in this example.

From the elaborated criteria for determining upper and lower bounds of the amplifier operation, the power-consumption ranges are  $PCR_{LOW}=1/2$  and  $PCR_{HIGH}=2$  (with respect to the optimum-minimum biasing point, Eq. (5.29)). Namely, for a 2.2V supply voltage, and  $50\Omega$  load impedance, cascoded transistors (see Fig. 6.2) operate in active region for bias currents lower than  $I_{C,HIGH}=14\text{mA}$  (i.e.,  $PCR_{HIGH}=2$ ). On the other hand,  $I_{C,LOW}$  is a current level between 0 and the optimum biasing condition  $I_{C,OPT-MIN}=7\text{mA}$ . For the sake of simplicity, we choose for  $I_{C,LOW}=3.5\text{mA}$  (i.e.,  $PCR_{LOW}=1/2$ ). Note that high power consumption is due to the (close to) simultaneous  $50\Omega$  noise and power match in this example. Some design trade-offs are discussed in Section 5.2.3.

Referring to the ID LNA (Fig. 5.2), an operation frequency  $f=2.4\text{GHz}$  and dimensions of transistor  $Q_1$  as  $20\times(0.4\times5)\mu\text{m}^2$ , the parameters of the optimum-minimum point are:  $f_T=29.6\text{GHz}$ ,  $C_{IT}=1.45\text{pF}$ ,  $\beta_F=105$  and  $r_{EF}=5.2\Omega$ . The ( $50\Omega$ ) power-matching parameters are  $L_B=2.8\text{nH}$  and  $L_E=0.28\text{nH}$ .

For a  $k_{OPT-MIN}/k_{LOW}=2$  times reduction and a  $k_{HIGH}/k_{OPT-MIN}=2$  times increase in power consumption, the corresponding tuning ranges of real and imaginary part of the input impedance, voltage gain, optimum noise resistance and optimum noise figure are calculated as given by Table 5.3 (for  $50\Omega$  source and load impedances). The performance of the optimum-minimum design point resembles the results shown in Tables 5.1 and 5.2, though they refer to somewhat different matching parameters.

Table 5.3: ID-LNA tuning ranges.

Range \ ( $k, k_{OPT-MIN}$ )	(0.7, 1.4)	(2.8, 1.4)
$R_{ITR} [\Omega]$	-17	25
$I_{ITR} [\Omega]$	12	-12
$V_{GTR} [\text{dB}]$	-2.2	1.3
$R_{STR} [\Omega]$	11	-15
$N_{FTR} [\text{dB}]$	0.05	0.15

Altogether, over the whole range of the operation, i.e., 6dB change in power-consumption, the change in  $Re\{Z_{IN}\}$  is around  $40\Omega$ , voltage gain around 3.5dB, noise figure around 0.15dB, and  $IIP3$  around 10dB. Tuning ranges from Table 5.3 are indicated in Fig. 5.1.

To illustrate the relationships between the amplifier performance parameters and adaptivity models, an LNA  $K$ -loop diagram is shown in Fig. 5.5 [14] (a  $K$ -rail diagram with a “loop” formed between points 0 and 6). We will map different design requirements (resulting from different operating conditions or different standards) onto the design space of this diagram, and show how adaptivity can be employed to cover (satisfy) variable amplifier specifications.

The diagram in Fig. 5.5 has two rails ( $k_1$  and  $k_2$ ) that correspond to different dimensions of amplifier input transistors and accordingly different power-matching degenerative inductances:  $L_{E,0}$  is a low-impedance (e.g.,  $50\Omega$  source) power-matching inductance with the optimum-minimum noise figure of ID-LNA (i.e., its input transistor) at point (0);  $L_{E,HIGH}$  is a large-impedance (e.g.  $100\Omega$ ) power matching inductance with the optimum of the minimum noise figure at point (1). We assume that load impedances equal source impedances in both situations.

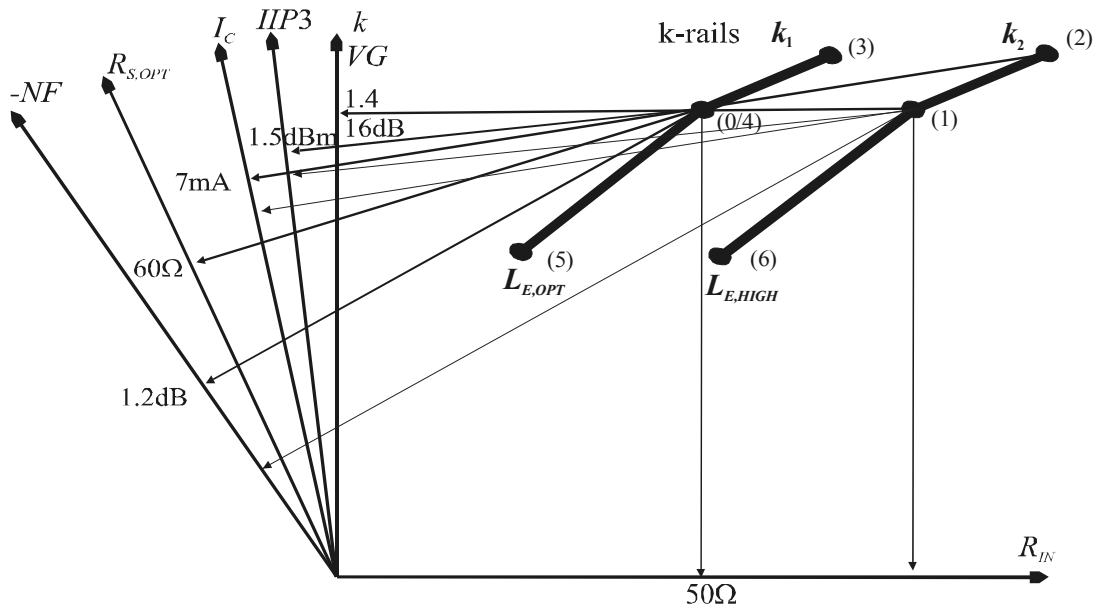


Figure 5.5: An LNA  $K$ -loop diagram.

Let us focus on three characteristic points of the diagram, points (0), (1) and (2). Compared to noise and power matched point (0) (see Example 5.1),

operating at point (1) has an advantage of lower power consumption and rather same voltage gain (Eq. (5.14)), at the cost of slightly degraded noise figure and worse linearity [9]. This low-power mode of operation can be chosen when a front-end receive signal is rather weak, necessitating a higher gain and a lower over-all noise figure.

On the other hand, operating at point (2) can be chosen when better linearity is required at the cost of increased power consumption compared to point (1). This design choice provides larger gain, and somewhat worse noise figure compared to design point (1) [9].

Operating at point (2) can be a design choice for the linearity (and power) demanding WCDMA standard, whereas point (6) can be a choice for the noise and linearity (and accordingly power consumption) relaxed DECT standard.

The K-loop diagram and Eqs. (5.33)-(5.37) provide control over amplifier performance parameters for designer. Given the tuning ranges (interpreted as tolerable performance degradations for single standard applications or as requirements for multi-standard applications), the relationships between power consumption and performance parameters can be determined.

## **5.4 CONCLUSIONS**

The varying nature of radio channels, and accordingly varying operating conditions of RF circuits promote a design concept that responds to such changes by simultaneously offering considerable power savings. The introduced amplifier adaptivity figures of merit show how low-noise amplifiers can trade performance for power consumption in an adaptive environment. It has also been shown what are the extremes of the performance tuning ranges within which an LNA is still functional.

Furthermore, the presented impedance, gain, noise, and linearity models and the K-rail diagrams provide full control for designers over the amplifier performance parameters for a number of operating conditions.

## REFERENCES

- [1] Third Generation Partnership Project (3GPP), “UE Radio Transmission and Reception (FDD)”, Technical Specification, 25.101, vol. 3.0.0, October 1999, <http://www.3gpp.org>.
- [2] A. Abidi et al., “Power-Conscious Design of Wireless Circuits and Systems”, *Proceedings IEEE*, vol. 88, no. 10, October 2000.
- [3] R. L. Lagendijk, Ubiquitous Communications – Updated Technical Annex 2000, P1.4: Low-Power Adaptive Front-End Circuits, STW, January 2000, <http://www.ubicom.tudelft.nl>.
- [4] A. Tasić, W. A. Serdijn and J. R. Long, “Concept of Noise-Figure Tuning of Low-Noise Amplifiers”, *Proceedings ECCTD*, pp. 74-77, September 2003.
- [5] M. J. O. Strutt and A. van der Ziel, “The Causes for the Increase of Admittance of Modern High-Frequency Amplifier Tubes on Short Waves”, *Proceedings IRE*, vol. 26, no. 8, pp. 1011-1032, August 1938.
- [6] S. P. Voinigescu et al. “A Scalable HF Noise Model for Bipolar Transistors with Application to Optimal Transistor Sizing for LNA Design”, *IEEE Journal Solid State Circuits*, vol. 32, no. 9, pp. 1430-1439, September 1997.
- [7] C. J. M. Verhoeven et al., *Structured Electronic Design of Negative-Feedback Amplifiers*, Kluwer, the Netherlands, 2003.
- [8] H. Fukui, “The Noise Performance of Microwave Transistors”, *IEEE Transactions on Electron Devices*, vol. ED-13, pp. 329–341, March 1966.
- [9] J. R. Long, “A Low-Voltage 5.1-5.8-GHz Image-Reject Downconverter RF IC”, *IEEE Journal of Solid-State Circuits*, vol. 35, no. 9, pp. 1320 – 1328, September 2000.
- [10] P. Wambacq and W. Sansen, *Distortion Analysis of Analog Integrated Circuits*, Norwell, MA: Kluwer 1998.
- [11] V. Volterra, *Theory of Functionals and of Integral and Integro-Differential Equations*, New York: Dover, 1959.

- [12] K. Fong, R. Meyer, and A. 1998, “High-Frequency Nonlinearity Analysis of Common-Emitter and Differential-Pair Transconductance Stages”, *IEEE Journal of Solid-State Circuits*, vol. 33, pp. 548–555, March 1998.
- [13] O. Shana et al., “Frequency-Scalable SiGe Bipolar RF Front-End Design”, *IEEE Journal of Solid-State Circuits*, vol. 36, no.6, pp.888-895, 2001.
- [14] A. Tasić, W. A. Serdijn and J. R. Long, “Adaptivity Figures of Merit and K-rail Diagrams - Comprehensive Performance Characterization of Low-Noise Amplifiers and Voltage-Controlled Oscillators”, *Proceedings ISCAS*, pp. 401-404, May 2003.



# **ADAPTIVE VOLTAGE-CONTROLLED OSCILLATORS**

The accommodation to varying radio channel conditions is usually addressed by switching between different circuits [1-3]. Indeed, this approach is simpler to implement, but is neither optimal in cost nor in power consumption.

On the other hand, adaptive RF front-end circuits offer reduced power consumption, chip area and over-all cost by sharing functional blocks ([4], Chapter 7). Concept of designing for adaptivity of oscillators is introduced in this chapter. It establishes a procedure for performance characterization of adaptive oscillators with qualitative and quantitative descriptions of the relationships and trade-offs between oscillator performance parameters.

The organization of the chapter is as follows. The adaptivity of oscillators is discussed in the following section. Section 6.2 introduces an adaptive quasi-tapped (QT) voltage-controlled oscillator (VCO). The phase-noise model of the adaptive QT-VCO is then described in Section 6.3. Section 6.4 discusses the phase-noise performance of the adaptive VCO. Adaptivity figures of merit, viz., phase-noise tuning range and frequency-transconductance sensitivity, are derived in Section 6.5. The subject of Section 6.6 is a comprehensive performance characterization of voltage-controlled oscillators by means of K-rail diagrams.

## **6.1 ADAPTIVITY PHENOMENA OF OSCILLATORS**

The importance of low-voltage and low-power design has resulted in circuits operating at the very edge of the required performance. Generally, analog RF front-end circuit designs are aimed at fulfilling a set of specifications resulting from specific, worst-case radio-channel conditions. However, radio channels are not fixed but variant. This should be taken into account in the design of RF circuits. Concept of *designing for adaptivity* [5] is suitable for mobile equipment that supports various services and operates with variable workloads in a variety of environments.

Designing for adaptivity of oscillators encompasses phase-noise tuning and frequency-transconductance tuning phenomena. These are elaborated in the remainder of this section.

### **6.1.1 PHASE-NOISE TUNING**

If the radio-channel conditions improve (or a relaxed communication standard is active), poorer phase noise of oscillators may be tolerable, leading to power savings. Responding to such a new situation, designing for adaptivity appears to be a solution as a standard, fixed design [6] is “blind” and “deaf” for volatile specifications set by communication systems.

By trading phase noise for power consumption, oscillators and oscillating systems can be adapted to varying conditions and satisfy the requirements of the complete RF front-end system as well. The concept of phase-noise tuning [7] shows explicitly how phase noise and power consumption trade between each other in an adaptive way.

The analytical description of this adaptivity phenomenon is presented later in this chapter.

### **6.1.2 FREQUENCY-TRANSCONDUCTANCE TUNING**

For low-power voltage-controlled oscillators a design is usually aimed at a loop gain slightly larger than the necessary minimum of one (e.g., two). In such cases, an increase in the capacitance of the oscillator’s LC-tank varactor in order to lower the oscillation frequency results in an increase of the effective tank conductance. If the design is “fixed” rather than adaptive, the oscillation condition deteriorates as the loop gain is lowered. Accordingly, this can bring an RF front-end to a halt, as there might be no oscillations.

In situations where power consumption is of less concern than oscillator phase noise, the repercussions are different but not less detrimental. The oscillation condition is rather relaxed, as the loop gain can be much larger than two. However, the voltage swing over the LC-tank will be reduced due to the increase in the effective tank conductance (reduced varactor capacitance), resulting in potentially poorer phase-noise performance.

In both of these examples, the oscillator could still fulfill the requirements if the bias conditions of the transconductor transistors were adapted (i.e., modified in a controlled fashion). Thus, *frequency-transconductance* ( $C$ - $g_m$ ) tuning [8] is the control mechanism compensating for the change in the VCO LC-tank characteristic (conductance is changed due to frequency tuning) by varying the oscillator's bias conditions (e.g., transconductance  $g_m$ ).

A figure of merit related to this adaptivity phenomenon is analytically described in Section 6.5.

## 6.2 AN ADAPTIVE QUASI-TAPPED VOLTAGE-CONTROLLED OSCILLATOR

The quasi-tapped bipolar VCO [9], shown in Fig. 6.1, is used to implement the adaptive oscillator. It consists of a resonant LC tank and a cross-coupled transconductance amplifier ( $Q_1$ ,  $Q_2$ ). The bias tail-current source provides current  $I_{TAIL}$  and includes degenerative impedance  $Z_D$ .

The relationships between the parameters of the oscillator are summarized in Table 6.1.  $L$  is the tank inductance,  $C_V$  the tank varactor capacitance,  $R_L$  and  $R_C$  model the inductors and varactors series losses,  $G_{TK}$  the effective tank conductance,  $n$  the quasi-tapping factor,  $-G_M$  the small-signal transconductance of the active part of the oscillator,  $-G_{M,TK}$  the small-signal conductance seen by the LC-tank,  $k$  the small signal loop gain,  $g_m$  the transconductance of bipolar transistors,  $C_{\pi}$  the base-emitter capacitance of the transistors  $Q_1$  and  $Q_2$ ,  $\omega_0$  the oscillation angular frequency and  $V_T$  the thermal voltage.

QT-VCO is the second-order, negative resistance oscillator with a feedback via capacitors  $C_A$  and  $C_B$  between the resonant LC-tank and the transconductor. The capacitive feedback has a manifold role. First, it maximizes the voltage swing across the LC tank, while active devices  $Q_1$  and  $Q_2$  remain far from heavy saturation. Moreover, freedom to set base bias  $V_B$  lower than the supply voltage  $V_{CC}$  allows for an even larger tank voltage, approaching the voltage swing of a CMOS implementation. Capacitors  $C_A$  and  $C_B$  allow direct coupling of the oscillation signal (oscillator) to the interfacing

circuitry, obviating the need for decoupling capacitors. Finally, they determine the performance (power consumption, frequency, phase noise) of the oscillator together with the other elements in the *ac* signal path.

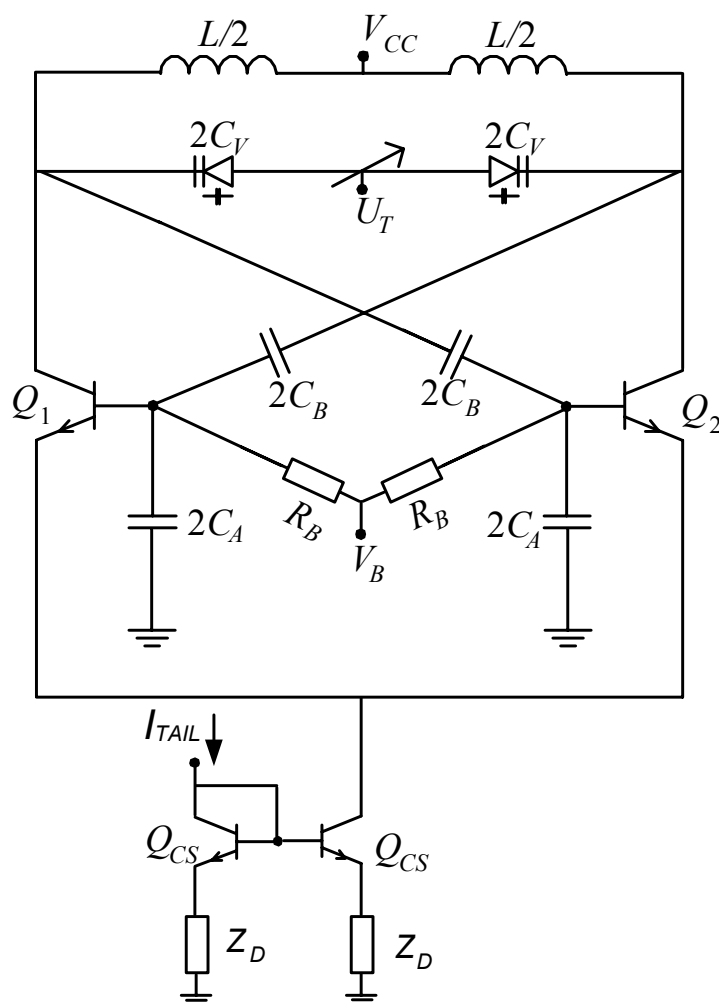


Figure 6.1: A quasi-tapped LC-oscillator.

Table 6.1: Parameters of a QT-VCO.

parameter	expression	equation
$G_{TK}$	$\frac{R_L}{(\omega_0 L)^2} + R_C(\omega_0 C_V)^2$	(6.1a)
$n$	$1 + \frac{C_A + C_{\Pi} / 2}{C_B}$	(6.1b)
$G_M$	$\frac{g_m}{2}$	(6.2a)
$G_{M,TK}$	$\frac{G_M}{n}$	(6.2b)
$k$	$\frac{G_{M,TK}}{G_{TK}}$	(6.2c)
$g_m$	$\frac{I_{TAIL}}{2V_T}$	(6.2d)
$L_{TOT}$	$L$	(6.3a)
$C_{TOT}$	$C_V + \frac{C_A C_B}{C_A + C_B}$	(6.3b)
$\omega_0$	$\frac{1}{\sqrt{L_{TOT} C_{TOT}}}$	(6.3c)

A simplified model of the quasi-tapped oscillator is shown in Fig. 6.2. The oscillation condition is satisfied when the equivalent LC-tank loss conductance  $G_{TK}$  is compensated by the equivalent negative small-signal transconductance of the active part  $-G_M$ , after being transformed to the resonating tank over the quasi-tapping capacitances, i.e.,  $G_{M,TK}=G_{TK}$ . This condition is often referred to as the start-up condition of the oscillations. The safe operation of the oscillator is guaranteed for  $G_{M,TK}/G_{TK}=k>1$  [10].

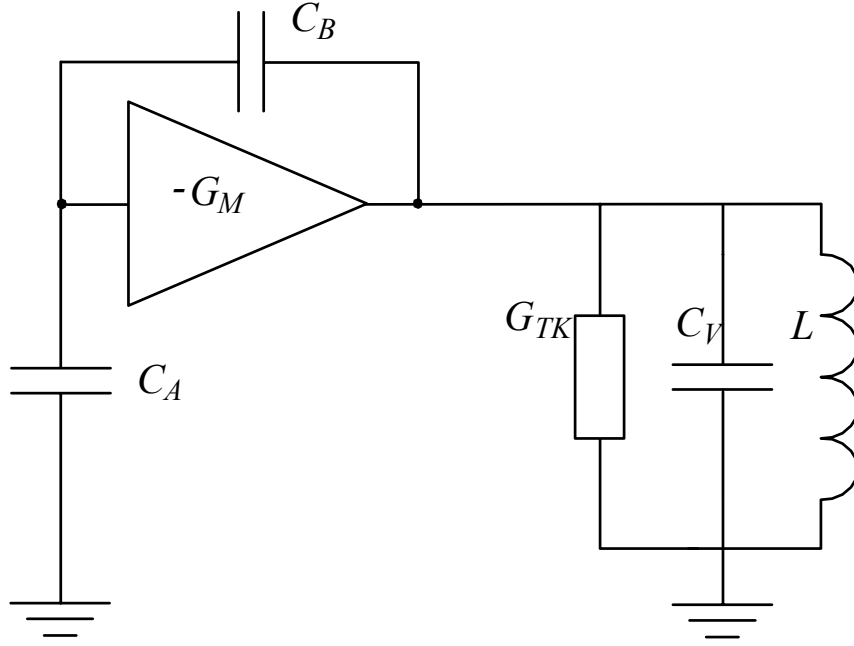


Figure 6.2: Simplified model of the quasi-tapped oscillator.

### 6.3 PHASE-NOISE MODEL OF QUASI-TAPPED VOLTAGE-CONTROLLED OSCILLATORS

Phase noise ( $\mathcal{L}$ ) of an oscillator is defined as the ratio of the noise power in a 1Hz bandwidth at an offset frequency  $f_0 + \Delta f$  to the carrier power [11]:

$$\mathcal{L} = \frac{\bar{V}_{TK,TOT}^2}{v_s^2} \quad \bar{V}_{TK,TOT}^2 = |Z(f_0 + \Delta f)|^2 \bar{I}_{TK,TOT}^2 = \frac{\bar{I}_{TK,TOT}^2}{(4\pi C_{TOT} \Delta f)^2} \quad (6.4)$$

$\bar{V}_{TK,TOT}^2$  and  $\bar{I}_{TK,TOT}^2$  stand for the total voltage and current noise spectral densities at the output of the oscillator (LC-tank),  $Z(f_0 + \Delta f)$  is the equivalent tank impedance at an offset frequency  $\Delta f$  from the resonant frequency  $f_0$ , and  $v_s$  is the amplitude of the voltage swing across the LC-tank.

The noise sources of the QT-VCO with an undegenerated tail-current source (see Fig. 6.3) are given in Table 6.2. These are the tank conductance noise  $\bar{I}_{GT}$ , the base-resistance ( $r_B$ ) thermal noise  $\bar{V}_B$ , the collector  $\bar{I}_C$ , and the base  $\bar{I}_B$  current shot noise sources, and the equivalent input voltage noise  $\bar{V}_{CS}$  of the current source transistor  $Q_{CS}$  (Eqs. (6.5-6.7)).

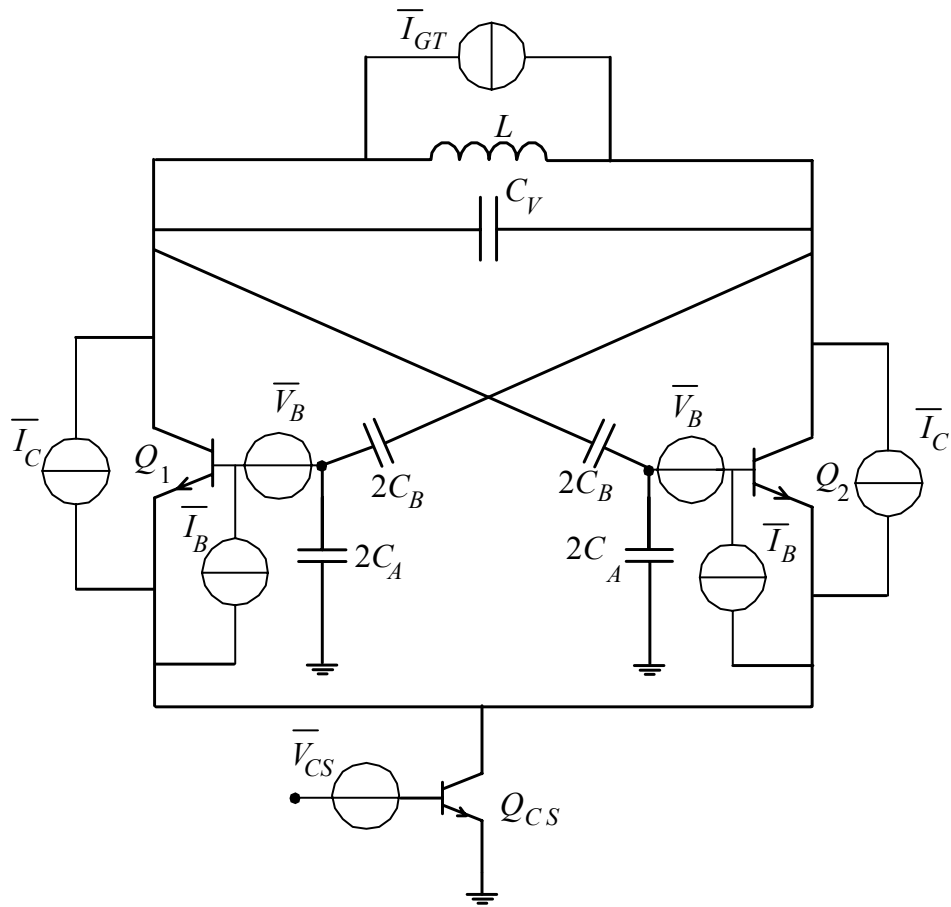


Figure 6.3 : QT-VCO noise sources.

Table 6.2: Oscillator noise parameters.

parameter	expression	equation
$\bar{I}_{GT}^2$	$4KTG_{TK}$	(6.5)
$\bar{V}_B^2$	$4KTr_B$	(6.6a)
$\bar{I}_C^2$	$2qI_C$	(6.6b)
$\bar{I}_B^2$	$2qI_B$	(6.6c)
$\bar{V}_{CS}^2$	$4KT \frac{1}{2g_{m,CS}} [1 + 2r_{B,CS}g_{m,CS}]$	(6.7)

$I_C$  and  $I_B$  stand for the collector and base currents,  $g_{m,CS}$  is the transconductance and  $r_{B,CS}$  the base resistance of transistor  $Q_{CS}$ , and  $K$  Boltzmann's constant.

The transformations of the indicated noise sources to the LC-tank ( $\bar{I}_{TK,TOT}$ ) must be known for estimation of the phase noise of the QT-VCO. Considering the transconductor as a nonlinear voltage-to-current converter (limiter) [12] allows for the inclusion of all the noise generating mechanisms in the oscillator. Namely, phenomena such as switching of the transconductor noise and the noise of the tail-current source, both resulting in the folding of noise [12,13], can be comprehended.

### 6.3.1 TIME-VARYING TRANSFER FUNCTION

The nonlinear voltage-to-current transfer function (referred to the LC-tank) of the transconductor and its equivalent time-varying transconductance in the presence of a large driving signal are shown in Fig. 6.4 [12].

As long as limiting of the oscillation signal ( $v_{IN}$ ) doesn't occur, the transfer function of an accompanying small signal has a constant value,  $g$ . When limiting occurs, the small-signal (e.g., noise) gain reduces to zero. If the large signal oscillation period is  $1/f_0$ , the period of a small signal time-varying gain ( $g_{IN}$ ) is  $1/2f_0$ . Considering the transformation from the bases to the collectors of the transconductor  $Q_1$ - $Q_2$ , the small-signal gain  $g$  is  $g_m/2$ .

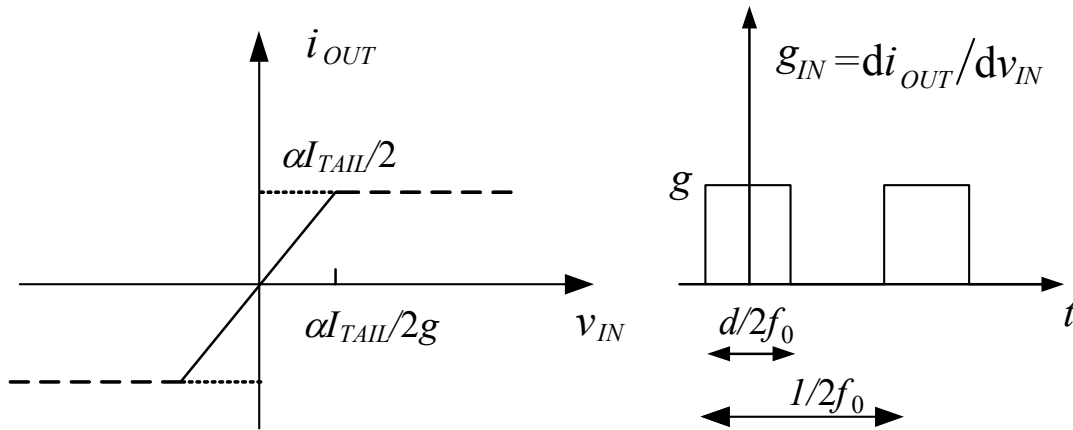


Figure 6.4:  $V$ -to- $I$  and time-varying transfer functions.



Let us first estimate the duty cycle  $d$  (Fig. 6.4) of the time-varying gain, before evaluating the contribution of the various noise sources to the phase noise of the oscillator.

If  $v_{S,B}$  is the voltage swing of the oscillation signal across the bases of the transconductor, and  $\pm 2\alpha V_T$  is the linear region of the transconductor, the duty cycle of the time-varying gain can be expressed as:

$$d = \frac{2}{\pi} \arcsin \left( \frac{2\alpha V_T}{v_{S,B}} \right). \quad (6.8)$$

With the aid of Eq. (6.2), the voltage swing across the tank (a product of the tank resistance  $1/G_{TK}$  and the first Fourier coefficient of the tail current  $I_{TAIL}$ ) equals:

$$v_S = \frac{8}{\pi} nkV_T = nv_{S,B}, \quad (6.9)$$

where  $k$  is for the small-signal loop gain of the oscillator and  $v_{S,B}$  is the voltage swing of the oscillation signal across the bases of the transconductor transistors. Assuming a 100mV ( $\pm 2V_T$ ) transconductor linear region [14] and a large loop-gain value ( $k \gg 1$ ), the duty cycle  $d$  can be approximated as:

$$d = 1/2k. \quad (6.10)$$

### 6.3.2 BASE-RESISTANCE NOISE

The noise from transistors  $Q_1$  and  $Q_2$  (both contributions) is switched on/off with the frequency of the time-varying gain  $g_{IN}$  ( $2f_0$ ). Consequently, noise folding occurs, i.e., noise from a number of frequencies is converted into the noise at one frequency. The harmonic components of the noise from the base resistance (multiples of  $f_0$ ) and the harmonic components of the time-varying gain are shown in Fig. 6.5.

As a result of the noise folding, the base noise ( $2r_B$ ) at odd multiples of the oscillation frequency is converted to the LC-tank at the resonance frequency, as given by Eqs. (6.11) and (6.12).

$$\bar{I}_{TK,VB}^2 = 2 \left( g_0^2 + 2 \sum_{m=1}^{\infty} |g_{2m}|^2 \right) \bar{V}_B^2 \quad (6.11)$$

$$\sum_{m=-\infty}^{\infty} |g_{2m}|^2 = \frac{1}{T_2} \int_{-T_2/2}^{-T_2/2} g_{IN}^2(t) dt \quad (6.12)$$

$g_{2m}$  are the (complex) Fourier coefficients and  $T_2$  is the period of the transfer function  $g_{IN}$  ( $g=g_m/2$ ).

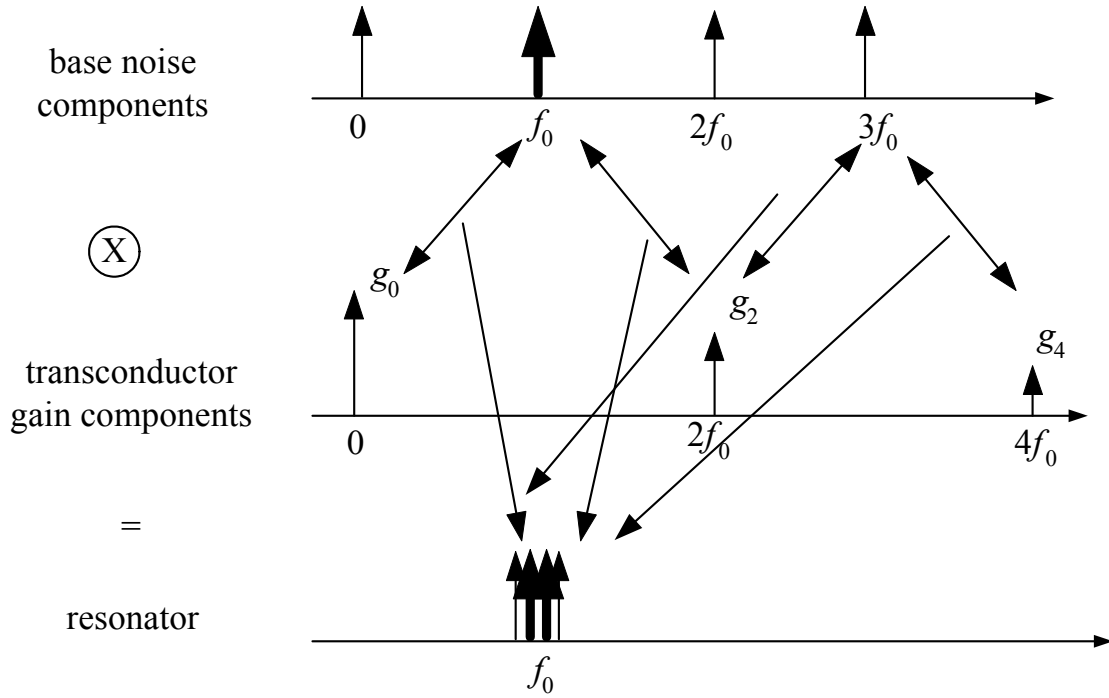


Figure 6.5: Base resistance noise folding.

With the aid of Eq. (6.2), the base resistance noise density transferred to the LC-tank equals:

$$\bar{I}_{TK,YB}^2 = 4KT \cdot kn^2 r_B G_{TK}^2. \quad (6.13)$$

Now, the contribution of the base-resistance noise at the output (LC-tank) becomes:

$$\frac{\bar{I}_{TK,YB}^2}{4KTG_{TK}} = nc \frac{k}{2}. \quad (6.14)$$

where  $c=r_B g_{ms-up}$  and  $g_{ms-up}$  is the start-up ( $k=1$ ) small-signal transconductance of the active devices  $Q_1$  and  $Q_2$ . This result is obtained from equality (6.15):

$$r_B G_{TK} = \frac{c}{2n}, \quad (6.15)$$

that is derived from Eq. (6.2).

### 6.3.3 TRANSCONDUCTOR SHOT NOISE

By splitting the current noise sources, the collector and base current shot noise transform to the resonator as given by Eq. (6.16).

$$\bar{I}_{TK,ICB}^2 = \frac{\bar{I}_C^2}{2} d + \frac{1}{n^2} \left(1 - \frac{d}{2}\right) \bar{I}_B^2 \quad (6.16)$$

The noise sources of both transistors are active for a fraction  $d$  of the period  $T_0$  ( $1/f_0$ ), whereas for the rest of the period the noise sources of only one transistor are active. With the aid of Eqs. (6.6), (6.10) and (6.16), the contribution of the transconductor's shot noise sources becomes:

$$\frac{\bar{I}_{TK,ICB}^2}{4KTG_{TK}} = \frac{n}{4}. \quad (6.17)$$

The same result would be obtained if averaging of the equivalent shot noise were considered. Namely, the transconductor shot noise when both transistors are active turns on and off with the rate of the transfer function  $g_{IN}$  (Fig. 6.4 with  $g=1$ ). Referring to Eq. (6.12), this would lead to Eq. (6.17) as well.

### 6.3.4 TAIL-CURRENT NOISE

The harmonic components of the equivalent tail-current noise (multiples of  $f_0$ ) and the harmonic components of an ideal switch (square-wave time function) are shown in Fig. 6.6.

The noise of the biasing current source is modulated by the oscillator switching action. Therefore, the tail-current noise (TCN) around even

multiples of the resonant frequency is folded back to the resonator at the oscillation frequency [15], as given by Eq. (6.18).

$$\bar{I}_{TK,CS}^2 = \frac{1}{4} 2(1-d) \sum_{m=0}^{\infty} |a_{2m+1}|^2 \bar{I}_{CS}^2 \quad \bar{I}_{CS}^2 = g_{m,CS}^2 \bar{V}_{CS}^2 \quad (6.18)$$

Here,  $\bar{I}_{CS}^2$  is the output current noise density of the tail-current source and  $a_{2m+1}$  relate to the (complex) harmonic components of the square-wave.

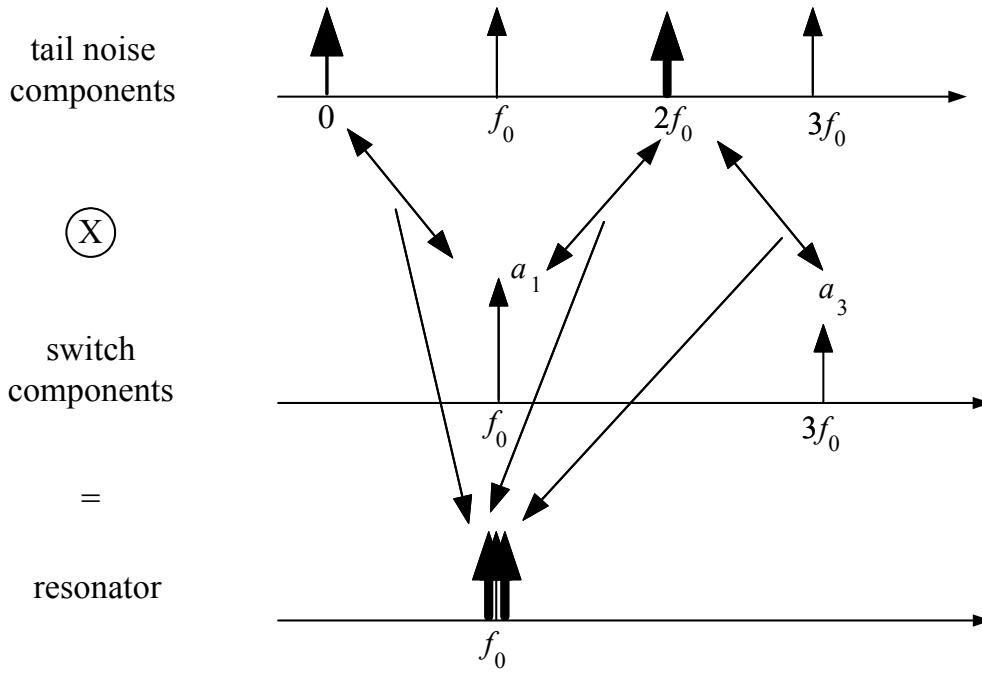


Figure 6.6: Tail-current noise folding.

To account for the finite switching time, a factor  $1-d$  is added, as the tail-current noise doesn't contribute to the phase noise when transistors  $Q_1$  and  $Q_2$  are simultaneously active. The factor  $1/4$  originates from the active part transistor's load impedance ( $1/2G_{TK}$ ).

Combining Eqs. (6.7) and (6.18), and using the well know weights of the square-wave amplitude components [16],

$$\frac{\pi^2}{8} = 1 + \frac{1}{3^2} + \frac{1}{5^2} + \frac{1}{7^2} \dots, \quad (6.19)$$

the tail-current noise converts to the resonant LC-tank as:

$$\bar{I}_{TK,CS}^2 = KTg_m [1 + 2r_B g_m]. \quad (6.20)$$

Finally, with the aid of Eqs. (6.2), (6.15) and (6.20), the contribution of the tail-current noise to the phase noise becomes:

$$\frac{\bar{I}_{TK,CS}^2}{4KTG_{TK}} \cong \frac{nk}{2}(1 + 2kc). \quad (6.21)$$

### 6.3.5 TOTAL OSCILLATOR NOISE

When assumed to be uncorrelated, all noise sources, viz., the tank conductance noise, the base resistance noise, the transconductor shot noise and the tail-current noise add to the equivalent output noise, as given by Eq. (6.22),

$$\bar{I}_{TK,TOT}^2 = \bar{I}_{TK,GT}^2 + \bar{I}_{TK,VB}^2 + \bar{I}_{TK,ICB}^2 + \bar{I}_{TK,CS}^2, \quad (6.22)$$

where  $\bar{I}_{TK,GT}^2 = 4KTG_{TK}$  is the tank conductance noise. The noise factor  $F$  of the oscillator is now calculated as:

$$F = \frac{\bar{I}_{TK,TOT}^2}{4KTG_{TK}} = 1 + \frac{n}{4} + \frac{nc}{2}k + \frac{n}{2}k(1 + 2kc). \quad (6.23)$$

We observe from Eq. (6.23) that the contribution of the tail-current source noise to the phase noise of the voltage-controlled oscillator (Fig. 6.3) is larger than all other contributions together [17,18]. Denoting the contribution of the active part noise and the LC-tank resistance noise as  $1 + A_{AP}$ , and the contribution of the tail-current noise as  $A_{CS}$ , we define the phase-noise difference ( $PND$ ) as the ratio of the corresponding noise contributions:

$$PND = 1 + \frac{A_{CS}}{1 + A_{AP}}. \quad (6.24)$$

Referring to Eqs. (6.14), (6.17) and (6.21), the  $PND$  of the QT-VCO becomes:

$$PND = 1 + \frac{1}{2} \frac{nk(1+2kc)}{1+n/4+nck/2}. \quad (6.25)$$

The  $PND$  compares the contributions of the  $TCN$  and all other noise sources. If  $n=1.4$  and  $c=0.1$  (VCO design data, [9]), then for a loop gain  $k=10$ ,  $PND=11.2$ : the tail-current source degrades the phase-noise performance of this VCO by 10.5dB.

### 6.3.6 RESONANT-INDUCTIVE DEGENERATION OF THE TAIL-CURRENT SOURCE

It is known that both the low-frequency and the high-frequency noise sources of the tail-current source have the most detrimental effect [17,18] on the phase noise of the oscillator. In particular, the tail-current noise at twice the oscillation frequency has the largest impact after being downconverted by the switching of the oscillator active part.

Therefore, the noise-optimization procedure is performed at twice the oscillation frequency. The basic idea lies in the *resonant-matching* [19] of the inductor ( $L_{RID}$ ) in the emitter of the biasing transistor  $Q_{CS}$  to its base-emitter capacitance ( $C_{\pi,CS}$ ) at twice the oscillation frequency.

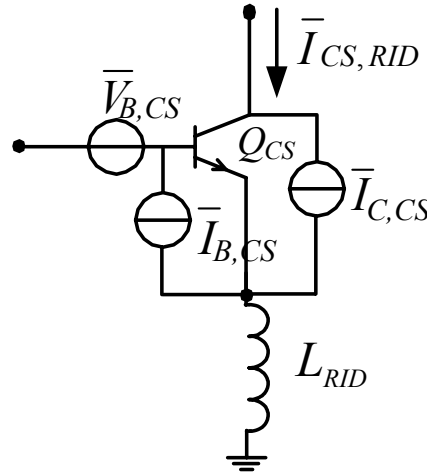


Figure 6.7: Noise sources of the tail-current source transistor.

The reduction of the equivalent output current noise density of the tail-current source results into the reduction of the “noise-portion” that is

transferred to the resonator. We will consider separately the transformation (reduction) of the base resistance noise, base-current shot noise and collector-current shot noise of the resonant-inductive degenerated tail-current transistor  $Q_{CS}$ , shown in Fig. 6.7.

### 6.3.6.1 Base Resistance Noise Transformation of the Resonant-Inductive Degenerated Tail-Current Source

As the input impedance of an inductively degenerated transistor equals [20,21]:

$$Z_{IN,CS}(f) = 2\pi f_{T,CS} L_{RID} + j \left[ 2\pi f L_{RID} - \frac{f_{T,CS}}{f} \frac{1}{g_{m,CS}} \right], \quad (6.26)$$

the matching condition at  $2f_0$ , i.e., the imaginary part is set to zero at  $2f_0$ , is determined:

$$R_{IN,CS} g_{m,CS} = \left( \frac{f_{T,CS}}{2f_0} \right)^2, \quad (6.27)$$

where  $f_{T,CS}$  is  $Q_{CS}$ 's transit frequency, and  $R_{IN,CS} = 2\pi f_{T,CS} L_{RID}$  is the real part of the impedance seen at the base of the current-source transistor.

The equivalent transconductance of the RID current-source transistor at  $2f_0$  equals [20, Chapter 5]:

$$g_{EQ,CS} \cong -\frac{1}{R_{IN,CS}} \frac{f_{T,CS}}{2f_0}, \quad (6.28)$$

whereas the part of the base resistance noise into the output current noise density of the degenerated tail-current source becomes:

$$\bar{I}_{CS,VB,RID}^2 = g_{EQ,CS}^2 \bar{V}_{B,CS}^2 = \left( \frac{2f_0}{f_{T,CS}} \right)^2 4KTr_{B,CS}. \quad (6.29)$$

### 6.3.6.2 Base- and Collector-Current Shot Noise Transformations of the Resonant-Inductive Degenerated Tail-Current Source

The RID tail-current source transistor  $Q_{CS}$  operates in a common-base-like configuration at twice the oscillation frequency. Therefore, the collector-current shot noise is suppressed while the base-current shot noise is completely transferred to the output of the current source. This intuitive observation can be analytically proved by determining the transfer functions of the corresponding noise sources. A detailed circuit model is shown in Fig. 6.8.

Let us first determine the transfer function from the position of the collector-current shot noise  $I_{C,IN}$  to the output of the current source  $I_{OUT}$  (superposition applied, i.e.,  $I_{B,IN}=0$ ). Kirchoff's current law equation applied to node  $E$  yields:

$$I_{C,IN} + g_{m,CS}V_{BE} = \frac{V_E}{sL_{RID}} - sC_{\Pi,CS}V_{BE}, \quad (6.30)$$

where  $V_{BE}=V_B-V_E$ . Analyzing  $BE$  branch, Eq. (6.31) results.

$$\frac{V_E}{r_{B,CS}} = -V_{BE} \left( \frac{1}{r_{B,CS}} + sC_{\Pi,CS} \right) \quad (6.31)$$

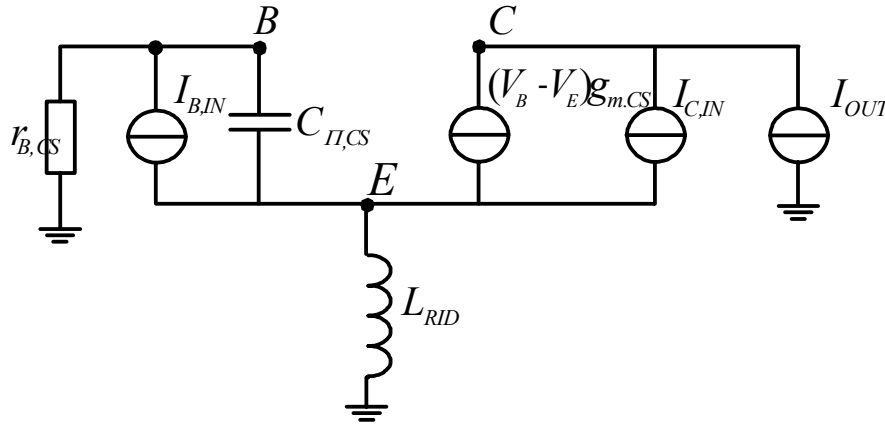


Figure 6.8: RID tail-current source; detailed circuit model.



Substituting Eq. (6.31) into Eq. (6.30), the relationship between the base-emitter voltage and the current  $I_{C,IN}$  becomes:

$$I_{C,IN} = -V_{BE} \left[ g_{m,CS} + j\omega C_{\Pi,CS} + \frac{1}{j\omega L_{RID}} + \frac{C_{\Pi,CS} r_{B,CS}}{L_{RID}} \right], \quad (6.32)$$

At the resonance ( $2f_0$ ) between  $L_{RID}$  and  $C_{\Pi,CS}$ , the expression simplifies to:

$$I_{C,IN} = -V_{BE} \left[ g_{m,CS} + \frac{C_{\Pi,CS} r_{B,CS}}{L_{RID}} \right]. \quad (6.33)$$

Finally, from the current-law equation for node C,

$$I_{OUT} = I_{C,IN} + g_{m,CS} V_{BE}, \quad (6.34)$$

and Eq. (6.33), the transfer function from the collector current noise source to the output of the TCS is calculated as given by Eq. (6.35).

$$\frac{I_{OUT}}{I_{C,IN}}(2f_0) = 1 - \frac{1}{1 + r_{B,CS} g_{m,CS} \left( \frac{2f_0}{f_{T,CS}} \right)^2} \cong 0 \quad (6.35)$$

As  $r_{B,CS} g_{m,CS}$  is a small constant, and  $2f_0/f_{T,CS} \ll 1$ , it becomes obvious that the collector-current shot noise is fully suppressed from the equivalent output current noise of the TCS.

In a similar manner, the transformation of the base-current shot noise to the output of the TCS can be calculated from Fig. 6.8 ( $I_{C,IN}=0$ ). The resulting transfer function becomes:

$$\frac{I_{OUT}}{I_{B,IN}}(2f_0) = \frac{1}{1 + r_{B,CS} g_{m,CS} \left( \frac{2f_0}{f_{T,CS}} \right)^2} \cong 1, \quad (6.36)$$

suggesting that the complete base-current shot noise is transferred to the output of the tail-current source.

### 6.3.6.3 Total Output Noise of the Resonant-Inductive Degenerated Tail-Current Source

Combining Eqs. (6.29) and (6.36), i.e., the base resistance noise and the base-current shot noise contributions, the total output current noise density of the resonant-inductive degenerated tail-current source becomes:

$$\bar{I}_{CS,RID}^2 = 4KT \frac{g_{m,cs}}{2} \left[ \frac{1}{\beta_F} + 2r_{B,CS} g_{m,cs} \left( \frac{2f_0}{f_{T,CS}} \right)^2 \right]. \quad (6.37)$$

This implies that by applying resonant-inductive degeneration, the contribution of the tail-current noise at  $2f_0$  is reduced by more than a factor  $(f_{T,CS}/2f_0)^2$ . It becomes clear after Eq. (6.37) is rewritten as:

$$\bar{I}_{CS,RID}^2 = \left( \frac{2f_0}{f_{T,CS}} \right)^2 4KT \frac{g_{m,CS}}{2} \left[ \left( \frac{f_{T,CS}}{2f_0} \right)^2 \frac{1}{\beta_F} + 2r_{B,CS} g_{m,CS} \right] < \left( \frac{2f_0}{f_{T,CS}} \right)^2 \bar{I}_{CS}^2. \quad (6.38)$$

Referring to  $n=1.4$ ,  $c=0.1$  and  $k=10$  (VCO design data, [9]), the simulations predict an improvement of 7dB for the applied *RID* and this loop-gain value.

### 6.3.7 RESISTIVE DEGENERATION OF TAIL-CURRENT SOURCE

Unlike resonant-inductive degeneration, which is effective in suppressing tail-current noise at twice the oscillation frequency, resistive degeneration [22] of a tail-current source is equally effective at all frequencies. However, as the resistor in the emitter of the TCS transistor requires some voltage headroom, this method of noise suppression has limited use (i.e., suitable for systems with large supply voltages).

The circuit diagram of the resistive degeneration (RD) TCS is shown in Fig. 6.9. Its effectiveness is discussed next.

The collector-current shot noise of the resistively-degenerated TCS is suppressed while the base-current shot noise is transferred to the output of the current source, as in the case of the RID TCS (Section 6.3.6.2). Moreover, the base-resistance noise and the degenerative-resistor ( $R_{RD}$ ) noise are transferred to the output of the current-source transistor with the equivalent transconductance  $g_{EQ,CS}=1/R_{RD}$ , assuming  $R_{RD} \gg 1$ .

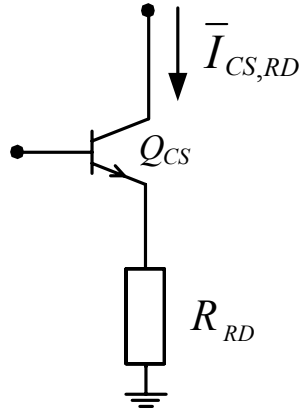


Figure 6.9: Resistive degenerated tail-current source.

Accordingly, the output current-noise density of the RD TCS becomes:

$$\bar{I}_{CS, RD}^2 = 4KT \frac{g_{m, CS}}{2} \left[ \frac{1}{\beta_F} + 2r_{B, CS} \frac{1}{g_{m, CS} R_{RD}} \left( \frac{1}{r_{B, CS}} + \frac{1}{R_{RD}} \right) \right]. \quad (6.39)$$

The effectiveness of the two noise-reduction procedures can be determined by comparing Eqs. (6.37) and (6.39). The resonant-inductive degeneration is more effective than the resistive degeneration, if condition (6.40) is satisfied.

$$\left( \frac{f_{T, CS}}{2f_0} \right)^2 \frac{1}{r_{B, CS} g_{m, CS}} > g_{m, CS} R_{RD} \quad (6.40)$$

As  $r_{B, CS} g_{m, CS}$  is a small constant, and  $2f_0/f_{T, CS} \gg 1$ , the resonant-inductive degeneration can be considered as a better solution than the resistive degeneration in a low-voltage environment (e.g.,  $V_{CC} < 3.3V$ ), as the latter requires a large resistor  $R_{RD}$  and accordingly a large supply voltage. If a high supply voltage is available (e.g.,  $V_{CC} > 5V$ ), the RD is preferable [19,22], as its implementation is rather straightforward.

### 6.3.8 ADAPTIVE PHASE-NOISE MODEL

For larger loop-gain values (in [9]  $k_{MAX}=19$ ), and accordingly larger transit frequencies ( $f_T$ ) of transistors, a factor of 100 bias-noise suppression of RID TCS is expected, making its noise contribution almost negligible. Therefore, the noise factor of the VCO with resonant-inductive degeneration of the bias tail-current source reduces to:

$$F = 1 + \frac{n}{4} + \frac{nc}{2}k. \quad (6.41)$$

When the noise contributed by the bias circuit is negligible, the oscillator phase-noise performance depends on the components in the *ac* signal path, viz., transconductance cell and resonator. With the aid of Eqs. (6.4), (6.9), (6.22) and (6.41), the adaptive phase-noise model now becomes:

$$\mathcal{L} \propto \frac{1 + n/4 + nck/2}{n^2k^2}. \quad (6.42)$$

This model is parameterized with respect to power consumption via the *small-signal loop gain*  $k$ . Unlike fixed, hardware determined design parameters, the loop gain and voltage swing can be varied by changing current  $I_{TAIL}$ , shown in Fig. 6.1. This allows adaptation of the oscillator's phase noise to different conditions. Parameter  $k=G_{M,TK}/G_{TK}$  defines how far the oscillator is from the start-up condition. As this is a key parameter used in the forthcoming analysis, let us explaining in more detail its meaning and importance.

In its simplest form  $k$  is the small-signal loop gain of the oscillator considered as a positive feedback amplifier. In addition,  $k$  relates to the excess of the negative conductance necessary for the compensation of the losses in the LC-tank. Namely, if the tank conductance is  $G_{TK}$ , then for the start-up of the oscillations, the equivalent negative conductance seen by the LC-tank must be  $G_{M,TK}=kG_{TK}$ , with  $k$  larger than one (for a guaranteed start-up usually set to a value of two).

#### 6.3.8.1 Linear Phase-Noise Model

The performance of the oscillator can be also determined if a linear analysis method is applied. Therefore, we will assume (in this sub-section) that the

oscillator operates in a near-linear fashion [11,24] such that noise close to the carrier contributes larger to the total oscillator noise, compared to other contributors such as base-band noise and the noise obtained after mixing from the other harmonics.

The oscillator phase-noise performance depends mainly on the components in the *ac* signal path, e.g., the transconductance cell and resonator, when noise contributed by the bias circuit is made negligible [19]. Moreover, linear operation regime assumes that transconductor devices  $Q_1$  and  $Q_2$  are active at all times (Fig. 6.1), and therefore there is no contribution of the tail-current noise being rejected as a common mode signal. These assumptions [24] enable easier interpretation of the rather complex noise generating mechanism in VCOs when used for qualitative inspection of the oscillators' phenomena.

We have denoted the main noise sources in the oscillator as shown in Fig. 6.9a. In order to switch to the equivalent model of Fig. 6.9b, it is necessary to transform the indicated noise sources to the corresponding LC-tank,  $Z(\Delta\omega)$ . Because of symmetry, only one-half of the oscillator circuit is depicted. However, in the following calculations, the complete oscillator is analyzed.

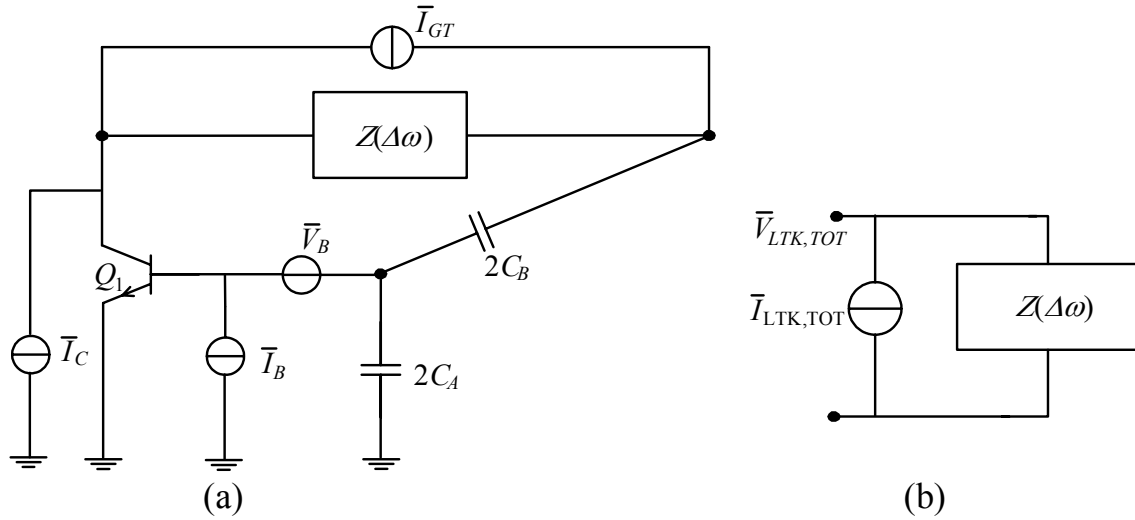


Figure 6.10: (a) Noisy oscillator model, (b) noisy LC-tank model.

Considered uncorrelated, all noise sources add to the equivalent noise source  $\bar{I}_{LTK,TOT}$ , as given by Eq. (6.43) and Fig. 10b.

$$\bar{I}_{LTK,TOT}^2 = \bar{I}_{LTK,GT}^2 + \bar{I}_{LTK,IB}^2 + \bar{I}_{LTK,IC}^2 + \bar{I}_{LTK,VB}^2 \quad (6.43)$$

The corresponding “linear” noise contributions equal:

$$\bar{I}_{LTK,YB}^2 = 2\bar{V}_B^2 n^2 G_{TK}^2, \quad (6.44)$$

$$\bar{I}_{LTK,IB}^2 = \bar{I}_B^2 / (2n^2), \quad (6.45)$$

$$\bar{I}_{LTK,IC}^2 = 1/2\bar{I}_C^2, \quad (6.46)$$

$$\bar{I}_{LTK,GT}^2 = 4KTG_{TK}. \quad (6.47)$$

With the aid of Eq. (6.4), the output voltage noise spectral density equals:

$$\bar{V}_{N,TOT}^2 = KT \frac{G_{TK}}{(\omega_0 C_{TOT})^2} \left( \frac{\omega_0}{\Delta\omega} \right)^2 \left[ 1 + \frac{qI_C}{4KTG_{TK}} + 2n^2 r_B G_{TK} + \frac{qI_B}{n^2 4KTG_{TK}} \right], \quad (6.48)$$

$$\bar{V}_{N,TOT}^2 = KT \frac{G_{TK}}{(\omega_0 C_{TOT})^2} (1 + A_T) \left( \frac{\omega_0}{\Delta\omega} \right)^2, \quad (6.49)$$

$$A_T = 2n^2 r_B G_{TK} + g_m (1 + 1/\beta_F) / 4G_{TK}. \quad (6.50)$$

From Eq. (6.2) and assuming  $\beta_F \gg 1$ , the noise factor  $A_T$  of the active part can be re-written for the start-up condition ( $k=1$ ) as:

$$A_{T,S-UP} = n(1/2 + r_B g_{ms-up}), \quad (6.51)$$

or for reliable (safety) start-up, corresponding to the case with an excess loop gain larger than one ( $k>1$ ), in this case  $k$ , it is given as:

$$A_{T,S\_S-UP} = n(k/2 + r_B g_{ms\_s-up} / k) = n(k/2 + r_B g_{ms-up}). \quad (6.52)$$

Note that indexes  $S-UP$  and  $S\_S-UP$  correspond to the start-up and the safety (guaranteed) start-up conditions of the oscillations.

Combining Eqs. (6.4) and (6.50), the “linear”-analysis phase noise of the quasi-tapped oscillator becomes:

$$\mathcal{L} \propto \frac{1 + 2n^2 r_B G_{TK} + g_m / 4 G_{TK}}{v_S^2}. \quad (6.53)$$

With the aid of Eqs. (6.2) and (6.9), and for an arbitrary distance from the start-up condition, the “linear” phase-noise model reads:

$$\mathcal{L} \propto \frac{1 + n \cdot (k/2 + r_B g_{ms-up})}{k^2 n^2}. \quad (6.54)$$

This phase-noise model can be used for the analysis of VCOs with lower loop-gain values [24], as their operation can be fairly approximated with the linear model. On the other hand, if the oscillator is designed for the large loop gain [9], the linear model is not suitable, as the oscillator operates deeply in the non-linear region. In that situation, the adaptive phase-noise model is applied (Eq. (6.42)).

## 6.4 PHASE-NOISE PERFORMANCE OF QUASI-TAPPED VOLTAGE-CONTROLLED OSCILLATORS

The performance of the quasi-tapped VCO will be characterized by comparing a quasi-tapped VCO and a non-tapped VCO. A non-tapped (NT) VCO is an oscillator with a directly coupled LC-tank and active part ( $n=1$ ), i.e., the oscillator shown in Fig. 6.1 with  $C_A=\infty$  and  $C_B=0$ . The LC-tanks of both oscillator types are assumed identical.

Referring to Eq. (6.42), the phase noise of a QT-VCO ( $n>1$ ) and an NT-VCO ( $n=1$ ) can be written as:

$$\mathcal{L}_{QT} \propto \frac{1 + n/4 + n c_{QT} k/2}{n^2 k^2}, \quad (6.55)$$

$$\mathcal{L}_{NT} \propto \frac{1 + 1/4 + c_{NT} k/2}{k^2}, \quad (6.56)$$

where  $c_{QT}=n c_{NT}=n r_B g_{ms-up,NT}$ , with  $g_{ms-up,NT}$  being the start-up ( $k_{NT}=1$ ) small-signal transconductance of an NT-VCO.

Now, the *ratio* between the *phase noise* of a non-tapped and a quasi-tapped oscillator,  $PNR(k_{QT}, k_{NT})$ , can be defined as:

$$PNR(k_{QT}, k_{NT}) = \frac{\mathcal{L}_{QT}(k_{QT})}{\mathcal{L}_{NT}(k_{NT})}, \quad (6.57)$$

$$PNR(k_{QT}, k_{NT}) = \frac{1 + n/4 + nc_{QT}k_{QT}/2}{n^2k_{QT}^2} \frac{k_{NT}^2}{1 + 1/4 + c_{NT}k_{NT}/2}. \quad (6.58)$$

For  $n=1$  and  $k_{QT}=k_{NT}$ , the QT-VCO reduces to the NT-VCO, and obviously, the ratio  $PNR$  becomes equal to one.

The operating conditions used for the comparison of oscillators are:  $k_{NT}=nk_{QT}$  (the same power consumption), and  $k_{NT}=k_{QT}$  (the same distance from the start-up condition). The latter because loop gain is an important oscillator parameter.

From Eq. (6.58), the phase-noise ratio for the same power consumption,  $k_{NT}=nk_{QT}=nk$ , equals:

$$PNR(k, nk) = \frac{1 + n/4 + n^2c_{NT}k/2}{1 + 1/4 + nc_{NT}k/2}. \quad (6.59)$$

Ratio (6.59) implies that a non-tapped oscillator has better performance than a quasi-tapped oscillator, with respect to the phase noise for the same power consumption. For example, if  $n=2$ ,  $k=2$  (the safety start-up condition),  $r_B=40\Omega$  and  $g_{ms-up,NT}=4.1mS$ , there is a  $PNR=1.3dB$  difference in phase noise in favor of the non-tapped oscillator. This result can be considered as a design tip. Namely, as quasi-capacitive tapping already allows for an increased voltage swing across the LC-tank by an independent base biasing of transistor transistors, the reduced power consumption and better phase noise can be achieved by setting  $n$  close to one.

In a similar manner, the phase-noise ratio for the same excess negative conductance ( $k_{NT}=k_{QT}=k$ ) is given as:

$$PNR(k, k) = \frac{1 + n/4 + n^2c_{NT}k/2}{n^2(1 + 1/4 + c_{NT}k/2)}. \quad (6.60)$$

This result shows that a quasi-tapped oscillator has better performance than a non-tapped oscillator, with respect to the phase noise for the same loop gain. Referring to  $r_B=40\Omega$ ,  $g_{ms-up,NT}=4.1mS$ ,  $n=2$  and  $k=6$ , the QT-VCO has  $PNR=3dB$  better phase noise than the NT-VCO.



## 6.5 ADAPTIVITY FIGURES OF MERIT OF VOLTAGE-CONTROLLED OSCILLATORS

Adaptivity phenomena can be qualitatively and quantitatively described by means of their figures of merit. Phase-noise tuning range describes phase-noise adaptivity of an oscillator with respect to power consumption. Frequency-transconductance sensitivity describes the effect of compensating for the change in the LC-tank characteristic due to frequency tuning. Both metrics are analytically derived in the remainder of this section.

### 6.5.1 PHASE-NOISE TUNING RANGE

Before detailing on the phase-noise tuning, let us broaden the meaning of the corner-stone parameter  $k$ . As in the oscillator under consideration, the start-up condition is also referred to the minimum power condition, apart from defining how far an oscillator is from this state, the parameter  $k$  also characterizes the increase in power consumption. Namely,  $k$ -times larger negative conductance of the active part of the oscillator requires a  $k$ -times increase in power consumption, with respect to the start-up condition. Power consumption is controlled by the tail current  $I_{TAIL}$ , shown in Fig. 6.1.

The figure of merit describing the oscillator's adaptivity to phase noise is the *phase-noise tuning range (PNTR)*. For a  $k_2/k_1$ -times change in power consumption, and with the aid of Eq. (6.42), the phase-noise tuning range for the QT-VCO is defined as:

$$PNTR(k_1, k_2) \propto \frac{k_1^2}{k_2^2} \frac{1 + n/4 + nck_2/2}{1 + n/4 + nck_1/2}. \quad (6.61)$$

We will first determine the loop gain  $k_{MAX}$  (related to the best phase noise) in order to estimate the achievable phase-noise tuning range. The start-up condition corresponds to  $k_{MIN}=1$ , whereas the guaranteed start-up to  $k_{MIN}=2$ .

For the maximum voltage swing across the LC tank that satisfies:

$$v_{S,QT,MAX} \leq \frac{2n}{n+1} (V_{CC} - V_B + V_{BE} - V_{CE,SAT}), \quad (6.62)$$

the detrimental effects of both hard saturation of the transistors in the active part of the oscillator and the additional current noise of their forward biased base-collector junctions are circumvented [25,26]. Here,  $V_{CC}$  is the supply

voltage,  $V_B$  the base potential of the core transistors,  $V_{BE}$  their base-emitter voltage and  $V_{CE,SAT}$  their collector-emitter saturation voltage. Assuming that the bases of the transistors are, for the sake of the simplicity, at the maximum supply voltage, i.e.,  $V_{CC}=V_B$ , the maximum voltage swing across the LC-tank ( $V_{CE,SAT}=0V$ ) equals  $v_{S,MAX1}=1.5n/(n+1)$  (it is assumed that  $V_{BE}=0.75V$ ). On the other hand, the maximum voltage swing corresponding to the non-saturation condition ( $V_{CE,SAT}=0.3V$ ) is  $v_{S,MAX2}=0.9n/(n+1)$ . Compromising between larger voltage swing on the one hand and weaker saturation on the other we opt for a maximum voltage swing across the tank  $v_{S,MAX}=(v_{S,MAX1}+v_{S,MAX2})/2$ .

Now, with the aid of Eq. (6.9), and for  $n=2$ , the maximal loop-gain value is found to be  $k_{MAX}=6$ .

For example, if  $k_{MIN}=2$  (the safety start-up condition) and  $k_{MAX}=6$  (expected best phase noise),  $c=0.65$  (design data, Section 7.1.1), and  $n=2$ , the control ranges of power consumption and phase noise are:

$$P_{MAX} / P_{MIN} = k_{MAX} / k_{MIN} = 3, \quad (6.63)$$

$$PNTR(2,6)[dB] = \mathcal{L}_{MIN} / \mathcal{L}_{MAX} = 6.7, \quad (6.64)$$

$P_{MAX}$  and  $P_{MIN}$  stand for maximum and minimum power consumption, and  $\mathcal{L}_{MAX}$  and  $\mathcal{L}_{MIN}$  represent the maximum and the minimum phase noise corresponding to the values of  $k_{MAX}$  and  $k_{MIN}$ , respectively.

This result shows that for the oscillator under consideration and with equal supply and transconductor base voltages, a phase-noise tuning range in excess of 6dB can be expected with a factor of 3 reduction (change) in power consumption.

### 6.5.2 FREQUENCY-TRANSCONDUCTANCE SENSITIVITY

Because of a change in frequency due to tuning of the LC-tank varactor capacitance ( $C_V$ ), the loop gain, the voltage swing and the phase noise of the oscillator change as well [27]. If the oscillator is designed at the very edge of the required specifications, the change of the oscillation condition (i.e., reduced loop gain), or the change of the noise produced (i.e., degraded phase noise), puts the oscillator out of correct operation. In order to preserve desired operation of oscillators, it is necessary to apply a control mechanism to the bias current  $I_{TAIL}$  (i.e.,  $g_m$ ).

The concept of  $C$ - $g_m$  tuning illustrates the relationship between the varactor diode tuning voltage  $U_T$  and the biasing tail current  $I_{TAIL}$ , both indicated in Fig. 6.1. The objective is to find the relationship between the tuning voltage  $U_T$  and the effective tank conductance  $G_{TK}$  on the one hand and the relationship between the tank conductance and the biasing tail current  $I_{TAIL}$  on the other. The resulting sensitivity of the tail current to the tuning voltage will show to what extent the biasing condition should be changed in response to a change in the frequency, in order to keep the oscillator operating under the specified conditions.

The sensitivity of the LC-tank conductance to a change in a tuning voltage is defined as:

$$S_{U_T}^{G_{TK}} \Big|_{U_T=U_{T0}} = \frac{\partial G_{TK}}{\partial C_V} \frac{\partial C_V}{\partial U_T}, \quad (6.65)$$

where tuning voltage  $U_{T0}$  corresponds to the resonant frequency  $f_0$ .

With the aid of Eqs. (6.1) and (6.3), the sensitivity of the LC-tank conductance to a change in varactor capacitance  $C_V$  can be expressed in terms of LC-tank parameters:

$$S_{C_V}^{G_{TK}} = \omega_0^2 \left[ 2C_V R_C \left( 1 - \frac{C_V}{2C_{TOT}} \right) + C_{TOT} R_L \right]. \quad (6.66)$$

If the varactor capacitance is related to a tuning voltage  $U_T$  as:

$$C_V(U_T) = \frac{C_{V0}}{\left( 1 + \frac{V_{CC} - U_T}{\varphi} \right)^{1/a}}, \quad (6.67)$$

where  $C_{V0}$ ,  $\varphi$  and  $a$  are the parameters of the varactor shown in Fig. 6.1, the sensitivity of the varactor capacitance to a tuning voltage equals:

$$S_{U_T}^{C_V} = \frac{C_V}{a(V_{CC} - U_{T0} + \varphi)}. \quad (6.68)$$

Note that the capacitance  $C_V$  is related to the tuning voltage  $U_{T0}$  and the frequency  $f_0$ .

Linearizing the sensitivity characteristics calculated around resonance, the change in the effective tank conductance can be related to the change in the tuning voltage as:

$$\Delta G_{TK} = S_{U_T}^{G_{TK}} \Delta U_T, \quad (6.69)$$

where the relating sensitivity has a form:

$$S_{U_T}^{G_{TK}} = \frac{2}{a(V_{CC} - U_{TO} + \varphi)} \left[ R_C \left( 1 - \frac{C_V}{2C_{TOT}} \right) + \frac{C_{TOT} R_L}{2C_V} \right] (\omega_0 C_V)^2. \quad (6.70)$$

To compensate for such a change in the tank characteristic, the conductance seen by the tank ( $-G_{M,TK}$ ) should be changed by the same amount. From Eq. (6.2), the relationships between the tail current, the transistors' transconductance and the conductance seen by the LC-tank are determined:

$$\Delta I_{TAIL} = 2V_T \Delta g_m, \quad (6.71)$$

$$\Delta g_m = 2k \cdot \Delta G_{M,TK}. \quad (6.72)$$

Combining these results, the change in the tail current relates to the change in the absolute value of the conductance seen by the LC-tank as:

$$S_{G_{M,TK}}^{I_{TAIL}} = 4n \cdot V_T. \quad (6.73)$$

Satisfying the condition (see Eq. (2)),

$$\Delta G_{M,TK} = k \Delta G_{TK}, \quad (6.74)$$

the sensitivity of the tail current to the tuning voltage, referred to the increase or the reduction in the tail current (power consumption) in order to sustain the desired loop-gain value (oscillation condition) is calculated as:

$$S_{U_T}^{I_{TAIL}} = S_{G_{M,TK}}^{I_{TAIL}} S_{G_{TK}}^{G_{M,TK}} S_{U_T}^{G_{TK}}. \quad (6.75)$$

With the aid of Eqs. (6.70), (6.73), (6.74) and (6.75), we finally obtain:

$$S_{U_T}^{I_{TAIL}} = \frac{8k \cdot n \cdot V_T}{a(V_{CC} - U_{TO} + \varphi)} \left[ R_C \left( 1 - \frac{C_V}{2C_{TOT}} \right) + \frac{C_{TOT} R_L}{2C_V} \right] (\omega_0 C_V)^2. \quad (6.76)$$

For the oscillator under consideration, we can now estimate to what extent the tail current should be changed, as a result of a change in the tuning voltage, i.e., frequency, so as to keep the oscillator operating under the required conditions.

For example, a sensitivity  $S_{U_T}^{I_{TAIL}} = 0.25 \text{ mA/V}$  infers that in order to sustain the oscillations under the same condition (i.e., the same loop gain) the tail current should be either increased or reduced (depending on the direction of the frequency tuning) by 0.25mA for a 1V change in a varactor voltage. The counterpart of the C-gm tuning in the circuitry is a simple amplitude control mechanism, as constant loop gain means constant amplitude of the signal across the LC-tank of the oscillator.

## 6.6 K-RAIL DIAGRAMS – COMPREHENSIVE PERFORMANCE CHARACTERIZATION OF VOLTAGE-CONTROLLED OSCILLATORS

The existing figures of merit [28,29], giving insight into the performance of oscillators operating under fixed conditions, have been reformulated in order to be useful for the performance characterization of adaptive circuits: phase-noise tuning range [7] and frequency-transconductance sensitivity [8]. These adaptivity figures of merit as well as other phenomena related to voltage-controlled oscillators can be both qualitatively and quantitatively interpreted by means of the K-rail diagrams. There are two types of oscillator K-rail diagrams: *K-rails* and *K-loop* diagrams, both using the construction rules outlined in Chapter 4.

The K-rails diagram is used as a tool for the comprehensive performance *comparison* of different voltage-controlled oscillators. In this section, a non-tapped VCO and a quasi-tapped VCO are used as an example.

The K-loop diagram is used for the performance *characterization* of adaptive voltage-controlled oscillators. Namely, K-loop diagrams show how the oscillator performance parameters (e.g., phase noise, loop gain, power consumption, voltage swing and tank conductance) relate to each other at any point of the design space. Moreover, these diagrams describe the effects of the particular design choice on the performance of oscillators.

In the following section, the concept of phase-noise tuning is described with a K-rail diagram. Then, a qualitative comparison of different VCOs is made using the K-rails (multiple K-rail) diagram. The concept of frequency-transconductance tuning and the accompanying K-loop diagram close the discussion on oscillators' K-rail diagrams. Finally, an example is presented that shows how performance parameters of an oscillator can be mapped onto these diagrams.

### 6.6.1 K-RAIL DIAGRAM

In the following analysis, we will refer to the adaptive quasi-tapped oscillator shown in Fig. 6.1. Parameters of the oscillator have already been defined in Section 6.2, and Eqs. (6.1)-(6.3).

Generally, K-rail diagrams reveal trade-offs between performance parameters of an oscillator. As suggested by the name K-rail, the parameter  $k$  is given the role of the cornerstone parameter in the analysis. Defined as  $k = G_{M,TK}/G_{TK}$ , it equally represents the small-signal loop gain, the excess conductance seen by the LC-tank as well as the excess power consumption. For the start-up condition it has a value of  $k=1$ , while for guaranteed (safe) oscillation a value  $k>1$ .

Let us consider phase-noise tuning range ( $PNTR$ ), an adaptivity performance parameter aimed not at a particular, but rather a set of operating conditions. Given by Eq. (6.61), this adaptivity figure of merit (AFOM) stands for a change in the oscillator's phase noise between two different biasing (design) points.

This phenomenon can be qualitatively described by means of the K-rail diagram [30] shown in Fig. 6.11. It is illustrated how the oscillator performance parameters, being loop gain, power consumption, phase noise and signal amplitude, relate to each other in an adaptive manner.

The arrows perpendicular to the corresponding axes represent lines of constant loop gain, phase noise and power consumption. Namely, each point in the design space (in this case a line; the k-rail) corresponds to a set of design parameters that are obtained as a normal projection of the design point on the rail to the indicated axes. Take, for example, point MAX on the k-rail. Its corresponding parameters are phase noise  $PN_{MAX}$ , loop gain  $k_{MAX}$ , and voltage swing  $v_{MAX}$ , respectively.

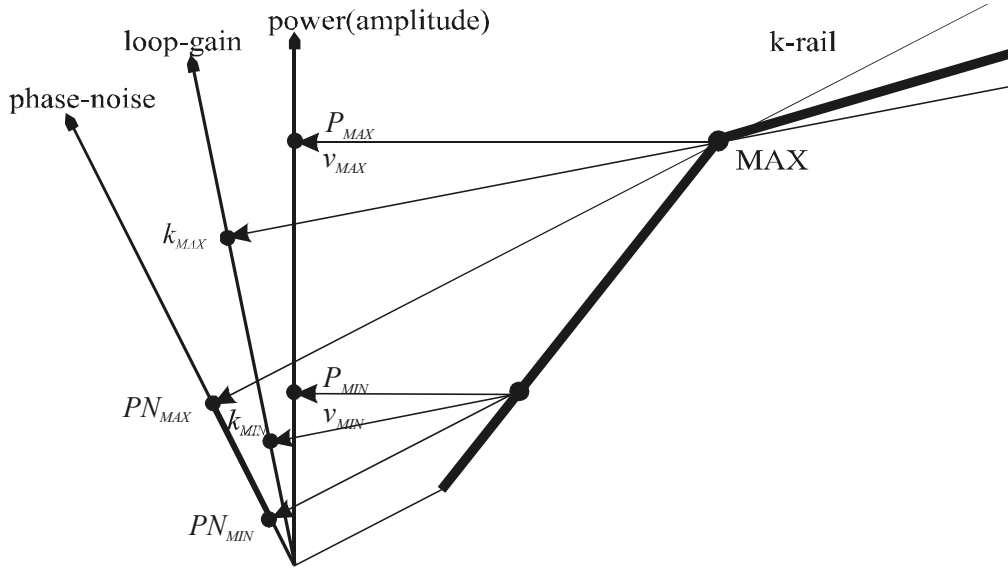


Figure 6.11: K-rail diagram for QT-VCOs.

The phase-noise tuning range shown in Fig. 6.11 between the points  $PN_{MIN}$  and  $PN_{MAX}$ , where  $PN_{MIN}$  ( $\mathcal{L}_{MAX}$ ) and  $PN_{MAX}$  ( $\mathcal{L}_{MIN}$ ) represent the maximum and minimum phase noise, corresponds to the values  $k_{MAX}$  and  $k_{MIN}$ . In addition, some well known phenomena can also be recognized. For example, it is seen that an increase in power results in an improvement in the phase noise, but only up to a level determined by  $k_{MAX}$ . Increasing the loop gain beyond this value only wastes power, as the phase noise no longer improves.

Finally, the diagram helps one to grasp the basic concepts regarding behavior and functionality of VCOs without plunging into the “sea” of figures of merit, theories and expressions.

### 6.6.2 K-RAILS DIAGRAM

The K-rails diagram [30] is used for the performance comparison of different voltage-controlled oscillators. In this section, we will construct a K-rail diagram by comparing non-tapped and quasi-tapped VCOs.

The operating conditions that are used for the construction of the K-rails diagrams are the same power consumption condition ( $k_{NT}=nk_{QT}$ ) and the same distance from the start-up condition, i.e., the same loop gain condition ( $k_{NT}=k_{QT}$ ).

The phase-noise ratio for the same power consumption (Eq. (6.59)) shows that a non-tapped oscillator has better performance than a quasi-tapped oscillator.

This expression can be qualitatively mapped onto the K-rails diagram shown in Fig. 6.12. The arrows  $L_1$ ,  $L_2$  and  $L_3$ , perpendicular to the corresponding axes, represent lines of constant loop gain, phase noise and power consumption, respectively. Apart from the indicated loop gain, phase noise and power (amplitude) axes, this diagram has two k-rails, each referring to the oscillators' design space (i.e., "design lines"). Here, the left rail corresponds to the non-tapped and the right rail to the quasi-tapped oscillator. For example, the design parameters of point A on the left-most rail (NT-VCO) are the phase noise  $PN_{NT}$ , loop gain  $k_{NT}$  and voltage swing  $v_{NT}$ .

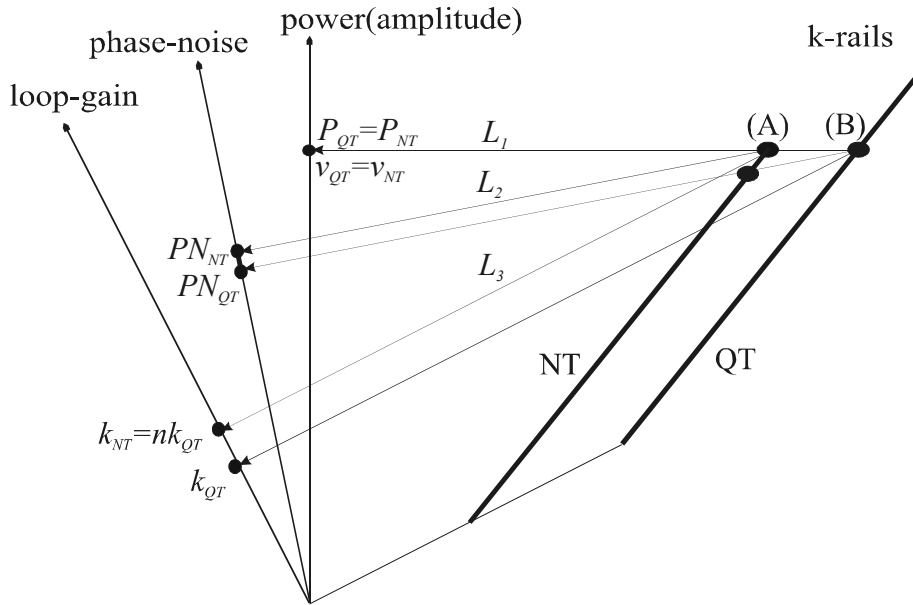


Figure 6.12: K-rails diagram for the same power consumption of NT- and QT-VCOs.

Following the diagram construction rules, it can be seen that for the same power consumption  $P_{NT}=P_{QT}$ , and accordingly  $k_{NT}=nk_{QT}$  (points A and B), it holds  $PN_{NT}>PN_{QT}$ . That is to say, the phase noise ( $\mathcal{L}=1/PN$ ) of a non-tapped oscillator is better than the phase noise of a quasi-tapped VCO (as already indicated by Eq. (6.57)).

In a similar manner, the phase-noise ratio for the same excess negative conductance ( $k_{NT}=k_{QT}$ ) that is given by Eq. (6.60) shows that a quasi-tapped



VCO has better performance than a non-tapped VCO in this case. This operating condition is depicted in Fig. 6.13, where for the phase noise corresponding to the points A and B ( $k_{NT}=k_{QT}=k$ ) holds  $PN_{NT}<PN_{QT}$ .

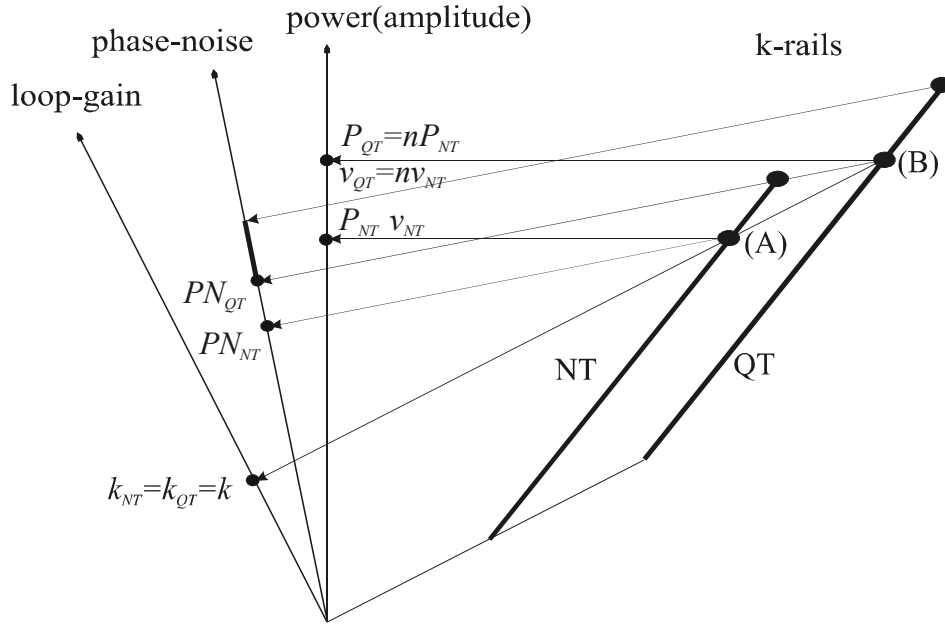


Figure 6.13: K-rails diagram for the same loop gain of NT- and QT-VCOs.

Finally, we can stress that the presented diagrams give a qualitative comparison between differently tapped VCOs. A number of parameters can simultaneously be compared, as it can also be seen to what extent the change in one parameter is reflected in other parameters.

### 6.6.3 K-LOOP DIAGRAM

The K-loop diagram [30] is used for a full performance characterization of adaptive oscillators. While in the case of the K-rails diagram it is assumed that the LC-tanks of the oscillators are fixed, phenomena related to the change in the resonating tank are described by K-loop diagrams.

The phenomenon of C- $g_m$  tuning (Section 6.4) and the resulting sensitivity of the tail current  $I_{TAIL}$  to the tuning voltage  $U_T$  (see Eq. (6.76) and Fig. 6.1) are qualitatively described by means of the diagram that is shown in Fig. 6.14.

Compared to K-rail diagrams, one more axis is added. It refers to the LC-tank conductance and the oscillation frequency. In addition, two more rails are

added ( $k_2$  and  $k_3$ ), each corresponding to a different LC-tank, viz., a tank at a lower ( $f_L$ ) and a tank at an upper oscillation frequency ( $f_U$ ).

To explain the use of K-loop diagrams we will make one loop, for example, from point (0) to point (4) in the diagram, shown in Fig. 6.14.

Increasing the varactor capacitance results in a lower oscillation frequency  $f_L$  as well as a larger effective tank conductance  $G_{TK,L}$ , both related to the right-most rail  $k_2$  in the diagram. The new operating point of the oscillator is found at the intersection of the new k-rail ( $k_2$ ) and the power consumption level ( $P_0$ ). As the tail current inserted is at the same level, i.e.,  $I_{TAIL0}$ , the oscillator state is therefore changed from point (0) to point (1). It can be noticed that at point (1), the voltage swing across the resonator, the loop gain and the phase noise are all decreased.

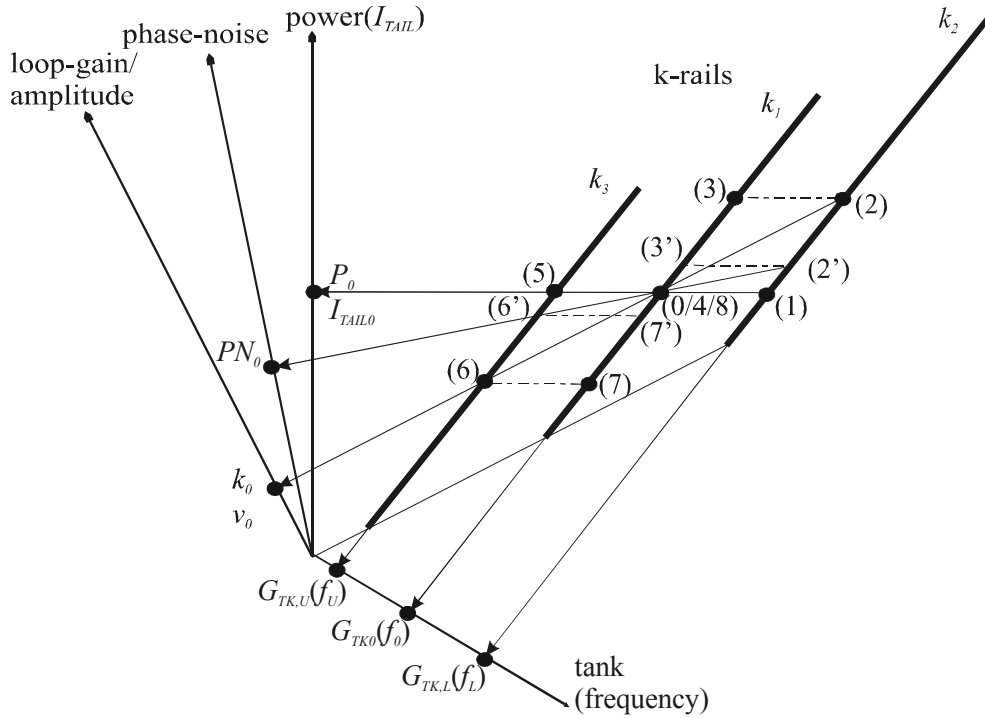


Figure 6.14: K-loop diagram for QT-VCOs.

To compensate for such deterioration in performance, the power level (tail current) must be increased for the amount indicated by Eq. (6.76). This corresponds to the next position in the diagram, point (2). At this operating point, the loop gain and the amplitude of the oscillation signal are restored to their previous levels (i.e., before the tuning action;  $v_0$  and  $k_0$ ). Moreover, the phase noise can even improve compared to the starting operating point  $PN_0$ .

On the other hand, the reduction of the varactor capacitance, and according increase of the oscillation frequency and reduction of the tank conductance, corresponds to point (3) on the middle k-rail,  $k_1$ . As the phase noise, the loop gain, the amplitude of the voltage swing, and the power consumption are at unnecessarily higher levels, the tail current can be reduced for an amount given by Eq. (6.76) so that all specifications are satisfied again. This brings us to point (4). As shown in the diagram, point (4) corresponds to starting point (0). In a similar manner, the left loop is constructed, consisting of points (4) to (8).

On a journey throughout the K-loop diagram, not only can all the previously addressed phenomena be recognized, but also all the trade-offs between power consumption, phase noise and loop gain can be qualitatively interpreted. Ending this journey, let us just name this particular phenomenon “frequency-transconductance tuning for a *constant loop gain*”. Note that the counterpart of the preceding concept in the circuitry is a simple amplitude control mechanism, as constant loop gain means constant amplitude of the signal across the LC-tank of the oscillator.

#### 6.6.4 AN ALL-ROUND EXAMPLE

An example is now presented addressing the concepts introduced in this chapter and showing usefulness of the K-loop diagram for both qualitative and quantitative representation of the adaptivity phenomena. As in the previous sections, we will refer to the quasi-tapped bipolar VCO (shown in Fig. 6.1) in the forthcoming analysis.

The values of the oscillator parameters are:  $f_0=900\text{MHz}$ ,  $2C_V=2\text{pF}$ ,  $Q_C=15$ ,  $L/2=12.5\text{nH}$ ,  $Q_L=4$ ,  $2C_A=1\text{pF}$ ,  $2C_B=1\text{pF}$ ,  $V_{CC}=2\text{V}$ ,  $U_{T0}=1\text{V}$ ,  $\varphi=0.5\text{V}$ ,  $a=2$ , and  $k=2$ , where  $Q_C$  and  $Q_L$  are the quality factors of the corresponding varactors and inductors.

To see what are the effects of both the voltage tuning and the corresponding C- $g_m$  tuning, we will use the diagram shown in Fig. 6.15 for the analysis. In addition, it will be shown how the loop gain, the tail current, the effective tank conductance and the phase noise values can be found at any point of the diagram.

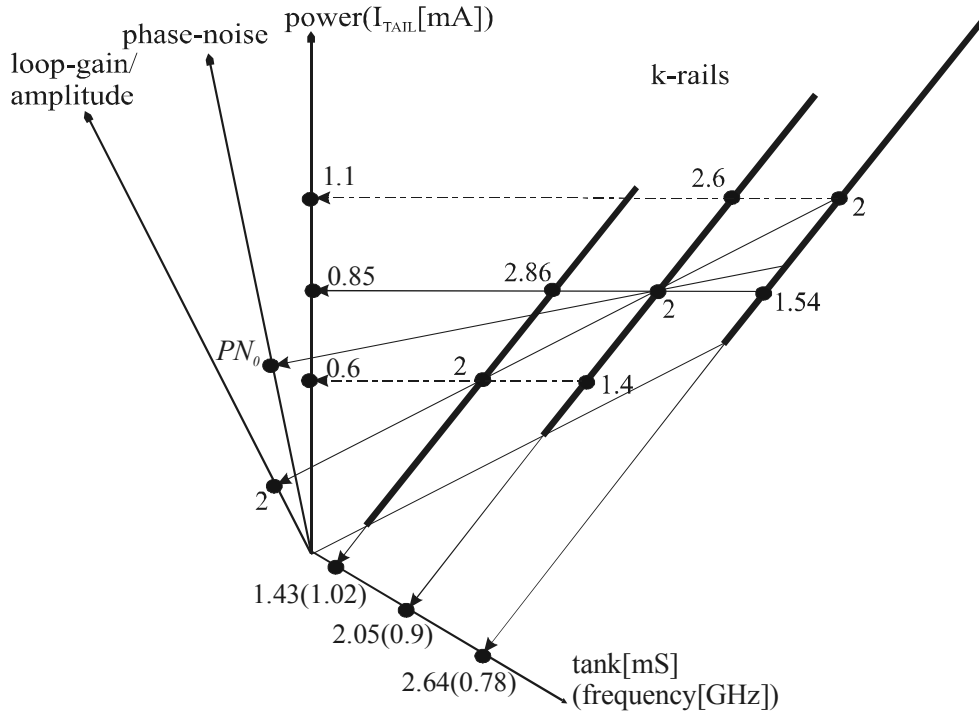


Figure 6.15: K-loop diagram for given parameters of the oscillator.

First, we will determine the values of the tank conductance for the lower, the central and the upper oscillation frequency. From Eq. (6.1), it is found that the tank conductance equals  $G_{TK}=2.05\text{mS}$  at the frequency  $f_0=900\text{MHz}$ , while from Eq. (6.2) the tail current is found to be  $I_{TAIL0}=0.85\text{mA}$ . For a maximum voltage tuning range of  $1\text{V}$ , from Eq. (6.76) the maximum change in the tail current is expected to be  $S_{U_T}^{I_{TAIL}}=0.25\text{mA/V}$ . In order to sustain oscillations under the same condition (i.e., the loop gain of two), the tail current should be either increased or reduced by this amount as a response to frequency tuning.

Keeping the order of points the same as in Fig. 6.14, points (2) and (3) of the diagram correspond to a tail current of  $1.1\text{mA}$ , while points (6) and (7) correspond to a current of  $0.6\text{mA}$ . Knowing the loop gain at operating point (2) and referring to the tail current of  $1.1\text{mA}$  as the safety start-up current for a new LC-tank, we can calculate the new tank conductance from Eq. (6.2). Corresponding to a lower resonant frequency  $f_L=780\text{MHz}$ , its value is  $G_{TK,L}=2.64\text{mS}$ . This holds for a tuning range of  $\pm 120\text{MHz}$ . The loop gain for point (3) is  $k=2.6$ , after the tuning system is linearized near the loop gain point  $k=2$ . The parameters of the left loop ((4) to (8)) are calculated following the same procedure.

Finally, the phase-noise ratio  $PNR$  and the phase-noise tuning range  $PNTR$  can easily be found and allocated to the points of the K-loop diagram. From Eqs. (6.59) and (6.60), the ratio  $PNR$  between points (0) and (2) is estimated to be around 1dB, while from Eq. (6.61), the  $PNTR$  between points (0) and (3) is calculated to be around 2dB.

## 6.7 CONCLUSIONS

Enhancing performance of wireless devices to cover multiple standards and provide more services offers more functionality to communication systems, but better performance only if systems can be adapted (i.e., respond actively to varying channel conditions). This necessitates a new design philosophy for analog RF front-end circuits. Therefore, a concept of designing for adaptivity has been introduced in this chapter, establishing a procedure for performance characterization of adaptive oscillators with qualitative and quantitative descriptions of the relationships and trade-offs between oscillator performance parameters.

The concept of phase-noise tuning explains how the designers can trade off RF performance for power consumption of an oscillator in an adaptive way. The extremes of the phase-noise tuning range and the power consumption reduction have been illustrated.

Furthermore, the concept of frequency-transconductance tuning has been presented. The analytical expressions derived show how this concept can be employed in order to achieve full control over the operation of the oscillator.

Finally, the performance characterization of oscillators using conceptual K-rail diagrams has been presented. It has been shown how K-rail diagrams can be used to interpret adaptivity phenomena and adaptivity figures of merit of oscillators.

## REFERENCES

- [1] J. Ryynanen, K. Kivekas, J. Jussila, A. Parssinen, K. Halonen, "A Dual-Band RF Front-End for WCDMA and GSM Applications", *Proceedings CICC*, pp. 175-178, May 2000.
- [2] Adiseno et al., "A Wide-Band RF Front-End for Multiband, Multistandard High-Linearity Low-IF Wireless Receivers", *IEEE Journal of Solid-State Circuits*, vol. 37, no. 9, pp. 1162-1168, September 2002.
- [3] X. Li and M. Ismail, "Architectures and Specs Help Analysis of Multi-Standard Receivers", <http://www.planetanalog.com/story/OEG20030312S0038>.
- [4] A. Tasić, W. A. Serdijn and J. R. Long, "Design of Multi-Standard Adaptive Voltage-Controlled Oscillators", accepted for *IEEE Transactions on Microwave Theory and Technique*, vol. 53, no.2, February 2005.
- [5] A. Tasić, W. A. Serdijn and J. R. Long, "Adaptivity of Voltage-Controlled Oscillators – Theory and Design", accepted for *IEEE Transactions on Circuits and Systems, part I*, 2005.
- [6] J. Craninckx and M. Steyaert, "A 1.8-GHz Low-Phase-Noise Voltage-Controlled Oscillator with Prescaler", *IEEE Journal of Solid-State Circuits*, vol. 30, no. 12, pp. 1474-1482, Dec. 1995.
- [7] A. Tasić and W. A. Serdijn, "Concept of Phase-Noise Tuning of Bipolar Voltage-Controlled Oscillators", *Proceedings ISCAS*, pp. 161-164, May 2002.
- [8] A. Tasić and W. A. Serdijn, "Concept of Frequency-Transconductance Tuning of Bipolar Voltage-Controlled Oscillators", *Proceedings ISCAS*, pp. 555-558, May 2002.
- [9] A. Tasić, W. A. Serdijn and J. R. Long, "Multi-Standard/Multi-Band Adaptive Voltage-Controlled Oscillator", *Proceeding RFIC*, pp. 135-138, June 2004.
- [10] J. Millman, and C. C. Halkias, *Integrated Electronics: Analog and Digital Circuits and Systems*, McGraw-Hill, New York, 1972.

- [11] D. B. Leeson, "A Simple Model of Feedback Oscillator Noise Spectrum", *Proceedings IEEE*, pp. 329–330, February 1966.
- [12] C. A. M. Boon, *Design of High-Performance Negative Feedback Oscillators*, PhD thesis, Delft, 1989.
- [13] C. Samori and A. Lacaita, "Spectrum Folding and Phase Noise in LC Tuned Oscillators", *IEEE Transactions on Circuits Systems*, vol. 45, pp. 781–790, July 1998.
- [14] P. Grey and R. Mayer, *Analysis and Design of Analog Integrated Circuits*, 2<sup>nd</sup> edition, John Wiley & Sons, Inc. New York, USA, 2001.
- [15] H. Darabi and A. Abidi, "Noise in RF-CMOS Mixers: A Simple Physical Model", *IEEE Journal of Solid-State Circuits*, vol. 35, no. 1, pp. 15-25, January 2000.
- [16] Maths Online, <http://www.univie.ac.at/future.media/moe/galerie.html>.
- [17] E. Hegazi et al., "Filtering Technique to Lower Oscillator Phase-Noise", *Proceedings ISSCC*, pp. 364-365, February 2001.
- [18] P. Andreani and H. Sjöland, "Tail Current Noise Suppression in RF CMOS VCOs", *IEEE Journal of Solid State Circuits*, vol. 37, no. 3, pp. 342-348, March 2002.
- [19] A. Tasić, W. A. Serdijn and J. R. Long, "Resonant-Inductive Degeneration of Voltage-Controlled Oscillator's Tail-Current Source", *Proceedings ISCAS*, pp. 673-676, May 2003.
- [20] A. Tasić, W. A. Serdijn and J. R. Long, "Matching of Low-Noise Amplifiers at High Frequencies", *Proceedings ISCAS*, pp. 321-324, May 2003.
- [21] S. P. Voinigescu et al. "A Scalable HF Noise Model for Bipolar Transistors with Application to Optimal Transistor Sizing for LNA Design", *IEEE Journal Solid State Circuits*, vol. 32, no. 9, pp. 1430-1439, Sep. 1997.
- [22] A. van Staveren et al., *Structured Electronic Design: High-Performance Harmonic Oscillators and Bandgap References*, Kluwer Academic Publishers, Boston 2001.

- [23] J. Craninx and M. Steyaert, "Low-Noise Voltage-Controlled Oscillators Using Enhanced LC-Tanks", *IEEE Trans. Circuits and Systems, Part II*, vol. 42, no. 12, pp. 792-804, December 1995.
- [24] A. Tasić, W. A. Serdijn and J. R. Long, "800MHz Voltage-Controlled Oscillator with 6dB Phase-Noise Tuning Range", *Proceedings MIEL*, pp. 559-562, May 2004.
- [25] B. Razavi, *RF Microelectronics*, Prentice Hall, Upper Saddle River, 1998.
- [26] M. Zannoth et al., "A Fully Integrated VCO at 2 GHz", *IEEE Journal of Solid State Circuits*, vol. 33, no. 12, pp. 1987-1991, December 1998.
- [27] J. Craninx and M. Steyaert, "A 1.8GHz Low-Phase-Noise CMOS VCO Using Optimal Hollow Spiral Inductors", *IEEE Journal of Solid State Circuits*, vol. 32, no. 5, pp. 736-744, May 1997.
- [28] A. Ham and A. Hajimiri, "Concepts and Methods in Optimization of Integrated LC VCOs", *IEEE Journal of Solid-State Circuits*, vol. 36, no. 6, pp. 896-909, June 2001.
- [29] M. Soyuer et al. "A 5.8GHz 1V Low-Noise Amplifier in SiGe Bipolar Technology", *Proceedings RFIC*, pp. 19-22, June 1997.
- [30] A. Tasić and W. A. Serdijn, "K-Rail Diagrams – Comprehensive Tool for Full Performance Characterization of Voltage-Controlled Oscillators", *Proceedings ICECS*, pp. 97-100, September 2002.



# **DESIGN OF ADAPTIVE VOLTAGE-CONTROLLED OSCILLATORS AND ADAPTIVE RF FRONT-ENDS**

Today's portable communication devices enable a growing variety of applications, ranging from text messaging, telephony and MP3 audio to full video. These devices must maintain connectivity while running multiple applications, they must track position, and (in the near future) be wearable rather than just portable. However, the energy supply for portables is fixed by the size and weight of the batteries in a hand-held device. Consequently, the current consumption of circuitry in hand-helds must be reduced in order to meet these increasing functional and concurrent operational requirements. Limited gains can be made through further improvements in circuit efficiency, radio architectures, and by sharing circuit blocks wherever possible. Another potential solution is circuit adaptivity. This requires scaling parameters such as current consumption to the demands of the signal-processing task at hand.

Demands for new telecom services requiring higher capacities and higher data rates have motivated the development of broadband, third-generation wireless systems. The coexistence of second- and third-generation cellular systems requires multi-mode, multi-band, and multi-standard mobile terminals. To prolong talk time, it is desirable to share and/or switch transceiver building blocks in these handsets, without degrading the performance compared to single-standard transceivers.

In multi-standard terminals, power can be saved by using adaptive circuits that are able to trade off power consumption for performance on the fly [1]. Adaptive RF circuits allow for reduced area, reduced power consumption, and most importantly, have the potential for lower cost in both single-standard and multi-standard terminals.

In this chapter, three design examples of adaptive circuits and systems for hand-held transceivers are presented: a low-power 800MHz voltage-controlled oscillator, a multi-standard second/third-generation (2G/3G) voltage-controlled oscillator, and a multi-standard 2G/3G front-end.

## 7.1 AN ADAPTIVE LOW-POWER VOLTAGE-CONTROLLED OSCILLATOR

In portable devices, oscillators and other RF circuits are exposed to worst-case conditions only for a short period during operation. Over-designing for the worst-case condition is therefore inefficient. On the other hand, circuit adaptation to varying channel conditions and application requirements ensures lower cost as the adaptivity allows for power savings, reduced silicon area, and longer battery life. Design of an 800MHz adaptive low-power voltage-controlled oscillator is presented in this section.

Operating from a 3V supply, the oscillator achieves -135.8dBc/Hz phase noise at 10MHz offset from the 800MHz oscillation frequency at a current consumption level of 5mA, and a phase noise of -128.6dBc/Hz at 10MHz offset and 1.5mA bias current. This oscillator achieves a phase-noise tuning range of 7dB with a factor 3.3 change in power consumption [2]. For a 0V-3V tuning voltage, a frequency tuning range of 120MHz is achieved (i.e., from 715MHz and 835MHz).

### 7.1.1 DESIGN FOR ADAPTIVITY OF VOLTAGE-CONTROLLED OSCILLATORS

The quasi-tapped voltage-controlled oscillator [1,2], shown in Fig. 7.1, consists of a resonating LC tank, two capacitive voltage dividers and a cross-coupled transconductance amplifier.  $L$  stands for the tank inductance,  $C_V$  the varactor capacitance,  $C_A$  and  $C_B$  the quasi-tapping capacitances and  $R_D$  the tail-current source degenerative resistance. This oscillator topology is extensively discussed in Chapter 6.

Selection of design parameters for an adaptive oscillator is discussed next. The phase-noise adaptivity figure of merit (Eq. (6.61)) that accounts for a number of oscillator operation conditions and required specifications forms a base for design of adaptive oscillators [3]. For given phase-noise tuning range ( $PNTR$ ), the maximum loop gain ( $k_{MAX}$ ) can be determined from Eq. (6.61) (the minimum loop gain is already known, e.g.,  $k_{MIN}=2$ ). On the other hand, if the maximum and minimum loop gain values are known, the obtainable  $PNTR$  can be determined from Eq. (6.61) (i.e., the range of oscillator adaptation with respect to phase noise).

Furthermore, from the maximum phase-noise requirement and the frequency tuning range requirement, the LC-tank parameters can be determined, i.e., coil inductance and varactor capacitance. Once the resonator

components are known, the equivalent tank conductance ( $G_{TK}$ ) and the minimum power consumption (current  $I_{TAIL,MIN}$ ) can be determined from Eqs. (6.1) and (6.2), respectively.

Finally, from the maximum loop gain on the one hand and the maximum tail current on the other, the minimum power consumption (tail current) and power consumption range can be estimated that provide an oscillator with the required phase-noise tuning range.

For  $k_{MIN}=2$  (guaranteed start-up condition),  $k_{MAX}=6$  (expected best phase noise for  $V_B=V_{CC}$ ), a quasi-tapping ratio  $n=2$ , and a parameter  $c=r_B g_{ms-up}$  of 0.65, a phase-noise tuning range  $PNTR$  of 6.7dB is estimated from Eq. (6.61). For oscillators operating at low loop-gain values, the “linear” phase-noise model, Eq. (6.54), can also be used for estimation of the phase-noise tuning range (Section 6.2.8.1).

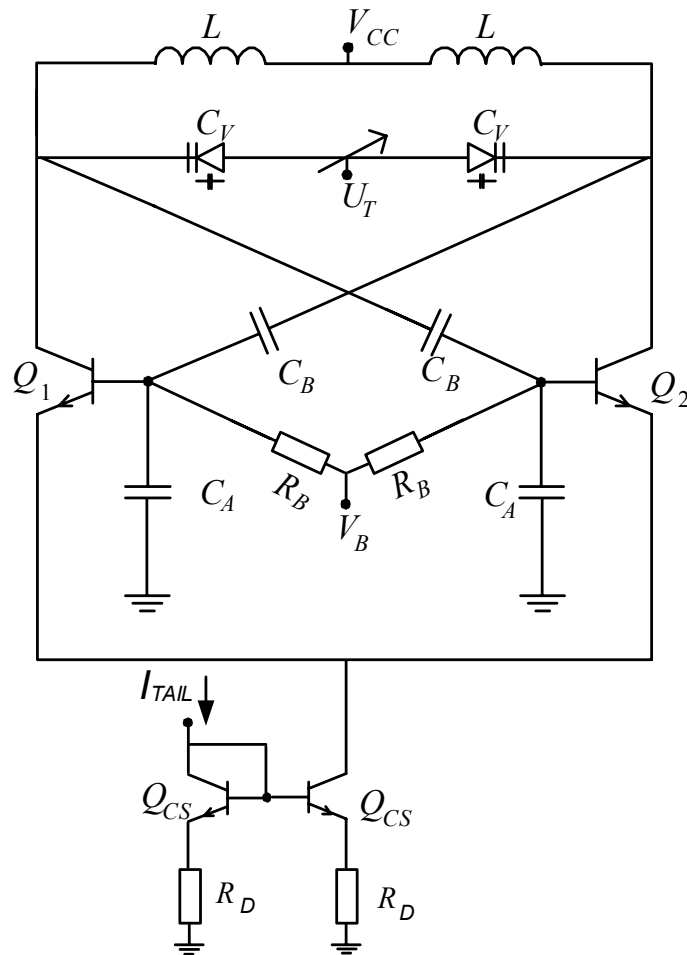


Figure 7.1: An adaptive LC-oscillator.

### 7.1.2 CIRCUIT PARAMETERS OF THE ADAPTIVE VOLTAGE-CONTROLLED OSCILLATOR

For a quasi-tapping ratio of  $n=2$ , the quasi-tapping capacitances  $C_A=1\text{pF}$  and  $C_{II}+C_B=1\text{pF}$  have been chosen,  $C_{II}$  being the base-emitter junction capacitance of devices  $Q_1$  and  $Q_2$  in Fig 7.1.

The reverse biased base-collector junctions of available transistors have been used for variable capacitors (varactors). The quality factor of the varactors is estimated at 15 from simulations (around 800MHz).

Optimized for low-power operation, a relatively large inductance value of 12nH is chosen, which was laid out in 1 $\mu\text{m}$  thick top (second) metal layer. The low quality factor of the inductor ( $Q=2$ ) in 800MHz band is the result of the 6 $\Omega\text{cm}$  substrate resistivity, operating frequency and relatively thin metal windings close to the substrate. The 6.25-turn inductor has an outer diameter  $d_{OUT}=360\mu\text{m}$ , metal width  $w=18.5\mu\text{m}$ , and metal spacing  $s=1\mu\text{m}$ .

The equivalent lumped-element model of the on-chip spiral inductor is shown in Fig. 7.2. The model consists of an ideal inductance  $L$ , a series resistance  $R_L$  (representing the losses in the coil) and an inter-winding capacitance  $C_L$ . The oxide capacitance between the spiral and the silicon substrate is modeled by  $C_{OX}$ . The substrate resistance and capacitance  $R_{SUB}$  and  $C_{SUB}$  are added as well, representing the RF signal flow through the silicon substrate.

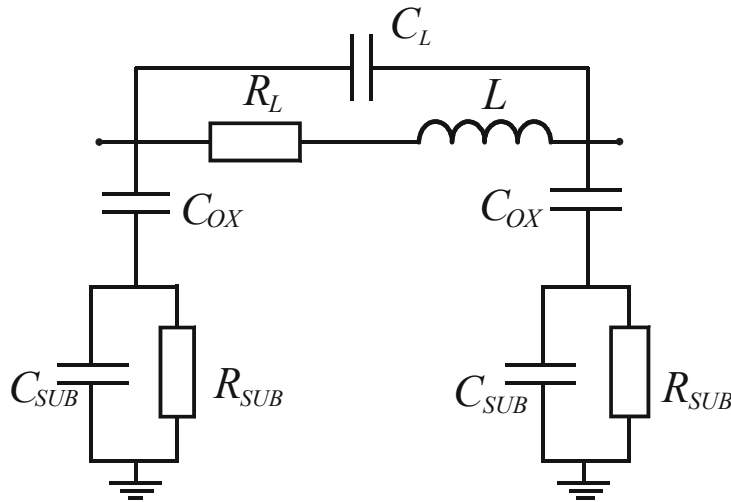


Figure 7.2: Lumped-element model of spiral inductor on silicon.

The model parameters of the inductor are estimated with the phase-noise-inductance (PNL) calculator [4]. The results are shown in Table 7.1.

Table 7.1: Model parameters of the employed integrated inductor.

Parameter	Value
$L$	12nH
$R_L$	18 $\Omega$
$C_L$	80fF
$C_{OX}$	0.8pF
$C_{SUB}$	40fF
$R_{SUB}$	150 $\Omega$

A two-stage common collector buffer has been used as an interfacing stage between the VCO and measurement equipment. Its current consumption is 2mA.

A good match is obtained between the results predicted by calculations and simulations on the one hand and the measurement results on the other, validating the design procedure.

### 7.1.3 MEASUREMENT RESULTS FOR THE ADAPTIVE VOLTAGE-CONTROLLED OSCILLATOR

The chip micrograph of the adaptive oscillator is shown in Fig. 7.3. It occupies an area of 1mm<sup>2</sup>, including bondpads. Wire-bonded into a 20-lead package, it is placed in a commercial test fixture.

For a 3V tuning voltage, a frequency tuning range of 120MHz is achieved, between 715MHz and 835MHz, as shown in Fig. 7.4.

Using a technology with a peak transit frequency  $f_T=8$ GHz, the VCO achieves a phase noise of -135.8dBc/Hz at 10MHz offset from the 800MHz oscillation frequency at a current consumption of 5mA. A phase noise of -128.6dBc/Hz at 10MHz offset is measured at a current of 1.5mA. The plots of the maximal and the minimal phase noise are shown in Fig. 7.5.

The phase-noise tuning range of 7dB is achieved for a 3.3 times change in power consumption. A phase-noise tuning range of 7.3dB is calculated for the ratio  $k_{MAX}/k_{MIN}$  of 3.3 using the “linear” model (Eq. (6.54)).

The frequency-transconductance tuning phenomenon (Section 6.5; [5]) can also be recognized in the oscillator under consideration. Fig. 7.6 depicts the C- $g_m$  tuning.

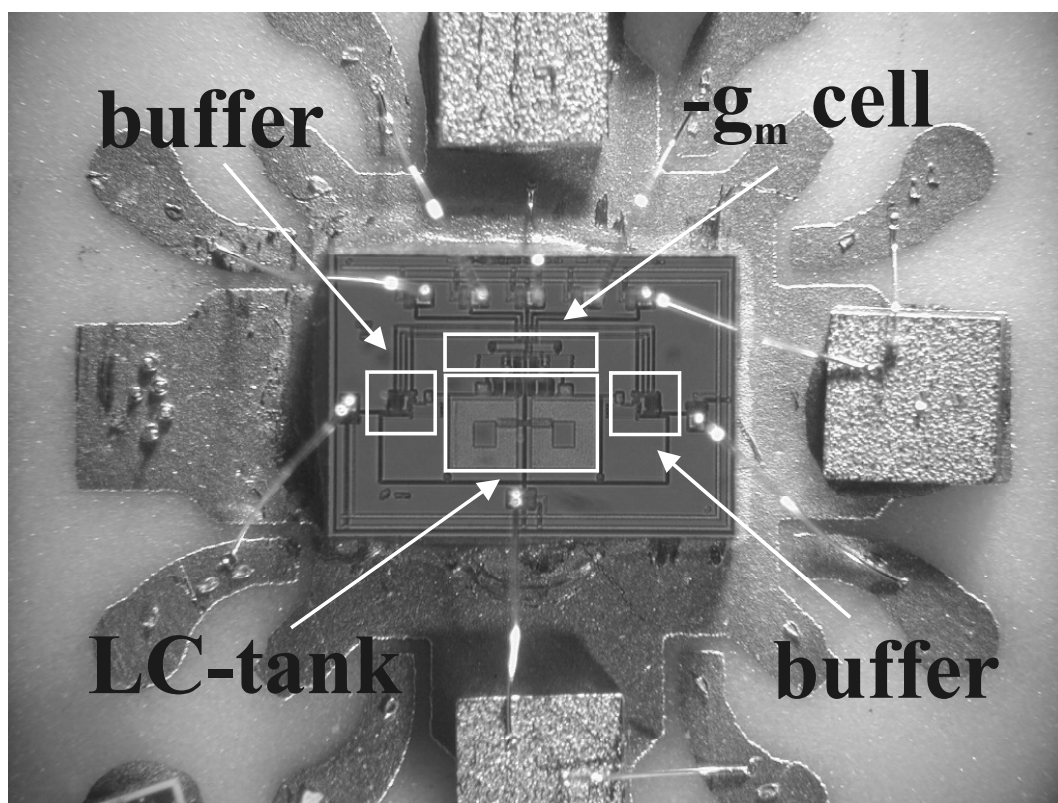


Figure 7.3: The 800MHz oscillator chip micrograph.

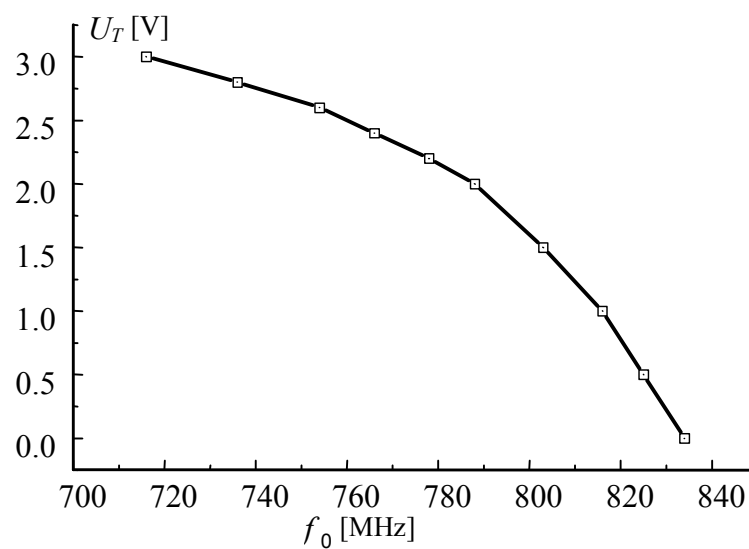


Figure 7.4: Oscillation frequency vs. tuning voltage for the adaptive VCO.

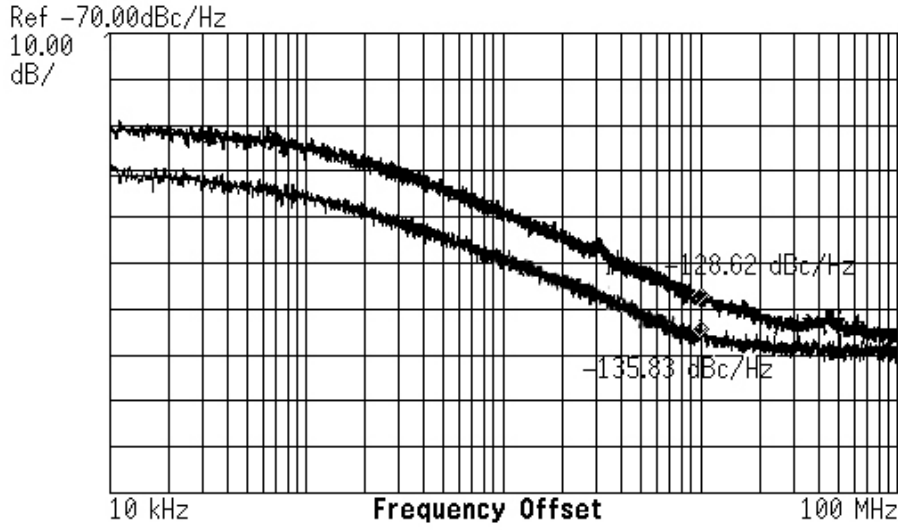


Figure 7.5: Maximum and minimum phase noise at 10MHz offset from the 800MHz oscillation frequency at 5mA and 1.5mA tail currents, respectively.

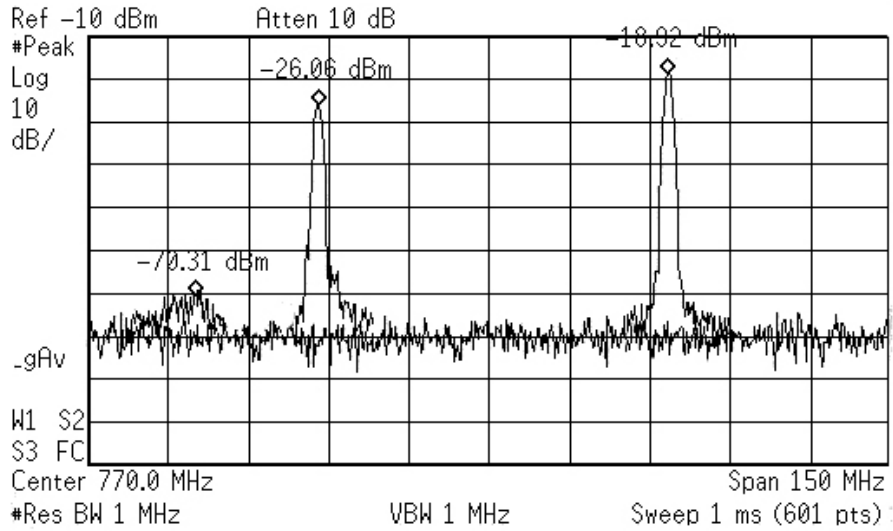


Figure 7.6: Frequency-transconductance tuning from 800MHz to 715MHz oscillation frequency at 2.5mA tail current.

In this case, the oscillator is tuned to the resonant frequency  $f=800\text{MHz}$  at a tail-current  $I_{TAIL}=2.5\text{mA}$ . The measured output signal power is  $-19\text{dBm}$ , and it corresponds to a loop gain value  $k$  equal to 3. By tuning the resonant frequency to  $740\text{MHz}$ , the output power of the oscillation signal changes to

-26dBm, and the VCO's loop gain  $k$  becomes one. Any further reduction of the oscillation frequency at the same power consumption results in disappearance of oscillations as the loop gain  $k$  is less than one. This is shown in Fig. 7.6 at left (-70dBm marker). The corresponding points in the K-loop diagram (Fig. 6.11) are point 1 (-70dBm) and point 5 (-19dBm).

Finally, let us stress that in this single-standard application, the adaptivity is utilized as a power saving mechanism by trading performance (7dB of phase noise) for power consumption (factor of 3.3 saving).

## **7.2 A MULTI-STANDARD ADAPTIVE VOLTAGE-CONTROLLED OSCILLATOR**

Multi-standard modules (MSMs) can be implemented in various ways:

- MSMs can be implemented as standalone fixed circuits that are designed for the worst-case condition of the most demanding standard [6]. Even though operating conditions might improve or a less demanding standard might be active, they always operate at the highest power consumption levels. This design approach is therefore power inefficient.
- MSMs can be implemented as multiple circuits, i.e., one per standard [7]. Even though simple to implement, this approach requires more silicon area, and is therefore area inefficient. Moreover, when multiple standards operate simultaneously, power consumption increases.
- MSMs can be implemented as standalone, adaptive circuits, by sharing circuit functions across multiple standards. This allows for reduced area and power consumption and, most importantly, has the potential for reduced cost.

An adaptive, multi-standard/multi-band (MS/MB) voltage-controlled oscillator that satisfies phase-noise requirements of both 2<sup>nd</sup> and 3<sup>rd</sup> generation wireless standards (DCS1800/WCDMA/WLAN–Bluetooth-DECT) is described in this section. A factor of 12 reduction in power consumption is realized, with a phase-noise tuning range of 20dB by adapting the VCO bias to the desired application. The VCO achieves -123dBc/Hz, -110dBc/Hz and -103dBc/Hz phase noise at 1MHz offset in a 2.1GHz band at supply currents of 6mA, 1.2mA and 0.5mA, respectively.



The design procedure for the multi-standard adaptive VCO, i.e., the design for the certain phase-noise tuning range, is outlined next. Parameters selection for the multi-standard oscillator and measurement results are discussed afterwards.

### 7.2.1 DESIGNING FOR ADAPTIVITY OF MULTI-STANDARD VOLTAGE-CONTROLLED OSCILLATORS

The receiver phase-noise requirements (dBc/Hz at 1MHz offset) for five different standards (i.e., DCS1800/WCDMA/WLAN–Bluetooth-DECT) are listed in Table 7.2 [8-12]. We will refer to the DCS1800 standard as a phase-noise demanding (PN-D) standard, to the WCDMA, WLAN and Bluetooth standards as phase-noise moderate (PN-M) standards, and to the DECT standard as a phase-noise relaxed (PN-R) standard.

Table 7.2: Multi-standard/multi-band VCO requirements.

<b>MSVCO</b>	<b><i>DCS1800</i></b>	<b><i>WCDMA</i></b>	<b><i>WLAN</i></b>	<b><i>Bluetooth</i></b>	<b><i>DECT</i></b>
PN@1MHz [dBc/Hz]	-123	-110	-110	-110	-100

The quasi-tapped bipolar VCO [1] shown in Fig. 7.7 is used to implement the multi-standard adaptive oscillator. Compared to the oscillator of Fig. 7.1, the resonant-inductive degenerated (RID) tail-current source in Fig. 7.7 is implemented with degeneration inductor  $L_{RID}$ . Degeneration of the current source is necessary to minimize the phase noise contributed by the bias circuit (Section 6.2.6; [13]). The oscillation signal is delivered to the measurement equipment (50Ω impedance) using an on-chip open-collector buffer and an external transformer balun,  $TR$ . Buffering the output from the bases of the transconductor transistors rather than from the LC-tank, the buffer can share the base bias voltage, thereby eliminating output coupling capacitors. Gain of the buffer is set by the emitter-degeneration resistance  $R_E$ .

Given the phase-noise requirements listed in Table 7.2, the phase-noise range between the demanding (PN-D) and moderate (PN-M) modes is  $PNTR=123-110-20\log(2.4\text{GHz}/1.8\text{GHz})=11\text{dB}$ . Taking into account the relaxed DECT mode (PN-R), the  $PNTR$  increases to  $123-100-20\log(2.4/1.8)=21\text{dB}$ . Therefore, a  $PNTR$  of 21dB is targeted.

After the effects of the noise from the biasing tail-current source are eliminating by means of RID (Eq. (6.27)), the minimum and the maximum

loop gain and tail current can be estimated from Eq. (6.61). Accordingly, a  $PNTR$  of 17.4dB can be realized between the loop gain  $k_{MIN}=2$  and  $k_{MAX}=19$ . However, if  $k_{MIN}$  is 1.5, the tuning range extends to  $PNTR=21.4$ dB, which is sufficient to accommodate multiple standards.

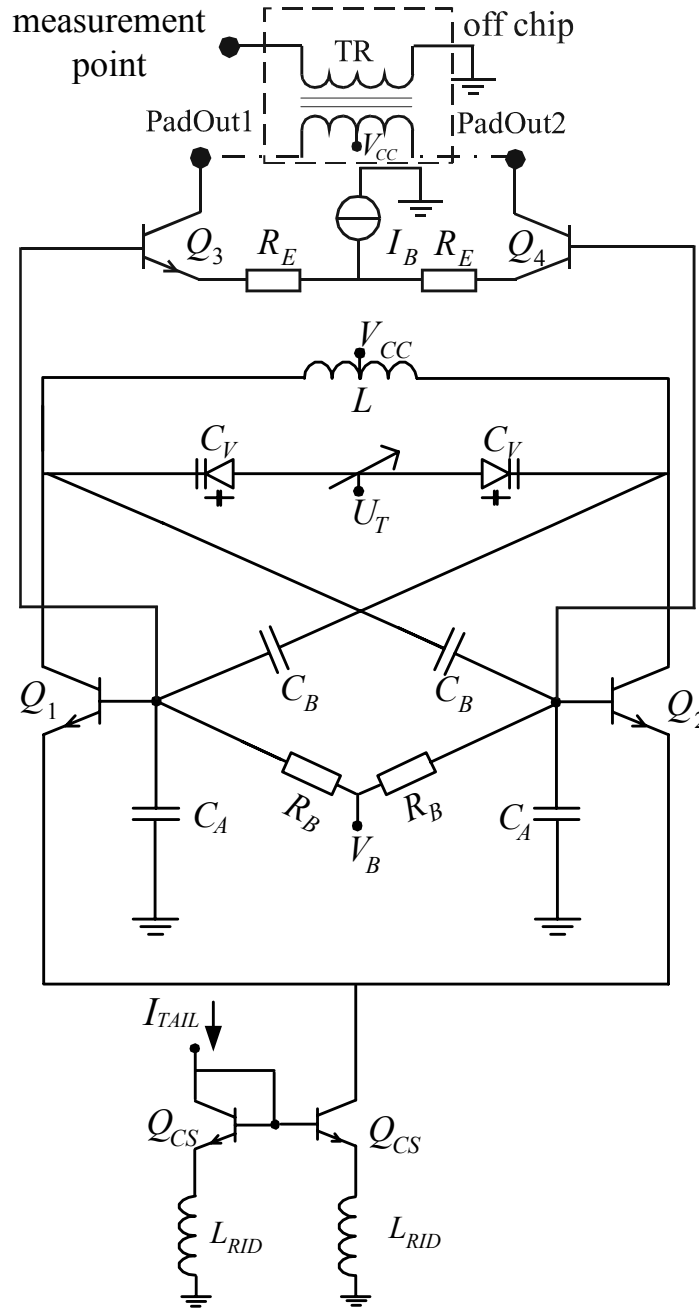


Figure 7.7: A resonant-inductive degenerated oscillator with an open-collector buffer.

Once the maximum loop gain is known, the oscillator bias point can be determined. The choice of the base-bias voltage  $V_B$  is a compromise between a large output voltage swing and saturation of transconductor devices  $Q_1$  and  $Q_2$  (Fig. 7.7). For maximum loop gain and lowest phase noise, a voltage swing across the bases of the transconductor devices of  $v_{S,B,MAX}=1.2V$  is estimated from Eq. (6.9). Further, to avoid the saturation of the transistors in the active part of the oscillator,  $v_{S,B}$  should satisfy Eq. (6.62), for the convenience given by Eq. (7.1) as well.

$$v_{S,B,MAX} \leq 2 \frac{V_{CC} - V_B + V_{BE} - V_{CE,SAT}}{n + 1} \quad (7.1)$$

The worst-case condition is derived assuming the largest base and the lowest collector potential, and therefore insures proper operation of the transistors in the active part at all times.  $V_{CC}=3V$  is the supply voltage,  $V_{BE}$  is the base-emitter voltage, and  $V_{CE,SAT}$  is the collector-emitter saturation voltage. For a capacitive quasi-tapping ratio  $n$  of 1.4, a base potential  $V_B$  of 2.1V is finally obtained from Eq. (7.1).

### 7.2.2 CIRCUIT PARAMETERS OF THE MULTI-STANDARD ADAPTIVE VOLTAGE-CONTROLLED OSCILLATOR

Tank inductor  $L=3nH$  is chosen as a compromise between low power consumption and high quality factor in the 2.1GHz band. The inductor is fabricated using 4um thick aluminum top metal in a 50GHz SiGe technology. The 3-turn inductor has outer diameter  $d_{OUT}=320um$ , metal width  $w=20um$  and metal spacing  $s=5um$ . The differentially-shielded symmetric inductor uses a ladder metal filling scheme as shown in Fig. 7.8 [14]. This improves the peak  $Q$ -factor by 40% ( $Q_L=25$  around 2.1GHz), but has only a minor effect on the inductor self-resonant frequency. It also satisfies the aggressive metal fill restrictions in modern VLSI backend technologies without compromising RF performance.

The quality-factor of the varactor can also limit the overall tank  $Q$ -factor in an integrated oscillator. The quality factor of the collector-base varactor is estimated at  $Q_C=40$  from simulation. The varactor consists of 2 base-collector diodes with 32 fingers, each 4um wide and 20um long.

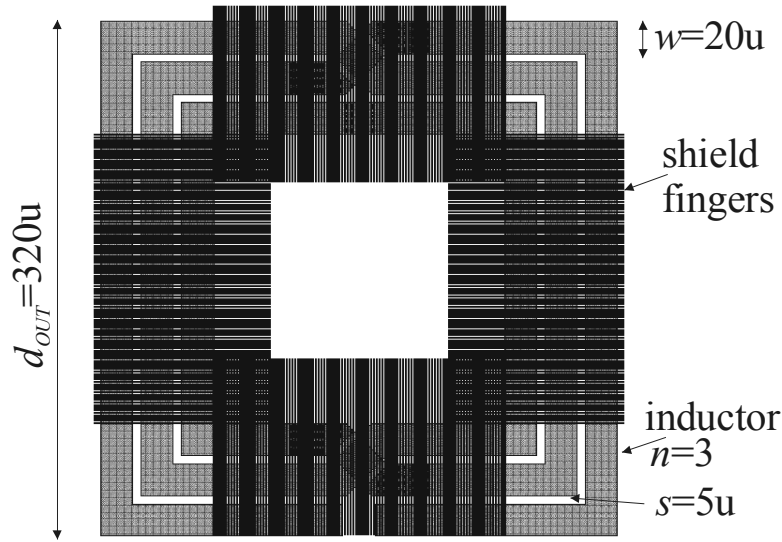


Figure 7.8: Shielded inductor layout (bottom view).

The metal-insulator-metal capacitances  $C_A=150\text{fF}$  ( $C_{IT}=90\text{fF}$ ) and  $C_B=600\text{fF}$  are chosen for a quasi-tapping ratio of 1.4. For effective suppression of the tail-current source noise,  $L_{RID}$  is set to  $3.4\text{nH}$  using the resonant-tuning design method outlined in Section 6.2.6. The degeneration inductor is realized in  $0.85\mu\text{m}$  thick second metal layer, as quality factor for this inductor is not of concern. The inductor outer diameter is  $d_{OUT}=140\mu\text{m}$ , metal width  $w=6\mu\text{m}$ , metal spacing  $s=1\mu\text{m}$  and it has seven turns.

Finally, the open-collector output buffer is designed with a linearization resistor  $R_E$  of  $750\Omega$  and a bias current  $I_B$  of  $1.1\text{mA}$ .

### 7.2.3 MEASUREMENT RESULTS FOR THE MULTI-STANDARD ADAPTIVE VOLTAGE-CONTROLLED OSCILLATOR

The chip photomicrograph of the multi-standard VCO is shown in Fig. 7.9. It occupies an area of  $700 \times 970 \mu\text{m}^2$ , including bondpads. Wire-bonded in a 20 lead RF package, the chip is tested in a metal fixture with filtering on all bias and supply lines, as shown in Fig. 7.10. On the test board, three-stage low-pass LC filters remove low-frequency noise originating from the power supply and bias interconnections. Heavy filtering of the supply and bias lines is needed to remove spurs from the VCO output caused by pick-up from the supply and tuning lines. This unwanted interference would otherwise modulate the VCO in both phase and frequency making accurate phase-noise measurements impossible without filtering.

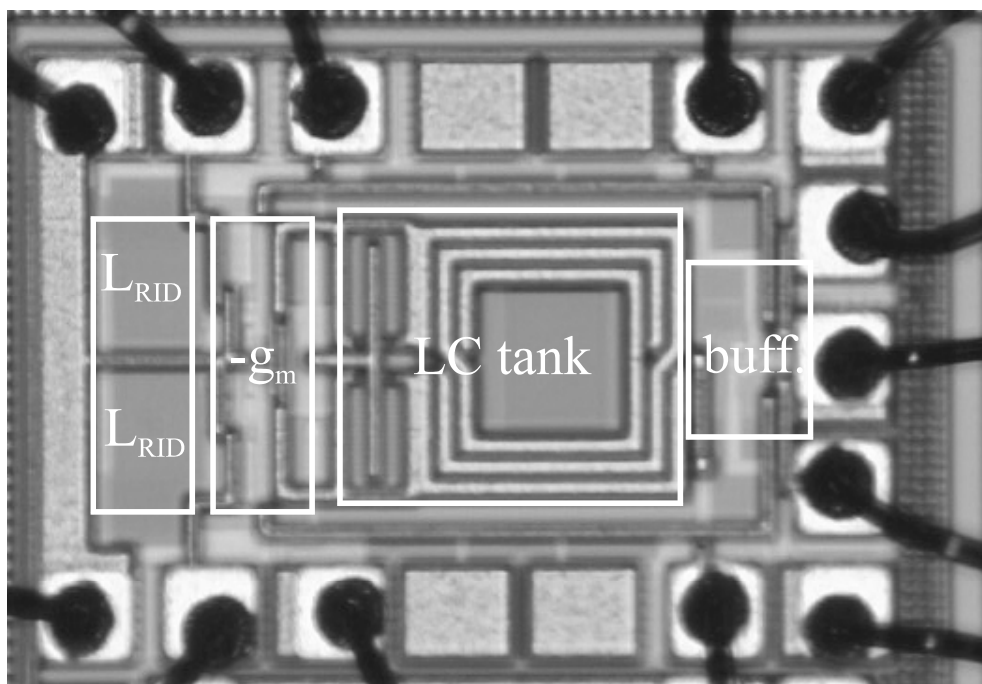


Figure 7.9: The photomicrograph of the multi-standard VCO.

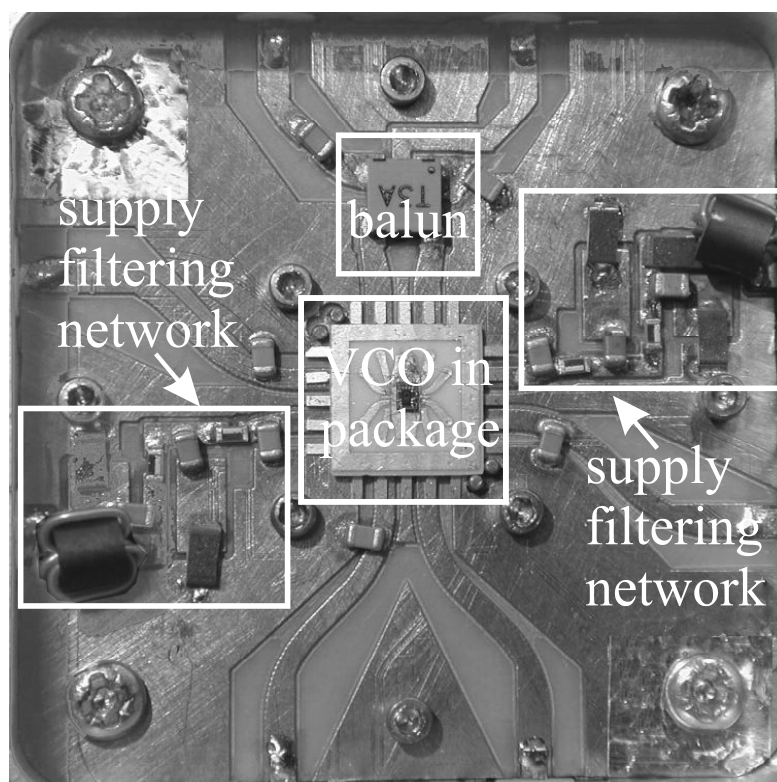


Figure 7.10: Packaged VCO IC on PCB in test fixture.

For a 3V supply, a frequency tuning range of 600MHz (i.e., output from 1.8GHz to 2.4GHz) is measured, as shown in Fig. 7.11. In order to relax the requirement of a large frequency tuning range from a variable capacitor, switched capacitor banks can be used [15]. They allow for switching between frequency bands (standards), whereas varactors perform fine frequency tuning within a band. For example, the complete 2.4GHz band can be covered using this method.

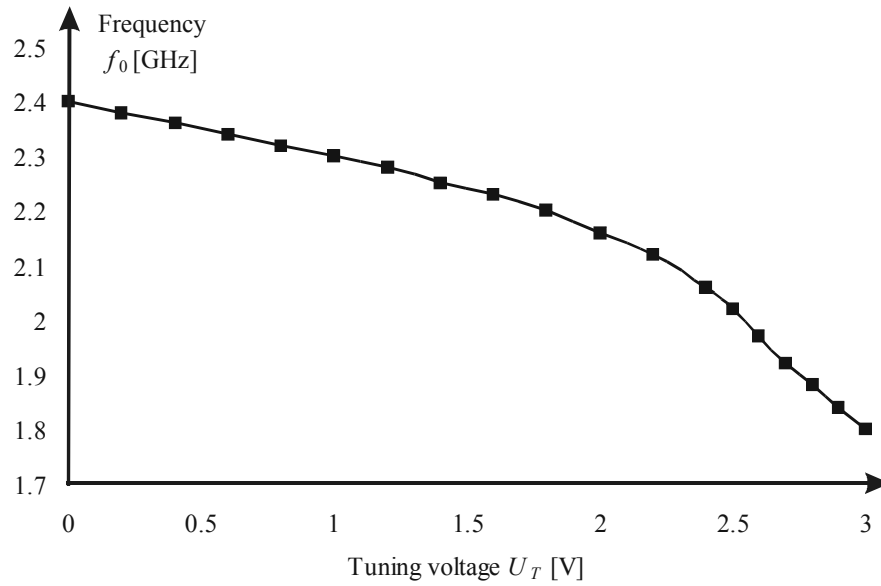


Figure 7.11:  $f_0$ -tuning curve for a 3V tuning voltage.

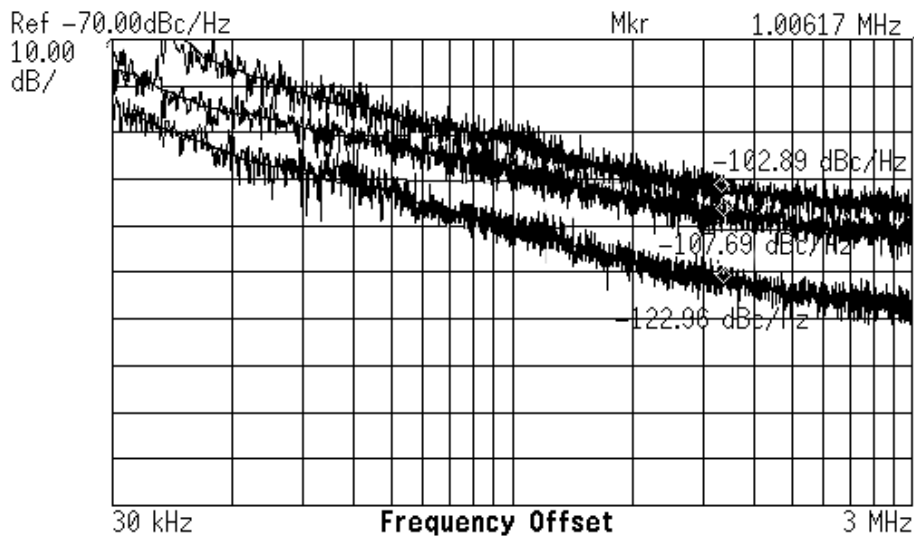


Figure 7.12: Phase noise at 1MHz offset in the 2.1GHz band.

Plots of the measured phase noise at 1MHz offset in the 2.1GHz mid-frequency band is shown in Fig. 7.12. Due to low gain in the output buffer, an output signal in order of -20dBm (maximum) is measured in a 50Ω system. This results in a noise floor for the phase-noise measurement of -130dBc/Hz, as seen in Fig. 7.12.

The operating conditions accompanying the measurements shown in Fig. 7.12 are listed in Table 7.3. As can be seen from this table, by adapting the bias tail current between 0.5mA/0.9mA and 6mA, a phase-noise tuning range of 20dB/15dB is achieved. This satisfies the requirements of five different wireless standards, as desired. Note that by following the measured phase-noise slope in the range 100KHz-1MHz, a phase noise better than -133dBc/Hz at a 3MHz offset is expected, fulfilling the stringent DCS1800 receiver requirement at this offset as well.

Table 7.3: Oscillator Performance in 2.1GHz band.

<b>PhaseNoise@1MHz</b>	<b>Loop gain</b>	<b><math>I_{TAIL}</math></b>
-123dBc/Hz	20	6mA
-108dBc/Hz	3	0.9mA
-103dBc/Hz	1.7	0.5mA

The power-consumption figure of merit,

$$FOM1 = \mathcal{L} (\Delta f_{OFFSET} / f_0) 2V_{CC} I_{TAIL} = 178, \quad (7.2)$$

and the tuning-range figure of merit,

$$FOM2 = FOM1 (f_0 / \Delta f_{TUNE})^2 = 167, \quad (7.3)$$

of the oscillator under consideration are compared with other designs from the recent literature [16-19] in Table 7.4 (modulus dB).  $\mathcal{L}$  stands for phase noise,  $\Delta f_{OFFSET}$  offset frequency, and  $\Delta f_{TUNE}$  tuning range. The adaptive VCO [1] shows a good compromise between phase-noise and frequency-tuning performance. Referring to Leeson's phase-noise formula [20], Eq. (7.4),

$$\mathcal{L} = F \frac{KT}{2P_{SIGNAL}} \frac{1}{Q_{TANK}^2} \left( \frac{f_0}{\Delta f_{OFFSET}} \right)^2. \quad (7.4)$$

$FOM2$  appears to be a useful VCO figure of merit. It accounts for the frequency dependency of the phase noise as well as the power consumption and the tuning range of the oscillator, the latter related to the LC-tank  $Q$ -factor.

Table 7.4: Power-consumption and tuning-range figures of merit.

<i>Reference</i>	<i>Process</i>	<i>FOM1 [dB]</i>	<i>FOM2 [dB]</i>
[16]	SiGe	178	148
[17]	SiGe	174	148
[18]	CMOS	172	152
[19]	CMOS	183	150
This work	SiGe	178	167

The procedure of designing for adaptivity can be applied to any standard. The standards chosen in this exploratory design serve a proof of concept of designing for adaptivity and validate the feasibility of the design procedure outlined.

### 7.3 MULTI-STANDARD ADAPTIVE RF FRONT-ENDS

Transceivers for multi-mode and multi-standard telephony are mostly implemented by replicating the RF front-end for each operating band or standard [7]. This allows applications such as GSM and WCDMA to operate concurrently (i.e., one can receive or make a call with either system at any time). Although high integration levels are possible in RF IC technologies, the increase in RF hardware required to implement this type of multi-standard radio increases the total current consumption, thereby reducing the overall talk time. In such situations, the ability to share circuit functions between different standards in an adaptive multi-standard RF front-end offers the advantages of reduced power consumption, less chip area, longer talk time, and, most importantly, has the potential for lower cost.

In this section, the results of an exploratory circuit design for a multi-standard adaptive RF receiver front-end (MSAFE) are described. The multi-standard adaptive RF front-end (oscillator and mixers) satisfies the requirements of the considered 2<sup>nd</sup> and 3<sup>rd</sup> generation standards. This design allows for adaptation between different standards by trading RF performance



for current consumption, which ranges from 9.9mA for the relaxed mode (2.4GHz DECT) to 20.2mA for the highest performance mode of operation (1.8GHz DCS1800). The quadrature downconverter (single-complex mixer-oscillator) has  $IIP3$  of +5.5dBm, single-side band (SSB)  $NF$  of 13.9dB (50 $\Omega$ ) and conversion gain (voltage and/or power) of -1.6dB, while drawing 10mA from a 3V supply. The adaptive VCO achieves -123dBc/Hz and -103dBc/Hz phase noise at 1MHz offset in a 2.1GHz band for bias current levels of 6mA and 0.5mA, respectively.

The following section describes the selection of performance for multi-standard adaptive RF front-end circuits. The design of the quadrature downconverter circuits used in the experimental implementation is then described. Finally, the measurement results are presented demonstrating that a 2:1 saving in power consumption is possible when adaptivity is employed.

### 7.3.1 SYSTEM CONSIDERATIONS FOR MULTI-STANDARD ADAPTIVE RF FRONT-ENDS

Concurrent operation of different wireless standards using a common RF receiver poses demands on performance (e.g., band selection, image-rejection and noise/power match prior to low-noise amplification) that are difficult to meet using a single RF path [21]. Therefore, multi-standard receivers typically use duplicate circuit blocks, or even multiple RF front-ends (i.e., one for each standard).

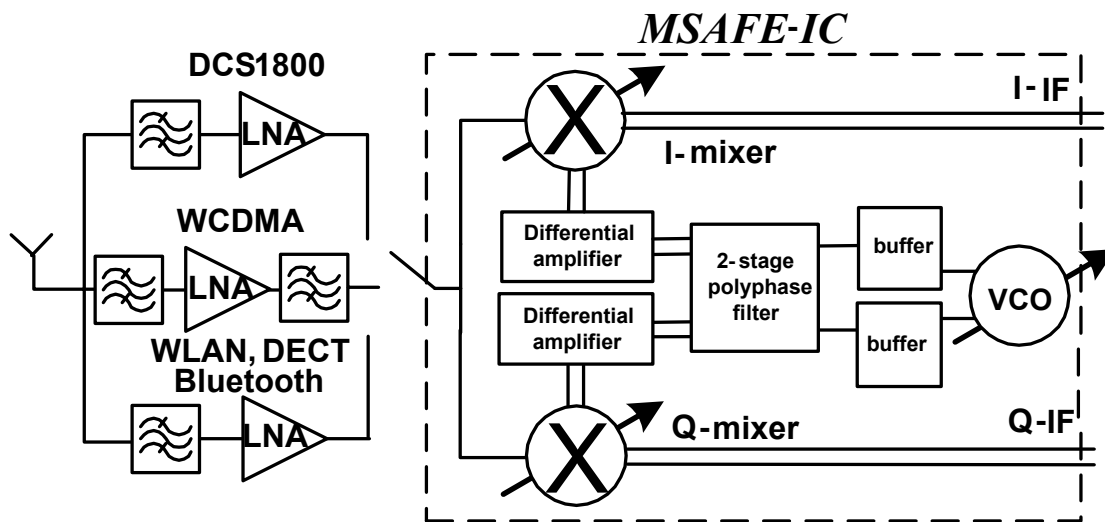


Figure 7.13: A multi-standard receiver.

The multi-standard receiver, shown in Fig. 7.13, is a compromise between these two approaches. Impedance matching, packaging and prefiltering requirements are relaxed and simplified by using multiple low-noise amplifiers. A single quadrature or image-reject downconverter can then be used to interface the RF and baseband sections of the receiver. An RF switch is used to select the standard of interest. If the VCO and mixer performance are adequate to cover the range of signals anticipated for each application, the downconverter enables a multi-standard receiver realization with a single circuit block (the MSAFE IC in Fig. 7.13).

Analog and digital baseband signal processing functions could be used to monitor quality of service (e.g., error rate of the detected bit sequences) and adjust the receiver parameters (e.g., tune a single bias current or multiple currents) in real-time to meet the requirements of a given standard.

For this work, the multi-standard adaptive downconverter is intended to operate as part of a zero-IF receiver for all standards except DCS1800, where low-IF operation is assumed. The MSAFE test circuit consists of an adaptive voltage-controlled oscillator, oscillator buffers, a two-stage poly-phase filter to generate in-phase (I) and quadrature-phase (Q) local oscillator signals, mixer buffer amplifiers and dual balanced mixers, as illustrated in Fig. 7.13.

Using mixer-oscillator models (Section 3.3), a single-channel representation of the adaptive RF front-end (Fig. 7.13) is shown in Fig. 7.14, consisting of an LNA, a single-complex mixer-oscillator (SC-MO; quadrature-downconverter) and (quadrature) baseband circuitry. Referring to Fig. 7.14, we will discuss the procedure for the selection of the specifications for the multi-standard receiver blocks.

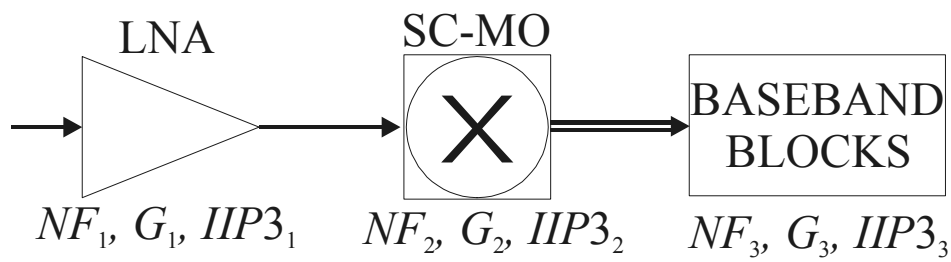


Figure 7.14: Simplified RF front-end receiver model.

### 7.3.1.1 System Requirements for a Multi-Standard Receiver

The noise (noise figure and phase noise) and linearity requirements ( $IIP3$ ) for 1.8GHz-DCS1800, 2.1GHz-WCDMA and 2.4GHz-WLAN(802.11b)/Bluetooth/DECT standards are listed in Table 7.5 [8-12, 22-25]. These

standards are chosen to show the feasibility of the adaptivity design concept for multi-standard applications. The procedure of designing for adaptivity can be applied to any standard.

The MSAFE operating modes are classified as: demanding (D), moderate (M), and/or relaxed (R) with respect to phase noise, noise figure and linearity requirements. Table 7.6 summarizes the noise and linearity requirements for different modes of operation for the system shown in Fig. 7.14 (thus prior to an LNA).

Table 7.5: Requirements for different standards prior to an LNA.

<b>MSAFE</b>	<b>DCS1800</b>	<b>WCDMA</b>	<b>WLAN</b>	<b>Bluetooth</b>	<b>DECT</b>
$f_0$ [GHz]	1.8	2.1	2.4	2.4	2.4
$NF$ [dB]	9 (D/M)	6 (D)	10 (M)	23 (R)	18 (R)
$IIP3$ [dBm]	-9 (D)	-9 (D)	-12 (M)	-16 (R)	-20 (R)
$PN@1\text{MHz}$	-123 (D)	-110 (M)	-110 (M)	-110 (M)	-100 (R)

Table 7.6: Performance requirements for different modes (desired specs).

<b>desired specification / mode</b>	<b>D (demanding)</b>	<b>M (moderate)</b>	<b>R (relaxed)</b>
$NF_D$ [dB]	6	10	18
$IIP3_D$ [dBm]	-9	-12	-16

Specifications for the multi-standard receiver blocks will be determined with the aid of Eqs. (4.3)-(4.5), (4.8)-(4.16), and the procedure outlined in Chapter 4. Accordingly, the noise and linearity equilibrium points are determined first. Using Eq. (4.4) and the inputs of Table 7.6, the equilibrium parameters are calculated as given by Table 7.7 (a three-block system of Fig. 7.14 is considered;  $n=3$ ).

Table 7.7: Receiver equilibrium performance.

<b>specification/mode</b>	<b>demanding</b>	<b>moderate</b>	<b>relaxed</b>
$NF_E$ [dB]	1	5	13
$IIP3_E$ [dBm]	-4	-7	-11

Required specifications for receiver blocks in different modes of operation will be determined in the following sections with the aid of the equilibrium design requirements given in Table 7.7.

Design procedure for an adaptive multi-standard circuit is different from design for a single standard. Figures of merit referring to a number of operating conditions and specifications are required for multi-standard designs, i.e., the adaptivity figures of merit (AFOM). For oscillators, the phase-noise tuning range (*PNTR*) (Section 6.4 and [3]) is used to specify the difference between the maximum and minimum achievable phase noise. Useful AFOM for mixers and amplifiers are the ranges of noise figure and the intercept point that are realized when a particular parameter, e.g., bias current, is adjusted (refer to Section 6.3).

Referring to Table 7.6 and Section 7.2.1 (Table 7.2), the phase-noise tuning range (*PNTR*), the noise-figure tuning range (*NFTR*), and the 3<sup>rd</sup>-order input-intercept point tuning range (*IIP3TR*) are given in Table 7.8 for the MSAFE system.

Table 7.8: Tuning ranges of the MSAFE desired performance parameters.

<i>PNTR</i>	<i>NFTR</i>	<i>IIP3TR</i>
21 dB	12 dB	7 dB

### 7.3.2 A MULTI-STANDARD ADAPTIVE QUADRATURE SIGNAL GENERATOR

The VCO shown in Fig. 7.7 (Section 7.2 and [1]) is used to implement the adaptive oscillator (without open-collector buffer shown in Fig 7.7). As the procedure for the selection of parameters of this adaptive VCO has already been discussed in detail in Section 7.2.1, in this section we will focus on the circuitry proceeding the VCO: two common-collector buffers, a polyphase filter (PPF) and two differential amplifiers, as shown in Fig. 7.15.

The common-collector buffers ( $Q_{CC}$ ) are added as an interface between the polyphase filter and the oscillator (from bases of  $Q_1$ ,  $Q_2$  in Fig. 7.7). They consist of  $0.5 \times 1.7 \mu\text{m}^2$  transistors and consume 1mA each.

The quadrature signals used to drive the mixers are derived from a two-stage polyphase filter. The first and second stage *R-C* filter sections provide rejection at 1.75 and 2.15GHz, respectively. This allows for more image-rejection in the 1.8GHz band where low-IF operation is presumed. Image-

rejection requirements are relaxed around 2.4GHz, as the zero-IF operation is assumed in this band.

The inevitable attenuation of the passive polyphase filter necessitates a differential buffer amplifier for the oscillation signal before driving the mixer quad (Fig. 7.15). The buffer provides  $160\text{mV}_{\text{pk}}$  oscillation signal swing across  $150\Omega$  load resistors while consuming  $1.1\text{mA}$  of bias current.

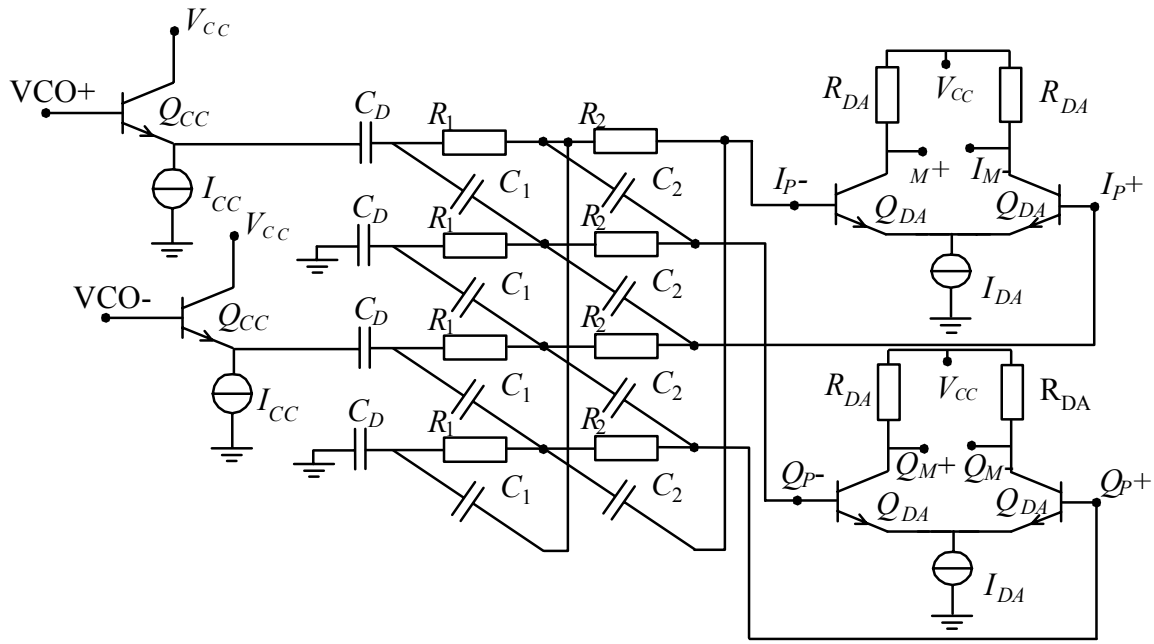


Figure 7.15: Buffers, a polyphase filter, and differential amplifiers.

### 7.3.3 A MULTI-STANDARD ADAPTIVE QUADRATURE DOWNCONVERTER

In order to determine the required specifications for the MSAFE quadrature downconverter blocks, we will apply the following procedure (see Chapter 4):

- I. determine the deviation ( $A$ ) from the noise and linearity equilibrium performance for an LNA using Eqs. (4.11) and (4.14).
- II. determine the deviation ( $B$ ) from the noise and linearity equilibrium performance for the quadrature downconverter (single-complex mixer-oscillator, SC-MO) using Eq. (4.5) and the deviation  $A$ .

- III. determine the noise and linearity performance for the quadrature downconverter using Eqs. (4.12) and (4.15) and the deviations  $A$  and  $B$ .

Without loss of generality, we will assume that the noise and linearity performance of the (quadrature) baseband circuitry is at equilibrium, i.e.,  $C_{NF}=C_{IIP3}=0$ . Typical LNA performance is assumed (see Table 4.1):  $NF_1=2\text{dB}$ ,  $IIP3_1=1\text{dBm}$  and voltage gain (from source)  $VG_1=13\text{dB}$  (for example, for  $50\Omega$  source and load impedances).

In accordance with the design procedure proposed (steps I-III), deviations from the equilibrium of the LNA noise and linearity performance in different modes of operation are calculated from Table 7.7 (step I). The results are shown in Table 7.9.

Table 7.9:  $NF$  and  $IIP3$  deviations from the LNA equilibrium point in different modes of operation.

deviation/mode	demanding	moderate	relaxed
$A_{NF}$ [dB]	1	-3	-11
$A_{IIP3}$ [dB]	-5	-8	-12

Table 7.10 is generated from Table 7.9 (step II). It shows the difference between the desired and equilibrium performance for the quadrature downconverter.

Table 7.10:  $NF$  and  $IIP3$  deviations from the equilibrium points of the quadrature downconverter in different modes of operation.

deviation/mode	demanding	moderate	relaxed
$B_{NF}$ [dB]	-1.3	1.75	2.8
$B_{IIP3}$ [dB]	2.26	2.65	2.87

Finally, from the inputs of Tables 7.8, 7.9 and 7.10, the required noise and linearity performance of the quadrature downconverter (Fig. 7.14) are determined as given in Table 7.11 (step III).

Table 7.11: Required performance for the quadrature downconverter.

specification/mode	demanding	moderate	relaxed
$NF_2$ [dB]	12.7	19.75	28.8
$IIP3_2$ [dBm]	6.74	3.35	-0.87

Now, the  $NF_{TR}$  and  $IIP3_{TR}$  of the quadrature downconverter (SC-MO) can be determined from Table 7.11. When the NF and IIP3 of the SC-MO are adapted between 12.7dB and 28.8dB, and 6.74dBm and -0.87dBm, respectively, the quadrature downconverter satisfies the requirements of the considered standards:  $NF_{TR_2}$  is 16dB, and  $IIP3_{TR_2}$  is 7.6dB

Assuming a voltage gain  $VG_2$  of 0dB for the quadrature downconverter (from signal source; see Section 2.1), the typical performance for the baseband block (demanding mode) are obtained from Eqs. (4.13) and (4.16):  $NF_3$  of 14dB and  $IIP3_3$  of 9dBm ( $C_{NF}=C_{IIP3}=0$ dB) [26].

The results obtained confirm that the proposed specification-selection scheme imposes realistic (realizable) requirements on the receiver circuits, covering all the standards of interest.

After the downconverted low-frequency signals (low-IF operation) are summed, the image signal will be removed as well as the noise residing in the frequency band of the image signal. As a result of this quadrature combining, the signal power increases 2 times, whereas the noise power stays the same (noise from 2 channels in a  $\frac{1}{2}$  bandwidth compared to the bandwidth of one a single quadrature channel) [27]. Accordingly, the SNR of the complete quadrature downconversion block (e.g., mixers, filters, variable-gain amplifiers) increases 2 times after quadrature combining [27]. The 3dB net gain in SNR corresponds to halving the noise contribution of quadrature circuits.

Therefore, the noise figure requirement for the quadrature downconverter relaxes 3dB when referred to the output of a quadrature mixer (e.g., the NF requirement for the SC-MO (thus for a single-channel) is 12.7dB, whereas the SSB noise-figure requirement for the mixer in a quadrature configuration is 15.7dB; Table 7.11). For zero-IF operation, only one noise bandwidth contributes to the noise figure (the noise in the band of signal), and therefore the double-side band (DSB) noise figure is considered in this case (which is equal to SSB noise figure after the rejection of the image (noise) band). More detail on the noise performance of the quadrature downconverter is given later in this chapter (Section 7.3.4, interpretation of measurement results).

Before closing the discussion on the selection of the specifications, we will shortly pinpoint the effects of 2<sup>nd</sup>-order intermodulation distortion on the

linearity of the system. As IM2 products fall close to DC, they interfere with the desired signal in zero-IF receivers (together with IM3 products).

However, the distribution of  $IIP2$  to the receiver building blocks is somewhat different from the  $IIP3$  distribution. Namely, the IM3 products lying in the desired signal band pass from an LNA to a mixer, whereas the IM2 products from an LNA are filtered by, for example, a resonating LNA load or AC-coupling between the LNA and mixer. Therefore, the  $IIP2$  specifications of the mixer (or SC-MO in Fig. 7.14) determine this type of distortion for a complete receiver. Typically, a receiver  $IIP2$  in excess of 45dBm would suffice for the standards under consideration (i.e., a SC-MO  $IIP2$  of 58dBm for the assumed LNA gain) [28].

### 7.3.3.1 Mixer Circuit Parameters

The schematic of the double-balanced mixer that is used to implement the quadrature downconverter (SC-MO) is shown in Fig. 7.16 [29].

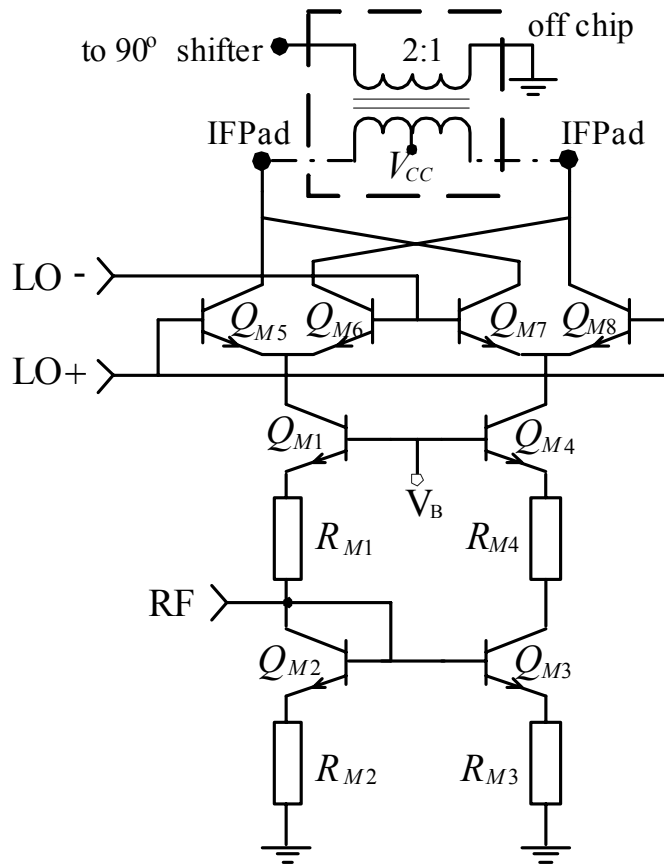


Figure 7.16: Mixer schematic.



The mixer consists of a class-AB input stage ( $Q_{M1-M4}$ ) for improved linearity [30], cascoded by the switching quad  $Q_{M5-M8}$ . The single-ended input is converted into a differential current via common-base stage  $Q_{M1}$  and current mirror  $Q_{M2}$ ,  $Q_{M3}$ . Distortion is further suppressed and the RF input impedance match improved by resistors  $R_{M1}-R_{M4}$ . Transistor  $Q_{M4}$  improves isolation in the input stage and attenuates local oscillator leakage to the RF input.

The transistors and resistors are sized to optimize conversion gain, noise figure, and linearity. For the mixer input stage, transistors  $Q_{M1-M4}$  have a length/width ratio of 40um/0.5um and resistors  $R_{M1-M4}$  are 21 $\Omega$ . For the switching quad, transistors  $Q_{M5-M8}$  have a length/width ratio of 8um/0.5um. The mixer performance parameters can be adaptively adjusted by changing the mixer bias current, which is set by the voltage applied to the bases of  $Q_{M1}$  and  $Q_{M4}$ .

Simulations show that a factor of two reduction in power consumption can be achieved between the moderate and demanding modes of operation for the mixer.

#### 7.3.4 EXPERIMENTAL RESULTS FOR THE MULTI-STANDARD ADAPTIVE RF FRONT-END

The 0.65x1.0mm<sup>2</sup> MSAFE testchip (excluding bondpads), shown in Fig. 7.17, is wirebonded into a 32-pin quad package for testing [31].

A custom printed-circuit board (see Fig. 7.18) with bias and supply line filtering was designed for testing. The differential quadrature IF signals ( $I$  and  $Q$ ) are converted to single-ended form via external transformers with a 2:1 turns ratio, giving an effective mixer load of 200 $\Omega$ . A 50 $\Omega$  quadrature hybrid (70MHz IF) is then used for final IF (intermediate frequency) signal combining.

The VCO performance was characterized using a separate test circuit [1]. Operating from a 3V supply, the adaptive VCO achieves a tuning range of 600MHz, ranging from 1.8GHz to 2.4GHz. A plot of the phase noise measured in the 2.1GHz band is shown in Fig. 7.18. The operating conditions are summarized in Table 7.12.

Table 7.12: Measured multi-standard VCO performance in a 2.1GHz band.

PhaseNoise@1MHz	-123dBc/Hz	-110dBc/Hz	-103dBc/Hz
$I_{TAIL}$ [mA]	6 (D)	1.2 (M)	0.5 (R)

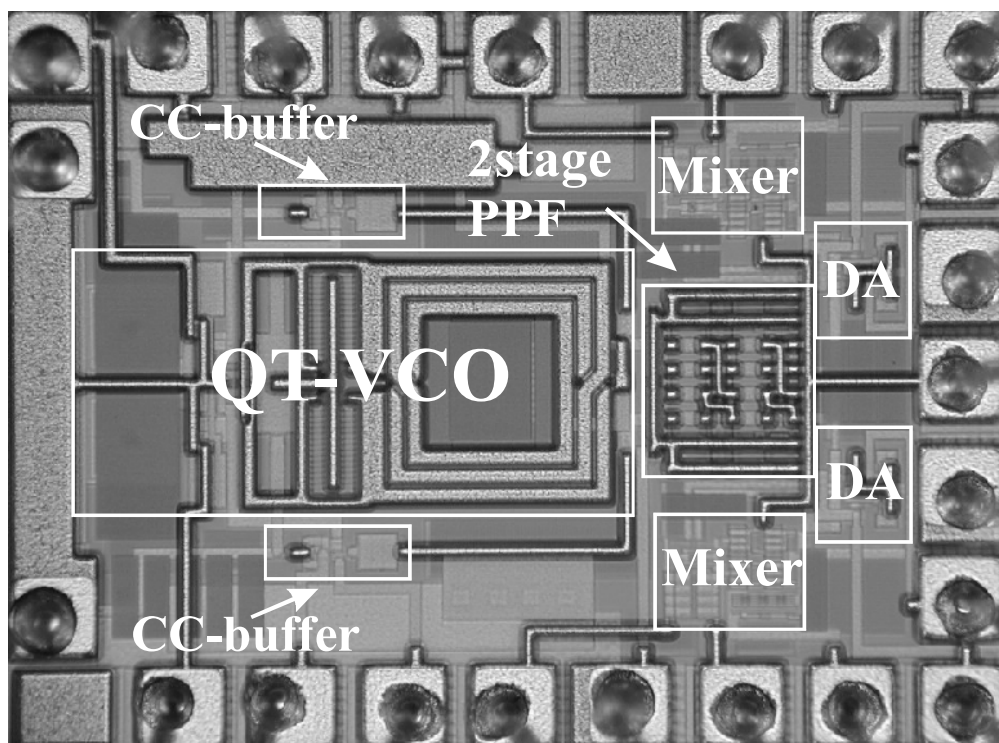


Figure 7.17: MSAFE IC photomicrograph.

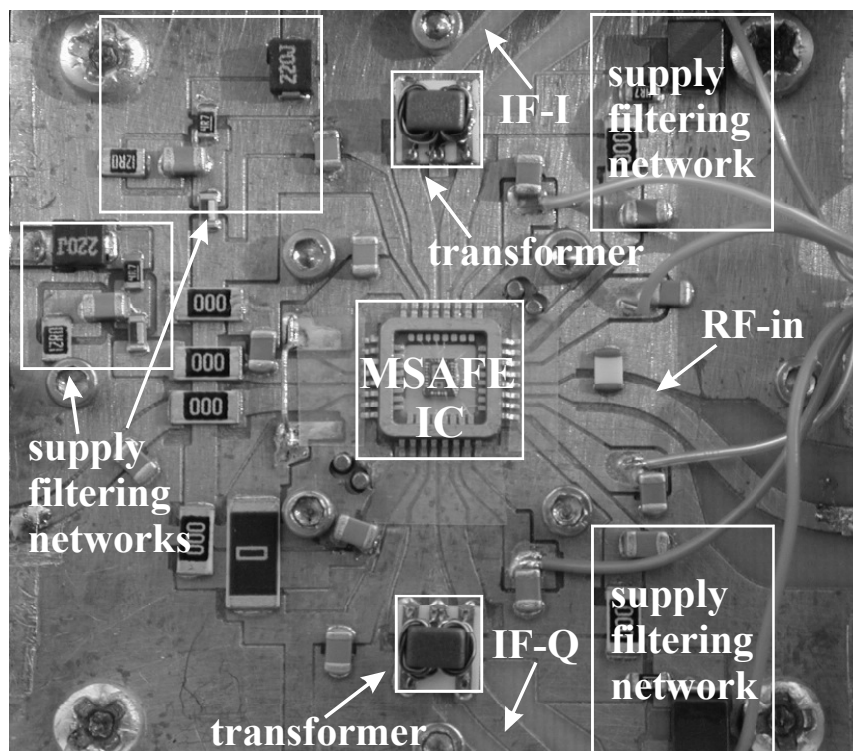


Figure 7.18: Packaged IC on PCB test fixture.

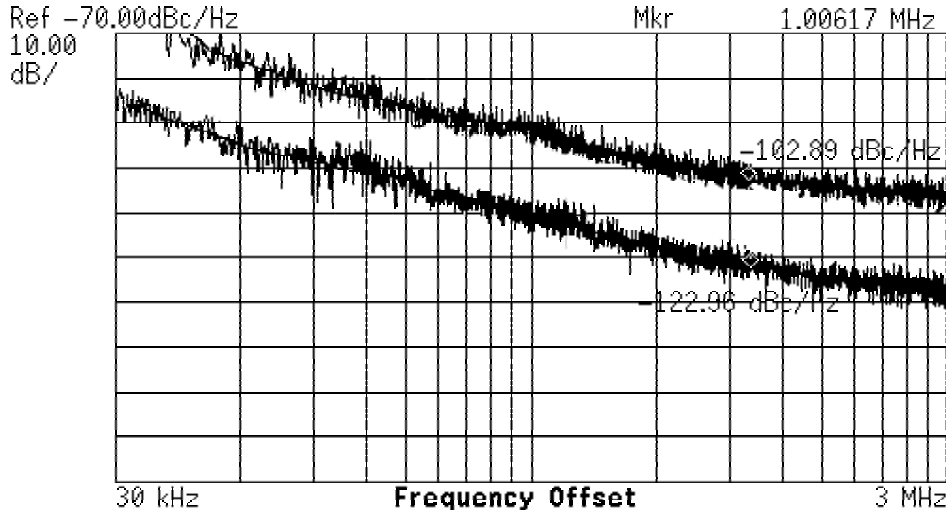


Figure 7.19: Phase noise at 1MHz offset in a 2.1 GHz band.

By adapting the bias tail current between 0.5mA and 6mA, a phase-noise tuning range of 20dB is achieved, which satisfies the requirements of five different standards. In addition, the VCO allows a factor of 12 reduction in power consumption when tuned from the 1.8GHz D-mode to the 2.4GHz R-mode.

After de-embedding the measurement results of the test set-up (Fig. 7.20), the MSAFE performance parameters (i.e., SC-MO in Fig. 7.14) have been determined (as they will be in a complete receiver).

The corresponding test set-up gain parameters (voltage gain and power gain) and noise parameters (noise power) are indicated for each block in Fig. 7.20 [25,27]. The signal voltage is denoted as  $V$ , the signal power as  $P$ , the source noise power as  $N$ , the mixer noise power as  $N_M$  (we assume that I-mixer and Q-mixer noise contributions are equal and uncorrelated),  $BW$  stands for the occupied signal bandwidth, and  $\alpha$  and  $\beta$  for the voltage and power gain from the input to the output of the quadrature mixers, respectively. As a 10dB noise figure of a mixer already corresponds to a  $500\Omega$  equivalent noise resistance, which is much larger than the noise power of a  $50\Omega$  source, we can assume that  $N_M \gg N$ . Note that the linearity parameter ( $IIP3$ ) is not shown in the diagram, as both the signals (1<sup>st</sup>- and 3<sup>rd</sup>-order components) and the gain proceeding mixers scale equally.

Based on the transformations shown in Fig. 7.20, the test set-up performance (power addition), the performance converted to the quadrature mixers in the test set-up and the performance converted to the mixers in the

single-channel representation (i.e., SC-MO) of the receiver (see Section 7.3.3) are compared in Table 7.13.

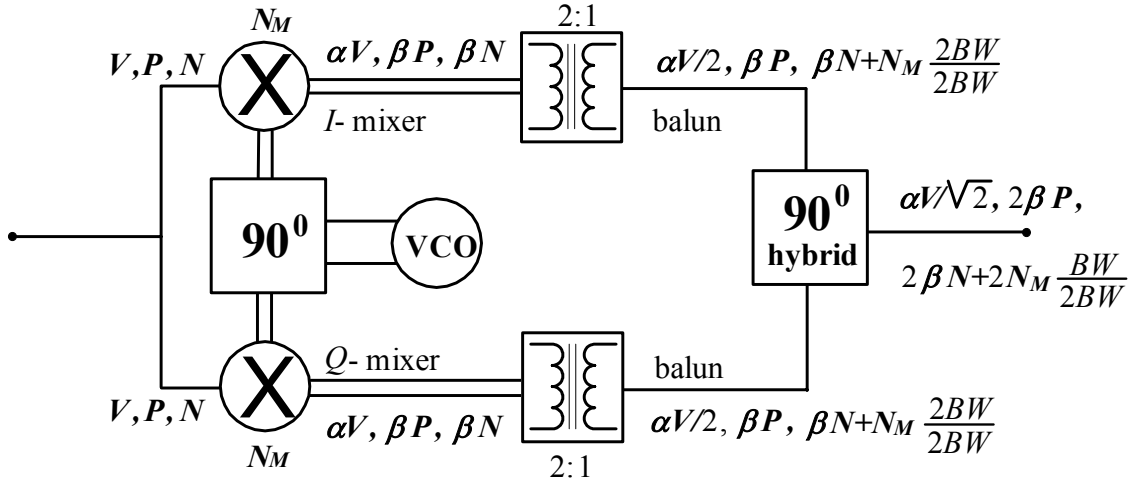


Figure 7.20: Measurement test set-up.

Table 7.13: Test set-up (image reject quadrature downconverter and mixers) vs. SC-MO (quadrature downconverter in Fig. 7.14) performance.

performance parameter	test set-up measurements	mixers in test set-up	SC-MO
$G$ [dB]	$G_M$ [dB]	$G_M - 3$	$G_M - 3$
$VG$ [dB]	$G_M$ [dB]	$G_M - 3$	$G_M - 3$
$NF$ [dB]	$NF_M$ [dB]	$NF_M + 3$	$NF_M$
$IIP3$ [dBm]	$IIP3_M$ [dBm]	$IIP3_M$	$IIP3_M$

The actual image rejection (in the low-IF mode) prior to detection is accounted for in the noise figure result of the quadrature downconverter (SC-MO). However, its gain corresponds to that of a single mixer in the test set-up (not the setup in Fig. 7.20, but the quadrature mixer output drives one of the quadrature baseband circuits in a complete receiver; see Section 7.3.3).  $G_M$  stands for the measured (test set-up) power gain,  $NF_M$  the measured noise figure and  $IIP3_M$  the measured 3<sup>rd</sup>-order input-intercept point of the test set-up ( $VG_M$  stands for the voltage gain from the source of the measurement system).

The noise figure of the SC-MO (the SSB noise figure with the rejection of the image noise band and referred to 50 $\Omega$ ) is 13.9dB (the single signal path,

Fig. 7.14). For zero-IF operation, the noise bandwidth is the same as in the low-IF mode after image (noise) rejection. The reported noise figure for the test set-up (low-IF) is also the noise figure for the zero-IF mode (13.9dB).

The linearity is characterized by an  $IIP3_2$  of 5.5dBm. IIP3 can be traded off for NF, a larger oscillator voltage swing reduces mixer noise figure, but can degrade its linearity, whereas a lower gain of the LNA improves receiver linearity but degrades its noise figure.

The measured  $IIP2_2$ , important for zero-IF operation, is 51dBm. An improvement of around 5dB can be expected after low-frequency baseband filtering [24,25]. Moreover, increasing the amplitude of the applied quadrature VCO signals (at the cost of increased power consumption of the VCO and/or differential amplifiers) improves the 2<sup>nd</sup>-order intermodulation distortion [32].

On-package capacitors on the output signal lines (10pF at each IF output) filter high-frequency output signals, and for the 70MHz IF used in testing, they attenuate the desired signal. Therefore, at the IF of the standards considered (MHz order), the gain of the quadrature blocks is 3dB better and equals -1.6dB. An even larger gain can be achieved if larger mixer load impedance is used (e.g.,  $2 \times 150\Omega$  mixer load in a receiver setup would result into mixer voltage gain of 1.9dB).

The measured image-rejection of 20dB is satisfactory for all standards except DCS-1800 when it employs a low-IF architecture. However, it could be improved if the quadrature combining is implemented on-chip at baseband (or in a digital back-end), or if a 3-stage polyphase filter is implemented for oscillator quadrature signal generation.

Isolation between the oscillator port of the quadrature downconverter and the input (RF) port is 45dB.

The quadrature downconverter consumes 10mA (2 mixers) in the D-mode.

Control of the circuits' bias currents could be realized by additional baseband circuitry.

The *hypothetical* multi-standard receiver has the potential to meet the system specifications in the demanding mode as summarized in Table 7.14 (see Section 7.3.3).

Table 7.14: Hypothetical receiver performance in the demanding mode.

Performance	LNA	SC-MO	BB
$VG$ [dB]	13	1.9 (-1.6)	-
$NF$ [dB]	2	13.9	13 (10)
$IIP3$ [dBm]	1	5.5	11 (8)

Due to relaxed requirements in the 2.4GHz band (R-mode), a considerable power consumption reduction can be realized with sufficient functionality. Table 7.15 indicates to what extent the MSAFE performance can be relaxed while satisfying the required specifications.

The total power consumption of the MSAFE testchip (VCO, 2 mixers and buffers) is varied from standard to standard, as indicated in Table 7.15. By trading power consumption for performance in an adaptive way, this multi-standard adaptive front-end offers more than a factor of 2 reduction in power/current consumption when switched between demanding (D) and relaxed (R) modes of operation.

Table 7.15: MSAFE power consumption in different modes of operation.

<b>MSAFE</b>	<b>DCS1800</b>	<b>WCDMA</b>	<b>WLAN</b>	<b>Bluetooth</b>	<b>DECT</b>
$P_{TOT}$ [mW]	>60.6 (D)	>48.6 (D/M)	<46.2 (M)	<31.2 (R)	<29.7 (R)

## 7.4 CONCLUSIONS

In single-standard applications, adaptivity can be utilized as a power saving mechanism, thereby enhancing the overall RF system performance. In multi-standard applications, sharing functional blocks between different standards using adaptive multi-band/multi-standard circuits offer reduced power consumption and chip area, and may reduce overall cost.

A proof-of-concept 800MHz adaptive voltage-controlled oscillator design has been described in this chapter, allowing for a phase-noise tuning range of 7dB and more than a factor three saving in power consumption.

A 2<sup>nd</sup>/3<sup>rd</sup> generation multi-standard adaptive VCO design - operating in DCS1800, WCDMA and WLAN-Bluetooth-DECT modes - has also been presented. It satisfies the phase-noise requirements of five different standards at 18mW, 3.6mW and 1.5mW power consumption, respectively.

The exploratory 2<sup>nd</sup>/3<sup>rd</sup> adaptive multi-standard front-end test circuit design satisfies the requirements of DCS1800, WCDMA, WLAN, Bluetooth, and DECT standards at current consumption levels of 20.2mA, 16.2mA, 15.4mA, 10.4mA and 9.9mA, respectively.

## REFERENCES

- [1] A. Tasić, W. A. Serdijn and J. R. Long, "Design of Multi-Standard Adaptive Voltage-Controlled Oscillators", *IEEE Transactions on Microwave Theory and Technique*, vol. 53, no. 2, February 2005.
- [2] A. Tasić, W. A. Serdijn and J. R. Long, "800MHz Voltage-Controlled Oscillator with 6dB Phase-Noise Tuning Range", *Proceedings MIEL*, pp. 559-562, May 2004.
- [3] A. Tasić and W. A. Serdijn, "Concept of Phase-Noise Tuning of Bipolar Voltage-Controlled Oscillators", *Proceedings ISCAS*, pp. 161-164, May 2002.
- [4] A. Tasić and W. A. Serdijn, "Effects of Substrate on Phase Noise of Voltage-Controlled Oscillators", *Proceedings ISCAS*, pp. 819-822, May 2002.
- [5] A. Tasić and W. A. Serdijn, "Concept of Frequency-Transconductance Tuning of Bipolar Voltage-Controlled Oscillators", *Proceedings ISCAS*, pp. 555-558, May 2002.
- [6] D. Wang et al., "A Fully Integrated GSM/DCS/PCS Rx VCO with Fast Switching Auto-Band Selection", *Proceedings RAWCON*, pp. , 2002.
- [7] J. Ryynanen, K. Kivekas, J. Jussila, A. Parssinen, K. Halonen, "A Dual-Band RF Front-End for WCDMA and GSM Applications", *Proceedings CICC*, pp. 175-178, May 2000.
- [8] ETSI 300 190 (GSM 05.05 version 5.4.1): *Digital Cellular Communication System (Phase 2), Radio Transmission and Reception*, European Telecommunications Standards Institute, August 1997.
- [9] Third Generation Partnership Project (3GPP), "UE Radio Transmission and Reception (FDD)", Technical Specification, 25.101, vol. 3.0.0, October 1999, <http://www.3gpp.org>.
- [10] IEEE standard 802.11b, "Wireless Local Area Network", 1999, [http://standards.ieee.org/getieee802/download/802.11b-1999\\_Cor1-2001.pdf](http://standards.ieee.org/getieee802/download/802.11b-1999_Cor1-2001.pdf).
- [11] *Specification of the Bluetooth System*, version 1.1, February 2001, <http://www.bluetooth.com>.

- [12] ETSI EN 300 175-2: "Digital Enhanced Cordless Telecommunications (DECT); Common Interface (CI); Part 2: Physical Layer (PHL)", <http://docbox.etsi.org/Reference>.
- [13] A. Tasić, W. A. Serdijn and J. R. Long, "Low-Noise Biasing of Voltage-Controlled Oscillator by Means of Resonant-Inductive Degeneration", *Proceedings ISCAS*, pp. 673-676, May 2003.
- [14] T. S. D. Cheung, J. R. Long et al., "Differentially-Shielded Monolithic Inductors", *Proceedings CICC*, pp. 95-98, September 2003.
- [15] D. M. W. Leenaerts et al., "A 15-mW Fully Integrated I/Q Synthesizer for Bluetooth in 0.18 $\mu$ m CMOS", *IEEE Journal Solid-State Circuits*, vol. 38, no. 7, pp. 1155-1162, July 2003.
- [16] J. O. Plouchart, et al., "3V SiGe differential VCO for 5GHz and 17GHz Wireless Applications", *Proceedings ESCIRC*, 1998.
- [17] M. Soyuer, et al., "An 11GHz 3V SiGe VCO with Integrated Resonators", *Proceedings ISSCC*, pp. 1451-1454, February 1997.
- [18] A. Mostafa et al., "A sub-1V 4GHz VCO and 10.5GHz Oscillator", *Proceedings ESCIRC*, 2000.
- [19] H. Wang, et al., "A 50GHz VCO in 0.25 $\mu$ m CMOS", *Proceedings ISSCC*, pp. 372-373, February 2001.
- [20] D. B. Leeson, "A Simple Model of Feedback Oscillator Noise Spectrum," *Proceedings IEEE*, pp. 329–330, February 1966.
- [21] H. Hashemi et al., "Concurrent Dual-Band LNAs and Receiver Architectures", *Proceedings VLSI*, pp. 247-250, June 2001.
- [22] M. Steyaert et al. "Low-Voltage Low-Power CMOS-RF Transceiver Design", *IEEE Transactions Microwave Theory and Techniques*, vol. 50, no. 1, pp. 281-287, January 2002.
- [23] X. Li and M. Ismail, "Architectures and Specs Help Analysis of Multi-Standard Receivers", <http://www.planetanalog.com/story/OEG20030312S0038>.



- [24] O. K. Jensen et al. "RF Receiver Requirements for 3G W-CDMA Mobile Equipment", *Microwave Journal*, pp. 22-46, February 2000.
- [25] J. Rudell et al. "An Integrated GSM/DECT Receiver: Design Specifications", UCB Electronics Research Laboratory Memorandum, Memo no. UCB/ERL M97/82, 1998.
- [26] A. K-Sanjani, H. Sjoland and A. A. Abidi, "A 2GHz Merged CMOS LNA and Mixer for WCDMA", *Proceedings VLSI*, pp. 19-23, June 2001
- [27] J. Janssens and M. Steyaert, *CMOS Cellular Receiver Front-Ends*, Kluwer Academic Publishers, The Netherlands.
- [28] D. Manstretta et al. "A 0.18 $\mu$ m CMOS Direct-Conversion Receiver Front-End for UMTS", *Proceeding ISSCC*, pp. 240, February 2002.
- [29] B. Gilbert, "The MICROMIXER: A Highly Linear Variant of the Gilbert Mixer Using a Bisymmetric Class-AB Input Stage", *IEEE Journal Solid State Circuits*, vol. 32, no. 9, pp. 1412-1423, September 1997.
- [30] S. T. Lim, "Mixers with Improved Linearity Performance", *Internal Report*, TU Delft, 2004.
- [31] A. Tasić, S. T. Lim, W. A. Serdijn and J. R. Long, "A Multi-Standard Adaptive Image-Reject Downconverter", *Proceedings RFIC*, June 2005.
- [32] D. Manstreta and F. Svelto, "Analysis and Optimization of IIP2 in CMOS Direct Down-Converters", *Proceedings CICC*, pp. 243-247, September 2002.

## CONCLUDING REMARKS

The communication devices of both today and the future will have not only to allow for a variety of applications, ranging from simple characters, via speech, audio, and graphics to video, but they will also have to maintain connection with many other devices rather than with a single base station, in a variety of environments. Extension of capabilities of wearable and wireless devices depends critically on battery endurance, as batteries continue to determine both the lifetime and size of mobile equipment.

The combination of huge functionality requirements on the one hand and a small energy supply on the other argues for the development of both *adaptive low-power hardware* and adaptive low-power software. Simply, as consumers' demands outstrip the cost benefits achieved by Moore's Law and low-power RF design, further improvements can be found in *adaptivity*. This eventually leads to even smaller sizes, longer standby and active times and enhanced functionality of mobile devices.

To support telecom trends such as provision of various services from different standards (text, audio, video, telephony), smooth migration towards future generation of wireless standards with higher capacities and higher data-rates for multimedia applications, and device wearability, *integrated* designs are required that can operate across *multiple standards* within *one device*. By sharing building blocks, *adaptive multi-standard low-power RF front-ends* gain advantage over their predecessors: they use a smaller chip area, consume less power, and have a potential for lower overall cost.

### 8.1 SUMMARY

RF-design phenomena have been investigated both at the level of RF-system design and RF-circuit design. In the remainder of this section, an overview of the results achieved is given.

### **8.1.1 INTRODUCTION**

The thesis “case” has been made in Chapter 1. “Why adaptive, why multi-standard, and why low-power RF design?” is a corner-stone question of the thesis, encompassing various issues relevant to RF design. Many system and circuit level design challenges related to the “case” have been systematically treated throughout the thesis.

### **8.1.2 RF CIRCUIT PERFORMANCE PARAMETERS**

A number of definitions essential to RF design have been outlined in Chapter 2. Gain, nonlinearity and noise parameters have been revisited, followed with a discussion on the dynamic range and over-all performance of RF systems.

### **8.1.3 SPECTRUM-SIGNAL TRANSFORMATION**

Combining complex signal processing techniques with signal and spectral presentations allows designers to both characterize and understand various phenomena related to RF front-ends.

An all-encompassing spectral analysis method in the form of a spectrum-signal transformation has been introduced in Chapter 3, addressing the issue of consistent presentation of transformation of signals and their spectra in the receive path of an RF front-end.

Mixer-oscillator models have been defined, offering a full interpretation of how both signals and spectra are transformed from the input to the output of different receiver topologies.

Finally, the application of mixer-oscillator models has been extended for the calculation of image-rejection ratio in quadrature downconverters.

### **8.1.4 SELECTION OF PERFORMANCE PARAMETERS FOR RF FRONT-END CIRCUITS**

In Chapter 4, a procedure for allocation of the performance parameters to RF front-end circuits has been proposed. By optimizing the system performance with respect to the ratio  $F/P_{IIP3}$  (the noise factor over the input-referred 3<sup>rd</sup>-order power intercept point), an optimal dynamic range design point has been determined, satisfying both the noise and the linearity requirements of the system.

It has been shown that there exists an equilibrium design point for which the contributions of each block performance parameter to the equivalent system performance parameter are equal. Furthermore, the equilibrium design point coincides with both design point for the optimal dynamic range and design point for the equal improvement of noise and linearity performance with respect to the requirements. Finally, some design trade-offs in a single RF front-end circuit are outlined using the K-rail diagram. Referring not only to one, but rather to a set of operating conditions and a set of design points, these diagrams describe relationships and trade-offs between performance parameters of RF circuits.

### **8.1.5 ADAPTIVITY OF LOW-NOISE AMPLIFIERS**

Chapter 5 discusses adaptivity phenomena of low-noise amplifiers. Adaptivity figures of merit (i.e., tuning ranges) have been introduced, viz., input-resistance tuning range, voltage-gain tuning range, noise-figure tuning range, and tuning range of input-referred 3<sup>rd</sup>-order intercept point. These figures have illustrated how low-noise amplifiers can trade performance for power consumption in an adaptive manner. Amplifier K-rail diagrams have been used to describe conceptually design trade-offs in low-noise amplifiers.

### **8.1.6 ADAPTIVE VOLTAGE-CONTROLLED OSCILLATORS**

A concept of design for adaptivity of oscillators has been outlined in Chapter 6. It establishes a procedure for performance characterization of adaptive oscillators with qualitative and quantitative descriptions of the relationships and trade-offs between oscillator performance parameters.

The concept of phase-noise tuning has been introduced, explaining how oscillators can trade performance for power consumption in an adaptive way. The extremes of the phase-noise tuning range and the achievable power consumption reduction have been shown.

The concept of frequency-transconductance tuning has been further elaborated on. The derived analytical expressions show how this concept can be employed in order to achieve control over the operation of the oscillator that is being changed because of the frequency tuning.

Conceptual K-rail diagrams have been used for the characterization of the oscillator performance. It has been shown how K-rail diagrams can be used for interpreting various phenomena and various adaptivity figures of merit of oscillators. Trade-offs between oscillator parameters, such as voltage swing,

LC-tank conductance, power consumption, phase noise and loop gain, have been both qualitatively and quantitatively described using K-rail diagrams.

### **8.1.7 DESIGN OF ADAPTIVE VOLTAGE-CONTROLLED OSCILLATORS AND ADAPTIVE RF FRONT-ENDS**

In single-standard applications, adaptivity can be utilized as a *power saving mechanism*, thereby enhancing the overall RF system performance. By sharing functional blocks between different standards, adaptive circuits for multi-band/multi-standard applications offer reduced power consumption, smaller chip area and may reduce overall cost. Chapter 7 has illustrated these issues with two oscillator IC designs and an RF front-end design.

A proof-of-concept 800MHz adaptive voltage-controlled oscillator design has been described. For a phase-noise tuning range of 7dB, more than a factor three saving in power consumption has been achieved.

In addition, a 2<sup>nd</sup>-generation/3<sup>rd</sup>-generation multi-standard adaptive voltage-controlled oscillator design has also been presented, operating in DCS1800, WCDMA and WLAN-Bluetooth-DECT modes. It satisfies the phase-noise requirements of five different standards at 18mW, 3.6mW and 1.5mW power consumption, respectively.

Finally, an exploratory 2<sup>nd</sup>-generation/3<sup>rd</sup>-generation adaptive multi-standard front-end test circuit design has been presented. The design satisfies the requirements of DCS1800, WCDMA, WLAN, Bluetooth, and DECT standards at current consumption levels of 20.2mA, 16.2mA, 15.4mA, 10.4mA and 9.9mA, respectively.

## REAL-TO-COMPLEX-TO-REAL TRANSFORMATION

An application of the introduced SC-MO models is found in the Weaver architecture [1] shown in Fig. A.1a. Using two SC-MO models, this topology can be presented by Fig. A.1b. Here both conversions take place, i.e., a real-to-complex and a complex-to-real conversion with the corresponding SC-MO models.

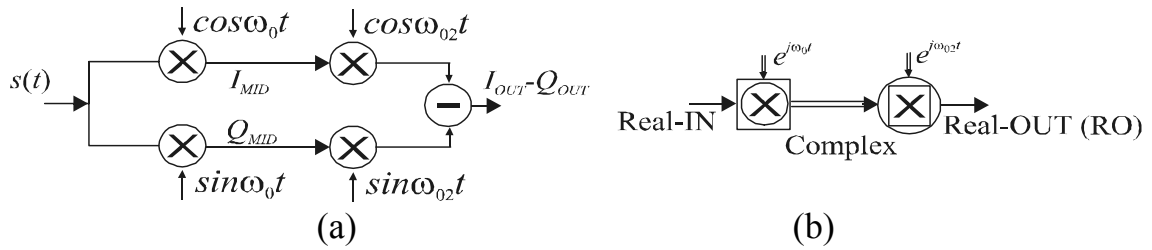


Figure A.1: (a) The Weaver architecture, (b) mixer-oscillator model.

Applying the SC-MO SS presentation models, the input real signal is downconverted first into a complex signal and then back into a real signal, as shown in Fig. A.2. The final SS form is a complex presentation of the real output signal. As expected, the desired signal component can be successfully detected from the downconverted signal ( $A-jB$ ).

The validity of the SC-MO models will be examined by performing the conversion using SR-MO models according to the scheme that is shown in Fig. A.1a.

First, the real input signal  $s(t)$  (Fig. 3.9) is converted by the LO signal (Fig. 3.10) into two real signal ( $I_{MID}$  and  $Q_{MID}$ ) as shown in Figs. 3.11 and 3.12 as well as Figs. A.3a and A.3b (SS presentation).

The SS form of  $I$  and  $Q$  signals ( $I_{OUT}$  and  $Q_{OUT}$ ) after the second down-conversion with SR-MO, but before the summation is shown in Fig. A.3.

Finally, combining the signals  $I_{OUT}$  and  $Q_{OUT}$  (their contents) from Fig. A.3, the finally downconverted signal has the SS form as given in Fig. A.4.

As the obtained result (the signal content is  $(A-jB)/2$  in Fig. A.4) is the same as the result shown in Fig. A.2 (the signal content is  $(A-jB)/2$ ), the validity of the introduced SC-MO models is proved.

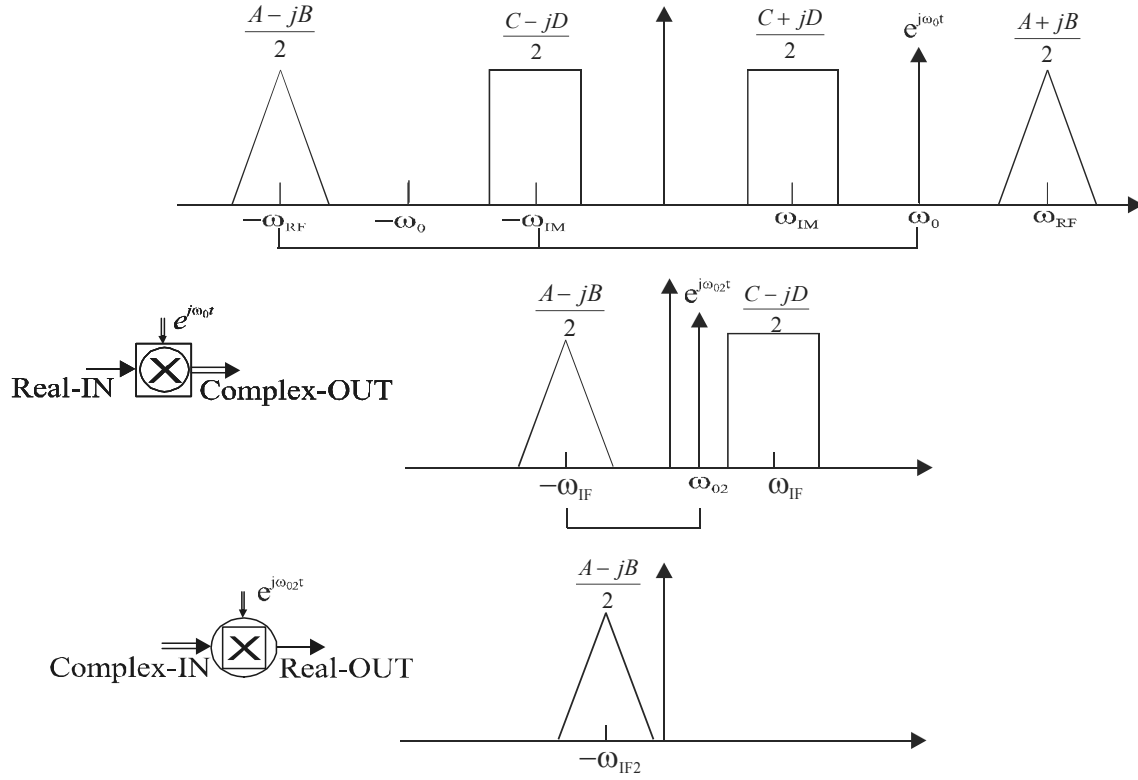
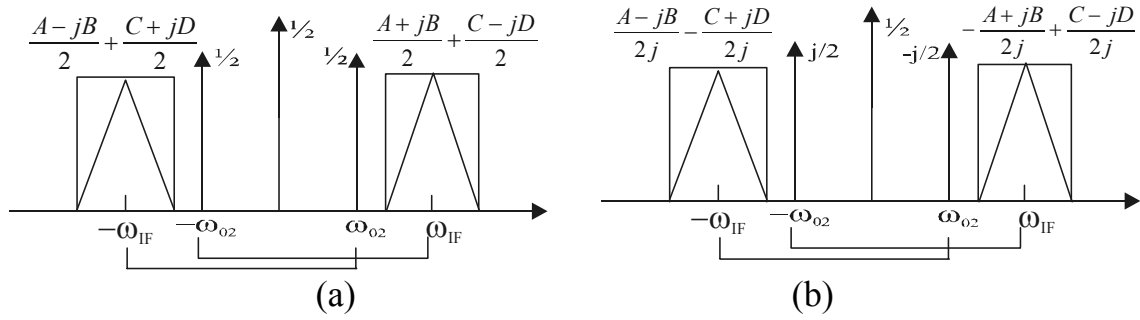


Figure A.2: SS transformation for the Weaver architecture.

Figure A.3: Spectrum-signal form after the first downconversion (Fig. 3.27)  
a)  $I_{MID}$  path, b)  $Q_{MID}$  path.

Finally, the content of the output real signal shown in Fig. A.5 is:

$$RO = \frac{A-jB}{4} e^{-j\omega_{IF2}t} + \frac{A+jB}{4} e^{j\omega_{IF2}t}, \quad (A.1)$$

$$RO = \frac{A}{2} \cos \omega_{IF2} t - \frac{B}{2} \sin \omega_{IF2} t, \quad (A.2)$$

where  $\omega_{IF2}$  is the final intermediate angular frequency. As can be seen from Eq. (A.2), only the desired signal is obtained while the image signal is rejected, as expected from the Weaver architecture.

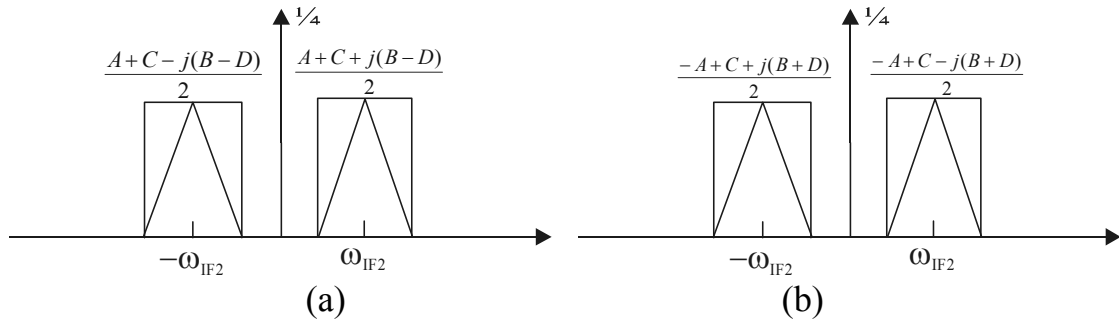


Figure A.4: Spectrum-signal form after the second downconversion  
a)  $I_{OUT}$  path, b)  $Q_{OUT}$  path.

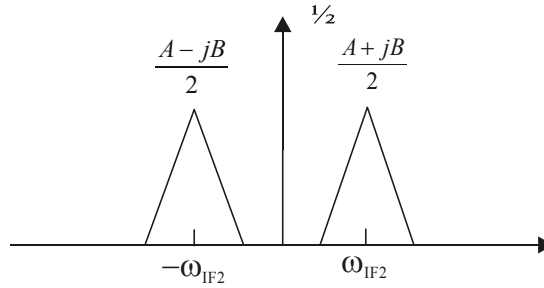


Figure A.5:  $I_{OUT} - Q_{OUT} = I_{OUT} + j(j Q_{OUT})$ .

## REFERENCES

- [1] D. Weaver, Jr., "A Third Method of Generation and Detection of Single-Sideband Signals", *Proceedings of the IRE*, pp. 1703-1705, June 1956.



## TRANSFORMER-FEEDBACK DEGENERATION OF LOW-NOISE AMPLIFIERS

The technique of transformer-feedback degeneration (TFD) is described, offering the possibility for low-noise amplifiers to achieve matching of both the real and the imaginary part of the input impedance in an orthogonal way [1]. The schematic (model) of a transformer-feedback degenerated low-noise amplifier is shown in Fig. B.1 (without a complete bias scheme).

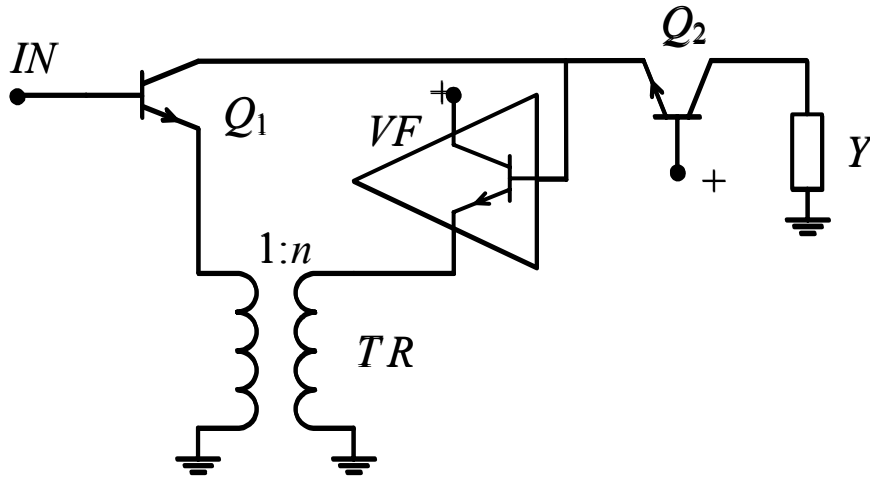


Figure B.1: A Model of a transformer-feedback degenerated LNA.

This amplifier topology is a traditional cascode configuration, with the addition of the feedback around the input transistor, which is realized by means of a voltage-follower (VF) (e.g., a single transistor in a common-collector configuration) and a transformer TR (orientation of the transformer is not shown; either negative or positive coupling is realized).

Controlling the amount of feedback, the TFD-LNA achieves orthogonal match of input impedance to source impedance. What is more, the power match is rather independent of the transistor transit frequency ( $f_T$ ), accordingly allowing for the matching even at very high  $f_T$ s [2].

In the remainder of this appendix, we will derive input-impedance and power-matching models for a TFD-LNA.

### B.1 INPUT-IMPEDANCE MODEL FOR TRANSFORMER-FEEDBACK DEGENERATED LOW-NOISE AMPLIFIERS

The input circuit of the TFD-LNA is shown in Fig. 6.2, where for the TFD topology,  $Y_E$  stands for the equivalent admittance seen at the emitter of transistor  $Q_1$ .

The equivalent circuit of the transformer-feedback degenerated LNA that is used for the calculation of the feedback function  $f$ , with a simplified transformer model [3,4], is shown in Fig. B.2:  $L_1$  and  $L_2$  are the transformer primary and secondary inductors,  $n$  is the transformer turn ratio, and  $k$  the coupling factor between the transformer inductors.

As the primary and the secondary inductors of the transformer  $TR$  are by definition related as  $L_2/L_1 = n^2/k^2$ , it is straightforward to calculate the voltage transfer function from node  $V_1$  to node  $V_3$ , and subsequently derive the function  $f(Y_1, Y_2)$  as:

$$f(Y_1, Y_2) = \frac{Y_1 + n^2 Y_2}{Y_{II} + Y_1 + n^2 Y_2 + g_m(1 \pm n Y_2 / Y_L)}, \quad (\text{B.1})$$

with  $Y_1 = 1/sL_1$  and  $Y_2 = 1/s(1-k^2)L_2$ .

Depending on the orientation of the transformer, the feedback can be either negative or positive, which is the origin of the  $\pm$  sign in Eq. (B.1). Note that the properties of the function  $f(Y_1, Y_2)$  depend on the transformer parameters.

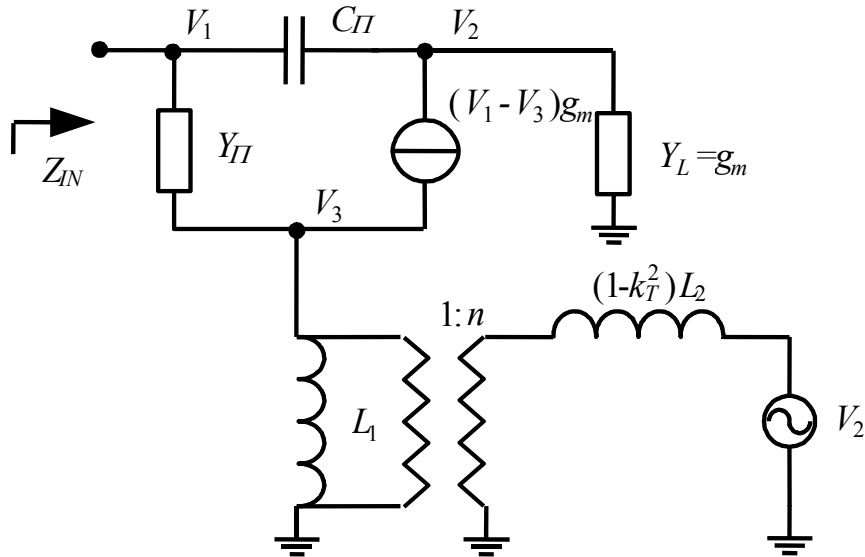


Figure B.2: Detailed schematic of a TFD-LNA.

With the aid of Eqs. (6.1) and (B.1), the input impedance  $Z_{IN}=1/Y_{IN}$  (with the condition  $C_\mu=0$ ) becomes:

$$Z_{IN}|_{C_\mu=0} = R + j \left[ \frac{\omega}{\omega_T} R \pm \frac{\omega_T}{\omega} \frac{k^2}{n} \frac{1}{g_m} - \frac{\omega_T}{\omega} \frac{1}{g_m} \right]. \quad (B.2)$$

$R=\omega_T(1-k^2)L_1$  stands for the real part of the input impedance, with  $\omega_T=2\pi f_T$  and  $\omega=2\pi f$  being the angular transit and desired signal frequencies.

A circuit equivalent of Eq. (B.2) is shown in Fig. B.3: Fig B.3a for a positive feedback, and Fig. B.3b for a negative feedback.

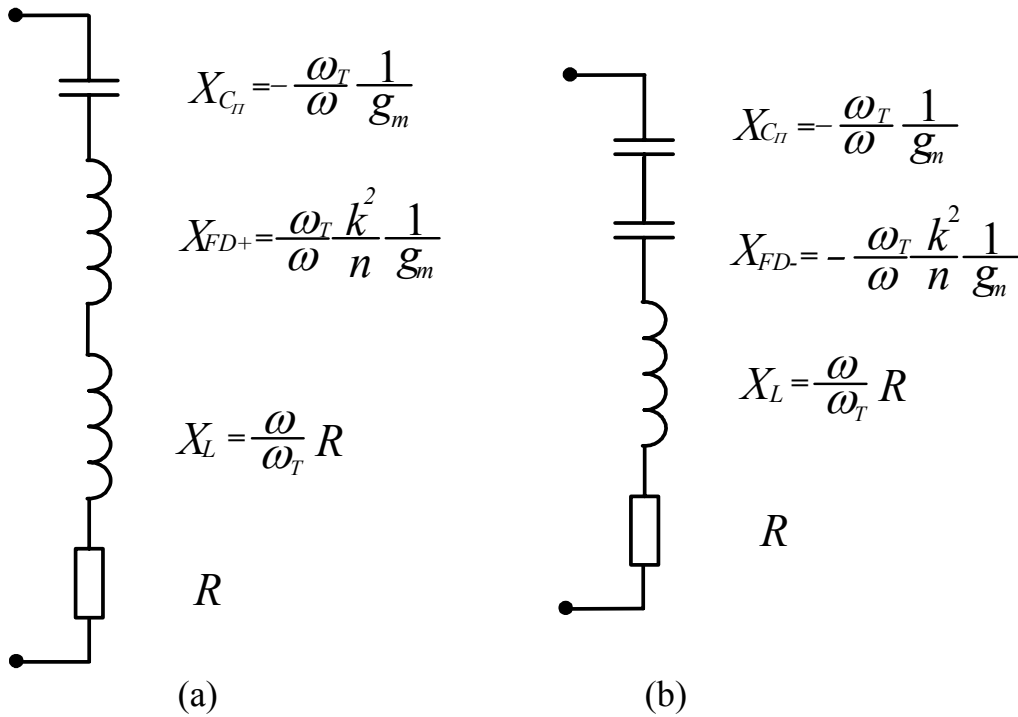


Figure B.3: Input impedance for  $C_\mu = 0$   
(a) a positive feedback model, (b) a negative feedback model.

Fig. B.3 shows that the effect of the transformer feedback is the additional reactance at the input of the TFD-LNA, i.e., a capacitance in case of negative feedback and an inductance in case of positive feedback.

We will calculate loop gain of the TFD-LNA to examine its stability (this topology employs a positive feedback for an additional feedback inductance ( $X_{FD}$  in Fig. B.3a). In order to evaluate the loop gain of the TFD-LNA, shown

in Fig. B.1, we will refer to the detailed schematic of Fig. B.2, with a difference of a source resistance  $R_S$  added at the input and the voltage-controlled current source  $g_m V_{BE}$  replaced with a uncontrolled current source  $I$ .

The loop gain can be determined from the transfer function between the current source  $I$  and the base emitter voltage  $V_{BE}$ . For the “critical” positive feedback, the loop gain (modulus squared) is calculated as:

$$|LG|^2 = \left| \frac{g_m V_{BE}}{I} \right|^2 = \frac{(k/n)^2 + (g_m R \omega / \omega_T)^2}{1 + (g_m R \omega / \omega_T)^2}. \quad (\text{B.3})$$

As for safe operation of the amplifier its loop gain should be below one, this condition reduces to:

$$k^2 / n < 1, \quad (\text{B.4})$$

which indicates that for stable amplifier operation, the transformer turn ratio should be larger than the square of the coupling coefficient  $k$ .

## B.2 POWER-MATCHING CONDITION FOR TRANSFORMER-FEEDBACK DEGENERATED LOW-NOISE AMPLIFIERS

With the aid of the input-impedance model for a slightly positive feedback (Fig. B.3b), the equivalent input circuit of the amplifier can be shown as depicted by Fig. B.4, where  $R_S$  is the impedance of the source (e.g., antenna).

The condition for the match of the real part of the input impedance to the source impedance is derived from Eq. (B.2) as:

$$\omega_T (1 - k^2) L_1 = R_S. \quad (\text{B.5})$$

The impedance match is possible even at high  $f_{TS}$  for a moderate value of primary inductance  $L_1$  (with a larger coupling coefficient  $k$ ).

On the other hand, setting the imaginary part of the input impedance to zero is facilitated, simply because the feedback-resulting inductance  $L_{FD}$  (Fig. B.3a and Eq. (B.6)) enables the cancellation of the transistor's reactive part, i.e., the capacitance  $C_{\Pi}$ .

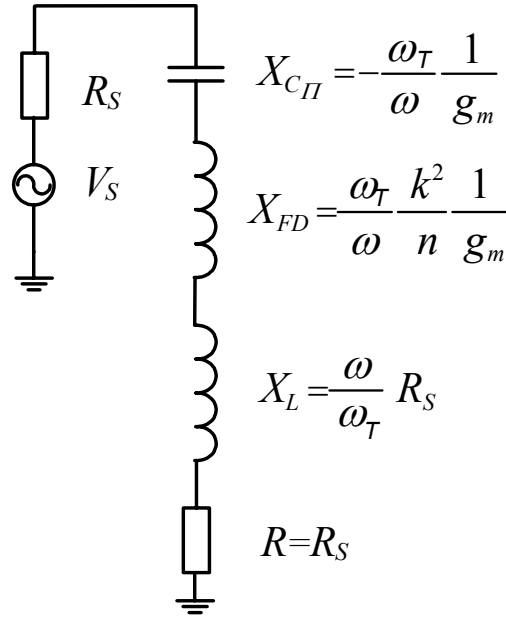


Figure B.4: Antenna and input-impedance models of a TFD-LNA.

$$L_{FD} = \frac{\omega_T}{\omega} \frac{k_T^2}{n} \frac{1}{g_m} \quad (\text{B.6})$$

The matching condition is derived from Eq. (B.2), by setting the imaginary part to zero:

$$\frac{k^2}{n} = g_m \left[ \frac{1}{g_m} - \left( \frac{\omega}{\omega_T} \right)^2 R_S \right] \quad (\text{B.7})$$

This condition implies that the stability criterion (Eq. (B.4)) is not violated. What is more, a small input bond-wire inductance, relaxes the loop-gain constraint to the extent that inherent stability is achieved.

For example, for a  $50\Omega$  input impedance match, using technology with  $f_T=100\text{GHz}$ , an inductance of  $0.075\text{nH}$  is required for an ID-LNA, whereas in case of a TFD-LNA with a transformer's coupling coefficient  $k=0.9$ , a primary inductance of  $0.39\text{nH}$  is required.

### B.2.1 Transformer Power-Matching Model

Another property of the proposed topology is the *orthogonal match* of real and imaginary parts of input impedance to source impedance. As indicated by Eq. (B.5), by choosing a certain value for the coupling factor  $k$  and the primary inductance of the transformer  $L_1$ , the real part of the impedance is matched. On the other hand, by choosing the right value for the transformer turn ratio  $n$ , according to Eq. (B.7), the imaginary part is set to zero (for the power match to a real source impedance).

The matching conditions (Eqs. (B.5) and (B.7)) can be translated into a transformer-parametric model that is shown in Fig. B.5, where model parameters  $E$  and  $D$  are expressed as:

$$E = \frac{R_S}{\omega_T}, \quad (\text{B.8})$$

and

$$D = 1 - g_m R_S \left( \frac{\omega}{\omega_T} \right)^2. \quad (\text{B.9})$$

This transformer model is suitable for simulation (design) purposes, where the real part of the input impedance is controlled by the parameter  $E$ , and the imaginary part depends on the parameter  $D$ .

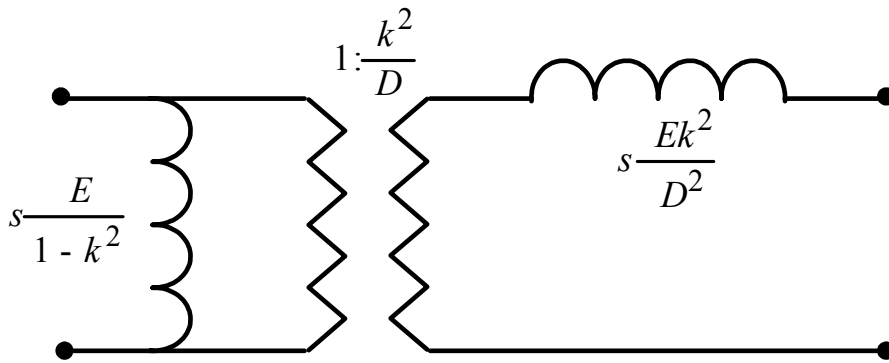


Figure B.5: Transformer power-matching model ( $s=j\omega$ ).

A favorable property of the transformer-feedback degeneration is that once the values for  $E$  and  $D$  are properly chosen, amplifier matching becomes

independent of the coupling coefficient  $k$ . Namely, from the model shown in Fig. B.5, the choice of  $k$  determines only the primary and secondary inductance values. Only if  $k=0$ , i.e., there is no coupling, the transformer-feedback degeneration reduces to the inductive degeneration.

The drawn conclusions are examined with an example.

**Example B.1:**

The operating conditions for the TFD-LNA are: a transition frequency  $f_T=24\text{GHz}$ , a frequency of operation  $f=2.4\text{GHz}$  and a collector current  $I_C=7\text{mA}$ .

With the aid of Eqs. (B.5) and (B.7), the corresponding  $50\Omega$  matching parameters are given by Table B.1.

Table B.1: Parameters of the power-matched TFD-LNA.

LNA \ parameter	$k$	$E [e-9]$	$D$	$L_1 [\text{nH}]$	$L_2 [\text{nH}]$	$n$
TFD1	0.9	0.33	0.86	1.74	1.9	0.95
TFD2	0.7	0.33	0.86	0.66	0.47	0.6
TFD3	0.5	0.33	0.86	0.44	0.16	0.3

The results show that in the case of the transformer degeneration, power matching is possible not only for one, but for a number of different transformer's parameters values. In addition, the parameters  $E$  and  $D$  of the transformer power-matching model (Fig. B.5) are indeed constant and the final choice of a primary and a secondary inductance of a transformer depends only on the factor  $k$ .

## REFERENCES

- [1] A. Tasić, W. A. Serdijn and J. R. Long, "Transformer-Feedback Degeneration of Low-Noise Amplifiers", *Proceedings ISCAS*, pp. 421-424, May 2003.
- [2] A. Tasić, W. A. Serdijn and J. R. Long, "Matching of Low-Noise Amplifiers at High Frequencies", *Proceedings ISCAS*, pp. 321-324, May 2003.

- [3] J. R. Long, "Monolithic Transformers for Si RF IC Design", *IEEE Journal Solid State Circuits*, vol. 35, no. 9, pp. 1368-1382, September 2000.
- [4] K. van Hartingsveldt et al., "High Frequency Low-Noise Amplifiers with Integrated Transformer Feedback", *Proceedings ISCAS*, pp. 815-818, May 2002.



# LIST OF PUBLICATIONS

## **Journal Publications:**

A. Tasić, W. A. Serdijn and J. R. Long: “Design of Multi-Standard Adaptive Voltage-Controlled Oscillators”, *IEEE Transactions on Microwave Technology and Technique*, vol. 2, no. 53. February 2005.

A. Tasić, W. A. Serdijn and J. R. Long: “Adaptivity of Voltage-Controlled Oscillators – Theory and Design”, *IEEE Transactions on Circuits and Systems - Part I*, accepted for publication, 2005.

A. Tasić, W. A. Serdijn and J. R. Long: “Multi-Standard Adaptive Circuits for Wireless Communications”, *Circuits and Systems Magazine*, invited for Special Issue on Software-Defined Radio, 2005.

## **Conference Publications:**

A. Tasić, S. T. Lim, W. A. Serdijn and J. R. Long: “A Multi-Standard Adaptive Image-Reject Downconverter”, accepted for *IEEE Radio Frequency Integrated Circuits Symposium*, Long Beach, USA, June 2005.

A. Tasić, W. A. Serdijn, J. R. Long and A. R-Vazquez: “Multi-Standard Adaptive Circuits and Systems for Wireless Communications”, accepted for Tutorial at *IEEE International Symposium on Circuits and Systems*, Kobe, Japan, May 2005.

A. Tasić, W. A. Serdijn and J. R. Long: “Multi-Standard Adaptive Voltage-Controlled Oscillator”, *Proceedings IEEE Radio Frequency Integrated Circuits Symposium*, Fort Worth, USA, June 2004.

A. Tasić, W. A. Serdijn and J. R. Long: “Optimal Distribution of Specifications to RF Front-End Circuit Blocks”, *IEEE International Symposium on Circuits and Systems*, Vancouver, Canada, May 2004.

**A. Tasić**, W. A. Serdijn and J. R. Long: “DCS1800/WCDMA Voltage-Controlled Oscillator”, *Proceedings IEEE International Symposium on Circuits and Systems*, Vancouver, Canada, May 2004.

**A. Tasić**, W. A. Serdijn and J. R. Long: “800MHz VCO with 6dB Phase-Noise Tuning Range”, *Proceedings MIEL*, Nis, Serbia, May 2004.

**A. Tasić**, W. A. Serdijn and J. R. Long, “Concept of Noise-Figure Tuning of Bipolar Low-Noise Amplifiers”, *Proceedings ECCTD*, Krakow, Poland, September 2003.

**A. Tasić**, W. A. Serdijn and J. R. Long: “Matching of Low-Noise Amplifiers at High Frequencies”, *Proceedings IEEE International Symposium on Circuits and Systems*, Bangkok, Thailand, May 2003.

**A. Tasić**, W. A. Serdijn and J. R. Long, “Low-Noise Biasing of Voltage-Controlled Oscillators by means of Resonant Inductive Degeneration”, *Proceedings IEEE International Symposium on Circuits and Systems*, Bangkok, Thailand, May 2003.

**A. Tasić**, W. A. Serdijn and J. R. Long: “Adaptivity Figures of Merit and K-rail Diagrams - Comprehensive Performance Characterization of Low-Noise Amplifiers and Voltage-Controlled Oscillators”, *Proceedings IEEE International Symposium on Circuits and Systems*, Bangkok, Thailand, May 2003.

**A. Tasić**, W. A. Serdijn and J. R. Long, “Concept of Transformer-Feedback Degeneration of Low-Noise Amplifiers”, *Proceedings IEEE International Symposium on Circuits and Systems*, Bangkok, Thailand, May 2003.

**A. Tasić** and W. A. Serdijn:” Concept of Quasi-Capacitive Tapping of Bipolar Voltage-Controlled Oscillators”, *Proceedings IEEE International Conference of Electronics Circuits and Systems*, Dubrovnik, Croatia, September 2002.

**A. Tasić** and W. A. Serdijn, “K-rail Diagrams - Comprehensive Tool for Full Performance Characterization of Voltage-Controlled Oscillators”, *Proceedings IEEE International Conference of Electronics Circuits and Systems*, Dubrovnik, Croatia, September 2002.

**A. Tasić** and W. A. Serdijn, “Effects of Substrate on Phase Noise of Bipolar Voltage- Controlled Oscillators”, *Proceedings IEEE International Symposium on Circuits and Systems*, Phoenix, USA, May 2002.

**A. Tasić** and W. A. Serdijn, “Concept of Frequency-Transconductance Tuning of Bipolar Voltage-Controlled Oscillators”, *Proceedings IEEE International Symposium on Circuits and Systems*, Phoenix, USA, May 2002.

**A. Tasić** and W. A. Serdijn: “Concept of Phase-Noise Tuning of Bipolar Voltage-Controlled Oscillators”, *Proceedings IEEE International Symposium on Circuits and Systems*, Phoenix, USA, May 2002.

**A. Tasić** and W. A. Serdijn: “Concept of Spectrum-Signal Transformation”, *Proceedings IEEE International Symposium on Circuits and Systems*, Phoenix, USA, May 2002.

# CONCLUSIES

De communicatiemiddelen van vandaag en de toekomst zullen niet alleen een verscheidenheid aan toepassingen mogelijk moeten maken, variërend van simpele karakters, spraak, audio en grafische voorstellingen tot video, maar ze zullen eveneens in verbinding moeten staan met een groot aantal andere apparaten in plaats van alleen met een enkel basisstation, in een verscheidenheid aan omgevingen. Uitbreiding van de functionaliteiten van mobiele en draadloze apparaten is afhankelijk van het uithoudingsvermogen van de batterijautonomie, omdat de batterij nog steeds bepalend is voor zowel de levensduur als de afmetingen van mobiele apparatuur.

De combinatie van toenemende functionaliteit enerzijds en een beperkte energievoorraad anderzijds (bijv. werking op batterijen) pleit voor de ontwikkeling van zowel adaptieve laagvermogenhardware als -software. Simpel gezegd, omdat de wensen van de consument uitstijgen boven het kostenvoordeel dat voortkomt uit Moore's Law en laagvermogen RF ontwerp, kunnen verdere verbeteringen worden gevonden door het aanwenden van adaptiviteit. Dit zal uiteindelijk leiden tot mobiele apparatuur met nog kleinere afmetingen, nog langere standby- en gebruikstijden en verbeterde functionaliteit.

Om trends in telecommunicatie te ondersteunen zoals het leveren van velerlei diensten met verschillende standaarden (tekst, audio, video, telefonie), evenals een vloeiende overgang naar de volgende generatie draadloze standaarden met een hogere capaciteit en hogere datasnelheden voor multimediale toepassingen, en draagbaarheid van het apparaat, zijn geïntegreerde ontwerpen nodig die met meerdere standaards in één apparaat kunnen werken. Omdat ze bouwstenen delen, hebben adaptieve multi-standaard laagvermogen RF front-ends een aantal voordelen ten opzichte van hun voorgangers: ze verbruiken minder vermogen, beslaan een kleiner chipoppervlak en bieden bovenal de mogelijkheid om de totale kosten te reduceren.

## **SAMENVATTING**

Verschillende aspecten van RF-ontwerp zijn onderzocht op zowel het niveau van het gehele systeem als dat van de circuits. In de rest van dit hoofdstuk wordt een overzicht van de behaalde resultaten gegeven.

## **INLEIDING**

De probleemstelling van dit proefschrift is beschreven in Hoofdstuk 1. “Waarom multi-standaard laagvermogen RF ontwerp?” is de hoofdvraag van dit proefschrift, welke verschillende relevante punten van RF ontwerp behelst. Veel uitdagingen op het niveau van het ontwerp van systemen en circuits zijn systematisch behandeld in dit proefschrift.

## **FUNCTIONELE PARAMETERS VAN RF- SCHAKELINGEN**

De definities die belangrijk zijn voor RF ontwerp zijn gegeven in Hoofdstuk 2. Parameters van versterking, nietlineariteit en ruis zijn opnieuw behandeld, gevolgd door een discussie over het dynamische bereik en de werking van RF systemen.

## **SPECTRAAL-SIGNAAL TRANSFORMATIE**

Het combineren van complexe signaalbewerkingstechnieken met de presentatie van signalen en spectra biedt mogelijkheden om verschillende verschijnselen met betrekking tot RF front-ends te karakteriseren en begrijpen.

Een alomvattende methode voor de spectraal-analyse in het vorm van de spectraal-signaal transformatie is geïntroduceerd in Hoofdstuk 2. De methode biedt een consistente presentatie van de transformatie van de signalen en spectra in de ontvanger van een RF front-end.

Modellen van de mixer-oscillator combinatie zijn gedefinieerd en deze bieden een volledige interpretatie van de manier waarop de signalen en spectra worden getransformeerd van ingang naar uitgang in verschillende ontvanger-topologieën.

Tenslotte is de toepassing van de mixer-oscillator modellen uitgebreid voor het berekenen van de spiegel-onderdrukingsverhouding in *quadratuurontvangers*

## SELECTIE VAN DE FUNCTIONELE PARAMETERS VOOR RF FRONT-END SCHAKELINGEN

In Hoofdstuk 4 is een procedure geïntroduceerd voor het toewijzen van functionele parameters aan RF front-end schakelingen. Met behulp van optimalisatie van de prestatie van een RF systeem met betrekking tot  $F/P_{IP3}$  (de ruisfactor gedeeld door het 3<sup>de</sup>-orde intercept-punt van het ingangsvermogen) is het optimale dynamische bereik gevonden, en is er tegelijkertijd voldaan aan de eisen ten aanzien van ruis en lineariteit.

We toonden aan dat er een evenwichtspunt bestaat waar alle bijdragen van de circuitparameters aan de systeempparameters gelijk zijn. Daarnaast is het zo dat de keuze van de waarden voor dit evenwichtspunt overeen komt met ontwerp voor een optimaal dynamisch bereik en ontwerp voor gelijke vermindering van de ruis en verbetering van het lineaire gedrag. Tenslotte zijn een paar ontwerp-compromissen voor RF circuits geschetst met behulp van K-rail diagrammen. Omdat ze niet slechts naar één maar naar een aantal *werkingsvoorwaarden* verwijzen, beschrijven deze diagrammen de relaties en compromissen tussen de functionele parameters in RF circuits.

## ADAPTIVITEIT VAN VERSTERKERS MET LAGE RUIS

Hoofdstuk 5 behandelde adaptiviteits-fenomenen van versterkers met lage ruis. Maatstaven die de kwaliteit aangeven van de adaptiviteit (d.w.z. het bereik van de aanpassing) zijn geïntroduceerd, namelijk die voor de ingangsweerstand, de spanningsversterking, het ruisgetal en het 3<sup>de</sup>-orde intercept punt van het ingangsvermogen. Deze laten zien hoe versterkers met lage ruis op een adaptieve manier functionele eigenschappen kunnen uitwisselen tegen vermogensverbruik. K-rail diagrammen van versterkers zijn gebruikt voor een conceptuele beschrijving van de ontwerp-compromissen in versterkers met lage ruis.

## ADAPTIEVE SPANNINGSGESTUURDE OSCILLATOREN

Het concept van ontwerp voor adaptiviteit van oscillatoren is beschreven in Hoofdstuk 6. Dit bewerkstelligt een procedure voor het karakteriseren van het gedrag van adaptieve oscillatoren samen met de kwalitatieve en kwantitatieve beschrijving van de relaties en compromissen tussen de functionele parameters van oscillatoren.

Het geïntroduceerde concept van faseruis-aanpassing beschrijft hoe oscillatoren op adaptieve wijze prestatie kunnen uitwisselen tegen vermogensverbruik. De extremen van het bereik van de faseruis-aanpassing werden beschreven evenals de haalbare reductie van het vermogensverbruik.

Daarnaast werd het concept van het aanpassen van frequentie-transconductantie uitgelegd. De afgeleide formules laten zien op welke manier dit concept kan worden gebruikt om de oscillatorwerking onder controle te krijgen die veranderd is door aanpassing van de frequentie.

De conceptuele K-rail diagrammen zijn gebruikt om de gedrag van de oscillatoren te beschrijven. We lieten zien hoe deze diagrammen kunnen worden gebruikt om verschillende fenomenen en maatstaven voor de kwaliteit van de adaptie van de oscillatoren te interpreteren. Compromissen tussen de oscillatorparameters, zoals spanningszwaai, LC-kring conductantie, vermogensverbruik, faseruis en lusversterking, zijn kwalitatief en kwantitatief beschreven op een makkelijk te begrijpen manier met behulp van K-rail diagrammen.

## **ONTWERP VAN ADAPTIEVE SPANNINGSGESTUURDE OSCILLATOREN EN ADAPTIEVE FRONT-ENDS**

In applicaties met één standaard kan adaptiviteit worden gebruikt als mechanisme voor vermogensbesparing, hetgeen de prestatie van het gehele RF systeem verbetert. Door functionele bouwstenen te combineren voor verschillende standaarden bieden adaptieve schakelingen voor meerdere standaarden en meerdere *banden* een verlaagd vermogensverbruik, een kleiner chip-oppervlak, en lagere totale kosten. Hoofdstuk 7 demonstreerde deze zaken via twee oscillator-IC ontwerpen en een RF front-end ontwerp.

Daarnaast werd een 800MHz adaptieve spanningsgestuurde oscillator beschreven. Door de faseruis over een bereik van 7dB te regelen werd een vermogensbesparing gerealiseerd van meer dan een factor drie.

Verder is het ontwerp van een 2<sup>de</sup>-generatie/3<sup>de</sup>-generatie adaptieve multi-standaard spanningsgestuurde oscillator geïntroduceerd die werkt in DCS1800, WCDMA en WLAN-Bluetooth-DECT modes. Deze oscillator voldoet aan de faseruis-eisen van vijf verschillende standaarden met een vermogensverbruik van 18mW, 3.6mW en 1.5mW, respectievelijk.

Tenslotte is het ontwerp van een experimenteel 2<sup>de</sup>-generatie/3<sup>de</sup>-generatie adaptief multi-standaard front-end beschreven. Het ontwerp voldoet aan de eisen van de DCS1800, WCDMA, WLAN, Bluetooth, en DECT standaarden en verbruikt respectievelijk 20.2mA, 16.2mA, 15.4mA, 10.4mA en 9.9mA.

<i>acknowledgements by</i> 01.09.2004.	LIFE				WORK		
	support	discussion	friendship	love	technical support	discussion	guidance
<b>Myself</b>	+ +	+ +	+ +	+ +	+ +	+ +	+ +
<b>Wouter</b>	+	+ +	+ +		+	+ +	+ +
<b>RPG</b>	+ +	+ +	+ +	+ +			
<b>Vojkan<sup>2</sup></b>	+	+ +	+ +	+		+	
<b>Family</b>	+ +	+ +	+	+ +			
<b>John</b>		+	+		+	+	+ +
<b>Koen</b>		+	+		+	+ +	
<b>CvB&amp;AB</b>		+	+			+	
<b>ChrisV</b>		+	+			+	
<b>Wil/Luc</b>			+		+ +		
<b>Marijon<sup>m</sup></b>		+	+		+		
<b>Jaap</b>		+	+				





## BIOGRAPHY

Aleksandar Tasić was born on the 25<sup>th</sup> of September 1974 in Niš, Serbia. He started primary school when he was almost seven years old. During his school years, he received many awards for best pupil and was often elected as the class representative by his classmates.

Aleksandar started his degree at the Faculty of Electronics Engineering of the University of Niš in 1993. During his studies, he was involved in many education and social activities. After having participated in the demonstrations following the Serbian election fraud in 1997, he began preparing for departure. Despite unearthy conditions in all those years, he graduated successfully within 5 years and received the Electrical Engineer degree.

Power cuts, the booms of fighter planes breaking the sound barrier and the whistling of bombs, accompanying his postgraduate period, made him even more resolute to continue his career abroad.

After an interview at the Delft University of Technology, the Netherlands, in 2000, Aleksandar joined the Electronics Research Laboratory as a PhD student.

In his spare time he is a football referee for the Dutch Royal Football Association. Aleksandar intends to apply for Dutch citizenship and become a Dutch citizen of Serbian origin.